Converting Road Kinetic Energy to Electricity for Smart City Infrastructure

By

Niloufar Zabihi

Submitted in fulfilment of the requirements

for the Degree of Doctor of Philosophy (PhD)

Lancaster University Engineering Department

Abstract

Smart cities are becoming a reality around the world. They rely on smart infrastructures that use sensors, signals, and telecommunication devices for data collection, such as air pollution, traffic, health monitoring of the infrastructures, and communication. The collected data is employed to improve and optimize the performance of the urban facilities, resources, and buildings, which eventually can optimize the costs and the efficiency of the city. The necessary devices of smart cities such as the Internet of Things (IoT) and sensors are able to communicate, exchange data, and optimize the performance of the city's facilities. These devices (sensors, signals and IoT) need extra power sources to operate, which implies the demand to have an extra power source for smart cities infrastructure.

On the other hand, the transportation is one of the major energy-consuming sectors in the world. In the UK in 2020, the transport sector accounted for 40.5 million tonnes of oil equivalent energy consumption, and a large portion of it is consumed in roads transport. From this significant amount of energy, a large share of it is wasted as kinetic and thermal energy. The surface of the roads experience excessive vibrations each time a car passes, and the high temperature of the surface of the road is a well-known phenomenon. This research revolves around the wasted energy in the roadways and attempts to recover a part of this waste by converting it to electricity as a new source for powering the sensors, signalling devices and potentially lighting infrastructure in smart cities.

The first step of this study was designing a compact mechanical energy harvester based on the crank mechanism. Following the design, the performance of the mechanism was checked using motion and finite element analysis. Through motion analysis, the critical factors to be studied experimentally were identified. In the next step, the crank's components and the other parts of the system were assembled, and the motion analysis and FEA were verified.

The assembled prototype was tested under mechanical loads resembling the real field applications. The testing scenarios were nine different combinations of displacement magnitude and displacement speed of the top plate. In the next phase of the experimental study, the harvester's performance was improved using a different set of springs (the supporting system of the harvester). Then, a similar experimental plan was conducted on the harvester with the new sets of springs. The focus of the experiments in all phases is the electrical output of the harvester. Next, a financial and technical feasibility study was conducted based on the performance of the harvester.

The crank-based road energy harvester performs well under mechanical loads and can convert the top plate's vertical movements to rotation. In this system, all the components are bolted. Therefore, it has the advantage of mitigating any risk of backlash or mismatch between the components and is more compatible with higher driving speeds, as opposed to the existing mechanical road harvesters.

Based on the results and the feasibility analysis, the average energy output of 90 crank-based energy harvesters with the current design in one day can generate enough power for illuminating one streetlamp, and more than 90 LED signals, and over 180 outdoors air quality meters, which are essential elements of smart cities, for one day. In addition, the system has a more compact design and provides a smooth ride for the drivers as the maximum vertical displacement is limited to a maximum of 25 mm.

Keywords: Energy harvesting, slider crank, road, pavements, renewable energy, safety, electromagnetism, piezoelectric, sustainable transportation

Acknowledgement

I want to thank and express my appreciation to my supervisors. Professor Saafi who believed in me and gave me the chance to work on this research project. During my PhD, Professor Saafi supported me, especially in the challenging periods, and encouraged me to pivot when new ideas came up, or when a certain path did not yield results. I also wish to thank Professor Ye, for his comments and encouragements.

The experimental phase of this research would not have been possible without the support of the technical staff of the Lancaster university engineering department, specifically Mr Malcolm Weightman, Mr Mark Salisbury and Mr Andrew Steventon. I am grateful for their precious help with manufacturing the mechanical parts of my prototype.

I would also want to thank the SaferUP! Project and the European Union's Horizon 2020 research and innovation program, under the Marie Skłodowska-Curie grant agreement No. 65057, for funding this project.

Last but not least, I would want to express my deepest appreciations to my mother, for her unconditional love and spiritual supports, to my father, a brilliant engineer, who inspired me, supported, and loved me unconditionally until the last moment, and to my grandfather, whose spirituality and beautiful soul has always been an inspiration to me. I am forever indebted to them.

Table of Contents

List of Figures

List of Tables

1 Introduction

1.1 Problem Statement

Smart cities and infrastructures have gained tremendous attention in the last decades. They are cities that employ digital data collection, connectivity, and data analysis to optimize the city's services performance and facilitate intelligent decision-making, such as waste and pollution management, traffic management and infrastructures health monitoring [1]–[3]. As defined, data collecting devices such as sensors and cameras, telecommunication and processing devices are essential modules of smart cities.

The smart city sensors and instruments depend on electrical power to operate. Therefore, it is essential to invent new energy harvesting devices to provide off-grid and environmentally friendly electricity to power the numerous features of smart cities such as the Internet of Things (IoT) and control systems for structural health monitoring, the sensors of air pollution monitoring, water quality, waste managements, and potentially to lighting systems, which are the crucial features of smart cities. In addition, it is often difficult and expensive to connect the civil structures in the remote areas to the grid lines. Therefore, providing them with a sustainable off grid power source to operate is crucial for their continuous performance.

A number of low power energy harvester systems have been proposed and studied; however, they have some limitations. Being high dependant on the climate and weather conditions, difficult and expensive to install, having complicated and large structures, not suitable for energy storage, and causing significant speed deceleration of the passing vehicles are examples of the current road energy harvesting systems.

This research attempts to address these issues, by designing and evaluating the performance of a new micro-energy road harvester, with a compact design, simple installation, and maintenance, which can be employed in roadways.

1.2 Energy Consumption and Waste in the Infrastructure

Huge amount of energy is consumed annually which is spent in 4 main sectors of domestic, industry, transportation, and commercial [4]–[7], and among them, transportation is a major consuming sector, as shown in Figure 1.1 [4].

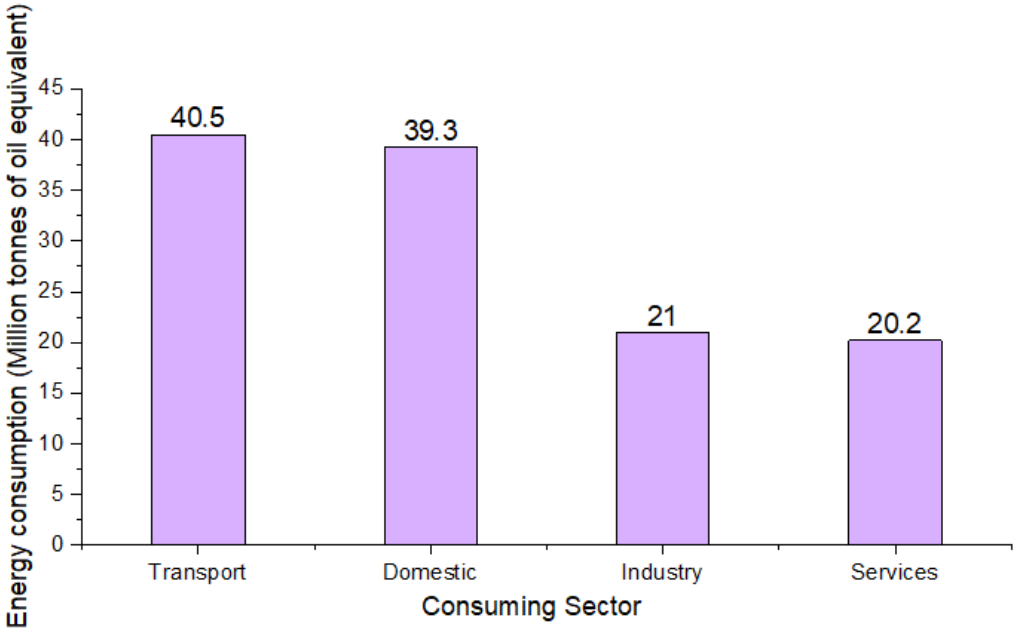

Figure 1.1: UK final energy consumption in each sector in 2020 [4]

According to Figure 1.1., the transportation industry was a significant energy consumer in 2020, with 40 million tonnes of oil equivalent spent on transferring goods and people through aviation, land, and marine transportation.

It is essential to acknowledge that from this amount of energy, a large portion is wasted in different forms of thermal energy, solar radiation, and vibration [8]. Considering the land transport, roadways and railroads experience extensive kinetic energy in the form of vibrations each time a vehicle passes. Moreover, hot surfaces of asphalt and concrete roads are a known phenomenon, especially in hot seasons of the year [9]–[11].

Over the past decades, commercial and academic research projects have been conducted to harness the wasted forms of energy in the roads and convert them to a usable form, such as

electricity. The potential sources of recovering wasted energy from land transportation and roadways are thermal energy and kinetic energy. Due to their output energy level, they are often categorised as micro-level energy harvesters, which are suitable for low-power devices [8], [12]

Roadway solar panels, solar collectors and piezoelectric road harvesters are examples of such projects [13]–[15]. Although the number of research items in this field of study has increased significantly over time, there are still obstacles preventing these projects from large scale implementation. The major obstacles are:

- High cost of manufacture and maintenance: devices such as piezoelectric elements and solar panels are generally expensive to manufacture and replace. They are also made of brittle components (piezoelectric ceramics and solar cells in this example). Therefore, they may also require extra maintenance sessions if applied on real roads. Consequently, their manufacturing and maintenance cost is remarkably higher than conventional energy generation methods.
- Very low energy output: piezoelectric and thermoelectric road harvesters often have a power output of nano and microwatts levels. This output may be suitable for remote areas signals; however, it is not suitable for continuous usage and storage due to their degradation.
- Dependence on the climate and daytime: the performance of solar panels, solar collectors and thermoelectric road energy harvesters highly depends on the time of the day, the weather conditions and even the climate of the region. For example, thermoelectric road harvesters perform well in arid and sun catching areas but will not perform well in cold and humid environments.

Another category of road energy harvester is designed within the concept of speed bumps. Their performance is based on vertical displacements of the road's surface [16]–[18]. The mechanical components of these systems are more commercially available, their power output is higher (in watt level), and they have a less complicated maintenance process [10], [19]. However, they often cause a significant reduction in the vehicles speed and have sizeable and heavy structures.

Moreover, although the performance of these systems has been examined in some studies, most of the studies have followed a specific mechanism of rack and pinion or hydraulic system [17], [18], [20], [21]. Hydraulic systems have a more complicated design, require more sophisticated components, and are therefore less practical for full-scale applications.

Therefore, it is necessary to design a new and compact system with a minimal effect on the driving speed and suitable power output for low power devices of smart cities. In this study, a new design of road energy harvester is proposed with a compact configuration and comprehensively studied through both simulation and experiments.

1.3 Aims and objectives

This study has designed and comprehensively studied a new electromagnetic road energy harvester through systematic simulations and laboratory experiments. Based on the discussed gaps, the following points have been addressed in this study:

1. To design a novel crank-based electromagnetic road energy harvester with a compact geometry and limited displacement level that can be installed as smooth road rumbles, generating clean and environmentally friendly electricity for sensors and devices of smart cities, with a minimum vertical displacement.
2. To ensure the mechanism of the crank harvester through deriving the equation of motion and conducting motion analysis. Decide about the maximum possible displacement level of the cap of the harvester, the influential factors on the output power of the system and design the experimental studies phase.
3. To control the designed harvester system using finite element analysis (FEA). As the system has a novel design, FEA was conducted to ensure that there is no critical stress concentration point in the mechanism, and under the applied force, the stress in none of the crank components exceeds the yielding strength of their material.

4. To build the designed prototype according to the dimensions and verify the motion analysis and FEA results by applying laboratory forces.

5. To conduct the experimental study based on the factors identified in the motion analysis and evaluate the performance of the crank harvester under various mechanical conditions in terms of the electrical outputs.

6. To evaluate and improve the performance of the crank harvester using different supporting components and assess the feasibility of having such an energy harvesting system on the roads.

1.4 Research Methodology

To conduct this comprehensive study, first, a crank mechanism was designed and adapted to the concept of a road rumble or smoot speed bump, performing under vertical displacements of the cap. The initial design of the system had a diagonal crank component. However, it was realised through motion analysis that the diagonal crank would result in a minimal rotation, and the chances of having a rigid body in the prototype will be significant. Therefore, the design was corrected, and a vertical crank was designed.

Once designed, it was modelled in Solidworks with appropriate mates to perform motion analysis, ensure its performance, and decide the maximum possible displacement on the harvester's cap. Moreover, as the system has an electromagnetic generator, the motion analysis was used to decide the experimental testing scenarios. It is known that the electrical output of an electromagnetic generator depends on its angular speed. Therefore, motion analysis was used to understand the effective factors on the angular speed of the crank, which is eventually connected to the generator. Moreover, FEA is used to ensure the mechanical stability of the harvester under mechanical forces.

As the harvester prototype was built, and its performance was evaluated under cyclic mechanical forces, then the performance of the system was further improved by using different sets of supporting springs.

1.5 Dissertation Outlines

After the brief introduction given is in this chapter, the succeeding chapters are outlined as follows:

Chapter 2: a comprehensive review of the literature and the published works on energy harvesting from roads is given. In this chapter, five different methods are discussed. First, a brief introduction to the background is given for each method, followed by the research highlights in the field.

Chapter 3: This chapter incorporates the details of the design of the novel crank road energy harvester, followed by its simulation in Solidworks and FEA results. Moreover, the laboratory verifications of these simulations are also presented in this chapter.

Chapter 4: presents the manufacturing and technical details of each component and the assembly of the system. After the assembly, the experimental plan of testing the first prototype in the laboratory is discussed, followed by the detailed results and discussions of testing the prototype.

Chapter 5: This chapter gives the detailed experimental results and discussions of the next phase of the research, in which the performance of the harvester was evaluated and improved using 4 other spring sets as the supporting system.

Chapter 6: In this chapter, the crank road energy harvester's financial and technical feasibility analysis is brought.

Chapter 7: This chapter summarizes the results and discussions made in this research, incorporating the design highlights and the simulations done on the model, the synopses of the

discussions and the primary outcomes of the research. Moreover, some recommendations are also given for further improvements and future research steps in this field.

2 Literature review

2.1 Introduction

With the concept of smart cities and infrastructures solidifying, there is an essential demand for having new environmentally friendly energy generating methods to run their low-power devices and facilities, such as the sensors and the IoT.

On the other hand, In the UK, annually, around 40.5 million tonnes of oil equivalent energy is spent in the transportation sector, from which a significant portion is wasted in the forms of kinetic or solar energy. The focus of this project is recovering a part of this wasted energy, to provide sustainable off-grid energy to the mentioned devices of the smart cities.

Different methods are available for converting kinetic or solar energy to electricity or storing it. Several projects have adopted these methods in roads, aiming to harvest energy from roads. In this chapter, these methods are explained briefly, and the highlights of the conducted projects on each method are described.

2.2 Potentials of harvesting energy from road pavements

Road pavements and carriageways are significant components of land transport facilitating the transference of passengers and goods. In this section, the forms of wasted energy in roadways are investigated, and the potential technologies to recover some of the wasted energy will be presented.

Road pavements, regardless of their material type, are usually exposed to direct sunlight during the day. Therefore, especially in hot seasons daytime, the temperature of the surface of the roads increases, while at a depth of the road, the temperature is lower. The solar energy received by the road surface is generally wasted, as one part of it is reflected from the surface, and the other part is absorbed by the road and is spent on increasing the surface temperature [19], [22]–[27].

Kinetic is the other form of energy available in the roads, referring to the vibrations and mechanical displacements of the road surface due to the vehicle's moving. In this case, a part of the kinetic energy of the vehicles is wasted through surface deformation and vibrations, which eventually dissipate. The vibrations (frequency and amplitude) and the displacements depend on the kinetic energy of the vehicles, directly related to their speed and mass. Effectively, it is shown experimentally that the road vibration frequency and vehicle' speed are linearly correlated [8], [19], [28]–[32].

Kinetic energy and solar energy are the main two wasted forms in the roadways transportation sector. Figure 2.1 shows the possible methods of recovering a part of this waste and converting it to a useful form of energy.

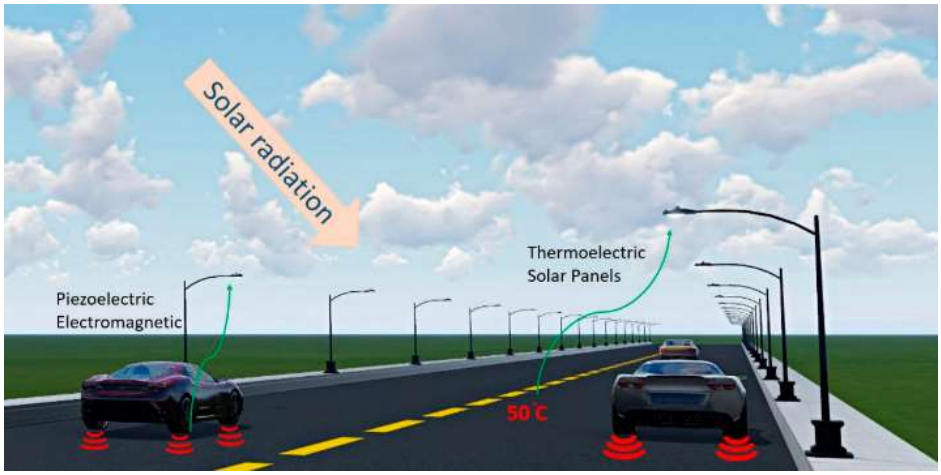

Figure 2.1: potentials of harvesting energy from road pavements [19]

Figure 2.2 outlines the technologies that can be used to harness energy from the wasted forms in road pavements.

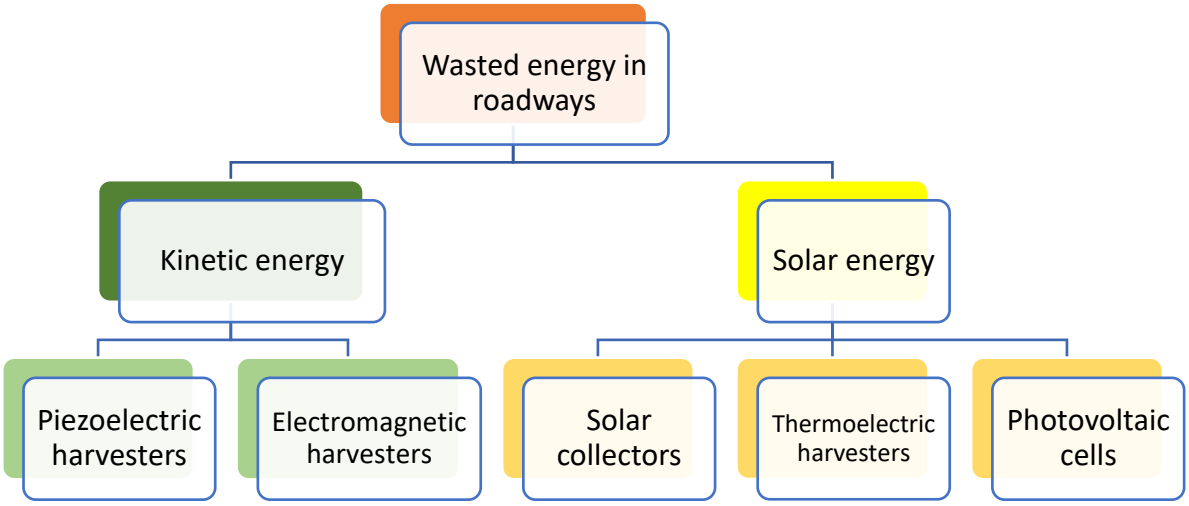

Figure 2.2: Roadways wasted energy diagrams and concepts to recover them to useful forms

In the following sections, each concept is explained, and the relevant projects carried out to employ that concept and recover energy from roads is briefly discussed.

2.3 Piezoelectric Harvesters

Piezoelectric harvesters are based on piezoelectric materials, which have the characteristic of converting mechanical vibrations to electricity. Quartz and Tourmaline are naturally occurring piezoelectric ceramics, while Barium Titanate and Lead Zirconate Titanate (PZT) are synthesized ceramics with a strong piezoelectric effect.

The piezoelectric effect is divided into two categories of direct and indirect piezoelectricity. In the direct piezoelectric effect, mechanical energy (vibrations) is converted to electricity, and in the indirect effect, an applied electrical potential (voltage) is converted to mechanical vibrations. All piezoelectric ceramics exhibit both direct and indirect piezoelectric effects.

These piezoelectric ceramics comprise of a charged particle (ion) in the middle of their lattice structure, which is mobile and displaces in a fixed direction (polarization direction) when a mechanical load is applied on (direct piezoelectricity). Conversely, when an electrical voltage is applied on the sides of a piezoelectric ceramic, they vibrate (indirect piezoelectricity).

As the road pavements are under constant vibrations from passing vehicles, the direct piezoelectric effect is a suitable method for converting those vibrations to electricity. In the following section, the mathematical model describing the piezoelectric effect is discussed.

2.3.1 Piezoelectric mathematical model

In direct piezoelectricity, the generated electricity is a function of the applied stress [33], [34]. The density of the generated charges on the surface of a piezoelectric ceramic under applied stress is expressed as:

$$P = d \times T \qquad \text{Equation 2.1}$$

Where *P* is the polarization vector, *d* is the material's strain coefficient, and *T* is the stress vector. It is worth explaining that the polarization vector's magnitude is equal to the charge density generated at the opposite surfaces of the ceramic. On the other hand, in the reversed piezoelectric effect, the strain caused by the piezoelectric effect is

$$S = d \times E \qquad \text{Equation 2.2}$$

Where *S* is the mechanical strain, *d* is the strain coefficient, and *E* is the magnitude of the electrical field applied on the piezoelectric ceramic.

As explained, mechanical and electrical variables are interchanged in the actual practice of piezoelectric materials. Hence linear electromechanical coupling tensor equations are used to describe the piezoelectric behaviour. However, these equations are only used for the linear state of the piezoelectric materials (low vibration frequencies stress and strain levels). The piezoelectric electromechanical tensor is as follows.

$$\begin{bmatrix} D \\ S \end{bmatrix} = \begin{bmatrix} d & \epsilon^T \\ s^E & d \end{bmatrix} \times \begin{bmatrix} T \\ E \end{bmatrix} \qquad \text{Equation 2.3}$$

Where D is the dielectric displacement, S is the mechanical strain, d is the charge coefficient of the piezoelectric material, s^E is the elastic compliance at the constant electric field, ϵ^T is the relative permittivity, E is the electrical field and T is the stress tensor.

Piezoelectric materials are anisotropic ceramics, meaning that their mechanical and electrical properties are not equal in different directions. Therefore, the materials' properties, such as the charge coefficients, are expressed as tensors with directions. Figure 2.3 shows the coordinate system for defining the tensors and the linear equations governing the piezoelectric materials.

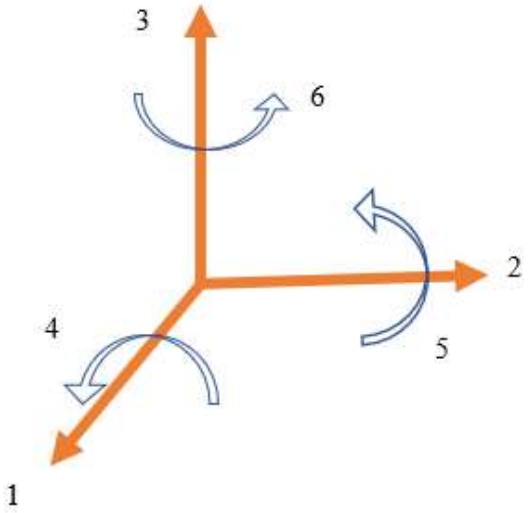

Figure 2.3: tensor directions for defining the properties of the piezoelectric material and the electromechanical equations

Needless to mention that the properties of the material required for analyzing piezoelectric element's behaviours are also given in matrix forms. The complete form of the linear set of equation 2.3 is:

$$\begin{bmatrix} D_1 \\ D_2 \\ D_3 \end{bmatrix} = \begin{bmatrix} d_{11} & d_{12} & d_{13} & d_{14} & d_{15} & d_{16} \\ d_{21} & d_{22} & d_{23} & d_{24} & d_{25} & d_{26} \\ d_{31} & d_{32} & d_{33} & d_{34} & d_{35} & d_{36} \end{bmatrix} \begin{bmatrix} T_1 \\ T_2 \\ T_3 \\ T_4 \\ T_5 \\ T_6 \end{bmatrix} + \begin{bmatrix} \varepsilon_{11}^T & \varepsilon_{12}^T & \varepsilon_{13}^T \\ \varepsilon_{21}^T & \varepsilon_{22}^T & \varepsilon_{23}^T \\ \varepsilon_{31}^T & \varepsilon_{32}^T & \varepsilon_{33}^T \end{bmatrix} \begin{bmatrix} E_1 \\ E_2 \\ E_3 \end{bmatrix}$$

$$\begin{bmatrix} S_1 \\ S_2 \\ S_3 \\ S_4 \\ S_5 \\ S_6 \end{bmatrix} = \begin{bmatrix} s_{11}^E & s_{12}^E & s_{13}^E & s_{14}^E & s_{15}^E & s_{16}^E \\ s_{21}^E & s_{22}^E & s_{23}^E & s_{24}^E & s_{25}^E & s_{26}^E \\ s_{31}^E & s_{32}^E & s_{33}^E & s_{34}^E & s_{35}^E & s_{36}^E \\ s_{41}^E & s_{42}^E & s_{43}^E & s_{44}^E & s_{45}^E & s_{46}^E \\ s_{51}^E & s_{52}^E & s_{53}^E & s_{54}^E & s_{55}^E & s_{56}^E \\ s_{61}^E & s_{62}^E & s_{63}^E & s_{64}^E & s_{65}^E & s_{66}^E \end{bmatrix} \begin{bmatrix} T_1 \\ T_2 \\ T_3 \\ T_4 \\ T_5 \\ T_6 \end{bmatrix} + \begin{bmatrix} d_{11} & d_{12} & d_{13} \\ d_{21} & d_{22} & d_{23} \\ d_{31} & d_{32} & d_{33} \\ d_{41} & d_{42} & d_{43} \\ d_{51} & d_{52} & d_{53} \\ d_{61} & d_{62} & d_{63} \end{bmatrix} \begin{bmatrix} E_1 \\ E_2 \\ E_3 \end{bmatrix}$$

Following the constitutive linear equations, it is possible to estimate the output of the piezoelectric harvesters under various loads and frequencies.

For a piezoelectric element that is under mechanical force (F) in the same direction of polarization, the generated electrical charge (Q) is calculated by [14], [33], [35]:

$$Q = d_{33}\, F \qquad \text{Equation 2.4}$$

Hence the charge density is

$$D = \frac{Q}{A} \qquad \text{Equation 2.5}$$

Where A is the cross-sectional area of the piezoelectric ceramic. Therefore

$$DA = d_{33}\, F \rightarrow D = \frac{d_{33}\, F}{A} = d_{33}\sigma \qquad \text{Equation 2.6}$$

Charge density (D) is also related to the electric field (E) as follows

$$D = \epsilon_0 \epsilon_r E \qquad \text{Equation 2.7}$$

Where ϵ_r and ϵ_0 are relative permittivity of the piezoelectric ceramic and the permittivity constant of vacuum (8.85x 10e-12 $C{\cdot}V^{-1}{\cdot}m^{-1}$). Therefore

$$E = \frac{d_{33}\sigma}{\epsilon_0 \epsilon_r} = g_{33}\sigma \qquad \text{Equation 2.8}$$

The voltage and electric field are interconnected as:

$$V = Eh \qquad \text{Equation 2.9}$$

Where h is the height of the sample, therefore, the generated voltage of a piezoelectric harvester is:

$$V = g_{33}\sigma h \qquad \text{Equation 2.10}$$

In the following section, the recent experimental and analytical studies on the piezoelectric road energy harvesters are presented.

2.3.2 Piezoelectric road energy harvesters

Piezoelectric harvesters come in various shapes such as cymbal, bridge and disks. Each of these forms has been studied in theoretical and experimental studies. The concept of incorporating piezoelectric harvesters in roadways started around developing sensors for applications such as speed detection or weight in motion systems. In early work in 1999, Szary et al., worked on developing and implementing polymer-based piezoelectric elements for such applications [36]. Their research work addressed the existing issue of uncertainty of piezoelectric road sensors that their response may be affected by time and temperature. Also, the high brittleness of the piezoelectric censors makes them unsuitable for embedding in the road grooves as sensors. They developed composites sensors of piezoelectric ceramic and polymers to tackle the brittleness problem. The laboratory results showed that compared to the other polymeric piezoelectric polymers (PVDF), the polymer ceramic composite outputs are more stable with regards to time and various passing vehicles [36]. Figure 2.4 shows the developed sensor in this study.

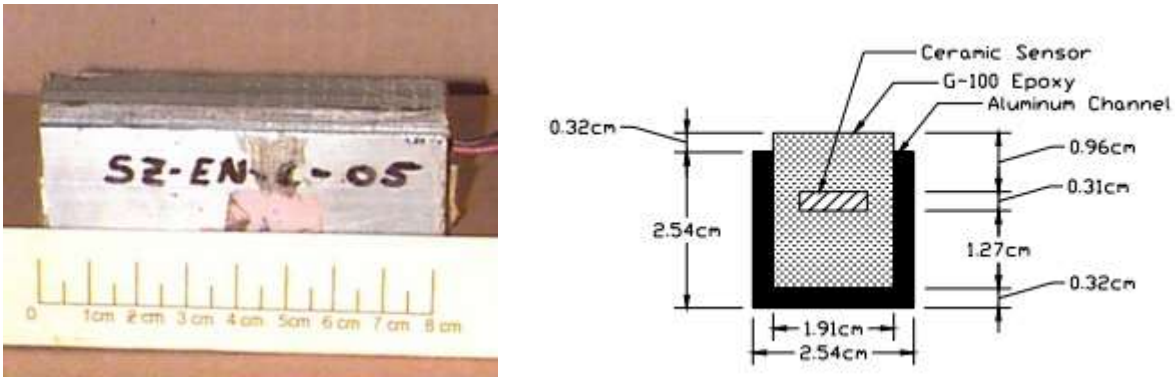

a b

Figure 2.4: Developed piezoelectric ceramic and polymer composite, a) Composite sensor's photo, b) composite's cross-sectional view. Reprinted with permission from [36]

Arms et al., in 2005, worked on developing a low-frequency piezoelectric based energy harvester that could assist in powering low consuming wireless sensing nodes. It was demonstrated that the output power significantly improves by affixing a resonant mass at the tip of the piezoelectric harvester to vibrate at the resonant frequency. Moreover, the higher strain in the piezoelectric beam generates higher power. At the resonant frequency (57 HZ), the piezoelectric harvester generates around 2000 μW. Since the vibration frequencies inroads are low, this harvester was also suggested to be suitable for such applications [37].

Zhao et al. conducted a few studies on implementing pile (cylinder) and piezoelectric cymbal harvesters in pavements to harvest energy. In their study, two cymbal harvester's performances were compared to each other. The models' geometries were identical; however, model A was directly in contact with the asphalt pavement and model B was encased in a metal box and placed in the asphalt layer. Through FEA analysis, it was shown that model A gave higher output voltage (97.33 V) than model B (76.53 V) due to experiencing higher strains resulting from being directly in touch with the pavement. Moreover, it was shown that the optimum geometry of the piezoelectric cymbal harvester is cymbal diameter of 32 mm, cavity diameter of 22 mm, and piezoelectric thickness of 0.3 mm gives a maximum output power of 1.2 mW. In another study by the same group, the pile piezoelectric harvester's performance in pavements was evaluated. It was shown that 8 to 16 piles of cylindric piezoelectric harvesters with the cross-sectional area of 0.04 m^2 [38]–[40].

More recent studies on piezoelectric road harvesters are more focused on increasing the output power of the harvesters.

In another attempt, bridge-shaped piezoelectric harvesters were built and tested to harvest energy from roads. A unit of 64 bridge piezoelectric harvesters was built, and the harvesters, which were electronically connected, were placed in a protective box. The unit was tested in the laboratory under the frequency of 5 HZ and the mechanical stress of 0.7 MPa. The output

power of the unit was measured using external resistors ranging from 50 Kohm to 1 Mohm. It was observed that the optimum resistor is 400 Kohm, at which the power maximizes around 2.1 mWatts. It was also observed that pavement's temperature is not effective on the output power; however, as the loading speed increases, the frequency increases, leading to higher power output. Moreover, it was proved that the power output reduces by increasing the harvester unit's embedding depth of the harvester unit. This is consistent with the observation in [41], which is related to a lower fraction of the vehicle's load transmitted to the harvester [42]. Figure 2.5 shows the built bridge harvester unit and the testing set-up.

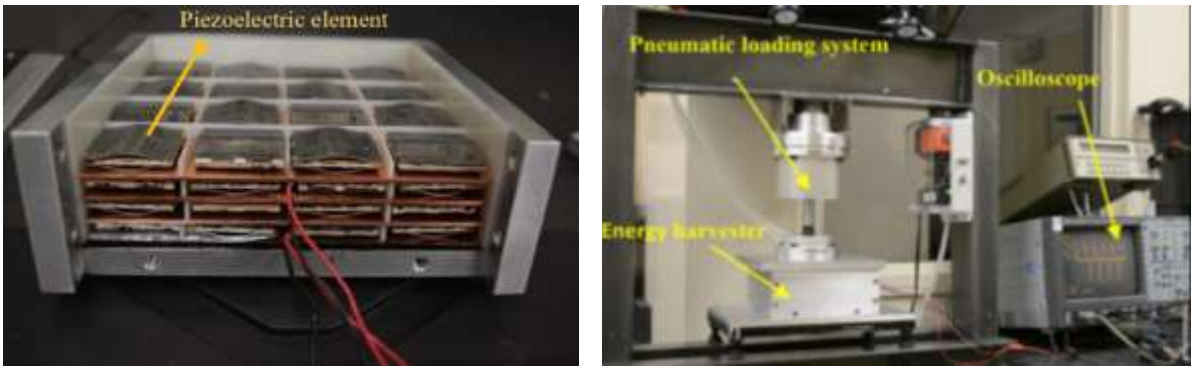

a b

Figure 2.5: a) Bridge harvester unit. b) The harvester unit's test set-up. Reprinted with permission from [42]

Cymbal piezoelectric harvesters were the focus of another study in 2019. Liu et al. developed a radially layered cymbal piezoelectric harvester for low-frequency applications (including roadways). The experimental study showed that this harvester could generate 0.92 mW, under the mechanical load of 500 N and 20 HZ and using the external resistor of 80 Mohm. Figure 2.6 shows the radially layered piezoelectric harvester.

a b

Figure 2.6: a) Internal arrangement of the piezoelectric cymbal harvester. b) Cymbal piezoelectric harvester. Reprinted with permission from [43]

In a thorough study that included experimental and field tests, Xiong et al. developed a road piezoelectric harvester unit, consisting of 9 piezoelectric disks, electrically connected in parallel. In total, 6 units of piezoelectric harvesters were built and embedded in the field test road. It was observed that the output power is directly affected by the type of the vehicle, i.e., the axle load applied on the harvesters. The average output power of the harvesters varies between 1.1 mW to 3.1 mW. It was shown that only about 14% of the axle weight is transmitted to the embedded harvesters, and it was recommended that by improving this percentage, the output power would increase [41], [44]. The built harvester unit and the embedding road is shown in Figure 2.7.

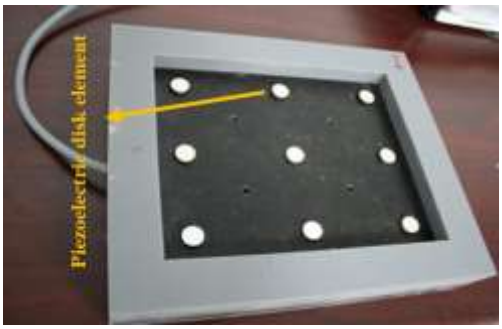

a

b

c

Figure 2.7: a, b) Disk piezoelectric energy harvester. c) Embedded piezoelectric harvesters in the road

Reprinted with permission from [41], [44]

Disk-shaped piezoelectric harvesters were also studied by Roshani et al. [14], [45], [46]. In their study, a piezoelectric road harvester was built and tested. The harvester unit was a thin board comprising 4 to 16 piezoelectric disks, fixed on the board and electrically connected in parallel. Figure 2.8 shows the configurations of the harvester unit and the testing setup. The harvester was tested under mechanical loads of 1 to 3 KN and the frequencies of 5 to 20 HZ, representing the mechanical loads applied from the vehicles.

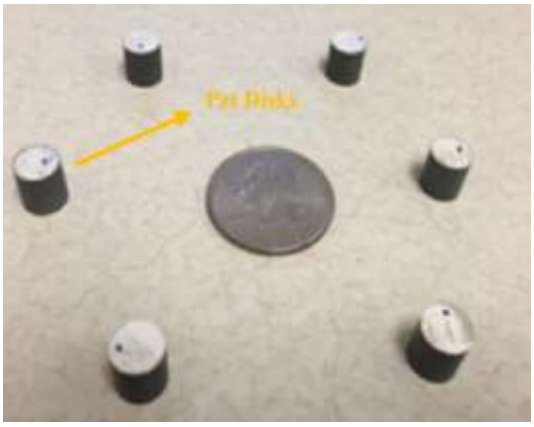

a

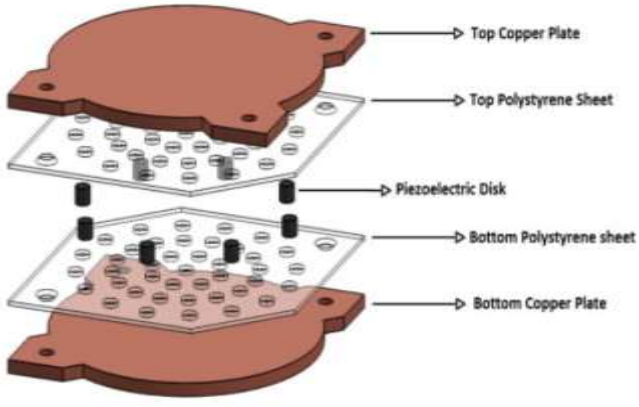

b

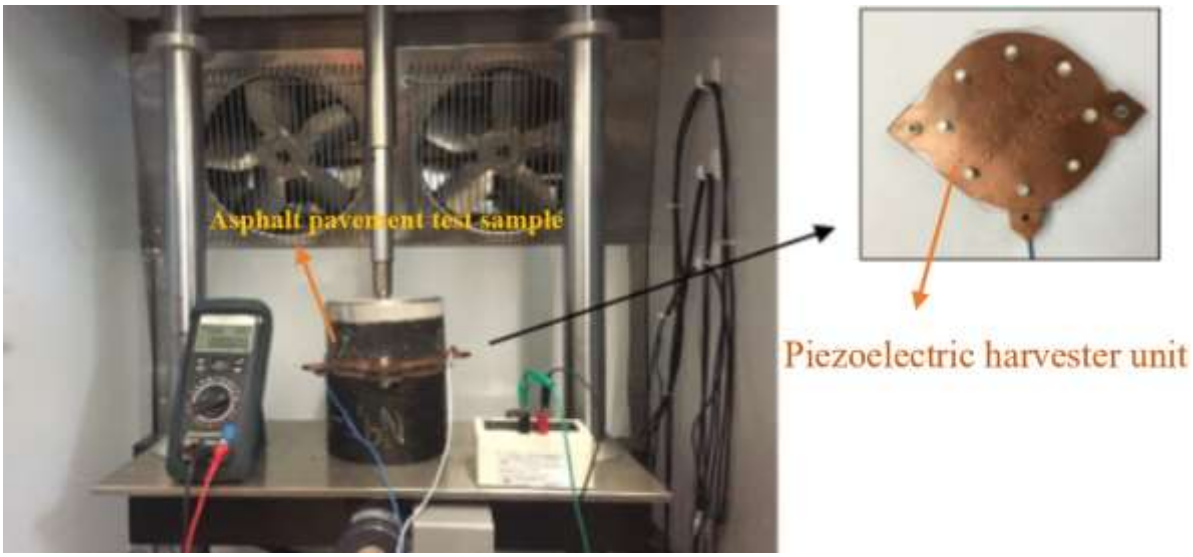

c

Figure 2.8: a) Piezoelectric disk, b) Disk's configuration in the harvester unit, c) Harvester unit's test set up. Reprinted with permission from [46]

The results of the study show that the external resistance of 17.5 Mohm, maximizes the output power. Increasing the load's magnitude from 1 to 3 KN, leads to an increase in the output power from 0.5 mW to around 3.8 mW. Increasing the frequency also results in having higher output power. Increasing the temperature has a minor influence on reducing the output power. The highest power (16 mW) was obtained from the 4 piezoelectric harvesters under 3 KN load and 20 HZ frequency [14].

Another form of the piezoelectric disk is the stack piezoelectric harvester, where the piezoelectric disks are piled on top of each other. The advantage of stack piezoelectric harvesters is that connecting the disks in series (as shown in Figure 2.9) makes it possible to make cylindrical piezoelectric of almost any height. According to equation 2.10, increasing the height of the piezoelectric harvester increases the output voltage, which is a positive point in energy harvesting.

Stack piezoelectric elements have also been implemented for harvesting energy from roads. Wang et al., conducted a preparation and testing stack piezoelectric harvesters for pavement energy harvesting purposes. The stack elements were tested in MTS machine at 10 HZ

frequency and 0.7 MPa of stress. The optimal external resistor of the stacked piezoelectric was found equal to 30 Kohm, resulting in the maximum power of 22 mW [47].

Khalili et al. also investigated the power generation and modelling of stack piezoelectric harvesters for pavement applications [48], [49]. The stacked piezoelectric generated a maximum power of 35 mW under the mechanical load of 6 KN, and the frequency of 10 HZ. the optimizing external resistor was found to be around 3 Mohm and was independent of the loading frequency and magnitude. In this research, the focus is also on analytically simulating the piezoelectric harvester's responses (voltage and current). The electrical equivalent circuit of the piezoelectric harvester was also analyzed in this study. The piezoelectric stack and the equivalent circuit are shown in Figure 2.9.

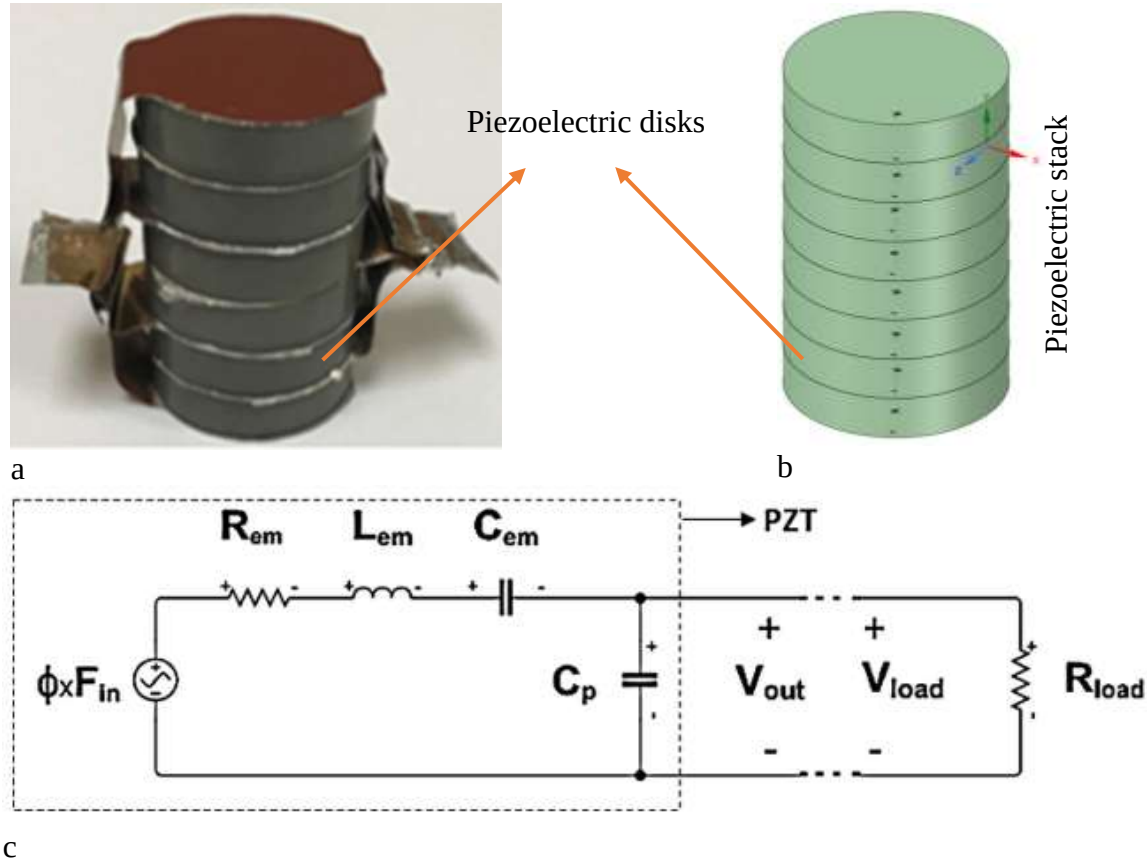

Figure 2.9: a and b) Piezoelectric stack, c) Equivalent electrical circuit of piezoelectric harvester used to analytically characterise the harvester. Reprinted with permission from [48]

In another study, stack piezoelectric harvesters were built consisting of 3 stacks of 36 piezoelectric disks. The power output of the harvester was evaluated through an experimental

study, in which the harvester was tested under cyclic mechanical loads of 1 to 6 HZ and load amplitudes of 680 N, 1020 N and 1360 N. The results showed that the output power increases by increasing both frequency and the load magnitude. The maximum harvester power was about 88 mW, obtained when the frequency is 6 HZ and the applied load is 1360 N [29].

Piezoelectric stacks were also used to build a piezoelectric energy harvester tower for road applications. Piezoelectric stack elements were placed in cylindrical harvester units and placed in the pavement. The harvester was tested under impact loads of 1333 N and low frequency (around 0.1 HZ) in the laboratory. The output power of the harvester was about 31 mW in loading and 69 mW in unloading [50].

Song et al. built and tested a road piezoelectric energy harvester comprised of piezoelectric cantilever beams with a tuned natural frequency. The concept is to have the cantilever beams vibrate almost at their natural frequency to maximize the output power. A harvester unit with 48 piezoelectric beams was made and tested in the laboratory under the frequency of 10 HZ and displacement of 1 mm. The piezoelectric beams are connected to the top plate of the harvester, which is held by 4 springs in the corners and attached to the bottom plate. Figure 2.10 shows their test set-up and harvester design.

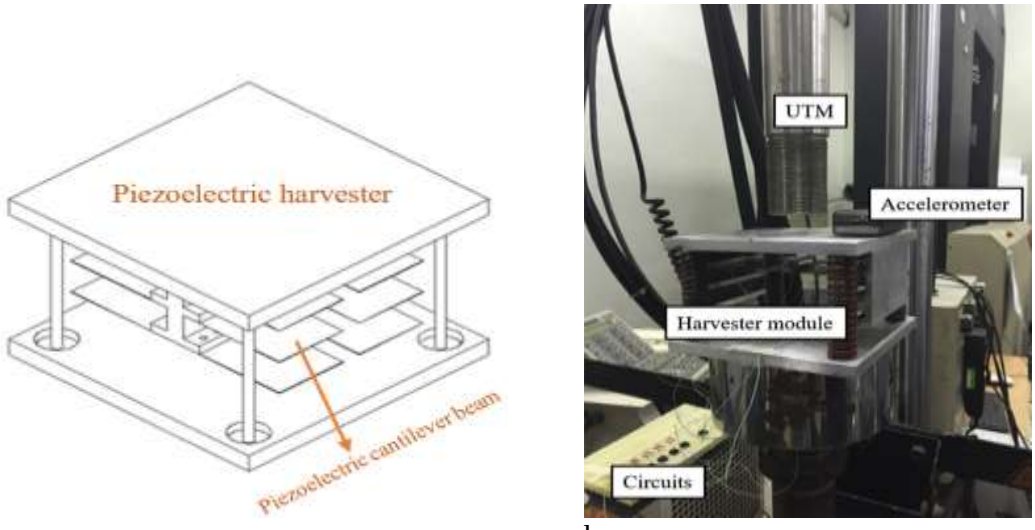

a b

Figure 2.10: a) Piezoelectric cantilever beam harvester, b) Testing the harvester under UTM.

Reprinted with permission from [28].

Through experimental studies, the maximum power harvested from this unit was 184 µW obtained by measuring the voltage around the optimizing resistance of 70 Kohm [28].

Yang et al. developed an impact based piezoelectric road harvester using beams of piezoelectric elements. Following the FEA, it was understood that having fixed ends piezoelectric elements is more suitable for energy harvesting, as it results in higher output voltage. Through experiments using UTM and MMLS3 testing devices, impact forces in the form of 1, 1.2, 2 mm and 2.5 mm displacement were applied on the harvester at the frequency of 5 to 15 HZ. The maximum power was 483 mW, occurring when both displacement and frequency are at their maximum values. The performance of the harvester is suitable for building smart highways and powering the signals and communication devices in smart roads [51].

2.3.2.1 Comparison Between the Piezoelectric Road Harvesters and Challenges

In the previous section, the suitable piezoelectric harvesters for low-frequency applications such as roadways were reviewed, focusing on their output power and performance. As a result, it was revealed that the piezoelectric road harvesters have a maximum output power in the order of a few milliwatts. Figure 2.11 shows the power output of each research project.

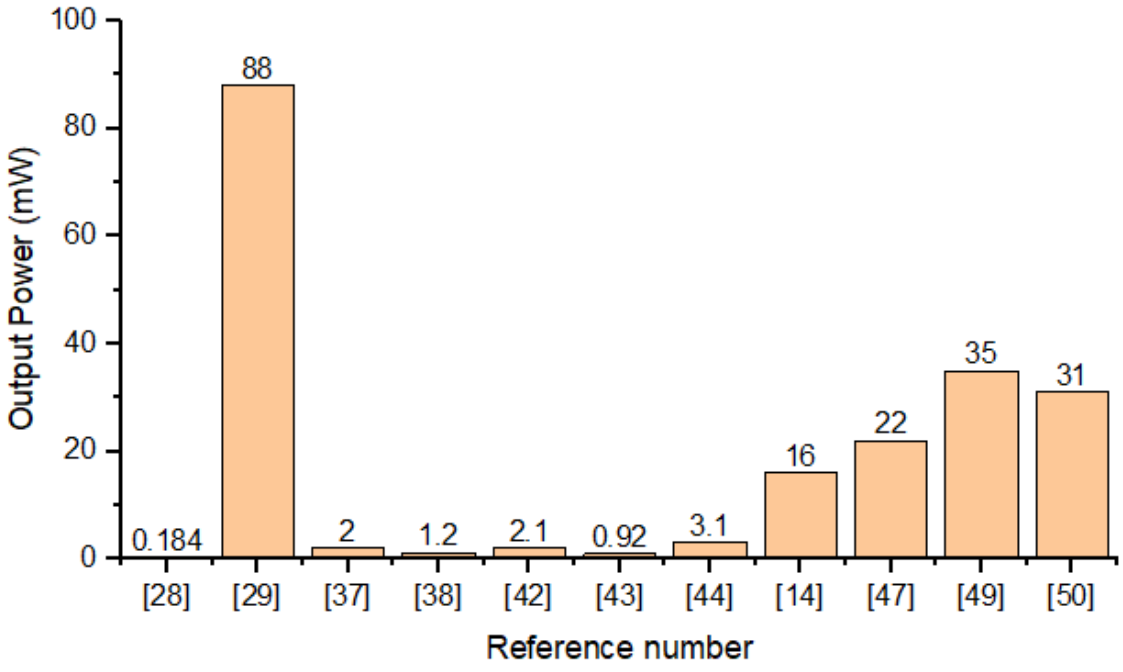

Figure 2.11: Power output results of piezoelectric road energy harvesters from different references

The results plotted in Figure 2.11 are from experimental or field test studies of road piezoelectric energy harvesters in the last 5 years. Except for the two cases, the majority of the results are between 0.184 mW and 31 mW. This level of output power is enough for powering the signals and telecommunication systems in smart highways.

The employment of piezoelectric harvesters in the roadways has some challenges that still need to be addressed. A significant challenge is their maintenance and their efficient service life. Although piezoelectric ceramics have high compressive strength, they are brittle and susceptible to sudden fracture failure. Therefore, it is important to encase them in a protective box as an extra reinforcement against the possible damages. In addition, as the harvesters are placed underneath the road, it is better to have its service life matching the pavement's maintenance periods to minimize extra traffic disruptions.

Another important aspect is the cost of the manufacturing and installation of the road piezoelectric harvesters. Table 2.1 shows the cost of a few piezoelectric road energy harvester projects.

Table 2.1: Cost analysis of piezoelectric road pavements

Reference	Project years	Levelized cost of energy using this harvester	Maximum output power of one unit harvester	Cost of one unit Harvester
[49]	2020	N/A	35 mW	$ 650
[52]	2017	$19.15/kWh	N/A	N/A
[41]	2013	$240/kWh	N/A	N/A

2.4 Electromagnetic Harvesters

Electromagnetic road energy harvesters rely on electromagnetism to convert mechanical to electrical energy. Most of these harvesters have an electromagnetic generator as a key element

that converts mechanical energy (rotational) to electrical energy. These generators were also developed based on electromagnetism, which was discovered and formulated by Faraday and Maxwell. The general Faraday Maxwell law outlined that a spatially alternating electrical field is always associated with an alternating magnetic field [53]. The mathematical expression is as follows

$$\nabla \times E = -\frac{\partial B}{\partial t} \qquad \text{Equation 2.11}$$

Where E is the electrical field, B is the magnetic field, t is time, and ∇ is the del operator. As the electromagnetic generator plays a key role in these harvesters, they are designed based on translating the vertical displacements of the pavement's surface to rotational movements. In order to have this translation, there are a number of mechanisms such as a hydraulic system, roller and rack and pinion. Figure 2.12 shows these mechanisms.

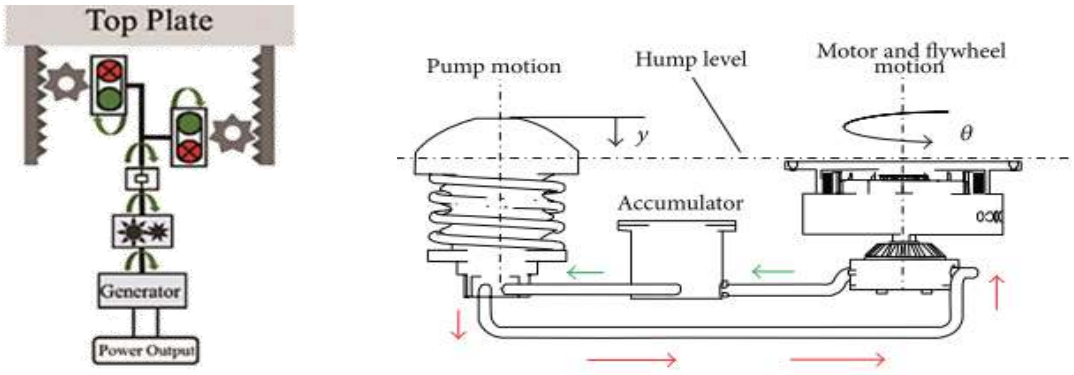

a b

Figure 2.12: a) Rack and pinion mechanism used in [54], b) the hydraulic mechanism [55]. Reprinted with permission from [54] and [55]

2.4.1 Electromagnetic Road Harvesters: Principles and Designs

From a mechanical design viewpoint, the performance of road electromagnetic harvesters is mainly based on converting reciprocating (vertical) displacements into rotation, which enables the system to generate electricity through having an electromagnetic generator installed in the system.

There are some mechanisms of converting the reciprocating to rotational displacement, which can be categorized into conversion using mechanical components and hydraulic systems. Examples of such mechanisms are crankshaft, and rack and pinion systems that have mechanical components, and hydraulic piston and turbines which employ hydraulic fluids to convert the reciprocal to rotational motion. Each of these mechanisms have a long history of being employed in various engineering applications. Crankshaft mechanism are employed in combustion engines, rack and pinion is commonly used in machineries and rack railways, and hydraulic systems are commonly used in piston pumps [56]–[58]. Figure 2.31 shows examples of these mechanisms.

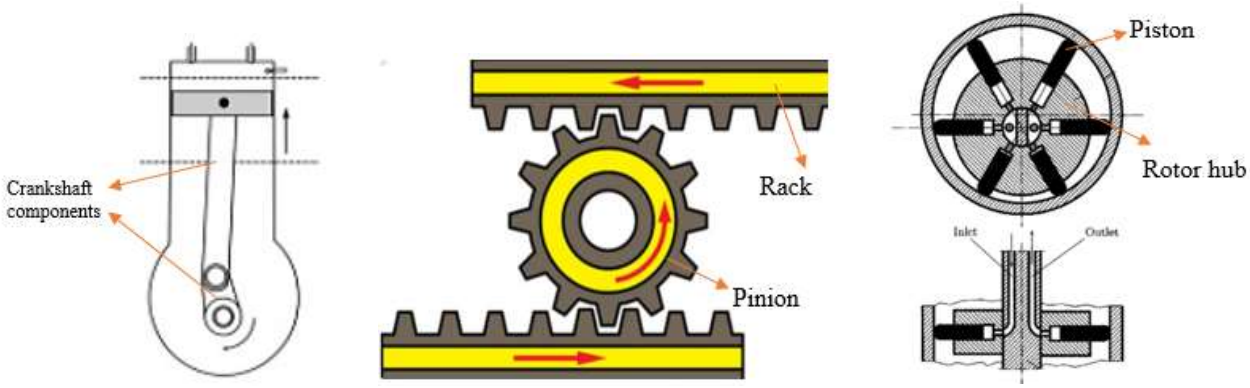

a b c

Figure 2.13: Crankshaft mechanism in a combustion engine (compression), reprinted with permission from [59] b) Rack and pinion, reprinted with permission from [60] c) Hydraulic radial piston pump, reprinted with permission from [61]

By comparing these mechanisms together, it can be seen that the crankshaft (Figure 2.31a) has a simpler design and as its components are joint together, there is no risk of backlash or mismatch, which is a risk factor in rack and pinion systems. Also, compared to the hydraulic systems, the systems with mechanical components have a less complicated mechanism design and connections.

In the following section, the mathematical model and the key factors governing the rack and pinion and the crank mechanisms are discussed.

2.4.1.1 Crank Mechanism's Design and Model

Crank mechanism, depending on the number of linkages are different and their set up, can be in-line or offset crank. Figure 2.14 shows an example of the free-body diagrams of crank an inline crank mechanism.

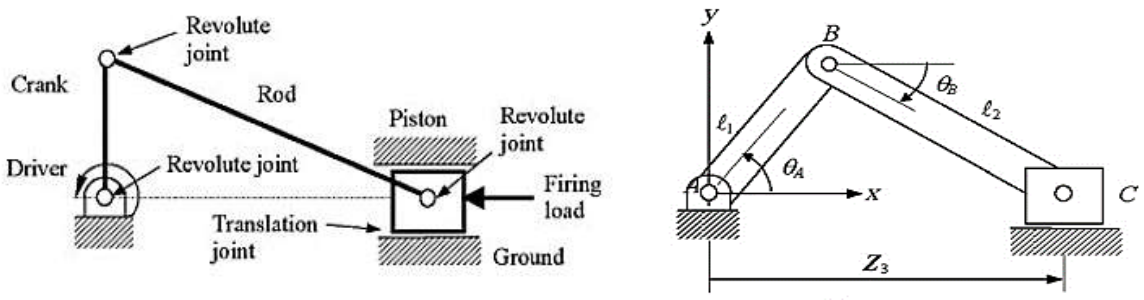

Figure 2.14: Crank mechanism, a) details of parts, b) Free body diagram. Reprinted with permission from [62]

The joint coordinates shown in Figure 2.14, and the equation of motion of the system is according to the following matrices.

$$\begin{bmatrix} \theta_A \\ \theta_B \\ Z_3 \end{bmatrix} = \begin{bmatrix} \omega t \\ \sin^{-1}(-\ell_1 \sin\theta_A/\ell_2) \\ \ell_1 \cos\theta_A \pm \sqrt{\ell_2^2 - (\ell_1 \sin\theta_A)^2} \end{bmatrix}$$

$$\begin{bmatrix} \dot{\theta}_A \\ \dot{\theta}_B \\ \dot{Z}_3 \end{bmatrix} = \begin{bmatrix} \omega \\ -\dfrac{\ell_1 \cos\theta_A}{\ell_2 \cos\theta_B}\dot{\theta}_A \\ \ell_1\dot{\theta}_A(\tan\theta_B \cos\theta_A - \sin\theta_A) \end{bmatrix}$$

As shown, the angular velocity of the crank (the driver) is directly related to the geometry of the system and the linear speed of reciprocal motion.

2.4.1.2 Rack and Pinion's Design and Model

Rack and pinion mechanism, as shown in Figure 2.13b, comprises of two parts of a linear gear bar called the rack and a circular gear called the pinion. The linear motion of the bar causes the circular part to rotate, and hence converting the linear motion to rotational. Examples of the

most common utilisations of this mechanism is in lifting systems, stirring, and industrial applications.

The important factors for designing a rack and pinion joint are number of teeth on the pinion, pinion pitch circle, and the geometry of the application. Figure 2.15 shows these key factors.

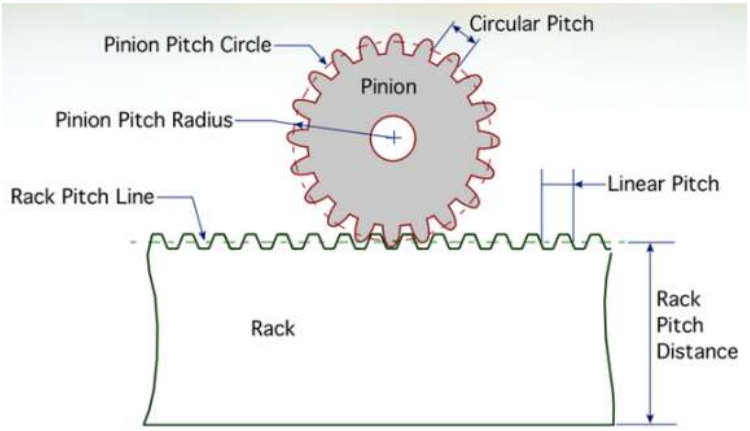

Figure 2.15: Key details of designing a rack and pinion joint. Reprinted with permission from [63]

Additionally, other features such as the tooth quality, which is the accuracy of the teeth shapes, backlash, which is the level of gap between the rack and pinion's teeth and pitch deviation, the deviation between theoretical and the actual length of the rack, are also essential when designing a rack and pinion mechanism.

As briefly explained in section 2.4, these systems have also been employed in road electromagnetic energy harvesters, due to their fundamental role in converting the vertical displacement of the roads, to rotation.

In the following section, the mathematics of an electromagnetic road energy harvester is discussed, followed by a review on the notable projects in this field.

2.4.2 Electromagnetic generators mathematical model

In an electromagnetic generator, the output power (P_{em}) is calculated through

$$P_{em} = T_g . \dot{\theta}_g \qquad \text{Equation 2.12}$$

$\dot{\theta_g}$ is the angular speed of the generator and T_g is the generator's torque, which is related to the electrical current of the generator by the following relation:

$$T_g = K_T . i_g \qquad \text{Equation 2.13}$$

Where K_T is the torque constant of the generator. Therefore:

$$P_{em} = T_g . \dot{\theta_g} = K_T . i_g \, \dot{\theta_g} \qquad \text{Equation 2.14}$$

According to Ohm's law, the electrical current of the generator (i_g) is:

$$i_g = \frac{V_g}{R} \qquad \text{Equation 2.15}$$

Where R is the summation of the internal resistance of the generator and the external resistor of the power harvesting circuit, and V_g is the output voltage of the generator, which is equal to:

$$V_g = K_g . \dot{\theta_g} \qquad \text{Equation 2.16}$$

K_g is the generator's electrical constant. Therefore:

$$i_g = \frac{V_g}{R} = \frac{K_g . \dot{\theta_g}}{R} \qquad \text{Equation 2.17}$$

Finally

$$P_{em} = T_g . \dot{\theta_g} = K_T . i_g \, \dot{\theta_g} = \frac{K_T . K_g . \dot{\theta_g}^2}{R} \qquad \text{Equation 2.18}$$

In addition to employing electromagnetic generators, there are some harvesters based on shear electromagnetism and are comprised of moving magnetic fields against coils to generate electricity. As mentioned before, these systems are based on translating the vertical movements of the surface to rotation. Since vertical displacements play a fundamental role in the harvesters' performance and outcome, they are designed within the concept of speed bumps and rumbles. In the following section, the latest projects conducted on electromagnetic energy harvesters from roads is summarised.

2.4.3 Electromagnetic Road Energy Harvesters

In a prior study, Duarte et al. built a rack and pinion road energy harvester comprised of horizontal rack linked to the cap of the harvester by diagonal hinges. Figure 2.13 shows the

schematic design of their system. With a peak power of about 31 W, their system was also capable of harvesting energy both in roads and pedestrian pathways through adjusting the system's suspension stiffness [12], [64]–[66].

Gholikhani et al. built a rack and pinion speed bump harvester in which the vertical pinion is linked to a clutch so that the rotations are transmitted in one direction. In the beginning, the project's findings showed a maximum power production of 1.96 mW; however, subsequent prototypes included a gearbox, which boosted the number of revolutions and, therefore, the maximum power output to almost 16 W [16], [54]. They identified the spring stiffness, loading and unloading time, and the applied force effective variables on the output of the harvester [20].

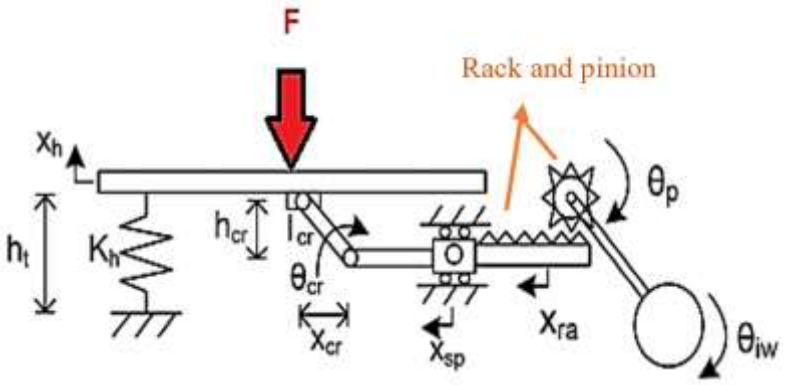

Figure 2.16: Horizontal rack and pinion road energy harvester. Reprinted with permission from [12]

Todaria et al. also developed a rack and pinion road energy harvester with the concept of the speed bump. In this research, the rack and pinion are also connected to a mechanical rectifying system to reverse the opposite rotations and have the generator spin in one direction in both loading and unloading of the cap (speed bump surface). This mechanical rectifier consists of two sets of rack and pinion with two one-way clutches. Figure 2.14 shows the schematic design of this harvester [21].

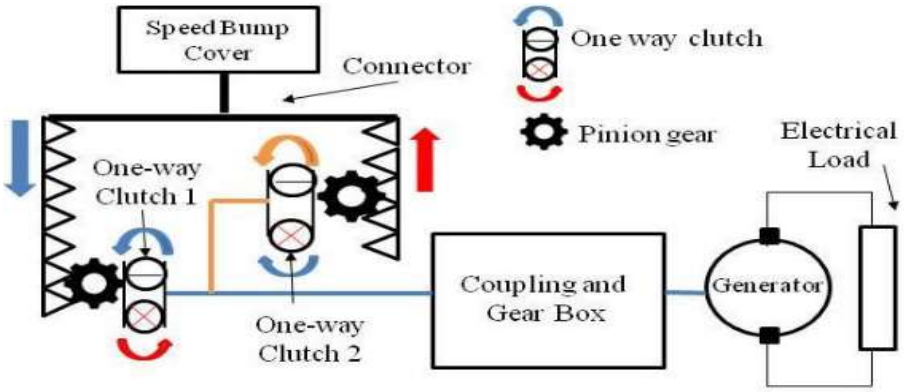

Figure 2.17: Rack and pinion road energy harvester and the mechanical rectifier system. Reprinted with permission from [21]

Through laboratory and field experiments, the harvester resulted in a maximum power of 550 W. The cap's displacement is around 25 mm, and the external resistance is 100 ohms. It was also revealed that the optimal driving speed of the car is between 5 to 10 Km/h [67], [68].

In addition to rack and pinion, electromagnetic sliding systems are another type of energy harvester based on speed bumps developed in a few researchers' works.

In 2013 Pirisi et al. developed and tested a sliding electromagnetic harvesting speed bump. Their sliding system's schematic design and site testing are shown in Figure 2.15. In their research, they designed the sliding system and optimized its geometry such that the output power was maximized. According to the preliminary results of this system, their peak power output is about 700 W [69].

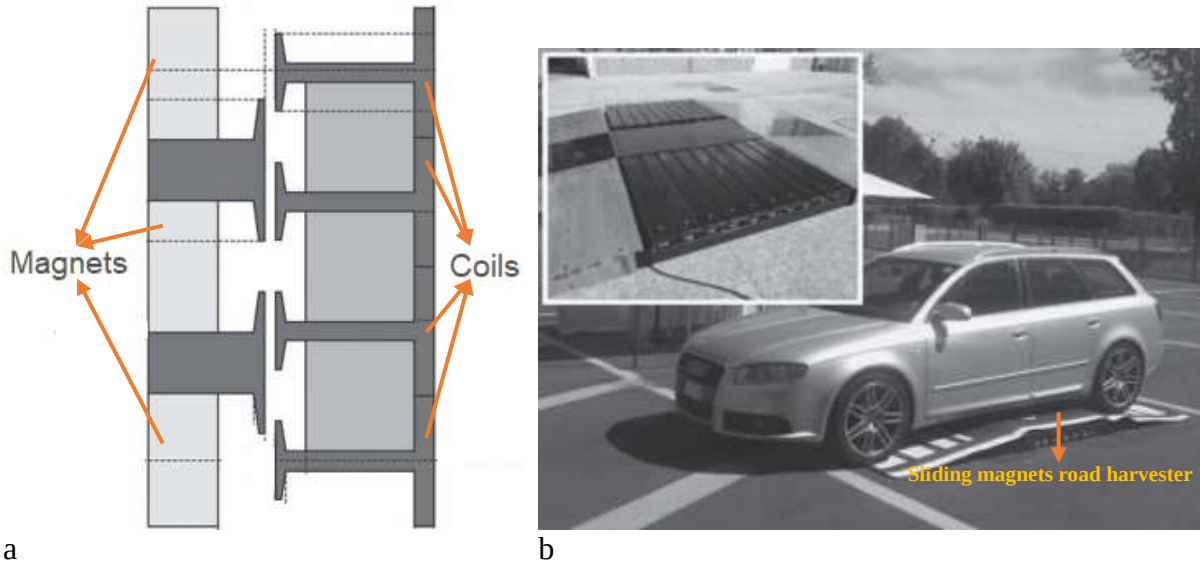

a b

Figure 2.18: a) Sliding magnets and coil harvester system, b) Performance of the harvester as a speed bump. Reprinted with permission from [69]

Another road harvester sliding system was developed by Gholikhani et al. in 2018. Their linear generator is also comprised of a set of permanent magnets fixed on a moving rod attached to the speed bump cap. As the rod slides, the magnets move against a set of fixed coils, generating electricity according to Maxwell Faraday's law. Figure 2.16 shows the design of their linear harvester. According to the experimental results, the root-mean square power output of the linear generator system is 80 mW which happens under the mechanical load of 4 KN applied at the frequency of 1.7 HZ [16], [20].

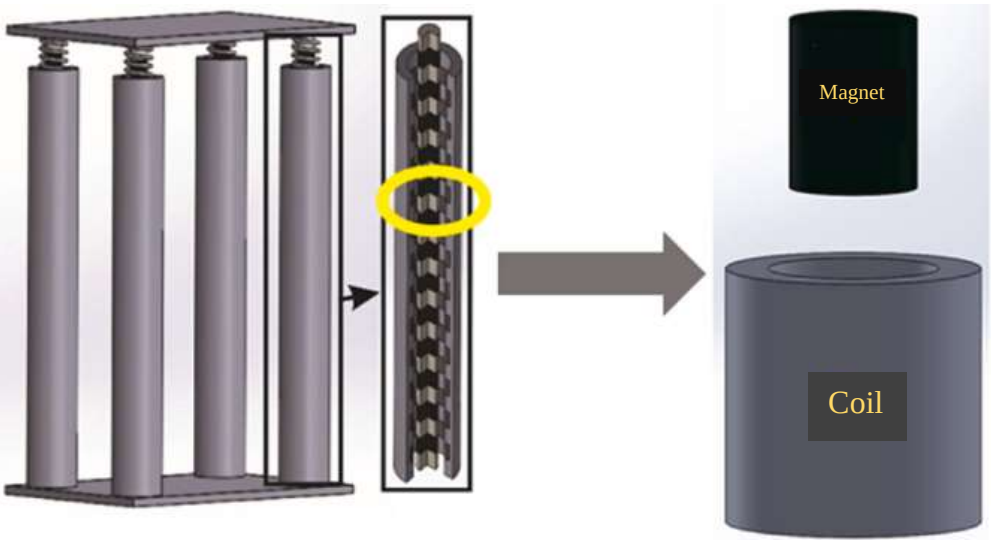

Figure 2.19: Linear electromagnetic generator mechanism. 1) set of the magnets. 2) Coil. Reprinted with permission from [20]

Roller electromagnetic speed bump harvesters were also built and studied in [70], [71]. Sarma et al. made a rolling speed bump system connected to a generator and spin it each time a car passed. The study showed that 1.67 W of electrical power could be harvested from a set of three roller speed bump harvesters.

Other electromagnetic road energy harvesters are based on hydraulic mechanisms to convert the vertical displacement to revolutions using hydraulic oils currents. This motion translation

is usually done by a turbine that spins using the fluid (oil) connected to the electromagnetic generator.

Hadi Obeid et al. conducted theoretical research on developing a hydraulic speed bump energy harvester. Their system consists of a hydraulic pump connected to a one-way clutch, flywheel, generator, and accumulator. Figure 2.17 shows the overall design of the harvester. The research results showed that an average car weighing 1000 Kg passing at the speed of 30 to 50 Km/h could generate an average electrical power of around 4 KW.

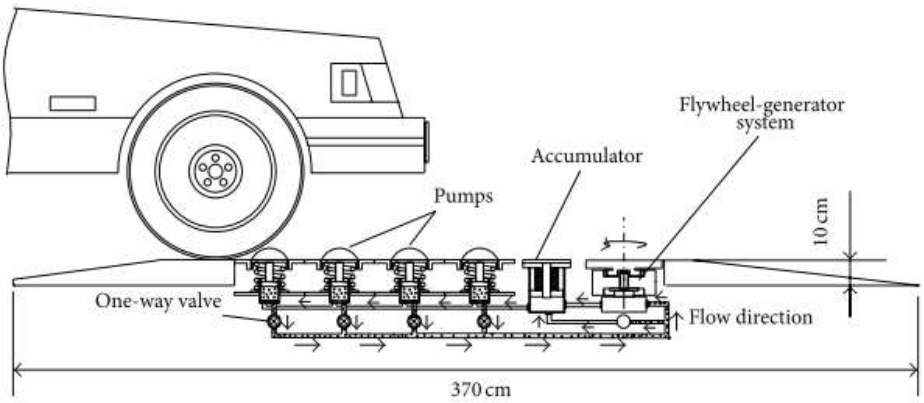

Figure 2.20: Hydraulic speed bump harvester design. Reprinted with permission from [55]

Moreover, in an experimental study, Ting et al. built a harvester especially for downhill and other deceleration zones in the roads. It comprises multiple small pistons (3 cm height) linked to a hydraulic accumulator and a generator. When the applied load is insufficient to generate energy effectively, the applied energy is conserved through the accumulator. As the accumulation equals a threshold, the fluid is circulated in the system, and the harvester starts to operate. The system can work at an efficiency of 41% and can generate an average power of almost 600 W [72].

In a similar study in 2015, Zhang et al. developed another hydraulic energy harvester with the same components of a tank (accumulator), hydraulic motor and a DC generator. The system generates an average power of 77 W, with an efficiency of 67.6% [73].

In addition to oil, compressed air was used in a study by Goodey et al. to harvest energy from roads. The harvester consists of cylinders of compressed air that act as road rumbles, collection manifolds and compressed air tanks. Based on the experimental data, they reported 904.11 KWh energy harvesting per day [74].

In addition to the hydraulic speed bump harvesters, hydraulic systems are also employed to develop energy harvester shock absorbers and suspension systems in the vehicles [18], [21], [73]. Li et al. developed a hydraulic energy harvesting damping system that could be used in suspension bridges and vehicle suspension systems. The laboratory results showed that the system could generate a maximum power of 435 W [75].

2.4.3.1 Comparison Between the Electromagnetic Road Harvesters and Challenges

As described in the previous section, electromagnetic road energy harvesters are mainly designed within the concept of speed bumps, which are traffic calming devices used in areas where deceleration is required to increase safety, such as residential zones and schools. In this section, the performance of the different electromagnetic harvesters is compared, and the challenges in employing them for real-scale applications are discussed.

The output power of the electromagnetic harvesters is in general higher than piezoelectric road harvesters and is usually in the range of watts and Kilowatts. In order to compare, Figure 2.18 shows the power that can be harvested from each harvester.

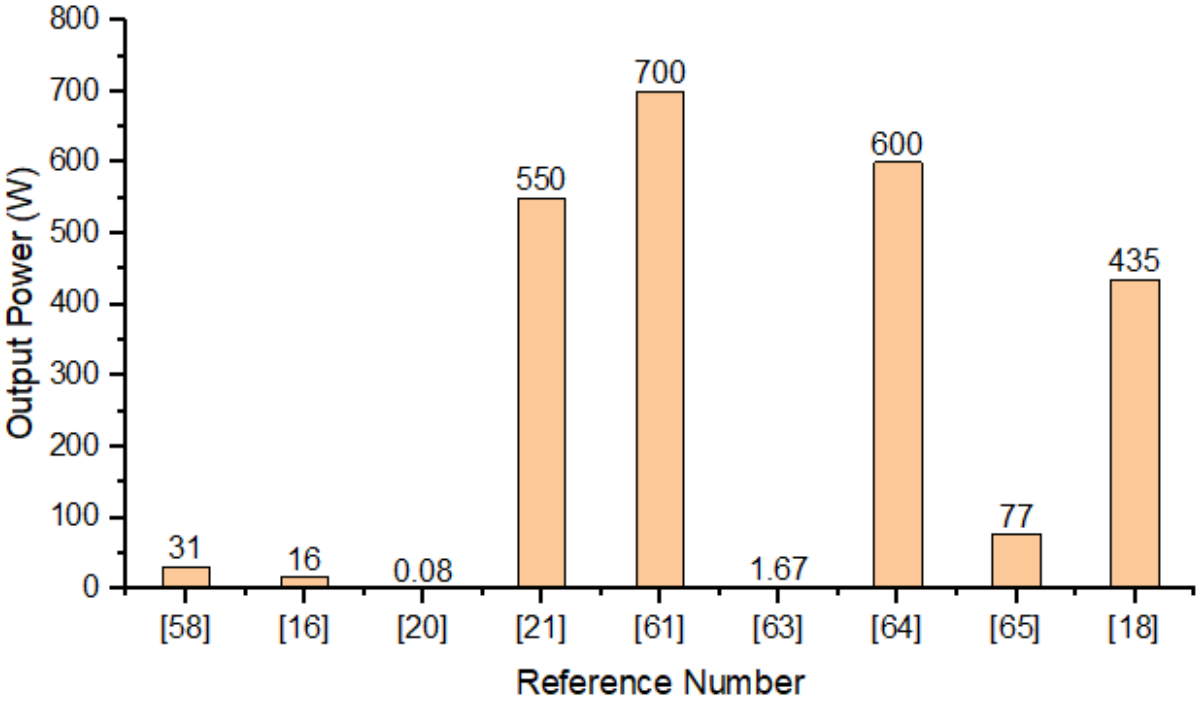

Figure 2.21: output power of the electromagnetic energy harvesters from various references

As it is summarized in Figure 2.18, most mechanical systems (rack and pinion, or the roller) have an output order of a few watts up to around 80 watts, except for one research ([69]). On the other hand, hydraulic harvesters result in higher output power, in the order of a few hundred watts.

As discussed, all electromagnetic road harvesters are designed within the concept of speed bumps and rumbles. Therefore, they should be installed in zones where the vehicles are decelerating, such as junctions and crosswalks.

Hydraulic and mechanical systems have different installation and maintenance issues to be addressed. The hydraulic systems have several components for installation, such as the piston, turbine, one-way valves, and the pipelines linking them to the generator and the accumulator. On the other hand, the mechanical systems have a more compact design and need more minor installation excavations. Moreover, the hydraulic systems have more associative elements placed on the side of the road, such as the generator and the accumulator. It is worth explaining that placing the accumulator underneath the pavement is not recommended for safety issues and the fact that it may increase the maintenance times.

Regarding the maintenance, it is recommended to install the harvesters such that their maintenance period will be equal to the maintenance period of the pavements. The hydraulic electromagnetic harvesters will need more complicated and frequent maintenance as they have more components and critical connections (the valves and pipelines). On the other hand, mechanical harvesters such as the rack and pinion system have fewer complications and a more straightforward maintenance process. The critical issue about the mechanical harvesters is their components' shape and materials, which should have enough strength against the applied cyclic loads from the vehicles.

Regarding the cost-effectiveness, limited information is available on the cost-effectiveness of the published projects. Table 2.2 summarizes the cost analysis of some of the projects.

Table 2.2: Cost analysis of electromagnetic road energy harvesters

Reference	Project years	Levelized cost of energy using this harvester	Maximum output power/ energy of one unit harvester	Cost of one unit Harvester
[74]	2016		904.11 KWh per day	$7000
[20]	2019	$209 per kWh		
[21]	2016		550 W	$5000

As it is given in Table 2.2, compared to piezoelectric road energy harvesters (Table 1), the cost of the electromagnetic road harvesters is less than piezoelectric harvesters, while their energy output is remarkably higher.

Both piezoelectric and electromagnetic systems are mechanical road energy harvesters that use the wasted kinetic energy and convert it to electrical energy. Regarding electrical power, electromagnetic road harvesters give better results and are more cost-effective. Moreover, like

traffic calming facilities, they improve the roads safety by being installed in suitable zones such as crosswalks and parking lots where is driving speed is low or is decreasing.

In the next sections, the road harvesters that convert the wasted solar energy are discussed.

2.5 Solar Collectors

The solar collectors are a method of harvesting energy from roads, in which fluid (air or liquid) circulation to convey the accumulated heat from the surface. The major application of them is heating and de-icing the roads in winter and cooling down the road surface in the hot summer season [76]. De-icing the road pavements using solar collectors instead of salts or de-icing agents mitigated the risk of asphalt corrosion and extended its service life, using the wasted form of energy. On the other hand, cooling the surface down in summer reduced the urban heat island effect [15], [16]. Unlike the other systems, collar collectors do not convert the form of wasted energy. Instead, the heat energy is conveyed and saved for further uses. They are also referred to as hydronic asphalt systems. Figure 2.19 shows a schematic illustration of these systems and a prototype of an ASC in performance.

One of the earliest projects was executed in Oregon in 1948. The project uses the available geothermal energy to melt the roadway's ice. Iron pipes were used to transfer the hot water to the pavement and melt the surface ice. The system worked for around 50 years when maintenance was required due to leakage from the pipelines [77].

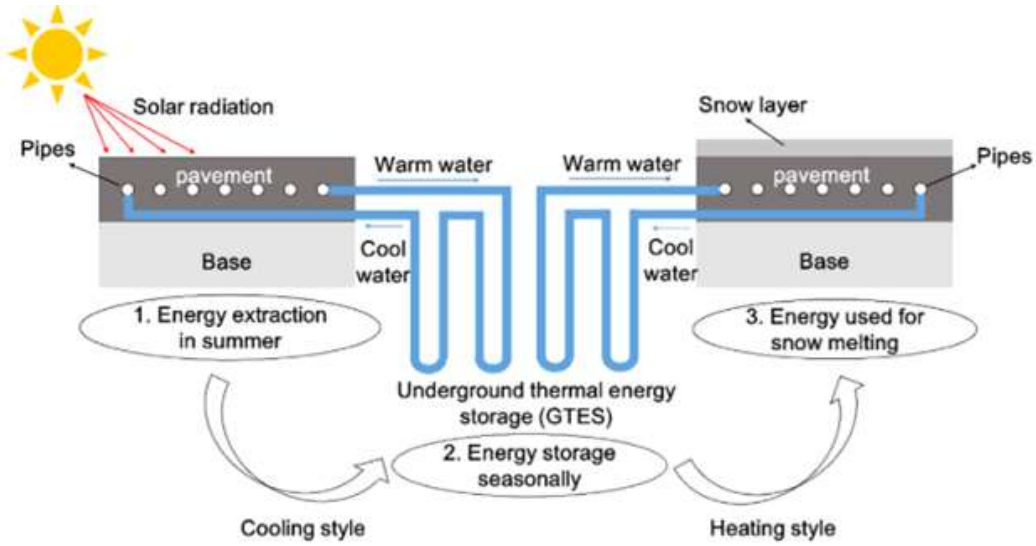

a

b

Figure 2.22: a) Asphalt solar collectors' performance, b) An ASC prototype in performance. Reprinted with permission from [15] and [78]

There are some research projects studying the application of asphalt solar collectors (ASC's) and the factors affecting their performance. These factors include the asphalt material, the material of the pipe, the size of the pipe, wind, water flow rate, etc. Thermal efficiency, which is an essential parameter in evaluating the efficiency of the ASC, is defined as the total harvested energy divided by the total amount of the received solar energy irradiance.

Gao et al. investigated slab solar collectors experimentally and studied the effects of water flow rate and pipes spacing on the efficiency rate of the ASC system. The collector slab consisted of three layers, the road surface, cushion, and the roadbed. It was observed that the water flow rate

had a positive effect on the amount of the harvested energy while having more space between the pipelines decreases the thermal efficiency. The average thermal efficiency of the system is around 37% [79]. Figure 2.20 shows the experimental plan of this study and the cross-section of the collector slab.

Mallick et al. investigated the effect of incorporating conductive aggregates in the asphalt mix on the efficiency and performance of the ASC system. They reported that having the asphalt mix with quartzite aggregates improves the heat energy capture efficiency of the ASC. Reducing the reflectivity of the pavement surface also increases the heat capture and the performance of the ASC system [80].

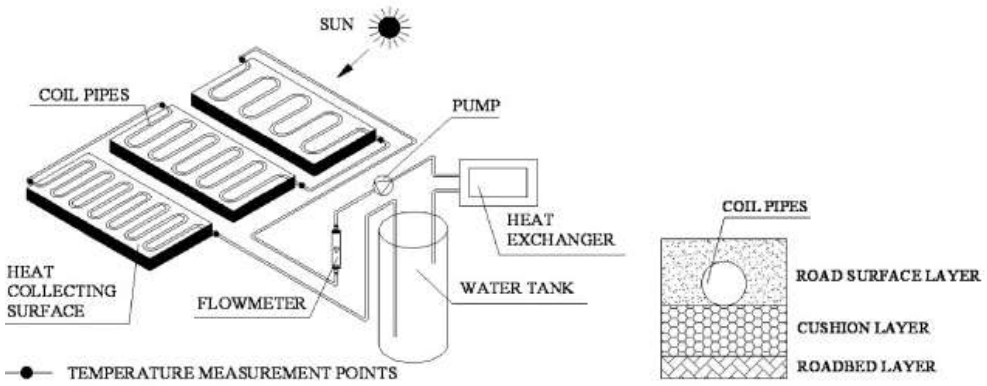

Figure 2.23: Slab solar collector experimental study apparatus and cross-section [79]

In 2017, Alonso-Estébanez et al. conducted an ASC system, studying various factors affecting its functioning. For the experimental study, a solar collector prototype was made in the lab, and four 300-watts light bulbs were used to simulate the solar radiation on the prototype. The experimental results showed that increasing the water's flow rate increases the amount of harvested energy. Similar observations were made in [81]. Irradiance and the size of the collector are other factors affecting the amount of harvested energy. These factors are interconnected, and the amount of the harvested (gained) energy increases by increasing the collector's surface area and irradiance. The thermal efficiency of the collector from the experimental results was between 45 to 60%. Figure 2.21 shows their experimental setup [82].

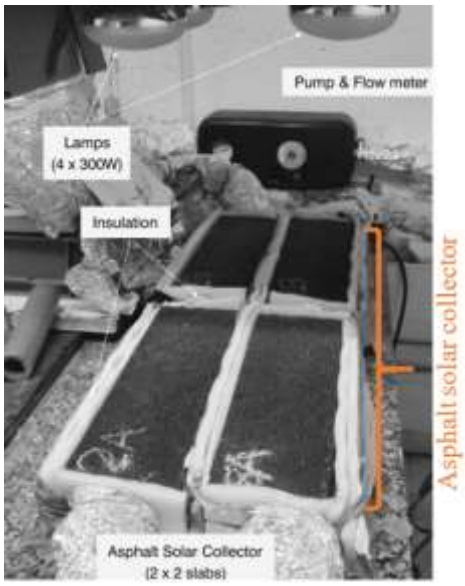

Figure 2.24: Experimental set up of testing Asphalt Solar Collector

Masoumi et al. investigated an ASC system using CFD, experimental validation and artificial neural networking (ANN) modelling. It was observed that comparing the influences of the inlet water temperature, the thermal conductivity of the asphalt and the surface irradiation, the temperature of the inlet water was more effective on the energy harvesting efficiency of the ASC system. Reducing the temperature of the inlet water improves the efficiency of the system significantly. The maximum thermal efficiency of the ASC system varies between 25 to 45% depending on the season [83].

In another study, Farzan et al. studied the effect of wind speed on glazed and unglazed ASC and its thermal efficiency through experiments and numerical simulations. Wind direction and speed is often randomly changing factor that greatly influences the performance of the ASC. Three different wind speeds of 0, 10 and 20 m/s were investigated. It was found that increasing the wind speed reduced the heat gain and the thermal efficiency of the ASC. However, having a glass glazing layer on ASC mitigates this reduction in performance. The thermal efficiency of the ASC in this study is between 2 to 16% depending on the wind speed and the glazing. Figure 2.22 shows their ASC unit [84].

Figure 2.25: ASC installation and testing set up. Reprinted with permission from [84]

In addition to the liquid circulation, air circulation was also proposed and studied in a number of works [85]–[87]. However, it was observed that the efficiency of these systems is around 4 to 5%, which is much lower than the liquid circulating systems, and hence they are not cost-effective [86]. Based on the reviews, ASC is a useful system providing an innovative solution for de-icing the frozen roadways in winter and cooling down the surface of the roads in hot seasons.

2.5.1.1 Comparison Between the Asphalt Solar Collectors and Challenges

Asphalt solar collectors (ASCs) were discussed, and the recent research works on them were briefly described in the previous section. Although ASCs have been studied and implemented for decades, further studies and practices must establish a solid framework for their widespread road application.

Maintenance of these systems is a critical issue as they mostly rely on a pipeline system where fluids (water) is circulated. Therefore, the employed pipelines need to be corrosion resistant and have remarkable mechanical properties, as they are constantly under dynamic loads from

the vehicles. Moreover, depending on the time of day and season, the temperature on the pipelines' surfaces changes which may cause thermal strains and tensions.

Another critical matter about ASC's is the mechanical compatibility between the pipelines and the pavement materials. Having different stiffnesses may cause excessive cracking on the asphalt surfaces and reduce its service life. To address this issue, it is recommended to place the pipelines at a suitable depth and have the asphalt material and the pipeline as compatible as possible.

Regarding the cost analysis of ASC systems, limited and unclear discussions have been made in the previous discussions. Mallick et al. mentioned that their system has a payback period of 10 years [80]. In addition to the sheer cost of the ASC system and its installation, some factors can affect the cost-effective analysis of ASC's. The climate and the latitude of ASC's installation location are important factors that affect the system's efficiency and, hence, its cost-effectiveness. For example, a system may be highly efficient in laboratory level studies but installing it in a windy environment reduces its efficiency to the point that it may no longer be cost-effective.

2.6 Thermoelectric Road Energy Harvesters (TEG's)

Thermoelectric generators (TEG's) are the fundamental elements of these types of harvesters. Thermoelectric generators are built based on thermoelectricity and the Seebeck effect, discovered and formulated by Seebeck in 1821. It states that in thermoelectric materials, the temperature difference between the opposite sides of them can generate electrical voltage. In these materials, the heat carriers are conductive particles. When there is a temperature difference between the two sides, the charged heat carriers begin to migrate from the hot side to the cold side resulting in an electrical potential difference (voltage) within the material [19], [88], [89]. Thermoelectric generators are a collection of interconnected P-type (charge carriers

are holes) and N-type (charge carriers are electrons) semiconductors that allow the heat (charge) carries to move in the generator and generate electrical voltage. Two thermally conductive but electrical insulative ceramics covers the semiconductor blocks. Figure 2.23 shows a P-N junction performance under the temperature difference and the internal of a thermoelectric generator.

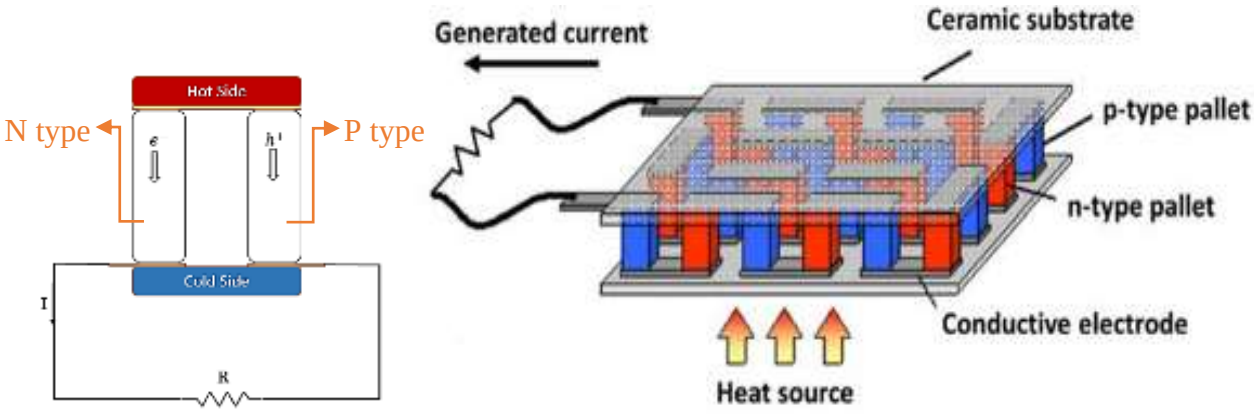

a b

Figure 2.26: a) P-N junction as an electrical generator. Reprinted with permission from [19], b) internal arrangement of a TEG [90]

2.6.1 Thermoelectric generators mathematical model

The performance and the efficiency of the TEG's depends on the properties of their thermoelectric elements, the number of the elements and the temperature difference between the two sides. Thermoelectric material's performance is evaluated by the figure of merit (ZT) [91], [92]. It is calculated through equation 2.19:

$$ZT = \frac{S^2 \sigma T}{K} \qquad \text{Equation 2.19}$$

Where S is the Seebeck coefficient (V/K), σ is the electrical conductivity (S/m), T is the temperature difference between the sides (K), and K is the thermal conductivity (W/mK). It can be deduced that the figure of merit increases if the thermoelectric material is electrically conductive but thermally insulative.

The Seebeck coefficient is the inherent characteristic of the thermoelectric material, and it is the change in voltage divided by the change in temperature.

$$S = \frac{\Delta V}{\Delta T}$$ Equation 2.20

Where V is the voltage and T is temperature.

Another important parameter to evaluate thermoelectric materials is the power factor. Unlike the figure of merit, the power factor (PF) is only about the electrical properties of the material, and it is calculated through:

$$PF = S^2\sigma$$ Equation 2.21

Where S is the Seebeck coefficient, and σ is the electrical conductivity.

Road surfaces, due to absorbing solar energy radiations and friction, usually have a higher temperature than the depth of the road. Therefore, if the temperature of the road profile is logged, the surface is the warmest point, and the temperature cools down by moving down in depth. Figure 2.24 shows a typical temperature log of the road's profile. This temperature gradient is the basis of employing TEG for harvesting electrical energy from the roads. The two sides of the TEG are connected to the warm and the cold sections of the road profile, generating electricity from the temperature gradient.

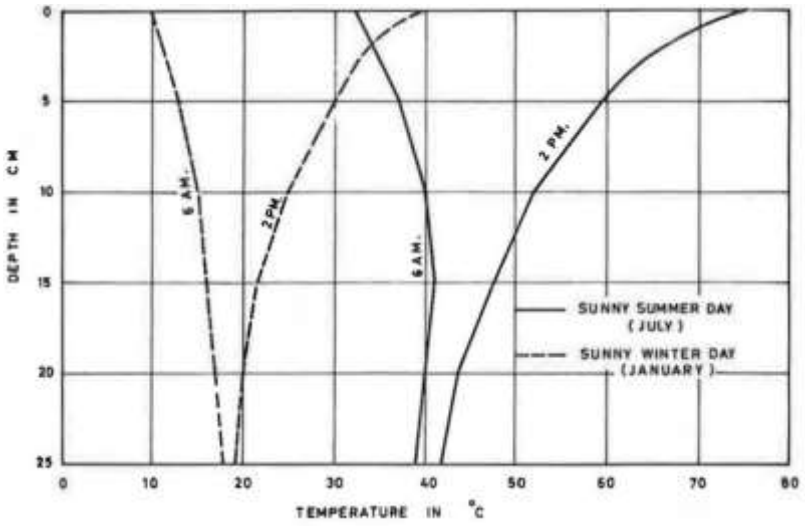

Figure 2.27: Temperature gradient over the depth of the asphalt concrete road. Reprinted from [93]

2.6.2 Thermoelectric Road Energy Harvesters

Thermoelectric road harvesters usually consist of a TEG module, heat sink and a thermal conductor. Datta et al., in 2017, studied a thermoelectric road harvester which consisted of a

TEG, a Z shaped thermal conductor and a water tank acting as the heat sink. The Z shaped conductor was connected to the road surface, transferring the heat to one side of the TEG. The other side of the TEG was attached to a water tank, acting as the heat sink, to have a maintained temperature gradient provided. In their experimental study, they compared the power output of two harvesters, one had 2 TEG modules with a larger overall surface area, and the other had four TEG modules with smaller total surface area. The results showed that the harvester with four TEG modules gave 11 mW power output, while the harvester with two TEGs gave 8mW of electrical power, despite having a larger surface area of TEG [11]. Figure 2.25 shows their harvester module. They also investigated the effect of copper and aluminium Z shaped conducting elements. The results showed that the copper plate transfers roads surface heat to the TEG more, resulting in a higher temperature gradient in the two sides of the harvester, giving a more recoverable temperature difference.

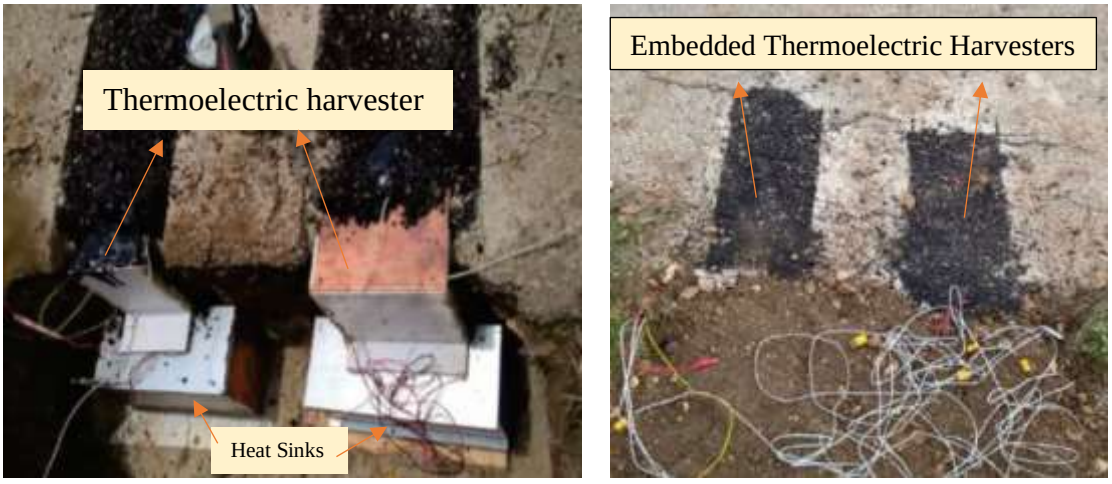

a b

Figure 2.28: a) Thermoelectric Road energy harvester with copper and aluminium conducting plates. b) Thermoelectric road energy harvester installed in the road. Reprinted with permission from [11]

Jiang et al. developed another road thermoelectric energy harvester using a TEG module attached to a cold-water tank. The heat from the road surface was transferred to TEG using aluminium vapour champers. The cold-water tank was placed beside the road and shaded with a covering. Small-scale experiments showed that the TEG could generate 0.73 V and 0.41 V in

indoor and outdoor environments. However, the output of the harvester was reduced in larger-scale experiments [94], [95].

Tahami et al. developed another thermoelectric harvesting unit, with an L shaped copper plate as the conducting element, TEG module and a heat sink of the cold side, which was made of a phase change material instead of the water tank. The experimental results showed that the harvester could generate a continuous power of 29 mW per day [96]. It was also observed that by increasing the number of TEG modules [9], in this harvester, the output power decreases, which is unlike the observation in [11].

Hasebe et al. built and tested a thermoelectric road energy harvester integrated with embedded pipelines in the road as solar collectors. The hot side of the TEG was connected to the solar collectors, and for the cold side, water from a nearby river was transferred using pipelines. The maximum power was 300 mW, obtained using the resistor of 30 Ω and the temperature difference of 40.5 K [97].

Khamil et al. developed another thermoelectric road energy harvester, in which the TEG was placed underneath the road surface, protected by two aluminium plates. The TEG was closely attached to the road surface. A long aluminium element was attached to the other side of the TEG, going down to the depth of the soil to conduct the cooler temperature to the TEG's other side. Two types of cooling elements, a rod, and a flat plate, was investigated in this study. It was observed that the aluminium rod performs better compared to the flat plate. Laboratory results showed that for a temperature difference of 8.99 C, the output voltage is about 0.35 V, which is in good agreement with field test results in which 7.95 C, results in the voltage output of 0.32 V. Using a voltage booster circuit of MPPT, the output power of the system reached a maximum of 3 mW, corresponding to the voltage of 5.3 V [98], [99].

2.6.2.1 Comparison Between the Thermoelectric Road Harvesters and Challenges

Thermoelectric road energy harvesters have TEG's as their fundamental energy conversion unit. The difference between the research works lies in the configurations of the whole harvester's system, the heat sink(s) and the heat transference methods. As a general observation, the system which could provide a higher and more long-lasting temperature difference between the hot and the cold side of the TEG, resulted in higher electrical energy output. The overall power output of thermoelectric road energy harvesters is in the range of milliwatts. The output power of the briefed projects is plotted in Figure 2.26.

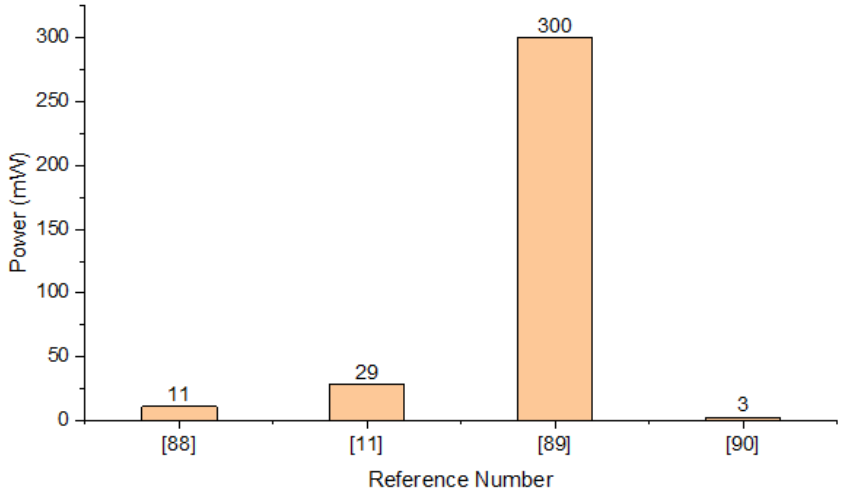

Figure 2.29: Power output of thermoelectric road energy harvesters

Considering the real scale applications of these harvesters, there are a number of obstacles and challenges that need to be resolved. The harvester pavement mechanical interaction is a critical point, as they have different mechanical properties. There are a number of projects in which the TEG unit is placed by the side of the road [9], [96], [97], [100], [101]. In these projects, the pavement's heat is transferred to the hot side of the TEG using thermally conductive elements such as metallic chambers and plates. These embedded elements in the road may cause some problems, as their mechanical and thermal properties are different from the asphalt or concrete pavements. In addition, additional cracks may occur on the surface of the pavement due to these elements, which will enforce extra maintenance on the road. It is worth noting that these elements are usually placed very close to the road's surface to increase the efficiency of the

energy conversions. However, having them in such low depth will make the problem of thermal and mechanical incompatibility between the asphalt and these elements more complicated.

In the other format, the TEG elements are directly placed in the road at a closed distance from the surface of the road, which eliminates the need for having the metallic conductive element [98], [102]–[104]. Although the TEG is directly embedded in the road in these systems, for real road applications, it needs to be protected with a strong metallic plate to convey the surface heat to the element. However, having the metallic plate in the road may cause extra cracks on the pavements due to the thermal incompatibility between the pavement and the metallic element, which can affect the service life of the pavement. Needless to say, putting the TEG ceramic directly on the pavement is not possible since, due to its brittleness, it will break under the mechanical loads leading to the system's failure.

Another important aspect is the cost-effectiveness of these harvesters. Although their output power is within milliwatts, these harvesters are relatively cheap and not disruptive to traffic. A summary of the cost analysis of some of these harvesters is brought in Table 2.3.

Table 2.3: Cost analysis of Thermoelectric road energy harvesters

Reference	Project years	Levelized cost of energy using this harvester	Maximum output power/ energy of one unit harvester	Cost of one unit Harvester
[11]	2017	N/A	170 KWh in 1 year	$190
[30]	2017	$2.31 /KWh	N/A	N/A
[9]	2020	$8.56 /kW-h per square meter	N/A	N/A

Compared to piezoelectric road energy harvesters (Table 2.1), which have a similar level of output power, thermoelectric harvesters are more cost-effective.

2.7 Photovoltaic Cells Road Energy Harvesters

Photovoltaic cells are known elements for converting solar radiation to electrical currents. They are made of p-type and n-type semiconductors that are responsible for converting solar radiation to electricity. When electromagnetic waves (such as solar radiations) reach the p-n junction of photovoltaic cells, the energetic photons excite the electrons, and holes, which start moving within the cell, generating electrical current [105]–[108]. Solar panels consist of a network of photovoltaic cells connected to each other, allowing the charge carriers (electrons or holes) to move in the network and generate electrical current. Nowadays, solar panels are used in different places, especially in sun-catching areas, on rooftops to generate environmentally friendly off-grid electricity. The efficiency of the solar panels depends on a number of factors, such as the size of the panel, the type of the cells, their connections in the panel and the weather conditions [19].

The employment of solar panels in road surfaces has recently been investigated in a number of projects [22], [24], [109]–[111]. Solarroadways in the USA was one of the first implemented projects of solar panels roadways. The installed panels were engineered to tolerate traffic loads. Each panel was capable of generating 36 W of power. The road was also equipped with LED lights and de-icing elements on the surface, and it was stated that the overall efficiency of the system was about 11.2% [13]. A sample of SolarRoadways pavement units is shown in Figure 2.27.

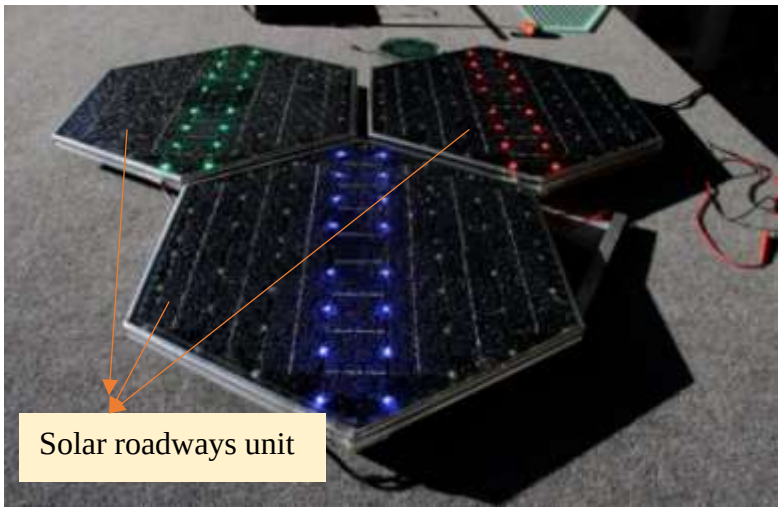

Figure 2.30: Solarroadways panels. Reprinted from [112]

In the Netherlands, the SolaRoad project developed and installed specially designed solar panels on a biking lane to generate energy. Based on the experimental results, it was estimated that the lane would generate 50- 70 KWh/m^2 in one year. The project was successfully installed and operating. However, due to the surface cracking and extensive surface damage, the lane had to be removed and replaced completely [111], [113]. The project was also adapted for roadways, but due to extensive damage on the surface, it was discontinued. A Solaroad slab installation is shown in Figure 2.28.

Figure 2.31: SolaRoad installation. Reprinted from [114]

The photovoltaic pavement was studied in another study for urban heat island mitigation. The solar pavement was tested in the real field, and the results showed that as the result of employing

this pavement, the ambient temperature was 0.8 K lower, and the pavement surface was 8 K cooler than the conventional pavements [109].

Dezfooli et al. also studied two types of photovoltaic pavements from mechanical points of view, such as rutting and flexural resistance. The two prototypes are solar panels between a layer of rubber and Plexiglas and the solar panel between two layers of porous rubber. It was reported that embedding the solar panel in the layers of plexiglass reduces the conversion efficiency by 26% while embedding the panel in two layers of rubber reduces the efficiency by 50% [22].

Moreover, Wattway was another project implemented in France in 2016 by engineering and installing photovoltaic pavement units on the road surface. The panels have a thickness of 7 mm, with various transparent and resistant layers protecting the panels while providing the necessary mechanical properties on the road's surface (e.g. friction) [112], [115]. Figure 2.29 shows the Wattway project in operation.

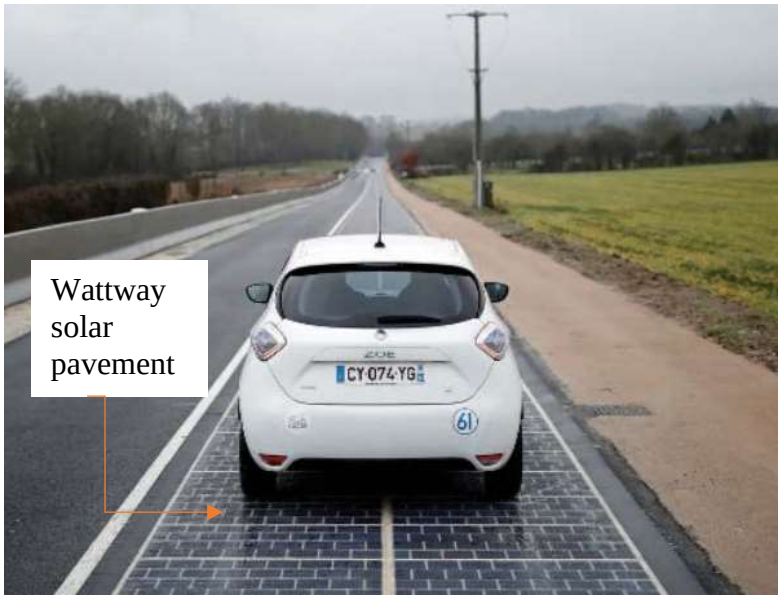

Figure 2.32: Wattway project in operation. Reprinted from [116]

2.7.1 Solar Panels Road Energy Harvesters Challenges

As summarized in the previous section, engineering solar panels and implementing them in roadways is gaining popularity in the commercial and research sectors. Solar panel pavements

are more prepared for real and large-scale applications in terms of implementation. However, there are still inevitable problems associated with this implementation. From the mechanical aspect, these panels are fragile and do not exhibit lifelong adequate mechanical properties. Most solar pavements required maintenance or were permanently damaged during their service life, significantly affecting their energy harvesting and mechanical performance. The other important issue is to have solar road pavements with enough skid resistance, which is critical for driving and safety. It is possible to have solar panel pavements with a suitable surface; however, this would compromise the performance of the photovoltaic cells [112], [117], [118]. Another issue associated with solar road panels is that their performance and efficiency is directly affected by the weather conditions and other environmental factors such as the amount of accumulated dust, dirt and the partial shadows on them caused by the surroundings [19], [117], [118].

Cost analysis of solar pavements is also a critical aspect since solar panels are a relatively expensive technology. Table 2.4 shows the cost analysis results of some of these projects.

Table 2.4: Cost-effective analysis of solar road pavements

Reference	Project years	Maximum output power per unit area of the panel (KWh/m^2)	Cost per unit area of the panel ($\$/m^2$)	Levelized cost of energy harvester ($\$/KWh$)
Wattway [118], [119]	2016	53.4	1700	31.84
SolaRoad [113], [114]	2014	78	14000	180
SolarRoadways [118], [120]	2012	70.5	11000	156
Dessouky et al. [25]	2019	N/A	N/A	19.8

According to Table 2.4, although some large-scale projects are implementing solar panels on roads with generally higher power output than the other road energy harvesting systems, their

Levelized cost of energy harvesting is still higher than the conventional methods. The higher cost of energy generation and the serious problems associated with implementing them raise serious doubts about their future continuation.

2.8 Comparison between the Road Energy Harvesters

In the previous sections, five different types of road energy harvesting technologies were discussed, and the research projects were summarised. In this section, these technologies will be compared to each other from the viewpoints of power or energy output, cost-effectiveness, technology readiness level (TRL), and challenges. This comparison is made based on the average harvester of the mentioned technology.

Considering the output power of piezoelectric and thermoelectric road energy harvesters, they have an output in the range of microwatts and milliwatts. In contrast, solar panel pavements, solar collectors and electromagnetic road harvesters have higher outputs in the range of watts and kilowatts. In this sense, electromagnetic and solar energy harvesters are more feasible options than piezoelectric and thermoelectric harvesters.

Through cost-effectiveness analysis, it can be seen that all the discussed technologies generate more expensive electrical power than the conventional power plants using fossil fuels. However, comparing the systems shows that the thermoelectric harvesters are more cost-effective than the others, even though their low power output depends on environmental conditions.

In terms of challenges, piezoelectric road energy harvesters have very low electrical energy output. They are made of expensive piezoelectric elements and may cause extra maintenances due to the brittleness of their elements. Thermoelectric road energy harvesters are also made of fragile thermoelectric elements. Although they are relatively cheaper, their energy output is

low, and their performance depends highly on the climate and the season. Asphalt solar collectors and solar panel pavements have the same problem, and their performance depends on the weather condition, season, and environment. Solar panel pavements are made of engineered expensive solar panels encased in protective layers. Finally, electromagnetic road energy harvesters generate higher power output, and their performance is regardless of the environmental conditions. Their only disadvantage is that as traffic calming facilities, they must be employed in specific zones of the roads, where a speed deceleration is required.

Moreover, the technology readiness level (TRL) is a method for evaluating the maturity of a technological invention or a project. It was developed in NASA [121], [122], and according to it, the technologies' readiness is divided into nine different levels, from 1 standing for the least readiness condition to 9 for the full-scale operation readiness. Table 2.5 shows the different levels of TRL in terms of projects focusing on harvesting energy from roads.

Table 2.5: TRL stages focusing on road energy harvesting projects [121], [123]

TRL Level	Description
1	Investigation of the fundamental principles of the road energy harvester
2	Analytical formulations of the harvester are derived
3	The concept of the road energy harvester is approved experimentally
4	The road energy harvester’s performance is validated in the laboratory environment
5	The road energy harvester’s performance is approved for a suitable environment
6	The road energy harvester’s performance is exhibited in a suitable environment
7	The road energy harvester’s prototype is revealed in the assigned road
8	The road energy harvester’s system is finalised and qualified
9	The qualified road energy harvester is approved in the assigned road

Of all the investigated technologies, solar panel roadways and solar collectors have performed on a real roadway scale and therefore have a TRL of 9. The next harvester technology is

electromagnetic road energy harvesters with a TRL of 4 to 6 depending on performing the field test. Finally, piezoelectric and thermoelectric road harvesters are mostly preliminary and have the TRL of 2 to 5.

Table 2.6 summarizes the key features of different road energy harvesters.

Table 2.6: Summary of the road energy harvesting projects

Harvesting method	Reference	Cost-effectiveness ($/KWh)	TRL
Piezoelectric	[14]	27.9	4
Thermoelectric	[9]	8.56	4
Electromagnetic	[20]	209	6
Solar collectors/panel pavements	[13]	156	9

2.9 Conclusions

In this chapter, the synopses of the available road energy harvesting methods are discussed. The primary forms of wasted energy in roadways are kinetic and thermal energy, caused by passing vehicles and solar radiation. Each of these forms can be converted to a valuable form of energy (i.e., electricity) using the discussed methods, and consequently, the amount of wasted energy would be reduced. Five different harvesting methods of piezoelectric, electromagnetic, solar panels, solar collectors and thermoelectric road harvesters are briefly discussed, and some examples of the conducted research on each are described. The following points can be extracted from this chapter.

1. Piezoelectric road energy harvesters employ direct piezoelectricity to convert the mechanical vibrations of the road to electrical voltage. Most of the developed piezoelectric energy harvesters are tested in the laboratory under mechanical loads. The major challenges facing

piezoelectric road harvesters is their low power output and brittleness and high cost of building and maintenance, which still need to be addressed through further research projects.

2. Electromagnetic road energy harvesters are the other method of converting the kinetic energy to electricity in the roadways. These harvesters are designed and built within the structure of the speed bumps, which are traffic calming facilities and are essential for road and pathways safety. Their power output is significantly higher than piezoelectric harvesters and in the range of watts and kilowatts. By implementing these harvesters in suitable zones such the speed deceleration or low-speed areas, an extra energy generation source would be available to be saved or used in smart roads for signals and telecommunication.

3. Thermoelectric road energy harvesters incorporate thermoelectric generators, which convert the temperature gradient within the profile of the road to electricity. The performance of these harvesters rely highly on the weather conditions, the climate of the area, and the season. Their electrical output power is in the range of milliwatts. However, compared to the rest of the systems, their Levelized Cost is cheaper.

4. Solar panel roads and solar collectors are two systems that directly convert solar radiation into electricity and thermal energy. Some solar panel roads and solar collector projects have been executed in full scale, and hence, in terms of readiness, these systems are more advanced than the other methods. Their efficiency and power output are high and within watt level. However, their performance is highly dependent on the climate of the region and the season. Moreover, the cracks and structural damages on these systems are a major challenge that requires further studies and research to be addressed.

3 Harvester Design, Simulation and Experimental Verification

3.1 Introduction

This chapter focuses on the mechanical details and performance of the current electromagnetic road energy harvester. A new electromagnetic road energy harvester with a novel design is developed, manufactured and its performance is investigated. The mechanism of the harvester is based on a slider-crank system, which is one of the mechanisms used to convert the linear to rotational displacements and vice versa [124], [125]. In this mechanism, the components are bolted to each other. Therefore, any risk of backlash, sliding or mismatch between the components is minimized, which gives it a remarkable advantage over the other systems with a similar function like the rack and pinion. Moreover, it has a more straightforward maintenance procedure than the hydraulic harvester units, as there is no need for an oil cylinder and pump.

In the following sections, first, the design concept and the mechanical and electrical details are discussed. Afterwards, the critical factors affecting the output power are analyzed, and the equation of motion is derived following the Lagrange equation. Next, the analysis results of the equation of motion are discussed to evaluate the harvester's mechanism. The results from the motion analysis are verified experimentally, and a good agreement is observed between the results. Finally, to evaluate the structure of the harvester, Finite Element Analysis (FEA) is performed on the system, and its results are discussed. These analyses focus on the crank system's components (the handle, disk, and holder) to ensure their performance.

According to the motion analysis, displacement speed and magnitude play an essential role in the system's output power. Therefore, the maximum displacement is around 25 mm, providing a feasible and sufficient angular displacement. Furthermore, finite Element Analysis shows that

at the ultimate state, the maximum stress is safely below the yield strength of aluminium which is the material used to manufacture the components.

3.2 Design concept and mechanism details

The concept of the current mechanical harvester is based on a slider-crank system. Due to its simplicity in maintenance and negligible risk of parts mismatch and backlash, such a system can have advantages over other systems such as the hydraulic mechanism and the rack and pinion. Slider crank is one of the mechanisms utilised to convert the linear motion of the slider to the rotational motion of the crank and vice versa. Figure 3.1 shows a free-body diagram of a typical crank system.

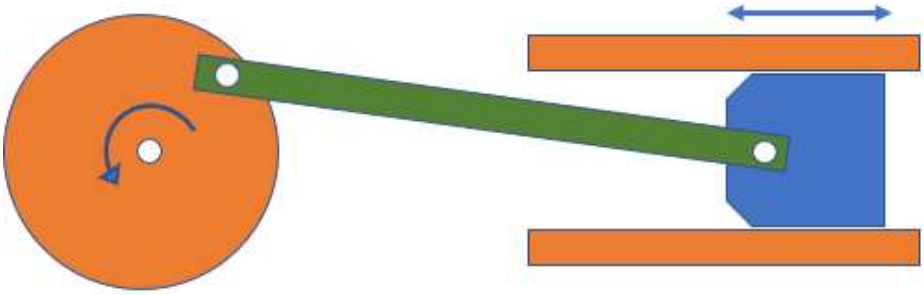

Figure 3.1: Slider crank mechanism

Figure 3.2 shows the details of the crank-based energy harvester and an assembled prototype. The prototype shown in the figure was built to verify the simulation results. Each component's properties and dimension details are brought in the next chapter. According to the Figure 3.2, the top plate of the harvester (1) linked to the crank handle (2) acts as the slider. The other end of the handle is connected to the disk (3) held by a bearer. Next, a 100-ratio planetary gearbox (4) is connected to the disk, increasing the rotations of the disk by 100 times. Finally, a DC generator (5) is connected to the gearbox. Once the top plate slides, the disk rotates. The rotation is transferred to the generator, generating electrical potential. Moreover, four springs placed in the corners of the plate support the top plate.

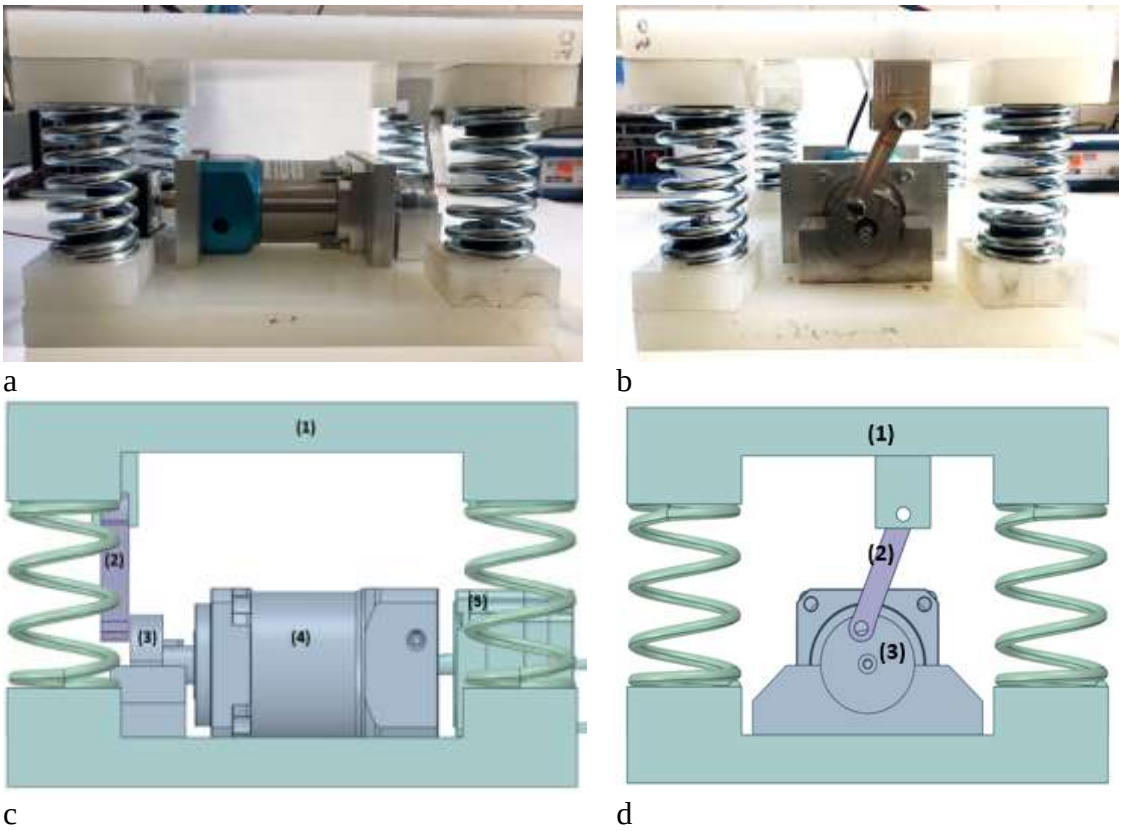

Figure 3.2: Mechanical harvester's model and the built prototype; a, c) side view; b, d) front view. (1): Harvester's cap; (2): Crank handle; (3): Revolving disk; (4): Gearbox; (5): Generator

Generalised Maxwell-Faraday theory explains the electrical generator's performance. It states that a time-varying magnetic field always accompanies a spatially varying electrical field. Equation 3.1 describes this phenomenon.

$$\nabla \times E = -\frac{\partial B}{\partial t} \qquad \text{Equation 3.1}$$

In which E is the electrical field, B is the magnetic field, t is time, and ∇ is the del operator. It is worth noting that when the harvester unit operates during both loading and unloading (top plate going down and up, respectively), both positive and negative voltages are generated due to the rotation in opposite directions. Therefore, a full bridge rectifier is attached to the generator to eliminate the negative and convert it to positive voltages. A regular full bridge rectifier consists of four diodes and is used to convert AC to DC. A diode allows the electrical current to pass only in one way. Therefore, connecting the diodes to form a full bridge rectifier, as illustrated in Figure 3.3c, can eliminate the negative and convert them to positive voltages.



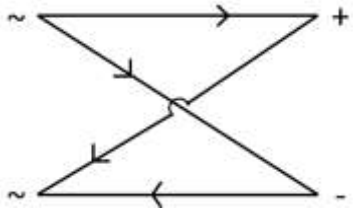

a b c

Figure 3.3: a) A one-way diode. b) Full bridge rectifier. c) Arrangement of the four diodes in a rectifier

3.3 Analytical Modelling of Crank Based Mechanical Harvester

3.3.1 Output Power of An Electromagnetic Harvester

The output voltage of a generator (V_g) is a function of the angular speed of it:

$$V_g = K_g \,.\, \dot{\theta}_g \qquad \text{Equation 3.2}$$

K_g is the generator's electrical constant and $\dot{\theta}_g$ is the angular speed of the generator. According to Ohm's law, the output voltage can also be written in terms of the output current (i_g) and the resistance (R),

$$i_g = \frac{V_g}{R} \qquad \text{Equation 3.3}$$

On the other hand, the output current is also related to the generator's torque (T_g), formulated as follows:

$$T_g = K_T . i_g \qquad \text{Equation 3.4}$$

In which K_T is the torque constant of the generator. Therefore, inserting the formulas (3.2) and (3.3) in (3.4) gives that

$$T_g = K_T \frac{V_g}{R} = \frac{K_T K_g \dot{\theta}_g}{R} \qquad \text{Equation 3.5}$$

Moreover, the mechanical power of an electromagnetic generator is as follows:

$$P_{em} = T_g . \dot{\theta}_g \qquad \text{Equation 3.6}$$

Subsequently, by inserting the formula 3.5 in the power equation 3.6 results in:

$$P_{em} = \frac{K_g K_T \dot{\theta_g}^2}{R} \qquad \text{Equation 3.7}$$

In addition, $\dot{\theta_g}$ is the angular speed of the generator, which is related to the crank's rotation, as follows:

$$\dot{\theta_g} = n\,\dot{\theta_C} \qquad \text{Equation 3.8}$$

The angular speed of the crank is denoted as $\dot{\theta_C}$ and n is the ratio of the gearbox. Finally, the output power of an electromagnetic generator is:

$$P_{em} = \frac{K_g K_T n^2 \dot{\theta_c}^2}{R} \qquad \text{Equation 3.9}$$

According to equation 3.9, in addition to the generator's inherent properties (K_g and K_T), the power produced by an electromagnetic generator is directly related to the generator's ratio (also constant), crank's rotation and angular speed and inversely correlated to the resistor of the harvesting circuit.

3.3.2 Crank System's Equation of Motion

The previous section showed that the power output depends on a few factors, including the angular speed of the crank. Therefore, in this section, the equation of motion of an offset slider-crank system, as illustrated in Figure 3.4, is analysed to better understand the system's motion.

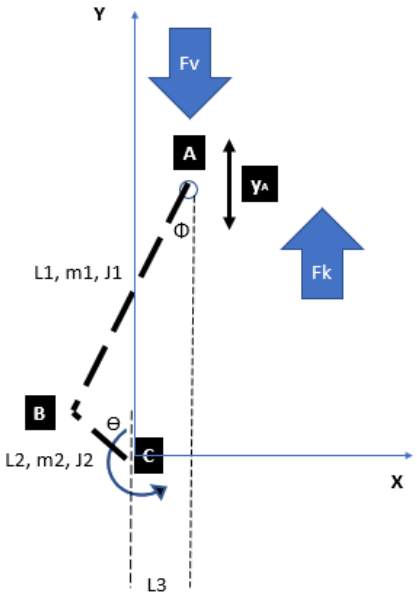

Figure 3.4: Free body diagram of the mechanical crank harvester

According to the free-body diagram:

$$L_1\,Sin(\emptyset) - L_2\sin(\theta) = L_3 \Rightarrow\ \emptyset = \sin^{-1}(\tfrac{L_3+L_2 sin\theta}{L_1}) \qquad \text{Equation 3.10}$$

And

$$y_A = L_1\cos\emptyset + L_2\cos\theta$$

Hence,

$$y_A = L_1\cos(Sin^{-1}\tfrac{(L_3+L_2 Sin\theta)}{L_1}) + L_2\cos\theta \qquad \text{Equation 3.11}$$

And taking the derivative of equation 3.11 gives the relationship between the displacement speed and the angular speed of the crank, which was shown in the previous section that directly affects the output power of the system.

$$V_A = \frac{d}{dt}(y_A) = -L_1\dot{\phi}\sin\phi - L_2\dot{\theta}\sin\theta = -L_2\dot{\theta}\left[\left(\frac{cos\theta(L_3+L_2 sin\theta)}{\sqrt{L_1^2-(L_3+L_2 sin\theta)^2}}\right)+sin\theta\right]$$

$$\dot{\theta} = \frac{-V_A}{L_2\left[\left(\frac{cos\theta(L_3+L_2 sin\theta)}{\sqrt{L_1^2-(L_3+L_2 sin\theta)^2}}\right)+sin\theta\right]} \qquad \text{Equation 3.12}$$

Equation 3.12 shows the direct relationship between the displacement speed of the harvester's top plate displacement speed.

To derive the equation of motion, the Lagrange equation of motion analysis has been followed. Accordingly, the Lagrangian of a system is defined as:

$$L = T - V \qquad \text{Equation 3.13}$$

And

$$\frac{d}{dt}\left(\frac{\partial L}{\partial\dot{\theta}}\right) - \frac{\partial L}{\partial\theta} = F \qquad \text{Equation 3.14}$$

Where L is the Lagrangian, T is the kinetic energy, V stands for the potential energy, θ is the degree of freedom of the system, and F represents the generalised forces. Inserting the equation 3.13 in 3.14 results in:

$$\frac{d}{dt}\left(\frac{\partial T}{\partial\dot{\theta}}\right) + \frac{\partial V}{\partial\theta} - \frac{\partial T}{\partial\theta} = F \qquad \text{Equation 3.15}$$

The kinetic energy of the system is the sum of the kinetic energy of the handle and the crank.

$$T = T_1 + T_2$$

$T_1 = \frac{1}{2} m_1 V_A^2 + \frac{1}{2} J_1 \omega_1^2$ and $T_2 = \frac{1}{2} J_2 \omega_2^2$

$$V_A = \frac{d}{dt}(y_A) = -L_2 \dot{\theta} \left[\left(\frac{cos\theta (L_3 + L_2 sin\theta)}{\sqrt{L_1^2 - (L_3 + L_2 sin\theta)^2}} \right) + sin\theta \right]$$

$$\omega_1 = \dot{\phi} = \frac{L_2 \dot{\theta} \cos\theta}{\sqrt{L_1^2 - (L_3 + L_2 Sin\theta)^2}}$$

Therefore,

$$T_1 = \frac{(L_2 \dot{\theta})^2}{2} m_1 \times \left[\left(\frac{cos\theta (L_3 + L_2 sin\theta)}{\sqrt{L_1^2 - (L_3 + L_2 sin\theta)^2}} \right) + sin\theta \right]^2 + \frac{1}{2} J_1 \left[\frac{L_2^2 \dot{\theta}^2 \cos^2\theta}{L_1^2 - (L_3 + L_2 Sin\theta)^2} \right]$$

$$T_2 = \frac{1}{2} J_2 \omega_2^2 = \frac{1}{2} J_2 \dot{\theta}^2$$

Consequently, the kinetic energy equals:

$$T = \frac{(L_2 \dot{\theta})^2}{2} m_1 \times \left[\left(\frac{cos\theta (L_3 + L_2 sin\theta)}{\sqrt{L_1^2 - (L_3 + L_2 sin\theta)^2}} \right) + sin\theta \right]^2 + \frac{1}{2} J_1 \left[\frac{L_2^2 \dot{\theta}^2 \cos^2\theta}{L_1^2 - (L_3 + L_2 Sin\theta)^2} \right] + \frac{1}{2} J_2 \dot{\theta}^2 \qquad \text{Equation 3.16}$$

In addition, the potential energy of the system is generated in the springs. Therefore

$$V = \frac{1}{2} K \, y_A^2$$

Where K stands for the spring stiffness. Since

$$y_A = L_1 \cos\emptyset + L_2 \cos\theta = L_1 \cos(Sin^{-1} \frac{(L_3 + L_2 Sin\theta)}{L_1}) + L_2 \cos\theta$$

Which results in

$$V = \frac{1}{2} K \left[L_1 \cos(Sin^{-1} \frac{(L_3 + L_2 Sin\theta)}{L_1}) + L_2 \cos\theta \right]^2 \qquad \text{Equation 3.17}$$

Finally, to formulate the generalised force, according to the virtual work principle:

$$\delta W = F \delta\theta \qquad \text{Equation 3.18}$$

Under the applied loads from the vehicles:

$$\delta W = F_V.\delta y_A = F_V.\delta(L_1\cos\emptyset + L_2\cos\theta) = F_V.(-L_1\delta\phi\sin\phi - L_2\delta\theta\sin\theta) =$$

$$F_V.\left[-\frac{L_2\,\delta\theta\cos\theta}{\sqrt{1-L_2^2\sin^2\theta}}\times\frac{L_3+L_2Sin\theta}{L_1} - L_2\delta\theta Sin\theta\right] = F_V.\left[-\frac{L_2\cos\theta(L_3+L_2Sin\theta)}{\sqrt{L_1^2-(L_3+L_2Sin\theta)^2}} - L_2Sin\theta\right].\delta\theta$$

Which gives out the generalized forces as:

$$F = -F_V.\left[\frac{L_2\cos\theta(L_3+L_2Sin\theta)}{\sqrt{L_1^2-(L_3+L_2Sin\theta)^2}} + L_2Sin\theta\right] \qquad \text{Equation 3.19}$$

By taking the respective derivatives from the equations 3.16 and 3.17 and inserting them in equation 3.15, the equation of motion of the system is derived as follows.

$$L_2^2\ddot{\theta}\left[\sin\theta + \frac{cos\theta(L_3+L_2\sin\theta)}{\sqrt{L_1^2-(L_3+L_2sin\theta)^2}}\right] + 2L_2^2\dot{\theta}\left[\sin\theta + \frac{cos\theta(L_3+L_2\sin\theta)}{\sqrt{L_1^2-(L_3+L_2sin\theta)^2}}\right]\left[\cos\theta + \frac{L_2\cos^2\theta}{\sqrt{L_1^2-(L_3+L_2sin\theta)^2}} - \frac{\sin\theta(L_3+L_2\sin\theta)}{\sqrt{L_1^2-(L_3+L_2sin\theta)^2}} + \frac{L_2\cos^2\theta\,(L_3+L_2sin\theta)^2}{\sqrt[2]{(L_1^2-(L_3+L_2sin\theta)^2)^3}}\right] +$$

$$\left[\frac{[J_1L_2^2\ddot{\theta}\cos^2\theta - 2J_1L_2^2\dot{\theta}\sin 2\theta]\left(L_1^2-(L_3+L_2Sin\theta)^2\right)+2J_1(L_2^2\dot{\theta}^2\cos^2\theta)(L_3+L_2sin\theta)(L_2\cos\theta)}{L_1^2-(L_3+L_2sin\theta)^2}\right] + J_2\dot{\theta}\ddot{\theta}$$

$$+K\left[L_1\cos(Sin^{-1}\frac{(L_3+L_2Sin\theta)}{L_1}) + L_2\cos\theta\right]\left[-L_2\sin\theta + (L_3+L_2Sin\theta)\frac{L_2\cos\theta}{\sqrt{L_1^2-(L_3+L_2sin\theta)^2}}\right]$$

$$+(L_2\dot{\theta})^2m_1\left[\left(\frac{cos\theta(L_3+L_2sin\theta)}{\sqrt{L_1^2-(L_3+L_2sin\theta)^2}}\right)+sin\theta\right]\left[\cos\theta + \frac{\left(sin\theta\,(L_3+L_2sin\theta)+cos\theta(L_3+L_2cos\theta)\right)\sqrt{L_1^2-(L_3+L_2sin\theta)^2}-(cos\theta(L_3+L_2sin\theta)\,(\frac{-(L_3+L_2sin\theta)(L_2cos\theta)}{\sqrt{L_1^2-(L_3+L_2sin\theta)^2}}}{L_1^2-(L_3+L_2sin\theta)^2}\right]+$$

$$\frac{1}{2}J_1\left[\frac{-L_2^2\dot{\theta}^2\cos 2\theta\left(L_1^2-(L_3+L_2Sin\theta)^2\right)+2(L_3+L_2Sin\theta)(\cos\theta)(L_2^2\dot{\theta}^2\cos^2\theta)}{\left(L_1^2-(L_3+L_2sin\theta)^2\right)^2}\right] + F_V.\left[\frac{L_2\cos\theta(L_3+L_2Sin\theta)}{\sqrt{L_1^2-(L_3+L_2Sin\theta)^2}} + L_2Sin\theta\right] = 0 \qquad \text{Equation 3.20}$$

Solving the equation of motion is done by either directly solving it using coding in platforms such as MATLAB, or using other designated software tools such as Solidworks, MBDyn and

Simcenter 3D [126]–[128]. In these tools, the components of the mechanical system are considered as rigid bodies and once the system is modelled by introducing the correct constraints, the relative motion of the rigid parts with respect to each other can be understood [127], [129]. In this study, Solidworks solver is utilised to solve the equation of motion, due to being also a visual tool to ensure the correct mechanism of motion is performed by the system against the applied loads, which is discussed in the next section.

3.3.3 Motion Analysis of the Slider Crank System and verification

Equation of motion was derived as discussed in the previous section. SolidWorks motion analysis solver has been used to solve the system's equation of motion described in the previous section. Motion analysis is a well-known simulation providing helpful information about the kinematics of a system. While in the Finite element analysis, the deformation, the strain, and the stress distribution are assessed, in motion analysis, the movement mechanism of the system is analysed, and its different components are treated as non-deformable rigid bodies. Therefore, it is also called the "rigid body dynamics" [126], [127].

The mechanical components of the crank road harvester were designed and modelled in Solidworks to perform the motion analysis simulation. The model was in the real scale, with the springs of 19.12 N/mm stiffness, equal to the springs used in the experiments to verify the model. The bottom plate of the unit was fixed, and the top plate's displacement was limited to only vertical displacements and was restricted in the other two directions. The crank’s disk was limited to only revolution movement, and the bolts’ joints were mated as concentric. The joints and the mates were also defined such that the crank would only have a revolving degree of freedom and be restricted in other directions, i.e., the horizontal and vertical displacement. The analysis was carried out on the motion conversion components, i.e., the slider, the crank, the top and the bottom plates the springs, to focus on the crank components' performance and ensure that the crank mechanism is working correctly. Figure 3.5 shows the modelled system.

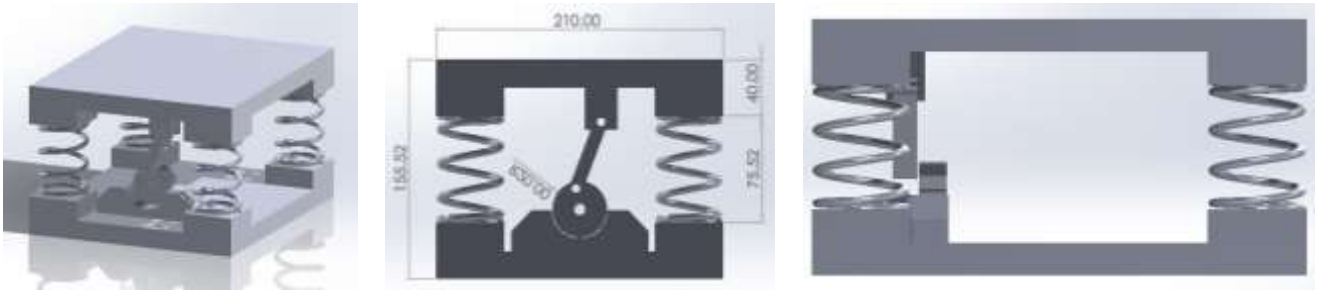

a b c

Figure 3.5: Solidworks model assembly. a) 3D view. b) Front view. c) Side view

In the following section, the results obtained from the motion analysis are discussed from both geometric and mechanical viewpoints.

3.3.4 Angular displacement of the crank

The angular displacement of the crank disk is one of the results that can be extracted from the motion analysis. Figure 3.6 shows the angular displacement of the crank disk under various displacement magnitudes but equal loading speed of 12 mm/s.

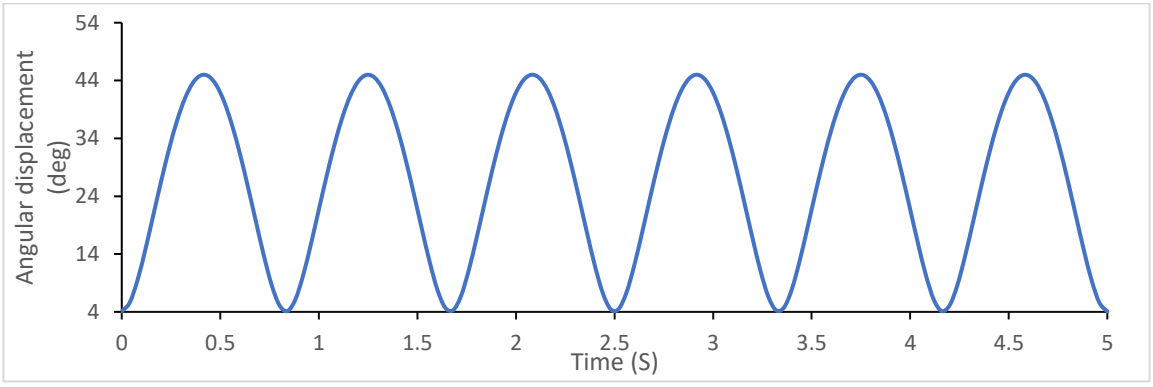

a

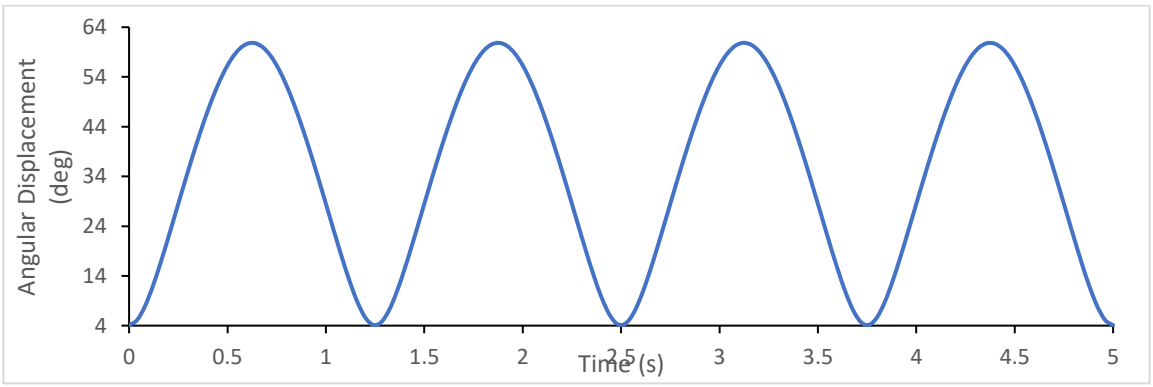

b

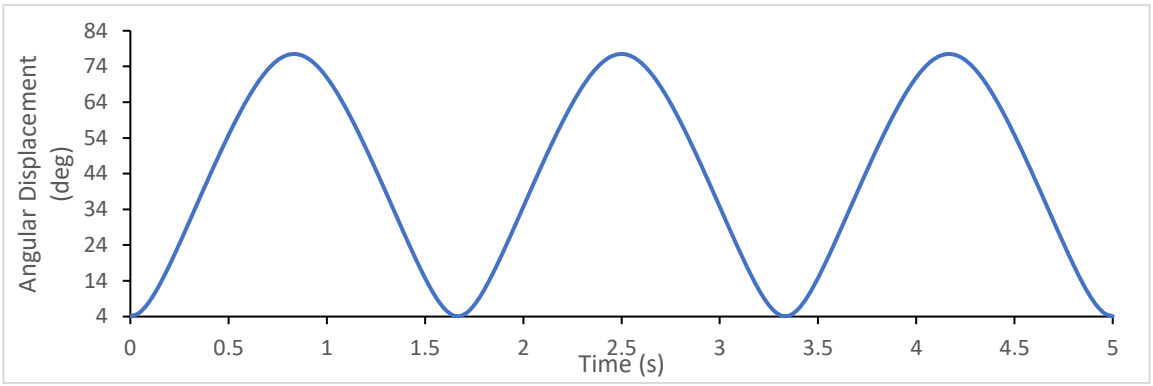

c

Figure 3.6: Displacement- time diagrams of the angular displacement of the crank under the loading speed of 12 mm/s and the displacement of a) 10 mm, 40.75 degrees b) 15 mm, 56.8 degrees and c) 20 mm, 72.9 degrees

The angular displacement of the crank under the same loading condition (displacement and loading speed) was recorded and measured visually to verify the results from the simulation geometrically. Images were taken from the crank at the beginning and end of the loading from a tripod (fixed position). Finally, the angular displacement was measured by processing the image using SpaceClaim software. Figure 3.7 shows the taken images in all three conditions, the displacement section (swept) and its magnitude.

Start End

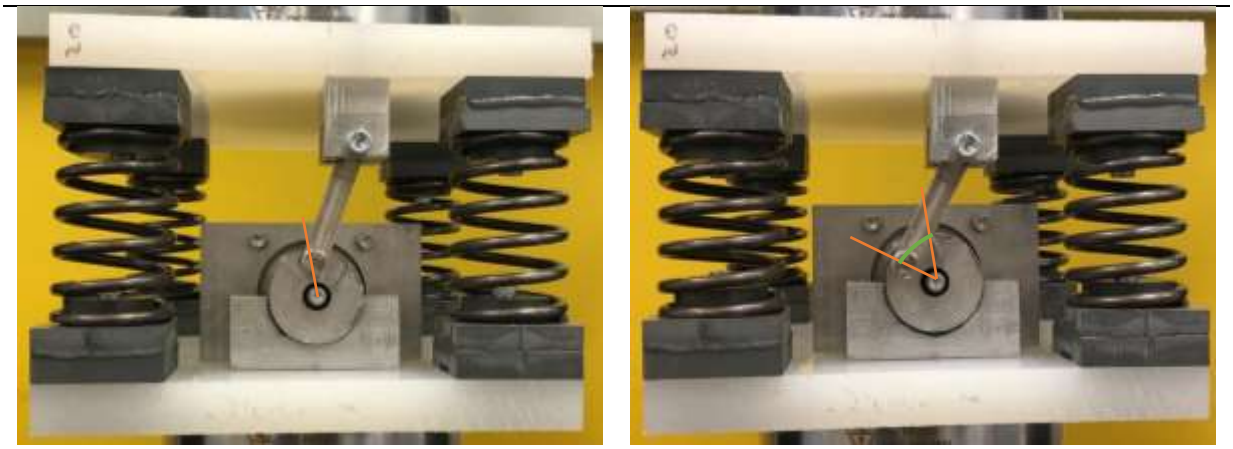

a

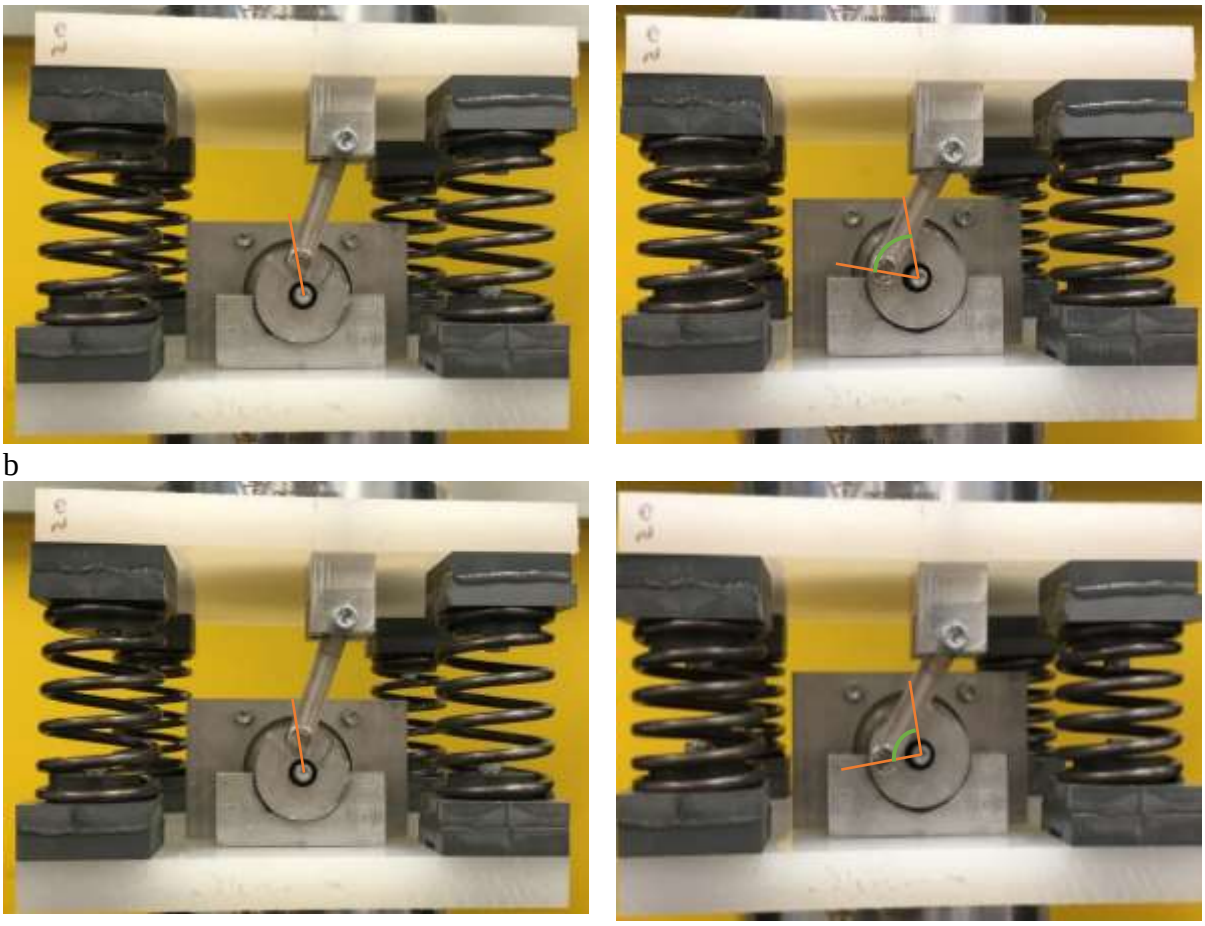

b

c

Figure 3.7: Start, end and the swept section of the crank under the displacement speed of 12 mm/s and the displacement of a) 10 mm: 39 degrees, b) 15 mm:56 degrees and c) 20 mm: 71 degrees

According to the images and the processing results obtained through the experiment, the angular displacement of the crank with the displacements of 10 mm, 15 mm and 20 mm was 39 degrees, 56 degrees and 71 degrees, respectively. On the other hand, through simulation of motion analysis, the crank's angular displacement was 40.75, 56.8 and 72.9 for the displacements of 10 mm, 15 mm, and 20 mm, correspondingly. Thus, it can be observed that the experimental and simulation results of the angular displacements match with each other very well, and the differences are only 1.75, 0.8 and 1.9 degrees for the displacements of 10 mm, 15 mm, and 20 mm, respectively, which are in an acceptable margin.

In all three conditions, the experimental results are lower than the simulation results due to the fact that in the motion analysis, the friction forces between the joints and the mechanical parts are neglected and not considered, while in reality, they play a significant role in the system's

performance. Moreover, the manufacturing process is far from being ideal, and the built components may have imperfections that do not occur in simulation.

As it was shown analytically, the angular speed of the crank ($\dot{\theta}$) plays an important role in the output power of an electromagnetic harvester, and through the motion analysis, the relationship between the angular speed ($\dot{\theta}$) and the top plate's displacement speed ($\dot{y_A}$) was revealed. Moreover, it was shown that the angular displacement of the crank (θ) is also related to the displacement magnitude of the top plate (y_A). In the following sections, motion analysis is employed to quantify the angular displacement and speed of the crank, which would give a better understanding of the behaviour of the harvester and form a decision foundation of the testing scenarios in the experimental studies, which is discussed in the next chapter.

3.3.5 Angular Speed of The Crank

According to the analysis results in section 3.3.1, equation 3.9, the crank's angular speed directly affects the system's output power. In this section, this effect is shown through motion analysis. Figure 3.8, shows the diagrams of the angular velocity of the crank, under the displacement magnitude of 10 mm and the displacement speeds of 10 mm/s and 15 mm/s. These values were chosen systematically as an example of possible real field displacement level under different speeds. Compared to the real field applications, these speeds are in fact lower, however, they were chosen systematically for the purpose of illustration.

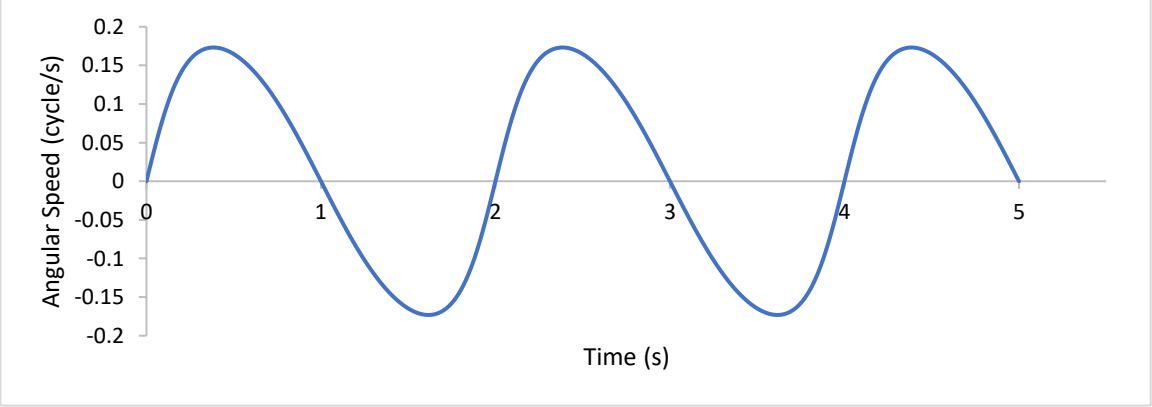

a

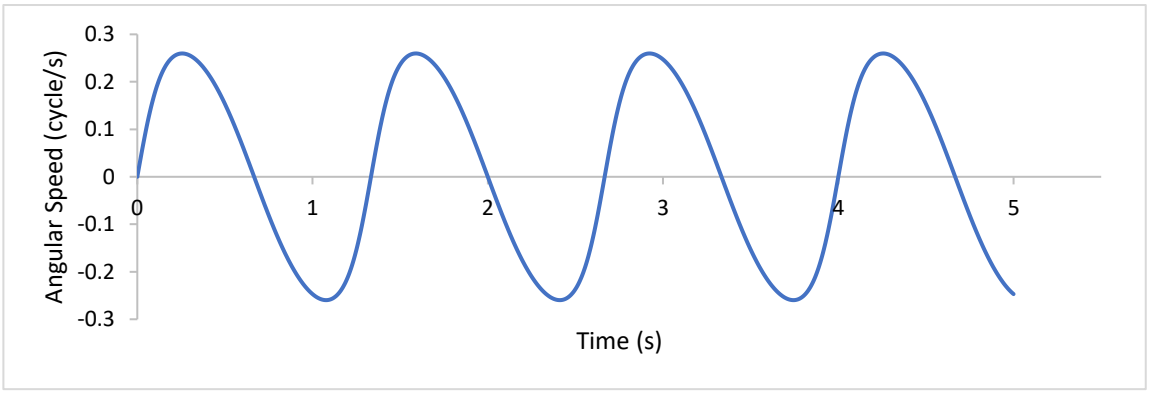

b

Figure 3.8: Angular speed of the harvester's crank under the displacement of 10 mm and the displacement speed of a) 10 mm/s, and b) 15 mm/s

As it is illustrated in Figure 3.8, there is a direct relationship between the displacement speed of the top plate of the harvester and the crank's angular speed.

In addition, the displacement level of the top plate is also an important factor, since it is a function the vehicles' mechanical loads (curb weight), and there are vehicles with various weights passing over the harvester in the real field applications, applying different levels of displacement.

Therefore, in the experimental study, the testing scenarios are combinations of different displacement speeds and magnitudes. It should be mentioned that other factors such as the friction between the components, the gearbox, and the electrical rectification affect the electrical power output, which will be studied experimentally and discussed in the next chapter.

3.3.6 Maximum Displacement of The Top Plate

Two different aspects should be considered when deciding the maximum displacement magnitude of the top plate. First, as the crank energy harvesting system is designed based on road rumbles and smooth speed bumps, safety and the effect of the speed bump on the traffic flow is an essential factor. The second important factor is limitations caused by the mechanism of the system.

Speed bumps come in different shapes and heights. A few guidelines and comparative studies suggest suitable shapes, lengths, and heights. According to the UK transport department, the road's speed bumps and rumbles, which come in sinusoidal, round or combined shaped profiles, may have various maximum heights ranging from 25 to 100 mm for speed bumps and 12 mm to 20 mm for rumbles [130]–[132]. Various heights affect the traffic flow and speed reduction differently. For example, the lower heights provide smoother rides, while the higher heights affect the traffic flow more and cause a more significant speed reduction.

Moreover, due to the design and the size of the harvester, some mechanical limitations affect choosing the right displacement magnitude range of the top plate of the harvester. Motion analysis was employed to investigate these factors. Since the primary goal of this research is to recover energy from the road, it is desirable to have the crank revolving as complete as feasible. Therefore, various displacements were applied on the top plate, and the angular displacement of the crank was obtained using the motion analysis, which was eventually used to decide about the feasible maximum displacement magnitude of the top plate. In this analysis, only the angular displacement is investigated under various vertical displacements, and the displacement speed is kept constant

Figure 3.9 shows the linkage of the crank components. It is worth mentioning that the current dimensions of the harvester's case were chosen in such a way as to have a minimal amount of excavation and an easy installation on the road.

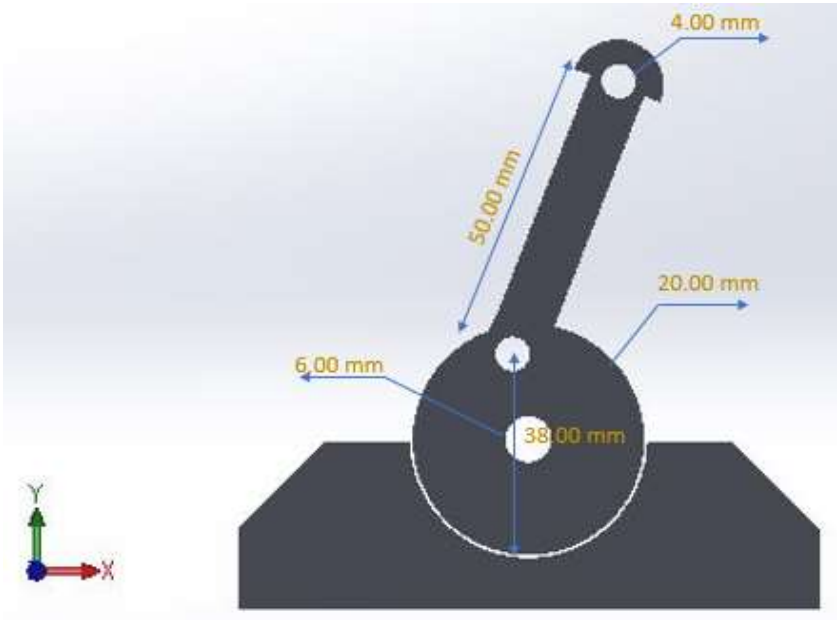

Figure 3.9: Dimension details of the crank system

The displacement speed, throughout this analysis, was kept equal to 10 mm/s, and six different displacement magnitudes of 10 mm, 15 mm, 20 mm, 25 mm, 30 mm, and 35 mm were applied on the top plate. It is worth noting that the vertical distance between the crank bolt and the lowest point of the disk is 38 mm. Therefore, no displacements greater than 35 mm could be applied. Figure 3.10 shows angular displacement at the ultimate position of the crank for each displacement.

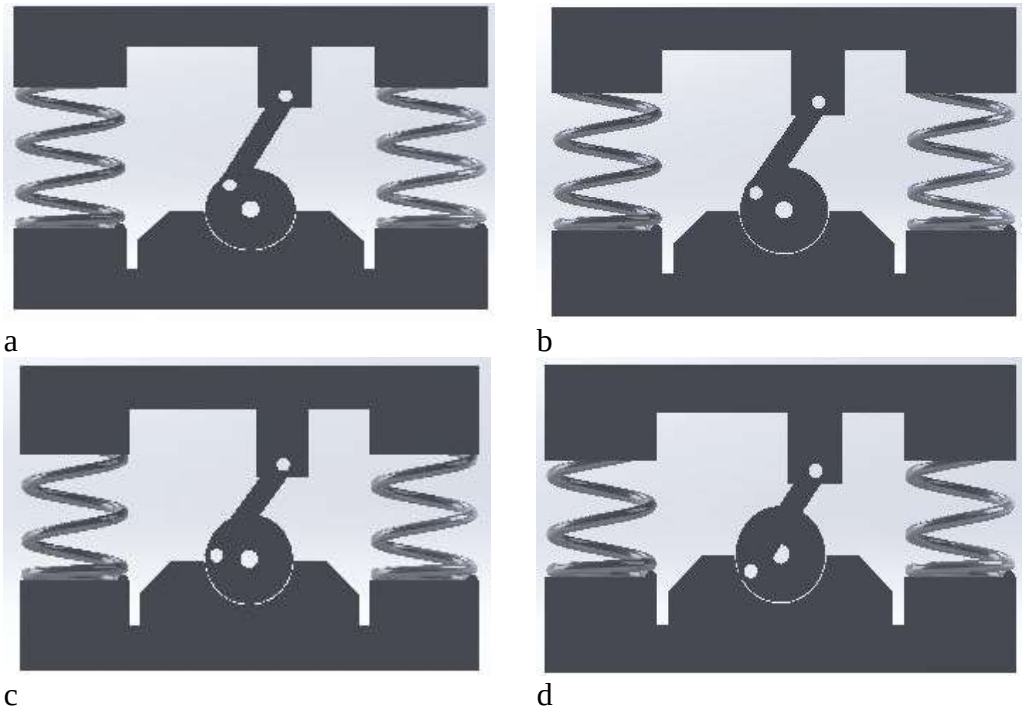

a b

c d

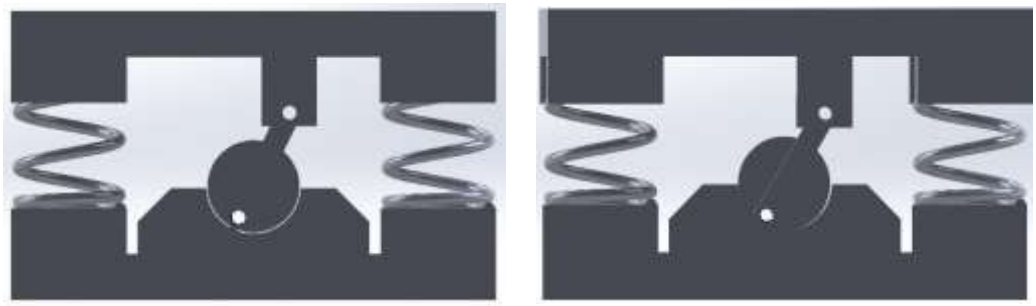

e f

Figure 3.10: Angular displacement (final states) of the harvester under 10 mm/s loading speed and the displacement magnitudes of a) 10mm: 0.114 cycle b) 15 mm: 0.158 cycle c) 20 mm: 0.203 cycle d) 25 mm: 0.261 cycle e) 30 mm: 0.4 cycle and f) 35 mm: 0.4 cycle

As shown in Figure 3.10, according to the motion analysis simulation, both displacements of 30- and 35-mm result in an angular displacement of 0.4 cycle, and the displacements of 10, 15, 20 and 25 mm caused the angular displacement of 0.111, 0.156, 0.203 and 0.2611 of a cycle. It is also observed at the displacement of 35 mm, that the crank mechanism is locked and cannot rotate further.

However, it is known that, unlike the simulation conditions, the manufacturing process accuracy is not ideal, which can slightly affect the dimensions of the crank and eventually influence the results. Therefore, once the crank was manufactured, the maximum possible displacement was validated through testing. While the top plate was loaded gradually, it was observed that displacements further than 25 mm were not possible due to the manufacturing and the frictions between the components. Therefore, it was decided to keep the maximum displacement of the top plate around 25 mm. Figure 3.11 shows the initial and the ultimate position and angular displacement diagram of the crank at the 25 mm displacement of the top plate.

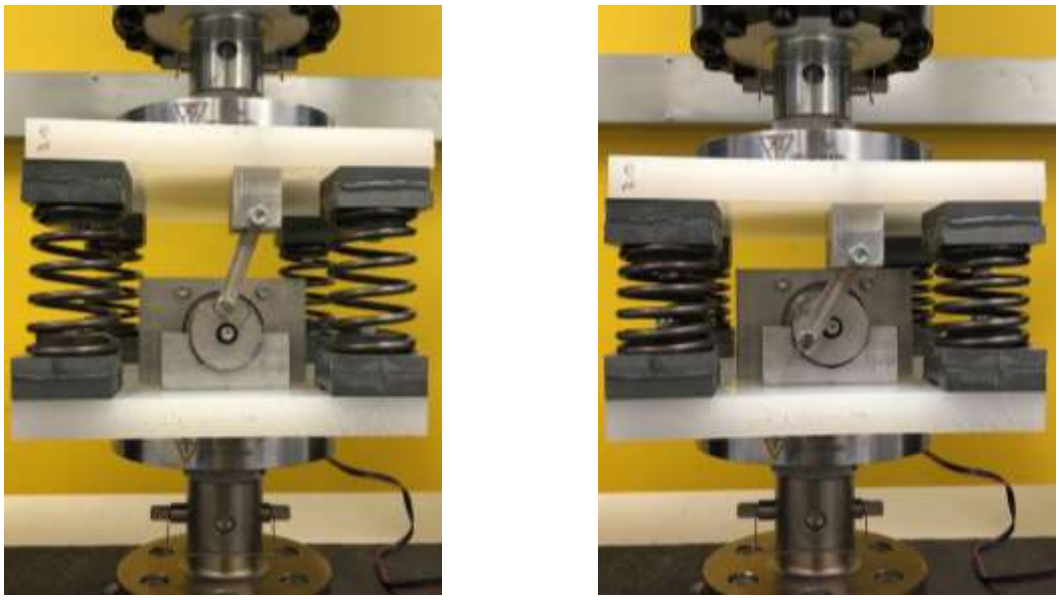

a b

Figure 3.11: Energy harvester unit at a) 0 mm displacement, b) 25 mm displacement

Figure 3.11b shows the unloaded and ultimate position of the crank at the displacement of 25 mm. It is worth noting that 25 mm is the maximum displacement of the top plate of the harvester. In the actual application, this parameter depends mainly on the weight and speed of the passing vehicle. Therefore, displacements smaller than 25 mm will also be considered in the experimental studies. By having 25 mm displacement of the top plate, this harvester is ideal for a smooth speed bump or road rumbles, with a minimal effect on the driver's speed.

3.4 Finite element simulation of the crank road energy harvester

Finite element analysis (FEA) of the crank harvester unit was conducted, using ANSYS software to study the structure of the harvester and the effect of its maximum loading condition on the mechanical components of the structure. Unlike motion analysis, the structural components are not merely rigid bodies in finite element analysis. Instead, they are analysed as flexible bodies and their stress and strain distribution is analysed. In this method, the complex body is divided into a network of several elements and nodes called mesh and the unknown function (called the field variable) is evaluated in each node and element. Motion analysis and

FEA are often employed together to verify the mechanism and determine the stress distribution in the components, especially at the most critical conditions.

The purpose of conducting FEA in this study is to ensure the mechanical stability of the system under the applied loads at critical conditions, i.e., high displacement magnitude. In the following sections, details of this analysis, including the meshing details, boundary conditions, and the FEA's mechanical results, are brought. Like the motion analysis, FEA was also performed only on the crank handle and disk since they are the system's critical components. It was observed experimentally that the minimum torque to rotate the other components of the harvester were negligible, so their effect was not considered in this analysis.

3.4.1 Mesh Network and The Boundary Conditions of The Harvester

As the harvester unit comprises different geometries, the meshing method of each geometry had to be defined differently. As a result, the system is divided into 580036 nodes and 134799 elements. Figure 3.12 illustrates the meshing of the whole unit and the details of the mesh in springs, the crank handle and disk separately.

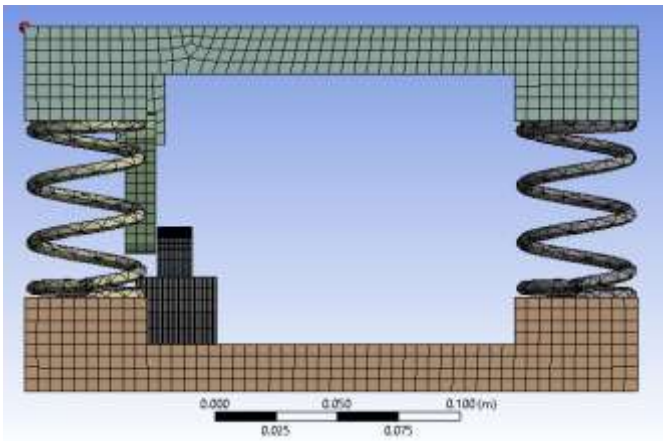

a

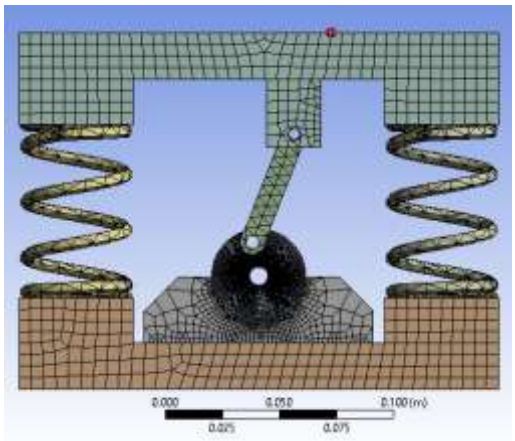

b

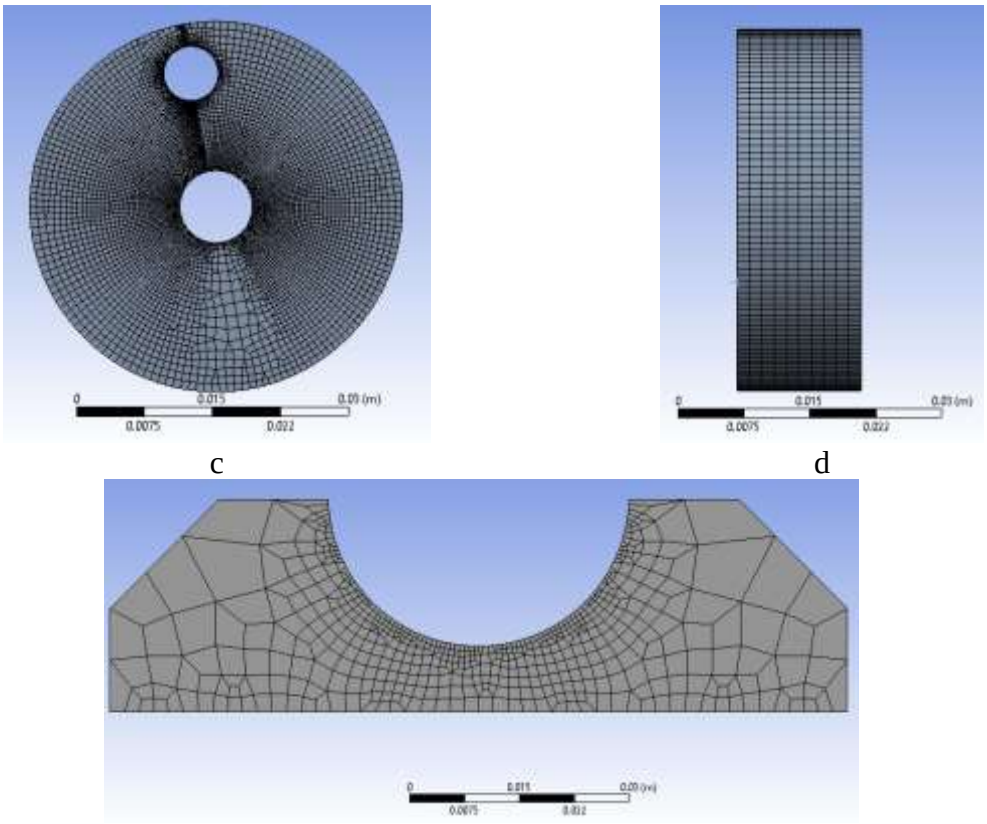

Figure 3.12: Mesh network of the Crank harvester unit: a) Side view b) Front view c) Crank disk front d) Crank disk side. e) Front of the disk holder

The boundary conditions of the simulation were similar to the motion analysis; the bottom plate was fixed, and the displacement of the top plate was restricted to only the vertical displacement. In the following section, the FEA results are discussed.

3.4.2 Structural Analysis of The Crank Energy Harvester

The structural response of the harvester was evaluated using static structural analysis of ANSYS software. The applied mechanical load was 25 mm of displacement, applied on the top plate of the harvester unit. Moreover, the springs were eliminated from displaying the result, as they are not critical components. Since the focus of this analysis was mainly on the evaluation of the structural response of the crank components, i.e., the crank handle and the disk, and this decision does not have any negative effect on this goal. Figure 3.13 shows FEA results at the top plate's displacement of 25 mm, which is the most critical stage.

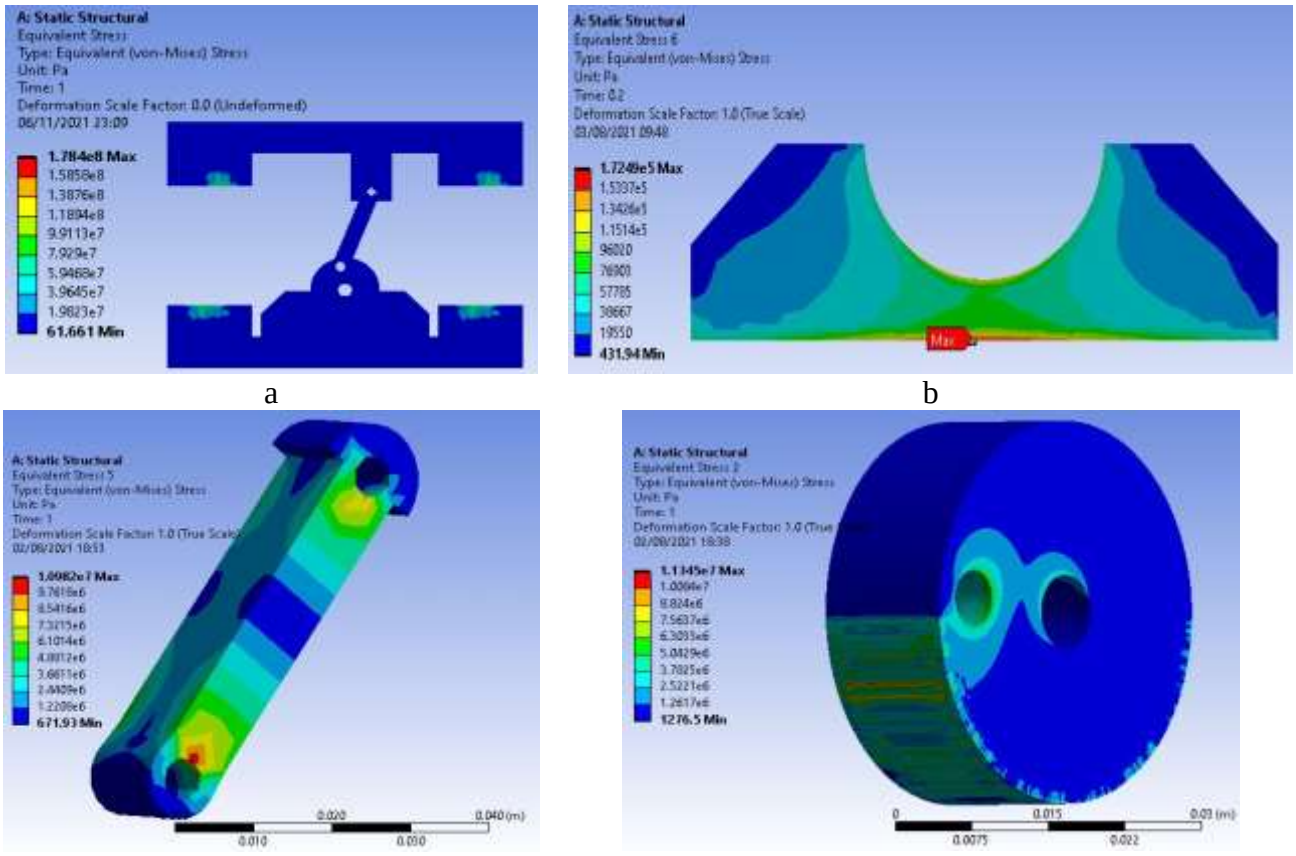

Figure 3.13: FEA results of a) whole system, b) the crank disk holder, c) crank handle, d) Disk

As shown in Figures 3.14d, the maximum stress in the crank disk is about 1.14e7, and it occurs on the contact area of the disk and the disk holder, which was expected considering the loading and rotation direction. The stress distribution on the crank holder (Figure 3.14c) also shows no critical points, and the maximum stress on it (1.72e5 Pa) is well below the yield strength of aluminium. Another critical component is the crank handle, which is responsible for transferring the movements to the crank disk and a portion of the applied load. Based on the simulation results shown in Figures 3.14c, the maximum stress that happens on the bottom bolt equals 1.098e7 Pa. Moreover, the reaction forces of the two bolt places were also evaluated, and they are equal to 72.68 N. In both holes, M6 bolts are going to be fixed, which have a shear capacity of 7.72 KN. Comparing the reaction forces with the shear capacity shows that the applied forces are far less than the bolt's capacity.

According to the FEA results, in the whole system (Figure 3.13a), the maximum stress is 3.61e7 Pa. This stress is well below the compressive yield strength of aluminium (2.8 e8 Pa), which is the material used to manufacture the components.

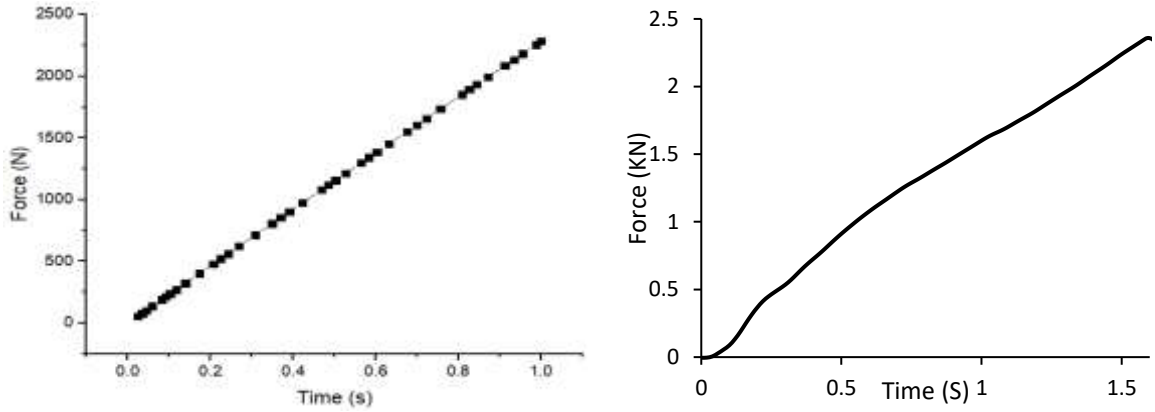

a b

Figure 3.14: Reaction force results, a) Result of the simulation, 2308 N, b) Result of the experiments, 2359 N

Figure 3.14 shows the reaction force results on the top plate from the simulation and experiments, which have a good agreement with each other. In a simulation (Figure 3.14 a), the maximum reaction force on the top plate is equal to 2308 N at the ultimate condition, which matches with the experimental results of 2359 N (Figure 3.14b).

3.5 Conclusions

In this chapter, the crank-based road energy harvester is studied from a structural and mechanical point of view. Slider crank mechanism was chosen as a new system to be implemented in this harvester unit. As its components are connected, this system has advantages over the other systems such as rack and pinion. Also, compared to the hydraulic systems, it has a simpler maintenance procedure. Moreover, the harvester's external dimensions were chosen to have minimal excavation and easy installation. Once the design was completed, motion analysis and finite element analysis were conducted in order to ensure the mechanism's performance and mechanical stability under the applied loads in experiments. The following points are the conclusions from these analyses.

1. The system's output power is directly related to the angular speed of the crank, which is affected by both top plate’s displacement speed and displacement magnitude. Hence, both displacement magnitude and speed are important to be studied.

2. According to the motion analysis, a displacement of 35 mm results in the crank's largest angular displacement, favouring the output power. However, in the actual condition, the manufacturing process is far from being ideal. Frictions between the components and also the presence of the gearbox and the generator also affect the angular displacement. Therefore, it was decided to keep the maximum displacement of the top plate around 25 mm. This value is the maximum displacement, which depends on the loads applied from the passing vehicles. Hence, in the experimental studies discussed in the next chapter, it is decided to have displacements ranging from around 10 mm to 25 mm, applied with various displacement speeds, suitable for applications of road rumbles and smooth speed bumps.

3. Finite Element Analysis was done on the system modelled in the real scale and the springs of 19.12 N/mm, which will be used in the experimental studies section. The mechanical load was 25 mm of displacement applied on the top plate. According to the FEA results, the maximum stress occurring in all the components, 3.61e7 Pa, is less than the yield strength of aluminium (2.8e8), which is the material used to manufacture the components. Thus, the system is stable and can withstand the mechanical loads applied to the harvester unit.

4. Both simulation results of motion analyses and FEA agreed with their corresponding experimental results. Angular displacement obtained from the experiments matches the simulation results, with a maximum deviation of 1.9 degrees (0.005 of a cycle) acceptable. Moreover, the reaction force result from FEA, equal to 2308 N, is in an acceptable margin of 2359 N, achieved from the experiments.

The next chapter focuses on the experimental studies and the laboratory tests conducted on the harvester unit. First, the testing scenarios are described, and then the experimental results are presented and discussed.

4 Experimental Studies

4.1 Introduction

Following the simulation and verification, the experimental studies on the crank-based harvester are discussed in this chapter. In the first part of the chapter, the manufacturing and assembly of different system components are thoroughly discussed. Details of all the components and their role in the performance of the energy harvesting system are described. Next, the data collection setup is described. Afterwards, the experimental setup and the experiments' setup are discussed, and the results are obtained from each scenario. The discussed results are the load-time diagram, the direct voltage output, the voltage and power recorded from the power harvesting circuit, and the system's efficiency. Finally, the behaviour of each variable in different scenarios was plotted and compared to each other.

4.2 The manufacturing procedure of the Energy Harvester

As described in the previous chapter, the crank-based energy harvester comprises various parts that have either mechanical or electrical functions. The crank’s handle, disk, and gearbox are purely mechanical parts, while the rectifier only has an electrical function. The electromagnetic generator has both characteristics as it converts mechanical to electrical energy. A harvester unit prototype was manufactured to examine the harvester in the laboratory. In the following sections, the specifications of each part of the prototype are given separately.

4.2.1 Energy Harvester Case

The prototype's exterior comprises two plates (top and the bottom plate) supported by four springs at the corners. Polypropylene Natural Sheet homopolymer is used for the bottom and the top plate, with the dimensions of 210 mm x 250 mm x 20 mm. Table 4.1 shows the mechanical properties of this material.

Table 4.1: Mechanical properties of natural polypropylene sheet [133]

Physical Properties	Unit	Result
Density	g/cm³	0.95
Yield Stress	MPa	32
Modulus of elasticity	MPa	1400

Four springs of 19.12 N/mm stiffness were placed on the box's corners, providing the support upon loading and unloading in the first prototype of the harvester. They are made of music wire which is a regular material for industrial springs manufacturing. These springs were initially chosen as their dimensions match the requirements of the box. In addition, by having an aspect ratio of 1.78, they perform well against buckling [58]. Table 4.2 shows some of the specifications of the spring, and in Figure 4.1, the dimensions of the exterior and the springs of the prototype are shown.

Table 4.2: Spring specifications [134]

Specification	Unit	Value
d - Wire diameter (mm)	mm	5.26
De - External diameter (mm)	mm	49.20
Di - Internal diameter (mm)	mm	38.68
Sn - Maximum travel (mm)	mm	26.26
R - Spring constant (N/mm)	N/mm	19.12

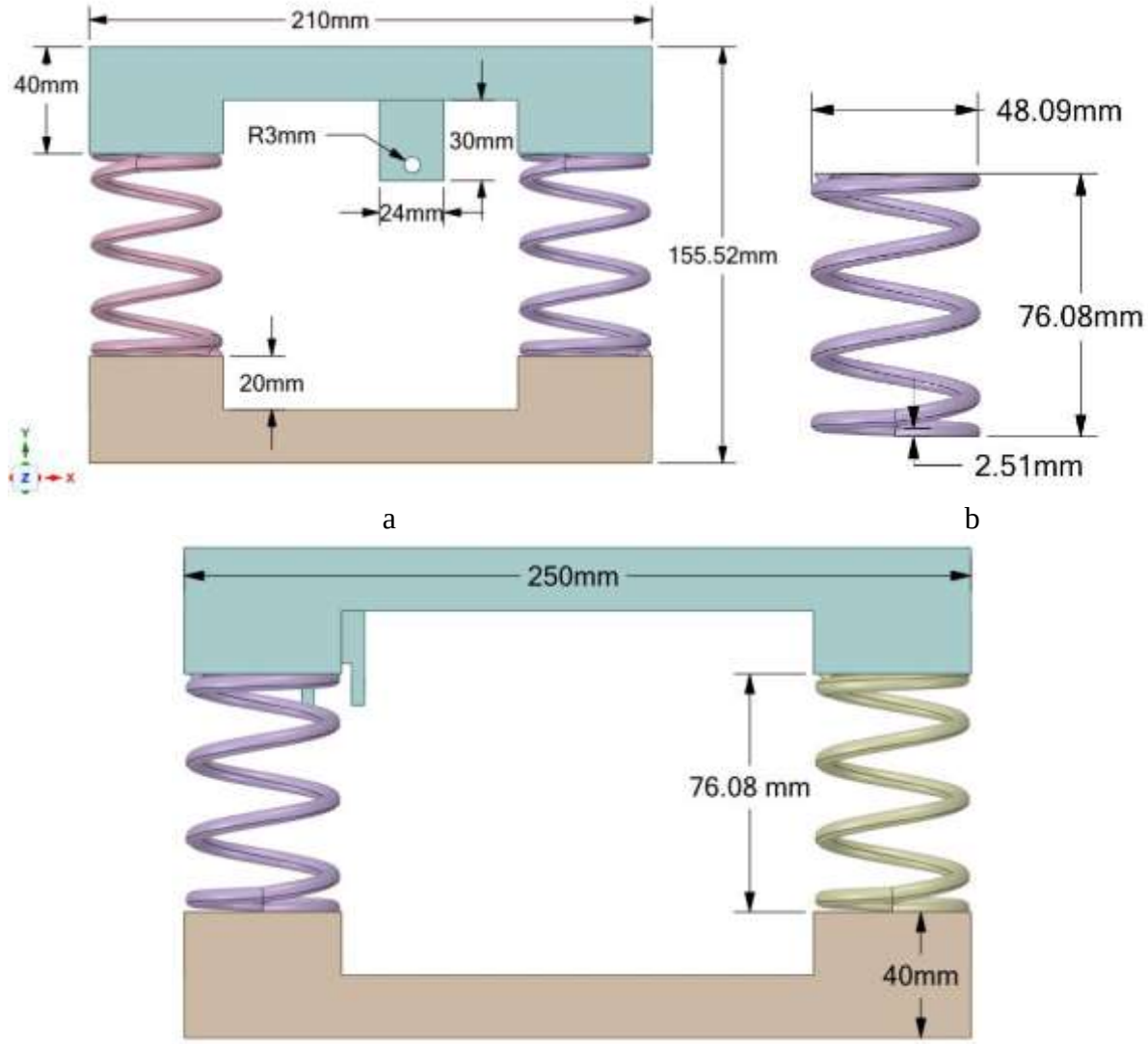

Figure 4.1: Dimensions of the a) front, b) spring and c) the side of the harvester unit

These dimensions were primarily chosen to be within the depth of the pavement of roads and have an easy maintenance process. The pavements depth of the roads depends on the service loads applied on them and their service area. However, it can vary between 3 inches to 9 inches (76.2 to 228.6 mm) [135], and the depth of the harvester is around the average of this range.

4.2.2 The crank mechanism

The crank mechanism comprises two parts of the handle, and the disk bolted together. A bearer has been added to ensure the crank disk's stability under the loading and unloading cycles in this design. The parts were manufactured out of aluminium, a high-strength, abundant material exhibiting sufficient corrosion resistance. Table 4.3 shows the mechanical properties of the

aluminium alloy used for manufacturing the parts, and Figure 4.2 shows the design details of the crank handle, disk, and bearer.

Table 4.3: Mechanical properties of the Aluminium Alloy

Physical Properties	Unit	Result
Density	g/cm³	2.77
Yield Stress	MPa	280
Modulus of elasticity	MPa	71000

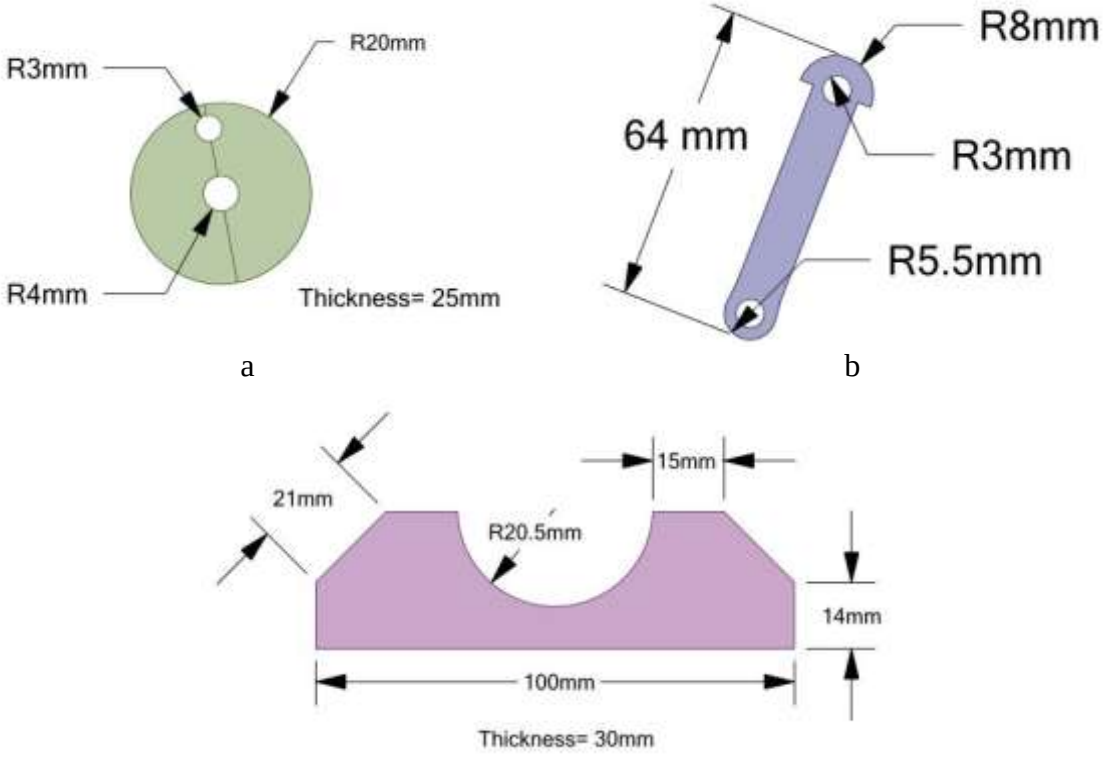

Figure 4.2: design details of the crank parts: a) Disk, b) Handle, c) Bearer

4.2.3 Gearbox

In this harvester, a planetary gearbox was decided to be the link between the generator and the crank to increase the angular speed while transferring to the generator. As shown previously, the angular speed of the generator plays a crucial role in its output power. In addition to the dimensional compatibility, the gearbox had to have high efficiency and low backlash. Table 4.4

shows the mechanical properties of the chosen gearbox, and its dimensions are shown in Figure 4.3.

Table 4.4: Mechanical properties of the employed gearbox

Specification	Unit	Value
Gear Ratio		100
Maximum backlash	Arc-min	25
Efficiency	%	95
Maximum torque	N.m	135

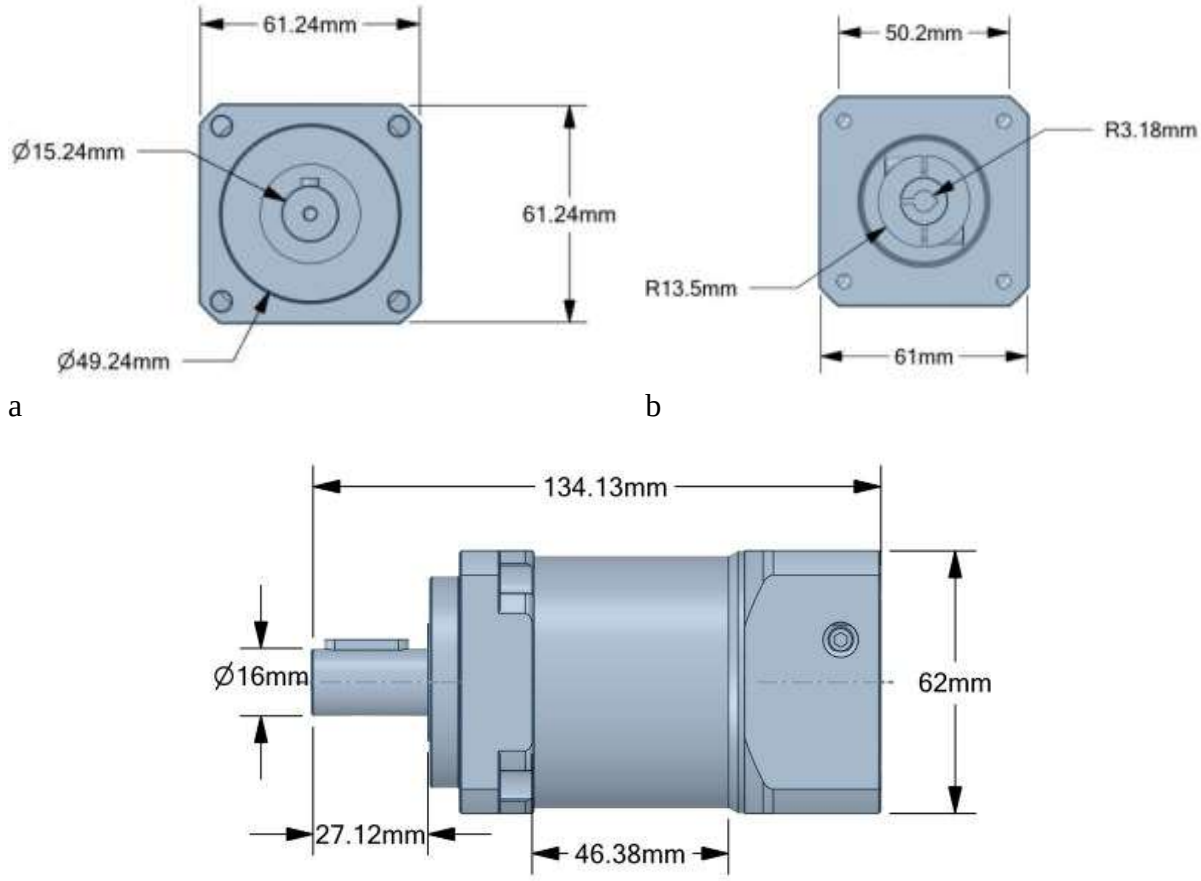

Figure 4.3: Dimension Details of the gearbox, a) front, b) back, c) side views

4.2.4 Generator

The electromagnetic generator is the hybrid component of this road energy harvester, which converts the mechanical to electrical energy. It is connected to the gearbox, and the angular displacement and speed, which are increased through the gearbox, make it revolve and generate

electricity. In this system, a 2-phase NEMA 17 generator having compatible dimensions with the gearbox was employed. Before installation, the generator was characterised using a heavy-duty drill to calculate the generator's electrical constant (Equation 3.2). Figure 4.4 illustrates the characterisation experiment done on the generator. In this test, the rotation speed is 350 rpm which results in 5.75 Volts electrical potential generation. This voltage is the output of one of the two phases of the generator.

Figure 4.4: Generation of 5.75 V at 350 rpm

According to Equation 3.2, the electrical constant of the generator is equal to 0.9836 Vs/r.

$$V_g = K_g \,.\, \dot{\theta_g} \xrightarrow{yields} K_g = 0.9863\ Vs/r$$

$$V_g = 5.75\ V$$

$$\dot{\theta_g} = 350\ rpm = 5.83\ rps$$

Table 4.5 shows the specifications of the employed generator, and Figure 4.5 shows its dimensions.

Table 4.5: Specifications of the generator

Specification	Unit	Value
Phase number		2
Phase angle	Degrees	1.8
Electrical constant	Vs/r	0.9836
Weight	Kg	0.34

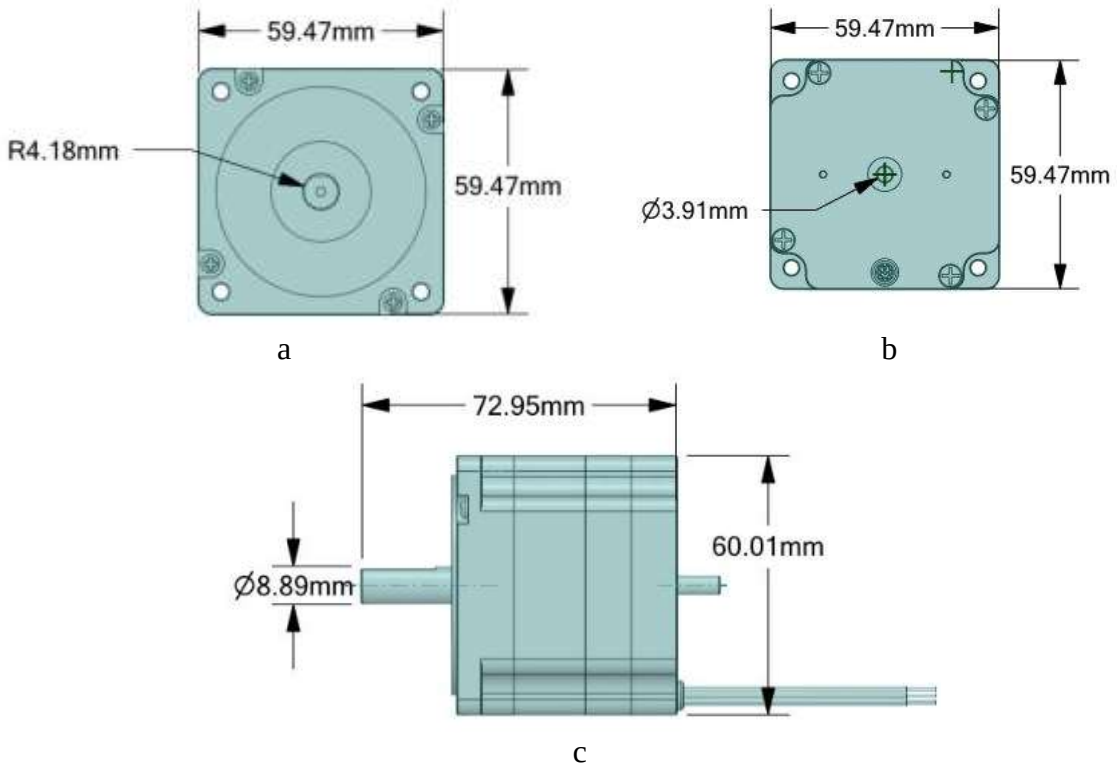

Figure 4.5: Dimensions of the employed generator, a) front, b) back, c) side views

4.2.5 Bridge Rectifier

As the crank-based road harvester is performing under cyclic loads of loading and unloading, in each cycle, the cap and consequently the generator's shaft rotates in opposite directions, generating alternating positive and negative voltages. However, the negative voltage is not useful and hence, to eliminate them and turn them into positive voltages, a full bridge rectifier, as explained in the previous chapter, is connected to the generator. Since there are two pairs of output, two rectifiers are required at the end of the generator. It should be mentioned that even though these rectifiers also cause voltage drop, they were used instead of a one-way clutch, which is a mechanical solution employed in previous studies [12], [67], [136], to reduce the mechanical complexity and simplify maintenance, as it is a small piece with easy installation and suitable for charging batteries [137]. Figure 4.6 shows the dimensions of the rectifier.

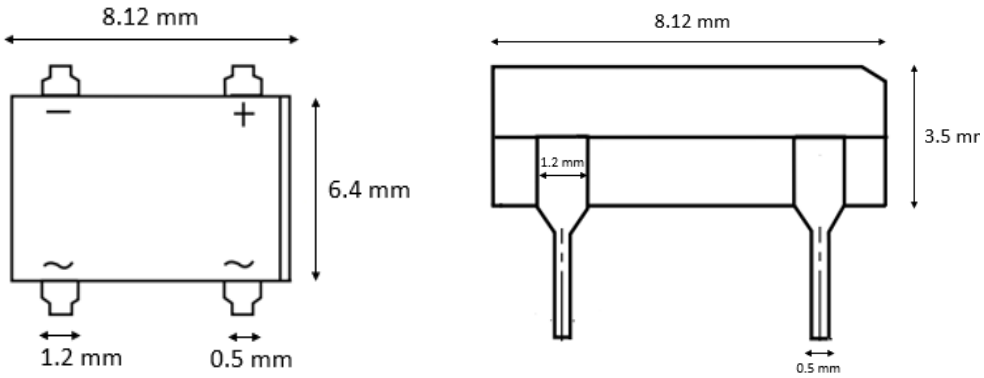

Figure 4.6: Dimensions of the employed rectifier

An experiment similar to the characterisation of the generator was performed to evaluate the voltage of the rectifier. Two generator terminals were connected to the rectifier, and the output was measured using a multimeter. Figure 4.7 shows the test setup and the result. The angular speed of the generator is 350 rpm, similar to the previous set-up. As it can be seen, the output voltage is dropped from 5.75 V to 5.31, which is due to the effect of the rectifier and its voltage loss. Therefore, around 0.08 V (1.4%) is lost at the angular speed of 350 rpm (5.83 rps).

Once these pieces were prepared, they were bolted to each other, and the whole system was setup.

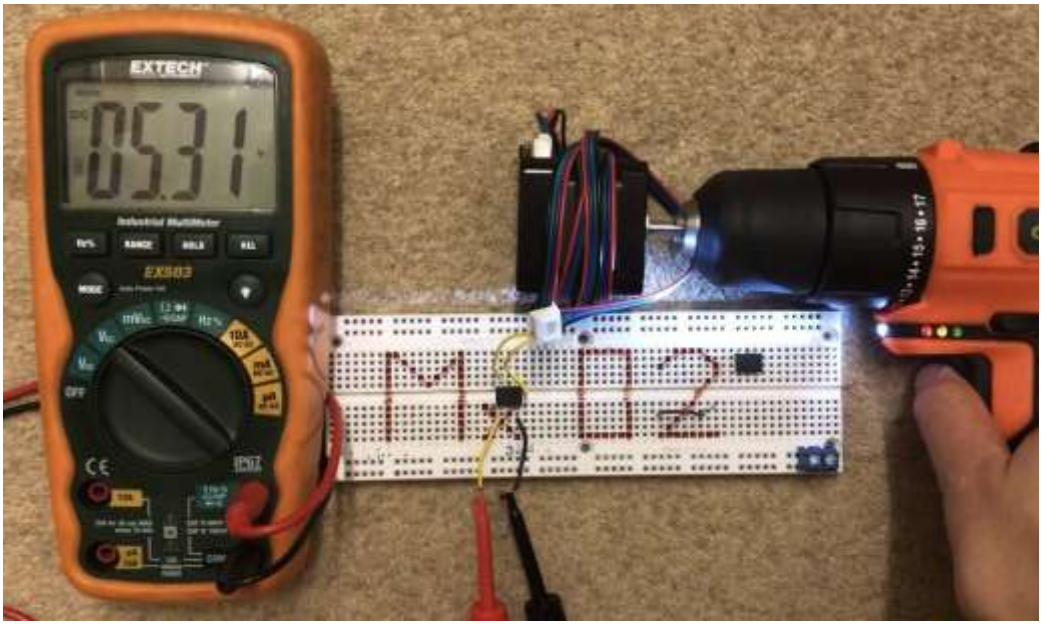

Figure 4.7: Test set up to evaluate the voltage loss due to the rectifier

In addition to the explained parts, a data logger device, program, and electrical resistors with different magnitudes were used throughout the experimental program.

4.3 Data logging and processing

Data logging was done using the NIDAQ data logger, and an exclusive LabView program to record the data was designed. Figure 4.8 shows the NIDAQ unit and the overview of the LabView program. The maximum logging speed of the NIDAQ is 100 HZ which was also used in this experimental study.

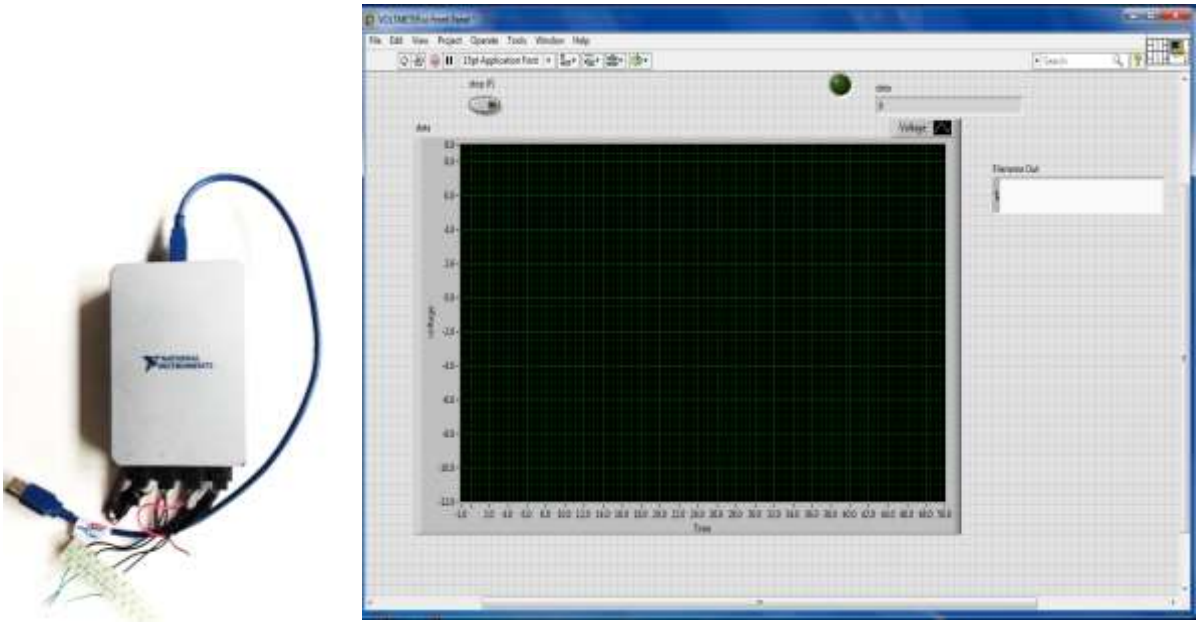

a b

Figure 4.8: NIDAQ unit (a) and the overview of the LabView program (b)

4.4 Experimental Setup and Results

The experimental program was designed in order to investigate the performance of the crank-based electromagnetic harvester. According to the analysis explained in the previous chapter, the important factors affecting the system's output power are the angular speed of the crank and the resistance of the circuit. The resistance comprises the internal resistance, an inherent property, and the external resistance of the energy harvesting circuit, which is a variable and can be optimized.

4.4.1 Power harvesting circuit

The schematic design of a power harvesting circuit is shown in Figure 4.9, and it is comprised of the generator (source of voltage) connected to an external resistance and a multimeter. In this study, the combination of the generator and rectifiers are the voltage source as the voltage had to be rectified. The electrical power is calculated by measuring the voltage around the external resistance and following the equations 4.1 to 4.3.

$P = VI$ Equation 4.1

Where P is the power, V is the voltage around the resistor, and I is the electrical current. According to Ohm's law:

$I = \frac{V}{R}$ Equation 4.2

R being the resistor's magnitude. Therefore

$P = \frac{V^2}{R}$ Equation 4.3

It should be mentioned that in the current study, as the generator has two pairs of leads, two sets of resistance were connected to the leads, and the voltage around both of them was recorded.

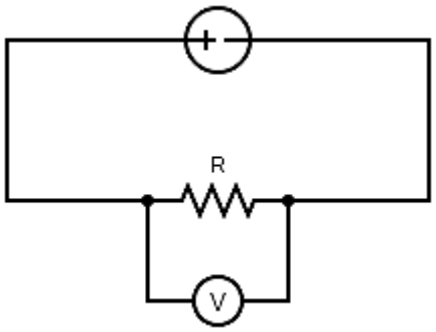

Figure 4.9: Power harvesting circuit

The scenarios of the laboratory testing were designed considering the external resistance and the angular speed of the crank. Based on the motion analysis in the previous chapter, the angular speed is affected by the top plate's displacement magnitude and speed. Consequently, the power output of the harvester was evaluated using different resistances and under various displacement

magnitudes and speeds. In real applications, different displacement speeds and magnitudes refer to passing vehicles with different speeds and weights that apply various loads in different time intervals.

In addition to the electrical outputs (the voltage and power), in each testing scenario, the experimental voltage output is compared to the theoretical estimation, calculated through motion analysis results. The division of the experimental over the theoretical values indicates the energy generation efficiency of the system, which is referred to as the "efficiency" and is discussed in the results section. Figure 4.10 shows the experimental procedure.

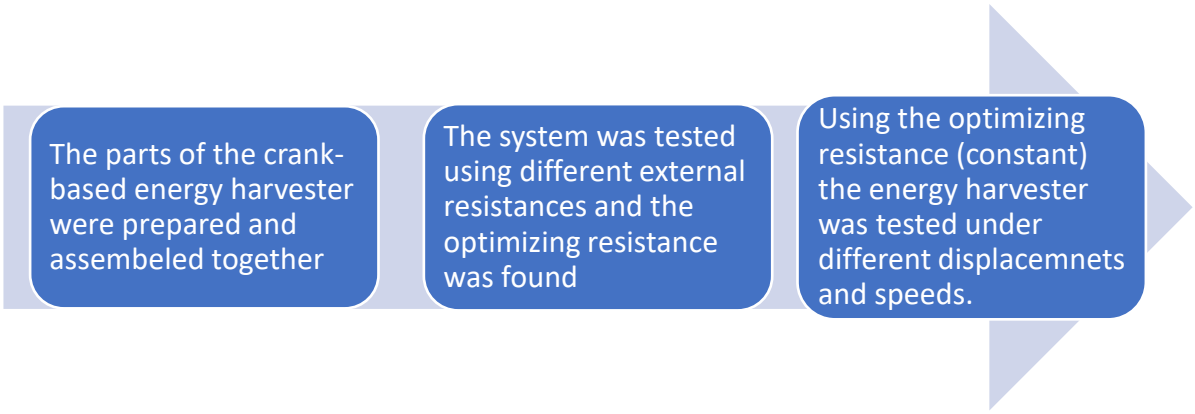

Figure 4.10: Experimental procedure

4.4.2 Optimizing the External Resistance

The output power of the harvester was tested using different resistances ranging from 8 to 270 ohms connected to the generator. Table 4.6 shows the values of the employed external resistances.

Table 4.6: External resistors values

External resistor (ohms)	
8.4	49.2
11.7	70.3
15.8	83.8
24.3	100
30	180
35.5	220
41.7	270

In this stage, the displacement magnitude and speed factors were kept constant at 18 mm and 13 mm/s, respectively. Figure 4.11 is the one-cycle voltage-time diagrams around 4 resistances of 8, 100, 180 and 270 ohms. It can be seen that although the mechanical loads are similar, the voltage around the resistors change as their values change. Therefore, as illustrated theoretically, the output power changes depending on the external resistance, and there is an optimizing resistor corresponding to the system's maximum power output. This observation is also consistent with the previous studies [33], [75], [138], [139]. The voltage around the resistor is recorded to find the optimizing resistor. Since the voltage-time diagrams are consistent, the average of one cycle matches with the average voltage of several cycles. Next, the average power is calculated following equation 4.3 and taking the numerical average of the power pulses.

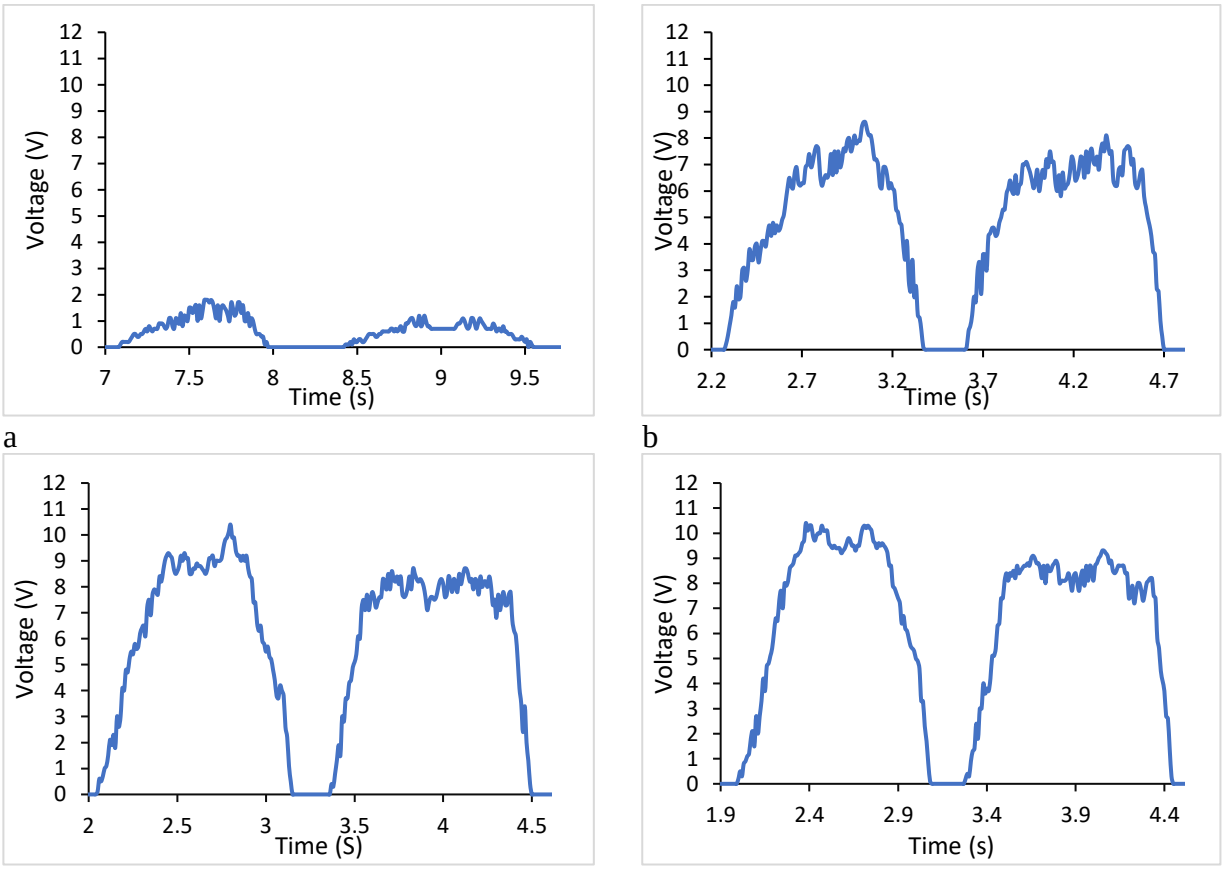

Figure 4.11: Voltage-time diagrams of the voltage around the resistors of a) 8 ohms, b) 100 ohms, c) 180 ohms and d) 270 ohms

According to Figure 4.12 that illustrates the average power–resistance diagram, the maximum average power of around 0.3 watts happens around the resistance of 35.5 ohms. This resistor will be used in the further steps of the experimental study.

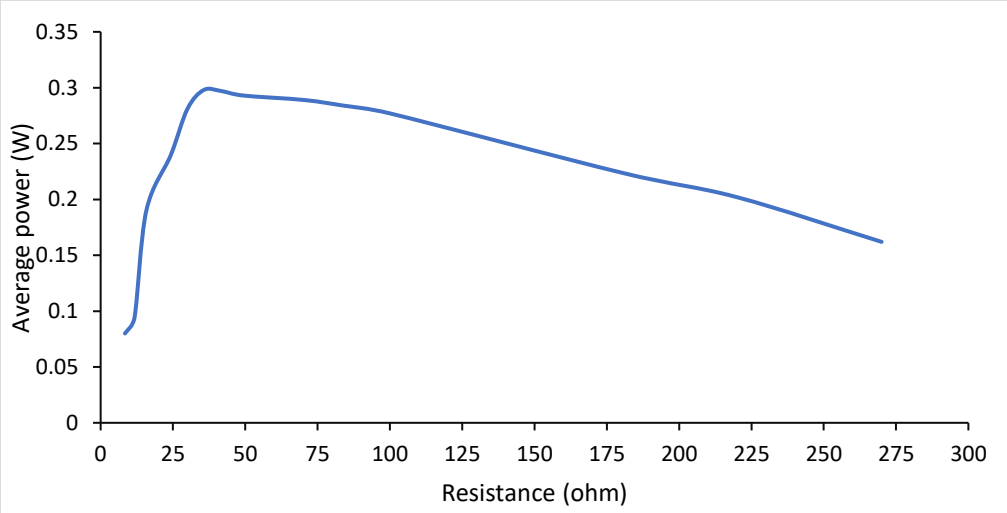

Figure 4.12: Power- resistance diagram

4.4.3 Energy Harvester Under Mechanical Loads

As it was shown before, both the displacement magnitude and speed are effective on the mechanical harvester's output power. Therefore, an Instron testing machine that is capable of applying cyclic loads with different loading speeds was used. In this device, the variable parameters of cyclic loading are the loading speed and the maximum displacement. The electromagnetic energy harvester was placed in the device and connected to the NIDAQ and to the data-logging computer. The testing setup is shown in Figure 4.13.

Figure 4.13: Test setup of the mechanical harvester using the Instron device

It should be mentioned that the device has a limit that the loading speed cannot exceed 14.67 mm/s. The other limitation is the accuracy of this machine, which was observed to be around 90%, meaning that the displacement applied on the harvester during the experiments is 25 mm$\pm$ 2.5 mm.

It was shown that both displacement magnitude and speed are important factors affecting the output power of the system. Therefor, in the experimental phase, the output of the system was evaluated under different combinations of loading speed and magnitude, ranging from 3.34 mm/s to 14.67 mm/s, and 10 mm to 25 mm, respectively. The combinations of the loading speed and displacement were chosen according to the statistical method of central composite design, using the software of Origin Design of Experiments extension, with an alpha value of 1.414 and 4 center points. This method is useful to study the effect of each factor and their interaction on the response of the system, which in the case of this study are the electrical outputs. It is worth mentioning that due to testing machine's precision, displacements of less than 10 mm were not applicable, and furthermore, the system was also tested under the maximum

displacement magnitude (25 mm) and speed (14.67 mm/s). The different testing scenarios are outlined in Table 4.7.

Table 4.7: Testing Scenarios of The Harvester Under Mechanical Loads

V (mm/s)	Displacement (mm)
3.34	16
5	19
5	10
9	16
9	25
13	10
13	18
14.67	18
14.67	25

As both variables are effective on the output power, this combination was designed to optimize the output power. In this design, the response is the output power, and it is evaluated in various combinations of the independent variables (loading speed and displacement). Given that the optimizing external resistance is equal to 35.5 ohms, this external resistor was used to evaluate the system's output power. In the following sections, the mechanical and electrical output of 4 scenarios of the total 9 combinations is presented. The remainder of the results is brought in the Appendix.

4.4.3.1 Loading Speed of 3.34 mm/s and Displacement Of 16 mm

Figure 4.14 shows the load-time diagram of the harvester under this loading condition.

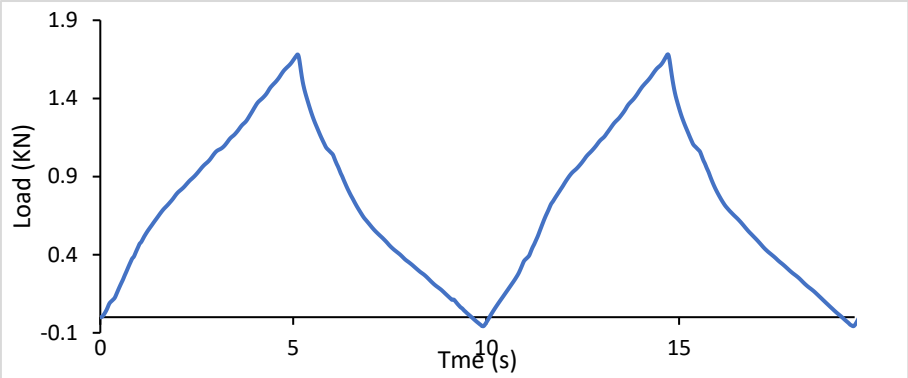

Figure 4.14: Force-time diagram of the harvester under 3.34 mm/s and Displacement Of 16 mm

Two cycles of loading and unloading are shown in Figure 4.14. The applied loads increase until 1.6 KN, around 5.1 s, and reduce at the same pace. The second peak is also formed similarly.

Figure 4.15 shows the voltage-time diagram of the harvester under 16mm of displacement and 3.34 mm/s loading speed. This voltage is the output of one pair of the generator's leads, connected to the rectifier. As it can be seen, the loading (first and the third peaks) and unloading cycles (second and fourth peaks) and their peak values are similar to each other, meaning that the unloading speed and displacement level matches with loading.

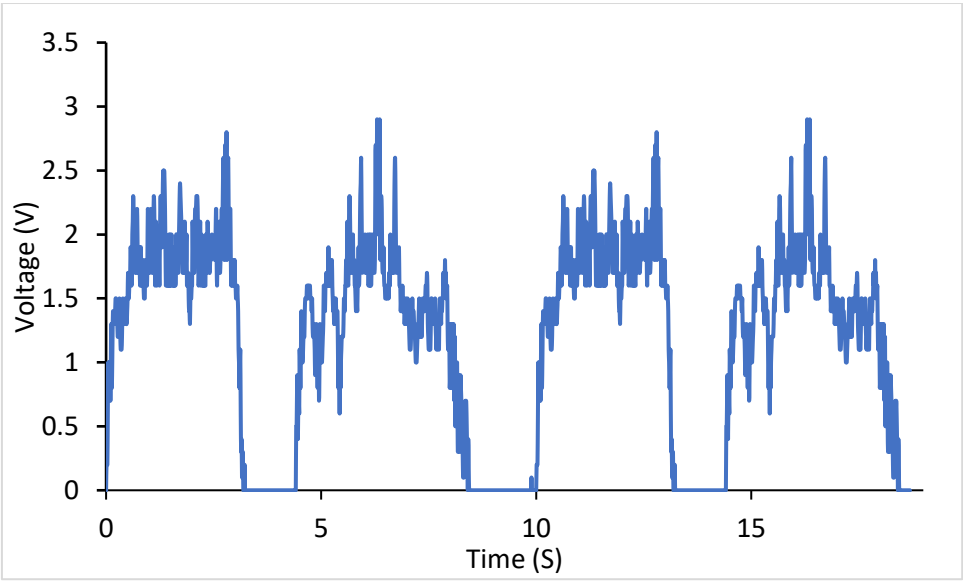

Figure 4.15: Voltage- time of the harvester under loading speed of 3.34 mm/s and displacement of 16 mm

According to the diagram, the voltage in the cycles reaches the maximum of 2.8 V and has a sharp drop around the time of 4.7 s, when the harvester is at its maximum compressed state.

Afterwards, as the unloading starts, the generator rotates again (in the opposite direction), which results in another voltage peak.

According to the motion analysis, this loading condition will result in the maximum angular speed of 18 deg/s, equal to 0.05 rps. Affected by the gearbox, the generator will have an angular speed of 5 rps. As the electrical constant of the generator was found equal to 0.9836, and the voltage loss was around 1.4%, the theoretical rectified peak voltage must be around 4.54 V. the experimental peak voltage is 2.8 V which is around 62% of the theoretical. The difference between the theoretical and the experimental peak voltage is the efficiency of the system and is due to the energy dissipation between the mechanical parts and the friction between them.

Figure 4.16 shows the output voltage around the resistance of 35.5 ohms and the power versus time.

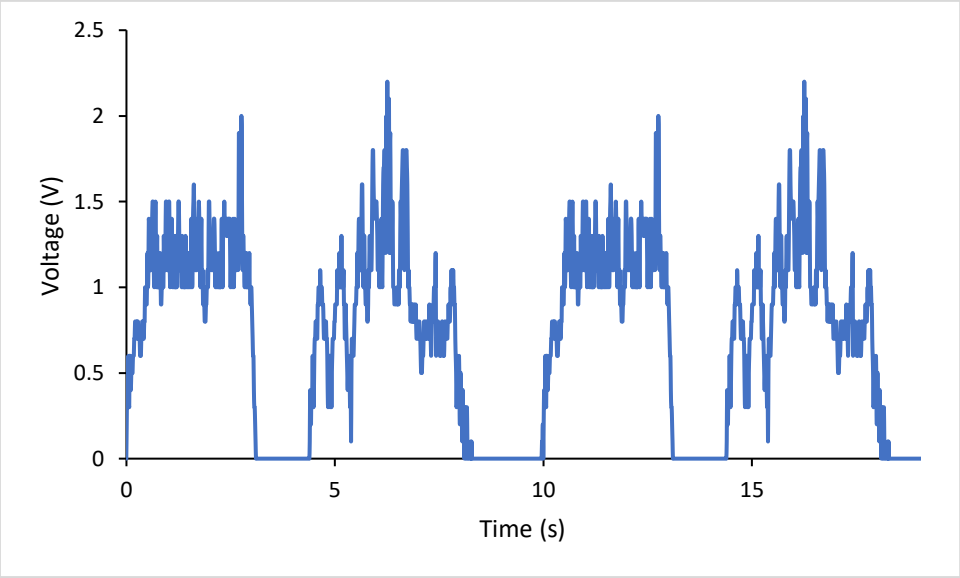

a

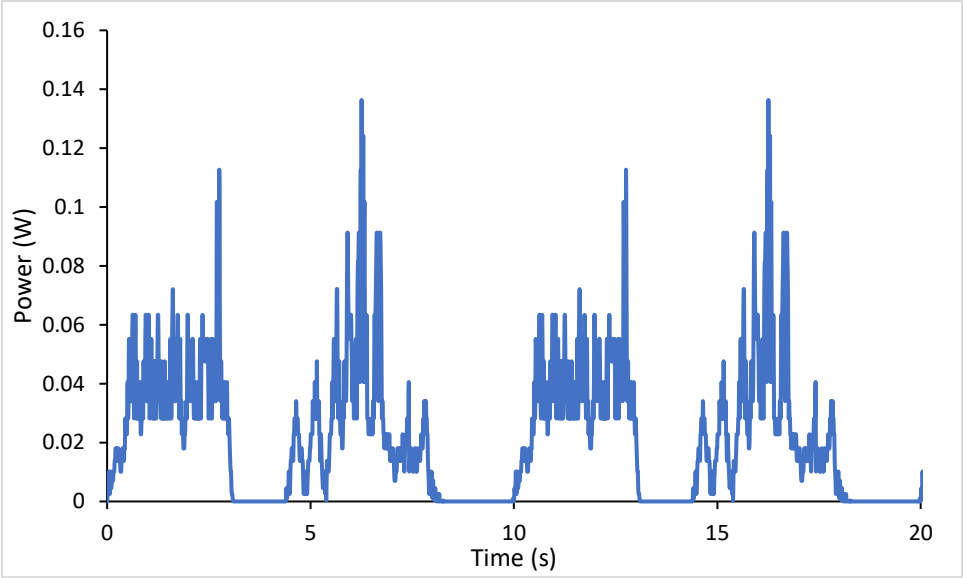

b

Figure 4.16: System's response under 3.34 mm/s and 16 mm displacement a) Voltage-time around the 35.5 ohms, b) Power-time

As it can be seen, the voltage around the resistor has decreased compared to Figure 4.15. According to the diagrams, the maximum power is around 0.14 W, corresponding to the maximum voltage of 2.2 V. Under this mechanical loading, the average power and voltage is around 0.0233 W and 0.075 V, respectively.

4.4.3.2 Loading Speed of 9 mm/s and Displacement Of 25 mm

Figure 4.17 is the force-time diagram of the system in this loading scenario.

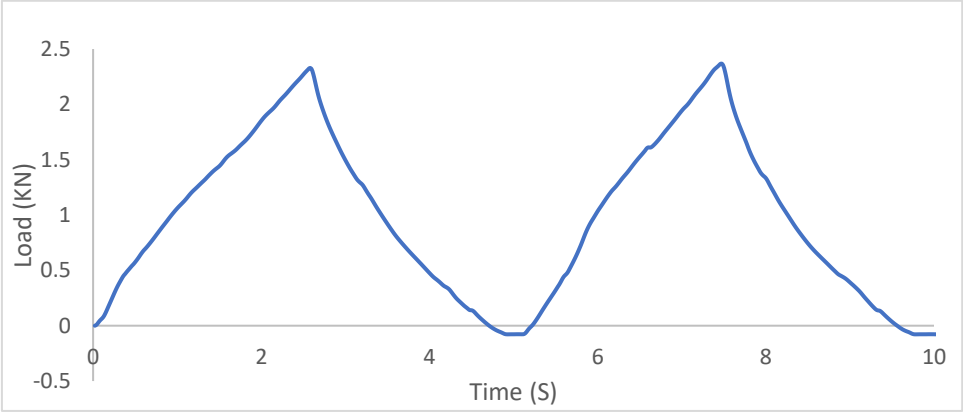

Figure 4.17: Force-time diagram of the harvester under 9 mm/s and Displacement Of 25 mm

As the loading starts, the force increases until it reaches a maximum of 2.25 KN, over around 2 seconds, followed by a decrease until complete unloading occurs. Then, the second peak is started and has a similar trend to the previous cycle.

Figure 4.18 shows the voltage-time diagram of the harvester under 25 mm of displacement and 9 mm/s loading speed. As it is shown, the loading and unloading peaks are similar to each other, with the maximum peak of about 5.3 V. Since the displacement is relatively large, enough reaction force is generated in the springs, which makes the system return back completely generating almost equal voltages.

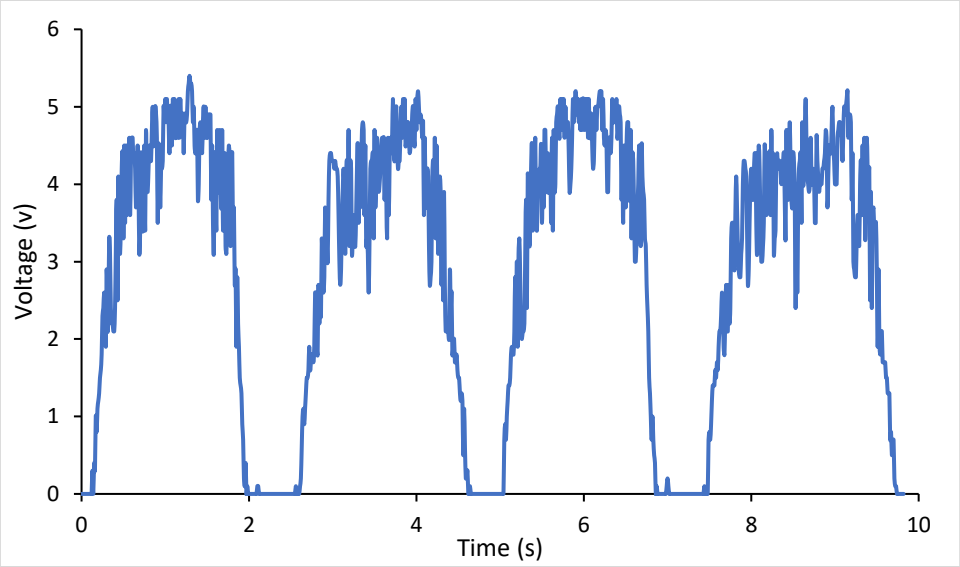

Figure 4.18: Voltage-time of the harvester under 25 mm of displacement and the speed of 9 mm/s

When the loading starts, voltage increases until it reaches the maximum value of around 5.4 V and as the loading continues, the voltage is generated until the maximum displacement level is reached, where the loading stops for a short time and hence, the voltage diagram shows a steep drop as no voltage is generated. However, once the unloading process starts, the voltage is generated again, and the unloading voltage peak is formed in the diagram.

According to the motion analysis, under this testing condition, the maximum angular speed of the crank is 46 deg/s which is the equivalent to 0.128 rps. Therefore, the maximum angular speed of the generator reaches 12.8 rps. Such angular speed, as affected by the electrical

constant and the rectifier loss, results in the maximum theoretical voltage of 11.63 V. The maximum experimental voltage is 5.4 V which is 46% of the theoretical value, and it is the generation efficiency of the system under this mechanical performance. This deviation is caused by the loss of energy in the generator and gearbox and the friction.

Figure 4.19 shows the voltage-time diagram around the resistor of 35.5 ohms and the power-time diagram under the current testing condition.

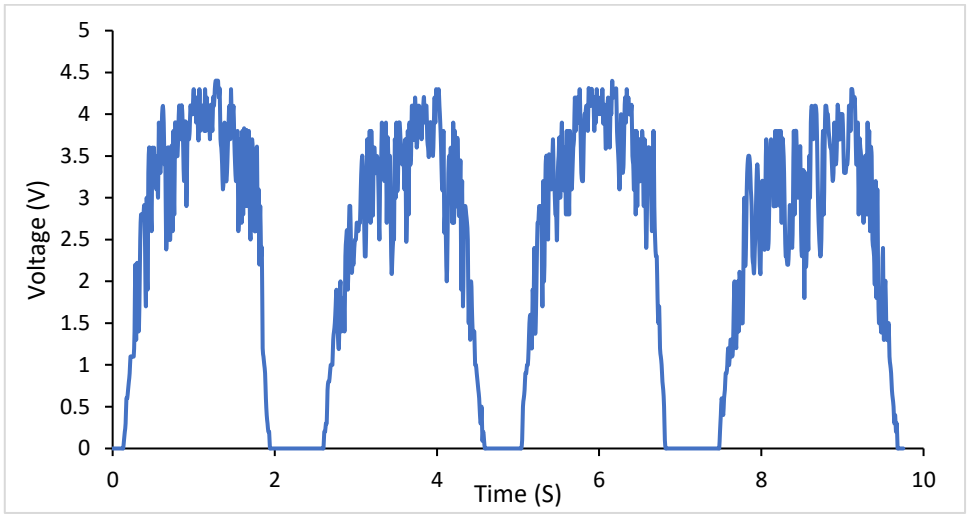

a

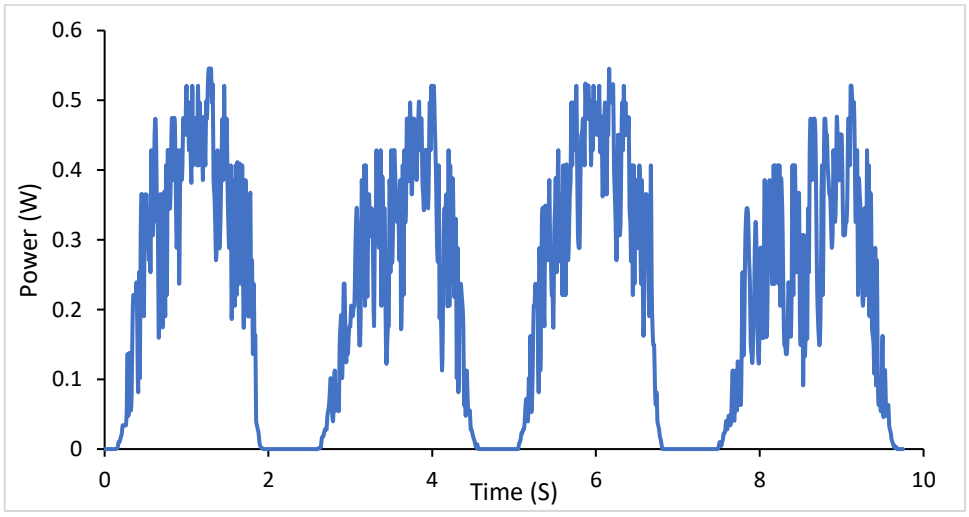

b

Figure 4.19: System's response under 9 mm/s and 25 mm displacement a) Voltage-time around the 35.5 ohms, b) Power-time

According to Figure 4.19, the maximum voltage around the external resistor is 4.4 V, resulting in peak power of 0.545 W. The average output power is around 0.217 W, and the average voltage is 2.315 V.

4.4.3.3 Loading Speed of 13 mm/s and Displacement Of 10 mm

The force-time diagram of this testing scenario is plotted in Figure 4.20. Similarly, as the loading starts, the force increases until around 1 KN and reduces during the unloading. The second cycle also starts and follows a similar pattern to the first one.

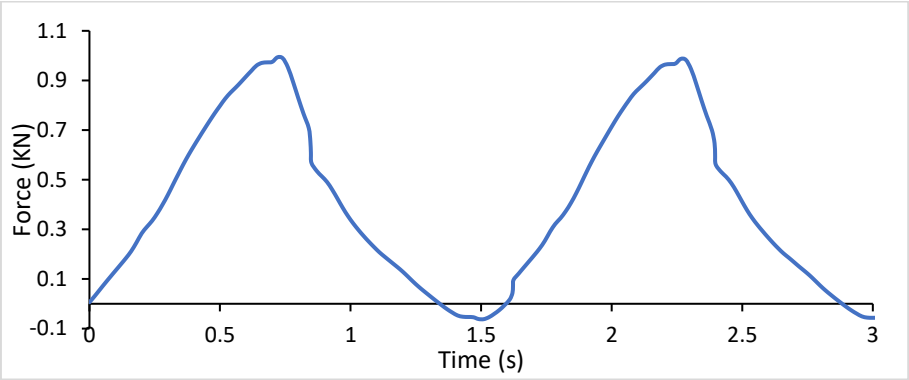

Figure 4.20: Force-time diagram of the harvester under 13 mm/s and Displacement Of 10 mm

The voltage-time response of the generator under the displacement of 10 mm and 13 mm/s speeds is plotted in Figure 4.21. As it can be seen, the unloading peaks (the second and the fourth) are smaller than the loading ones (the first and the third). Although the speed is relatively high because the displacement magnitude is short, the reaction forces generated in the springs make the harvester not return back entirely to its original state, causing this observation, which happens in every loading and unloading cycle.

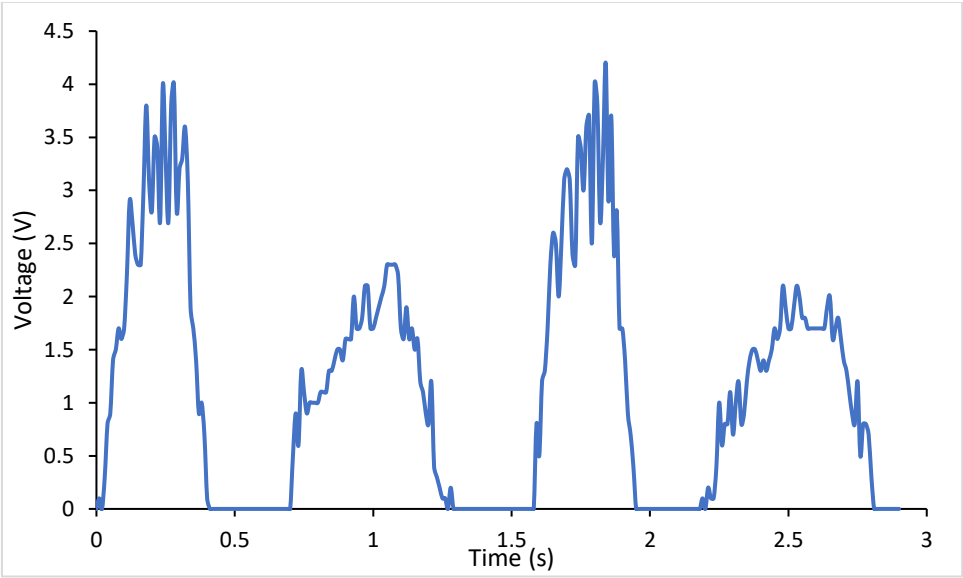

Figure 4.21: Voltage-time of the harvester under 10 mm of displacement and the speed of 13 mm/s

When the loading starts, the generator spins and the voltage increases until it maximises at the peak of about 4.2 V, followed by a sharp drop, as the harvester is at its maximum loading state and there is a short pause. Afterwards, the voltage is again generated when the unloading starts, and the unloading voltages are recorded.

According to the motion analysis, the maximum angular speed of the crank under this mechanical load is 81 deg/s, equivalent to 0.225 rps. When transferred to the generator, it will spin by 25 rps, giving a theoretical maximum voltage of 20.44 V. As the experimental voltage (4.2 V) is 21% of the theoretical voltage, it can be deduced that this loading condition causes a lot of energy loss and it is not an efficient one. This loss is caused by the friction between the mechanical parts and the efficiency of the gearbox and generator. Additionally, although the speed is high in this testing, the displacement is the lowest among all the scenarios. This displacement causes partial unloading, which also affects the further cycles, the harvester's performance, and reduces its efficiency. Figure 4.22 shows the voltage-time around the resistor of 35.5 ohms and the corresponding power diagrams.

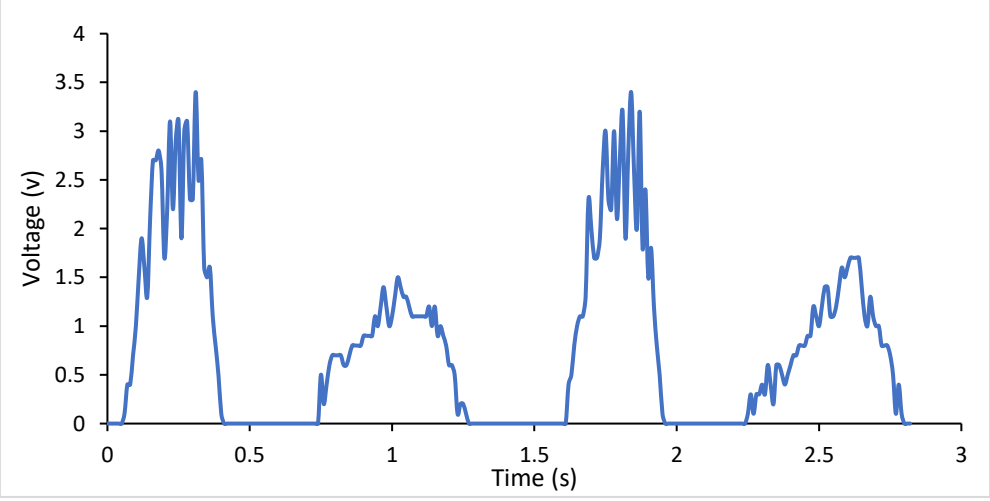

a

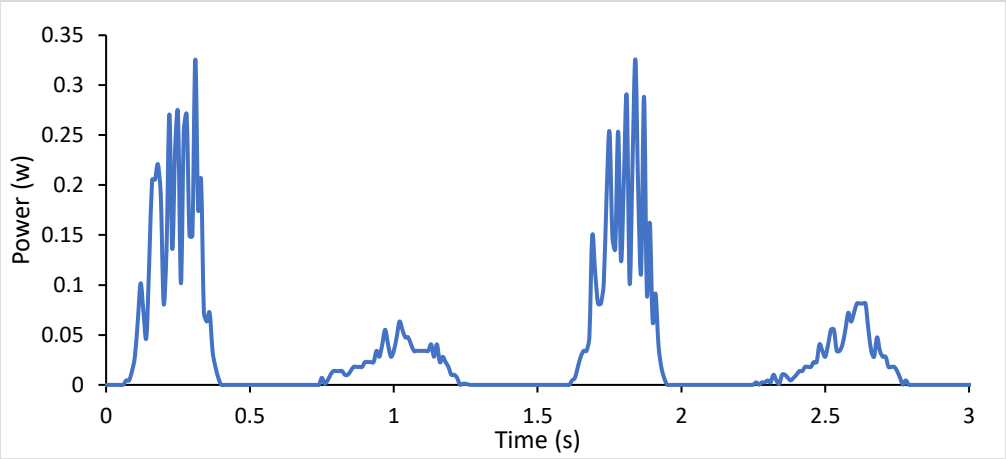

b

Figure 4.22: System's response under 13 mm/s and 10 mm displacement a) Voltage-time around the 35.5 ohms, b) Power-time

The voltage-time diagram has similar shapes but lower values than the voltages in Figure 4.21. When loading, the power increases and maximizes around 0.326 W, which is followed by a sharp decrease as the loading is finished. Similarly, when unloading starts, the power increases until 0.0633 W and then gradually decreases. The unloading peak is wider as the reaction force in the springs is small, and the system cannot rebound rapidly. The average voltage and power are around 3.4 V and 0.326 W, respectively.

4.4.3.4 Loading Speed of 14.67 mm/s and Displacement Of 25 mm

The Force time diagram of this scenario is plotted in Figure 4.23. As the loading begins, the force values rise until around 2.3 KN, over the period of 1.54 seconds, which is followed by slower unloading. As the system recovers, the next loading cycle starts, which follows a similar pattern.

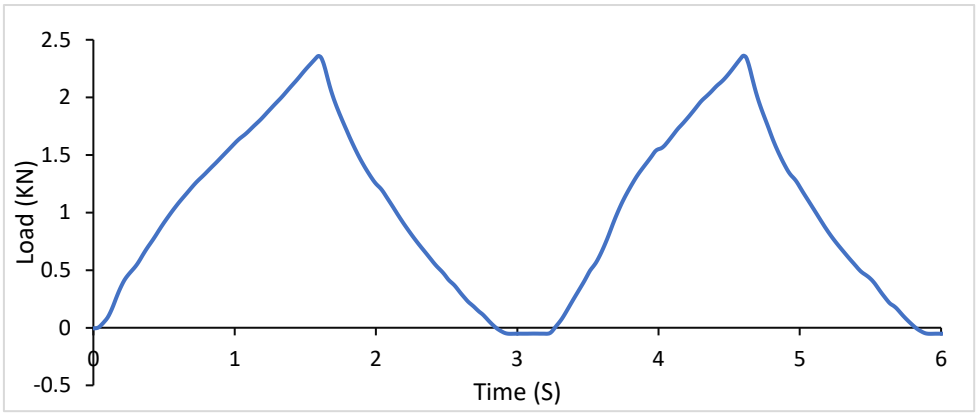

Figure 4.23:Force-time diagram of the harvester under 14.67 mm/s and Displacement Of 25 mm

The voltage-time diagram of the harvester directly connected to the rectifier, and under 14.67 mm/s speed and the displacement of 22 mm, is plotted in Figure 4.24.

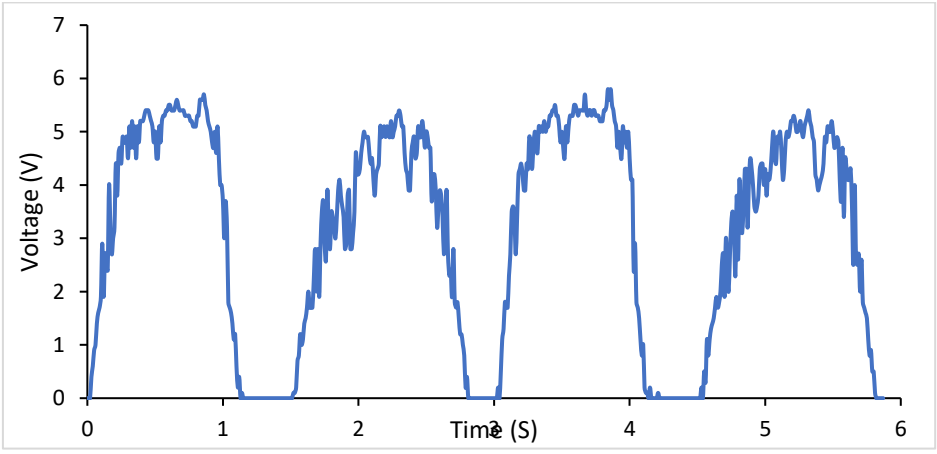

Figure 4.24: Voltage-time of the harvester under 25 mm of displacement and the speed of 14.67 mm/s

According to Figure 4.24, the loading and unloading peak values are close to each other, and as a large reaction force is generated in the springs, the system recovered almost completely. As the displacement starts and the system is loaded, the voltage starts to increase. This increase continues the peak value of around 5.8 V, in which the harvester is fully compressed; as there is a short pause, the voltage drops to zero until the unloading starts, and the unloading peak is formed, which maximizes around 5.4 V.

Based on the motion analysis, the maximum angular speed of the crank is equal to 74 deg/s, corresponding to 0.206 rps. As affected by the generator, the maximum angular speed of the generator is equal to 20.6 rps, which considering the electrical constant and rectifier, this

angular speed results in the maximum theoretical voltage of 18.71 V. The peak experimental value is equal to 5.8 V, 31% of the theoretical value, which indicates the efficiency of the system. These differences are caused by the friction between the mechanical parts and the loss in the gearbox and generator.

Figure 4.25 shows the voltage around the resistor of 35.5 ohms and the harvester's corresponding output power harvester.

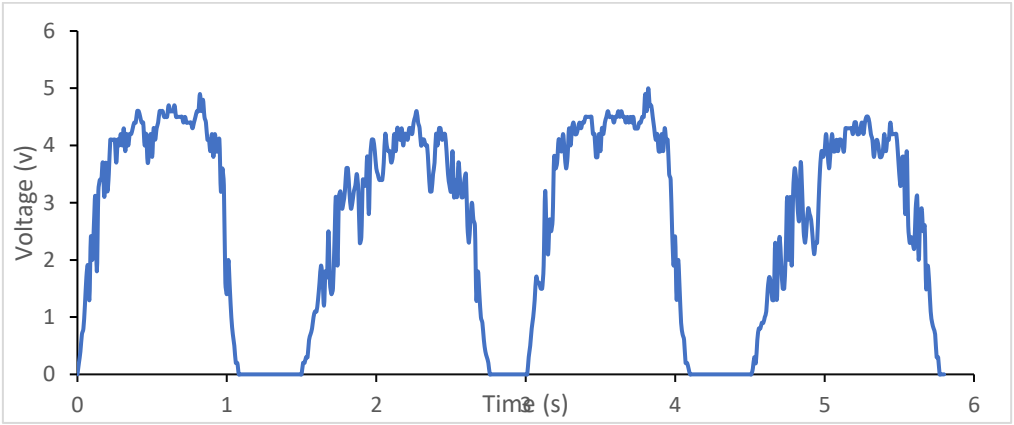

a

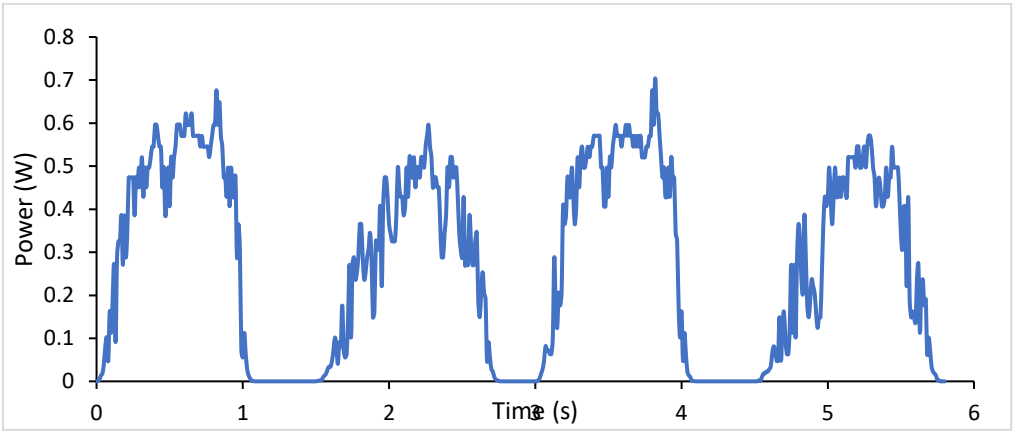

b

Figure 4.25: System's response under 14.67 mm/s and 22 mm displacement a) Voltage-time around the 35.5 ohms, b) Power-time

According to Figure 4.25, the maximum voltage around the external resistor is 5 V, occurring during the loading of the harvester, and consequently, the maximum power is also equal to 0.7 W. Moreover, the average voltage and the power under this loading condition equal 2.6 V and 0.275 W.

As discussed separately, in each mechanical condition, the electromagnetic energy harvester gives different maximum voltage and power, and the system's efficiency also changes, depending on the conditions. In the following section, the obtained results are discussed and compared to each other.

4.5 Comparison of the results

In this section, a thorough comparison is made between the results achieved from each testing scenario. In the previous section, the results were discussed separately, and it was observed that both loading speed and displacement level affect the results of the output power and voltage of the system. In addition, the system's efficiency was also different in each scenario. Given that the results are discussed over two loading and unloading cycles, they are comparable to each other. Each response's comparison is discussed separately, as follows.

4.5.1 Output Voltage of The System

Each testing scenario resulted in different maximum and average voltage due to producing a different angular speed and having different efficiency. Moreover, the voltage recorded directly from the rectifier is different from around the resistor. Therefore, these parameters are compared separately, as follows.

Table 4.8 shows the maximum and the average and voltages recorded from the harvester in each testing scenario.

Table 4.8: Direct rectified peak and average voltage of the system

Scenario Number	*V* (mm/s)	Displacement (mm)	Peak voltage (V)	Average voltage (V)
1	3.34	16	2.9	1.190

2	5	19	4.2	1.860
3	5	10	3.2	0.943
4	9	16	5.1	2.076
5	9	25	5.4	2.893
6	13	10	4.2	1.142
7	13	18	6.2	2.797
8	14.67	18	6.9	2.866
9	14.67	25	5.8	3.135

Figure 4.26a shows the contour diagram of the peak voltage, plotted against the loading speed and the displacement magnitude.

According to the diagram, the peak voltages of 5.9 to 6.9 V occur when the loading speed is around 13 to 14.67 mm/s, and the displacement is more than 15 mm. This observation is consistent with the theoretical analysis, as in these conditions, the angular speed of the crank is around the maximum. The average voltage of these loading conditions is more than 2.7 V, which is higher than the other conditions. However, as the average voltage also depends on the unloading peak voltage, it is higher when the loading and unloading cycles are similar, which is the case for the 7^{th}, 8^{th}, 9^{th}, as well as the 5^{th} case, where the loading speed is 9 mm/s, and the displacement is 25 mm. In this scenario, the loading and unloading cycles have equal peak value. Figure 4.26b is the contour diagram of the average voltage plotted with respect to the loading speed and the displacement.

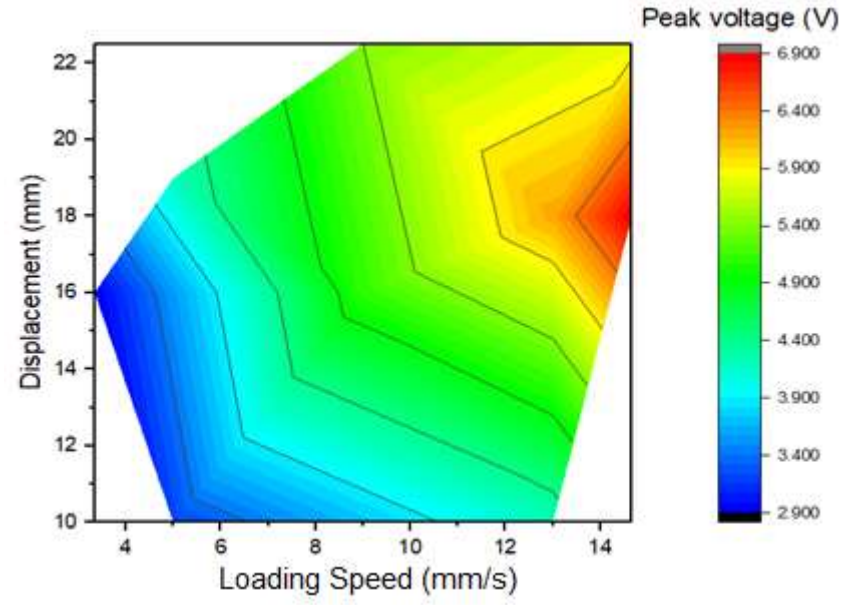

a

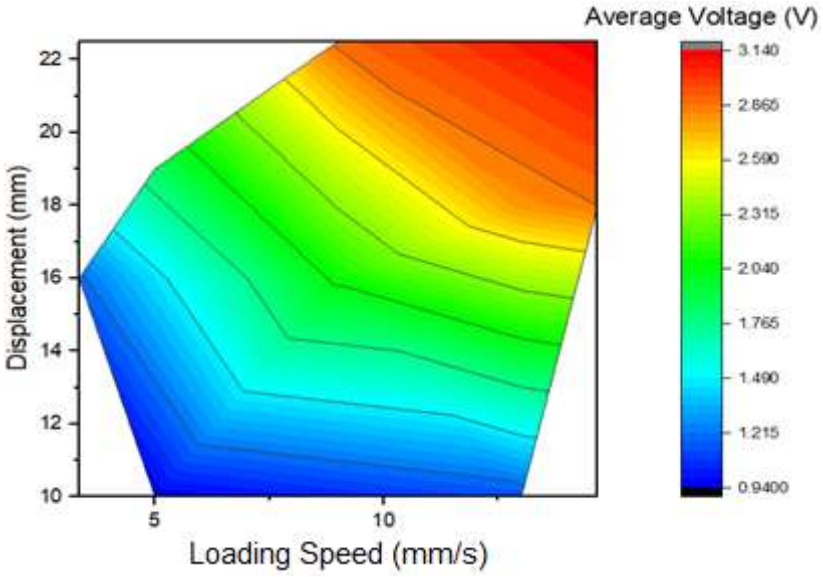

b

Figure 4.26: a) The maximum voltage. b) The average voltage

4.5.2 Output Power of The System

The system's output power was calculated by measuring the voltage around the optimizing external resistance, which is 35.5 ohms. As they are interrelated, in this section, the system's output power is compared in different mechanical conditions. Table 4.9 shows the average and the maximum power obtained from each scenario, and Figure 4.27 is the corresponding contour diagrams of the peak power and the average power against the loading speed and displacement.

Table 4.9: Average and the maximum power recorded from each scenario

Scenario Number	*V* (mm/s)	Displacement (mm)	Peak Power (W)	Average Power (W)
1	3.34	16	0.28	0.046
2	5	19	0.71	0.164
3	5	10	0.32	0.04
4	9	16	1.0	0.278
5	9	25	1.08	0.444
6	13	10	0.33	0.08
7	13	18	1.44	0.436
8	14.67	18	1.84	0.504
9	14.67	25	1.40	0.554

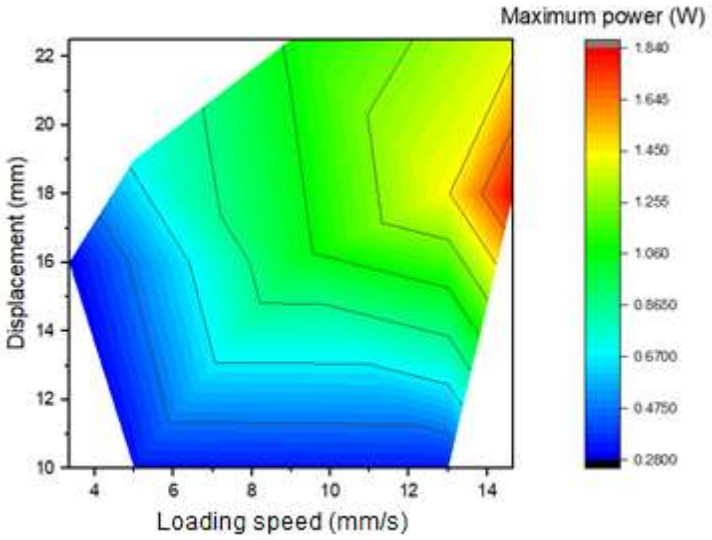

a

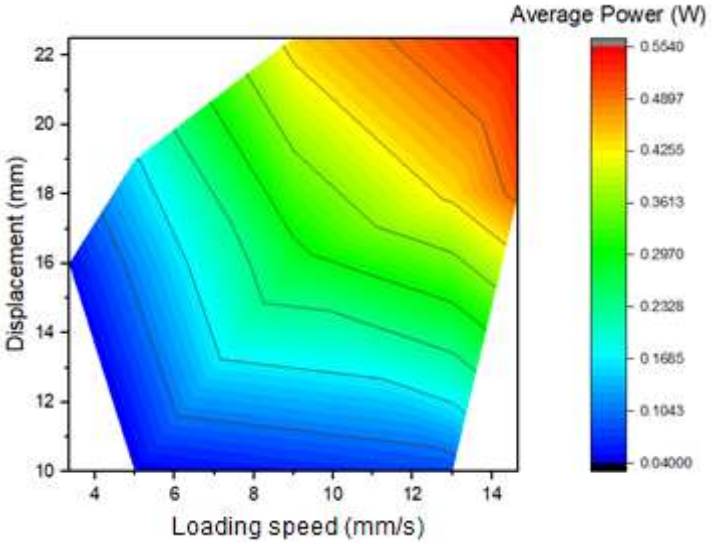

b

Figure 4.27:a) The maximum power, b) The average power

According to Figure 4.27, the maximum and average power have the same pattern as the voltage diagrams in Figure 4.26. The absolute maximum power of all the scenarios is equal to 1.84 W, occurring as the loading speed is around its maximum and the displacement is more than 15 mm. Similarly, the average power also peaks when both loading speed and displacement are around their maximum level. The maximum average power of one cycle is equal to 0.554 W.

4.5.3 The efficiency of the System

Figure 4.28 is the contour diagram of the generation efficiency for different loading speeds and displacements.

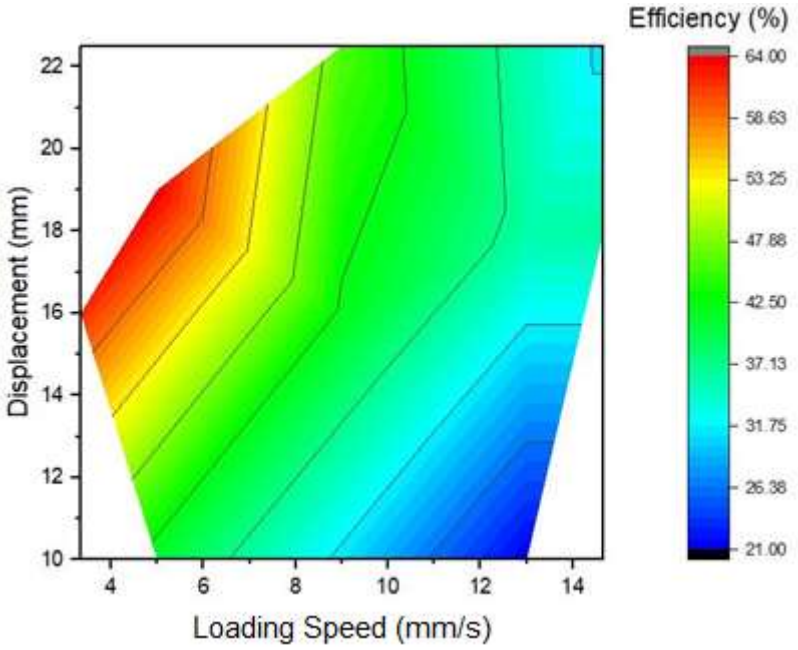

Figure 4.28: Efficiency of the system under different scenarios

The system's efficiency was evaluated by comparing and dividing the maximum theoretical voltage (through the maximum angular speed) by the maximum experimental voltage logged in the laboratory. This ratio was calculated for all the loading conditions and changes depending on the loading scenario. It was observed that the least efficiency of the system was obtained when the displacement level is 10 mm (minimum), and loading speed is 13 mm/s (relatively high), while it was maximized when the displacement is 19 mm (relatively high), and the speed is relatively low (5 mm/s).

Regarding the real applications, different displacements and loading speeds correspond to various passing vehicles (different peak forces) with various speeds. Faster loading speeds stand for the vehicles that pass the speed bump faster, and similarly, those vehicles passing slower correspond to the slower loading speeds. Likewise, as different vehicles have different curb weights, the maximum forces applied on the speed bump can differ, depending on their weights and speeds. Hence, this harvester is suitable for installation on urban roads, where the weights and the speeds of the passing vehicles are more diverse and closer to the loads applied in the laboratory. In the following section, the performance of the harvester is evaluated under anticipated real field conditions.

4.6 Real Field Performance of The Harvester

As mentioned in the previous section, the experimental evaluation of the harvester is limited by the displacement speed and frequency, implied by the testing machine. The maximum possible loading speed of the testing machine is 14.67 mm/s which is less than the loading speed in real conditions. Hence, in this section, the anticipated performance of the harvester is evaluated through simulation, under the loading conditions similar to the real field.

In real road application, this harvester can be installed as road rumbles along the edges of the road in turnarounds. Assuming that the average vehicles speed when passing is 75 Km/h [12], the time that takes for the vehicle to pass over one harvester (210 mm width) is:

75 km/h= 20.83 m/s $\xrightarrow{w=210\ mm=0.21\ m}$ t= 0.01 s

It is also assumed that the load applied by the passing vehicle is able to compress the harvester 25 mm, which is the full displacement capacity of the harvester. These parameters are employed as the inputs of the motion analysis, using Solidworks. The loading scenario is given as Data Points in the program, with linear interpolation type and 0.01 s time increment steps.

According to the motion analysis, under 25 mm displacement applied over 0.01 s, the maximum angular speed of the crank disk is equal to 35.45 cycles per second (rps). Considering the effect of the gearbox, the generator will revolve at the speed of 3545 rps. According to the generator's specifications, at high speeds (i.e., more than 5000 rpm) it can generate a maximum voltage of around 500 V. Considering the effect of rectifier and the resistor, the anticipated output voltage around the optimal resistor of 35.5 ohms, will be equal to 355.15 V.

It can be seen that the voltage output in real field application, due to higher loading speed, is higher than the experimental results. The current loading scenario applied on the harvester is very similar to the real field application, in which the harvester will be under impact load from the passing vehicles.

Furthermore, as this harvester can have versatile applications, higher power levels can be achieved by installing generators that are more compatible with higher speeds.

In this section, the expected performance of the harvester under real field conditions was estimated. However, it is worth mentioning that to avoid any over estimations due to misassumptions, in the following chapters, and for the feasibility evaluation of the harvester the actual experimental data taken from the laboratory results is utilised. The simulations and the estimated output of the harvester done in this section are to be validated in future work.

4.7 Conclusions

This chapter discussed the manufacturing and experimental study of the first prototype of the crank-based road energy harvester thoroughly. After the details of each component, the experimental plan was discussed, followed by the results presented and analyzed in each section, and eventually, the comparison of the obtained results. Based on the results, the following points can be concluded.

1. The external resistor of the energy harvesting circuit is an important factor affecting the system's output power. Through an experimental plan, the output power was evaluated against

different external resistors. The optimal resistor was found equal to 35.5 ohms. This resistor was used in the further steps of the experimental study.

2. In the force-time diagrams of the harvester, their maximum values depend on the maximum displacement level of the harvester and the speed. In equal displacements, if the loading speed is higher, the peak value of the forces increases slightly as well.

3. As the loading speed increases gradually, the maximum voltage obtained directly from the generator increases. This observation is consistent with the fact that the output voltage is directly related to the angular speed of the crank, which increases as the loading speed grows. The speed has an optimum of 14.67 mm.

4. Likewise, an increase in the displacement magnitude, especially after 8 mm, also increases the system's output voltage. However, its positive effect is less pronounced compared to the loading speed, and the maximizing displacement is around 18 mm, which is less than 25 mm (i.e., the maximum displacement).

5. Considering the output power of the system, as it is also related to the angular speed of the crank, it maximizes around the highest loading speeds and displacements, with a peak of almost 1.84 W, occurring with the loading speed of 14.67 mm/s and the displacement of 18 mm.

6. The system's efficiency was evaluated by comparing the maximum theoretical and experimental voltages, dividing the experimental over the theoretical. Based on the diagram, the highest efficiency occurs when the loading speed and the displacement are around 5 mm/s and 19 mm, respectively. By increasing the speed and the displacement, the efficiency decreases to around 42%, and further increase reduces it to around 36%. Hence, it can be deduced that in an average condition, the efficiency of the system is around 45%.

5 Performance Enhancement of Crank Road Energy Harvester

5.1 Introduction

In this chapter, improving the performance of the crank-based energy harvester is discussed in detail. In chapters 3 and 4, it was shown through simulations and experimental investigations that the prototype of the harvester is capable of enduring various loads matching the real field applications, with an absolute maximum endured load of about 2.3 KN, corresponding to a passenger car with a curb weight of 9200 KN (~940 Kg average mass). While this curb weight matches with some urban cars such as Suzuki Motor Corporation average curb weight [140], other regular passenger cars such as SUV's are heavier. Therefore, in this chapter, the performance of the harvester enhanced in terms of the loading capacity. Since the loading capacity of the harvester is strongly dependent on its suspension system's stiffness, this enhancement was investigated by incorporating different sets of springs, with higher stiffness. The harvester was assembled with different springs (different stiffnesses), and its performance was evaluated under various testing scenarios, with the loading speed and displacement as the independent variables. In addition to the loading capacity, the electrical output and the generation efficiency are the other key elements that were studied. It is worth mentioning that the other parameters such as the dimensions of the crank's components have none or negligible effect on the loading capacity of the harvester and therefore are not the considered in this study.

Besides the original spring stiffness of 19.12 N/mm, the system was reassembled with 4 more spring sets, with stiffnesses of 25.20 N/mm, 29.77 N/mm, 35.88 N/mm, and 43.54 N/mm, and tested in the laboratory for its mechanical stability (load-bearing capacity), average and maximum power output, their output voltage and efficiency.

The results are brought in separate headings in the following sections. Afterwards, the results are compared together, the optimizing condition and the best resulting spring set is identified from the mechanical and electrical aspects. Finally, the results are summarised in the conclusions.

5.2 Performance of the harvester with different springs

As explained in the introduction in this chapter, the performance of the crank-based road energy harvester built up with spring sets with different stiffnesses is evaluated under various mechanical and electrical loads. Four different spring sets were placed on the corners of the harvester unit, and the performance was evaluated under different scenarios of mechanical loads, similar to the previous chapter. Table 5.1 shows the materials and stiffnesses of the springs, and Figure 5.1 shows their dimensions.

Table 5.1: Springs' properties

Spring ID	Material	Materials Youngs modulus (GPa)	Stiffness (N/mm)
S1	Stainless steel	200	25.20
S2	Stainless steel	200	29.77
S3	Music wire	207	37.88
S4	Stainless steel	200	43.54

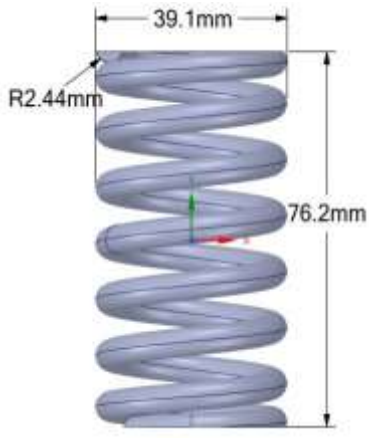

a

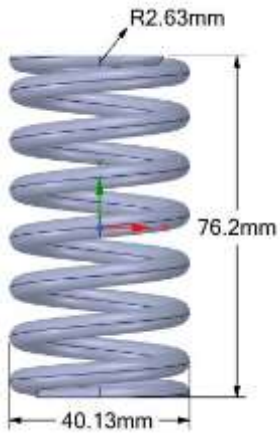

b

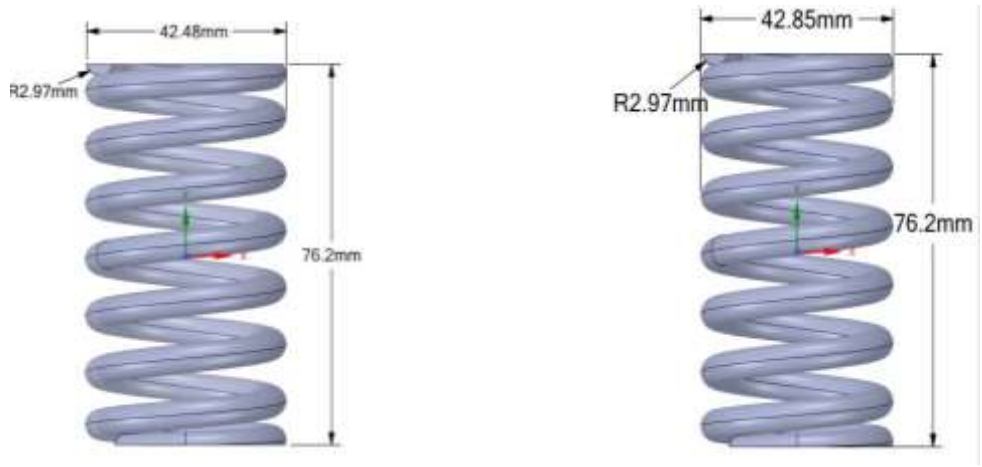

c d

Figure 5.1: Springs' dimensions, a) 25.20 N/mm, b) 29.77N/mm, c) 37.88 N/mm, d) 43.54 N/mm

A full experimental study was conducted for each spring set, similar to the scenarios and the tests carried out on the spring set of 19.12 N/mm, which was thoroughly discussed in the previous chapter. First, the optimal resistance of the system is measured by installing a range of resistors in the power harvester circuit. Secondly, the raw output voltage logged from the rectifier is analysed, and the system's efficiency is evaluated by comparing the theoretical and experimental voltages. Finally, the circuit voltage and the output power of the system is presented and discussed. Table 5.2 shows the testing scenarios of the electromagnetic harvester in different displacement magnitudes and loading speeds.

Table 5.2: Loading speed and displacement scenarios for testing the electromagnetic harvester

V (mm/s)	Displacement (mm)
3.34	16
5	19
5	10
9	16
9	25
13	10
13	18
14.67	18
14.67	25

5.2.1 Results of Spring Set of 25.20 N/mm

This section discusses the results taken from the crank harvester supported by the springs of 25.2 N/mm. The optimal external resistance of the system was measured by installing different external resistances in the circuit and measuring the voltage around them under a constant mechanical condition. Following Ohm's law (equation 4.2), the power output of each circuit is calculated and plotted against the resistance.

Figure 5.2 shows the voltage-time diagram of the harvester with the spring set of 25.2 N/mm, around various external resistors, under the displacement of 18 mm and loading speed of 13 mm/s.

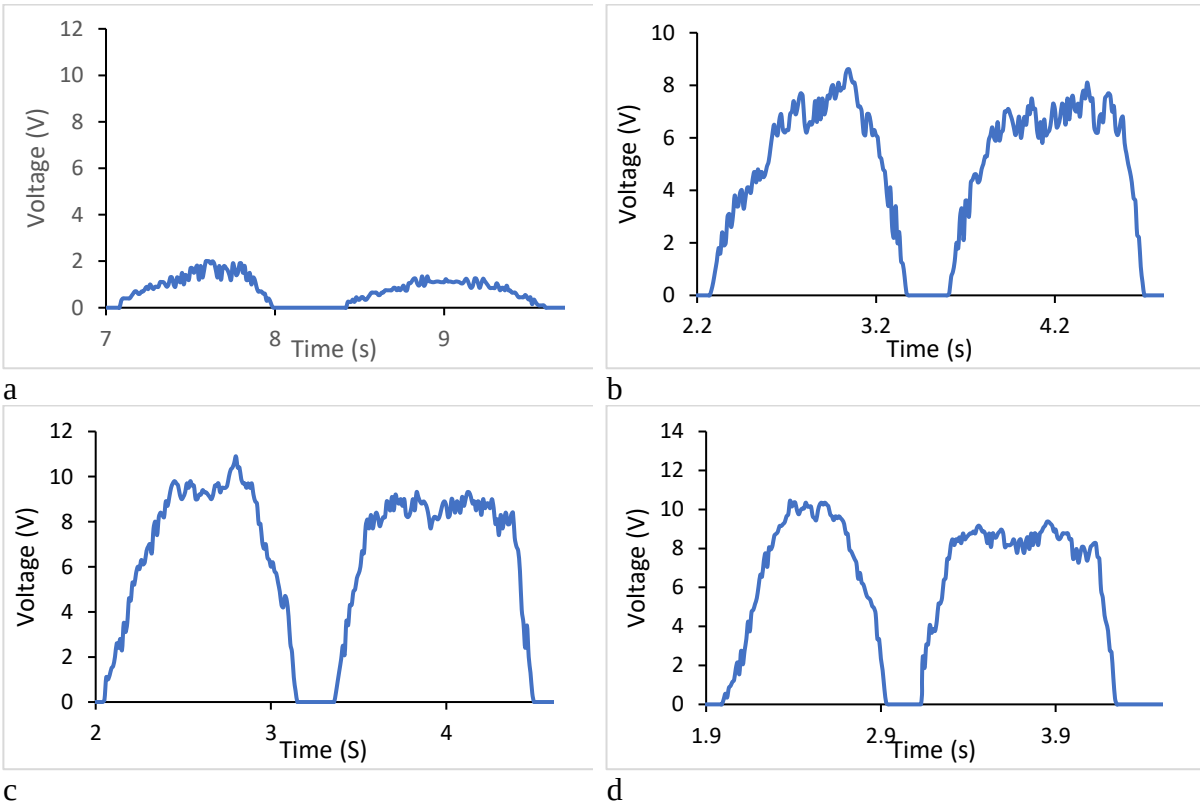

Figure 5.2: Voltage-time diagrams of the harvester with the spring set of 25.2N/mm, the voltage around the resistors of a) 8 ohms, b) 100 ohms, c) 180 ohms, and d) 270 ohms

Accordingly, the voltage around the resistors changes as the resistor changes. Compared to the resistance of 8 ohms, the rest of the voltages are higher. However, by plotting the power against

the resistance, it is observed that the power increases and, after a maximum peak, decreases gradually. Figure 5.3 shows the power-resistance diagram. The diagram shows the average power taken from the circuit in one loading and unloading cycle.

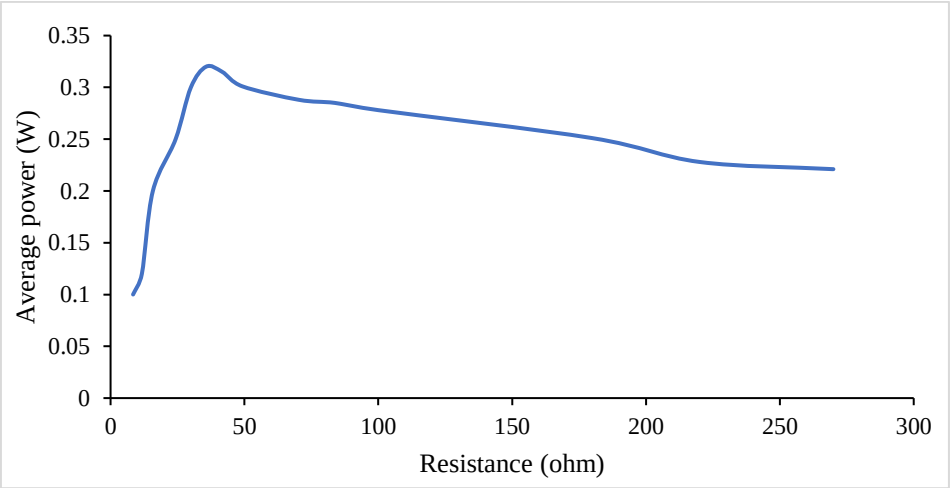

Figure 5.3: Power-resistance diagram- 25.2 N/mm spring stiffness

According to Figure 5.3, the output power maximizes around the resistor of 35.5 ohms. This resistor is equal to the same optimal resistor measured for the crank harvester with the spring set of 19.12 N/mm, in the previous chapter.

In the following parts, the electrical and mechanical output response of the crank harvester is evaluated using this external resistor. Similar to the previous chapter, 4 of the 9 testing scenario's results are discussed. The remaining results are brought in the Appendix.

5.2.1.1 Loading Speed of 3.34 mm/s and Displacement Of 16 mm

Force- time diagram of the crank harvester under the mechanical loads of 16 mm displacement and 3.34 mm/s loading speed is plotted in Figure 5.4.

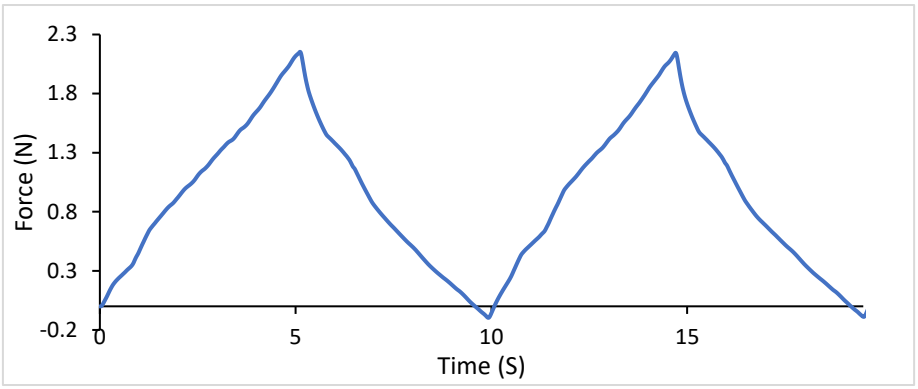

Figure 5.4: Force-time diagram of the harvester under 3.34 mm/s and Displacement Of 16 mm- 25.2 N spring stiffness

The loading speed of this scenario is the lowest compared to the other scenarios. As the loading begins, the force increases over almost 5 seconds, when it ultimately reaches a peak of 2.15 KN. The unloading also takes about 5 seconds until the force drops to almost 0. The rest of the cycles also repeat similarly.

The voltage-time diagram of the harvester logged directly from the rectifier, under the loading conditions of this scenario, is plotted in Figure 5.5. Two loading and unloading cycles outputs are illustrated in the diagram. As the loading starts, the voltage increases gradually, as the loading speed is minimal. The maximum voltage reaches a maximum of 3.3 V. Afterwards, due to a short pause between the loading and unloading, the voltage drops to zero. Once the unloading starts, the voltage values begin to rise again and maximise around 3.2 V. As observable, the loading and unloading voltage peaks are almost equal, and the cycles are similar. However, comparing the time spans of the loadings and unloading, the unloading occurs over a shorter duration.

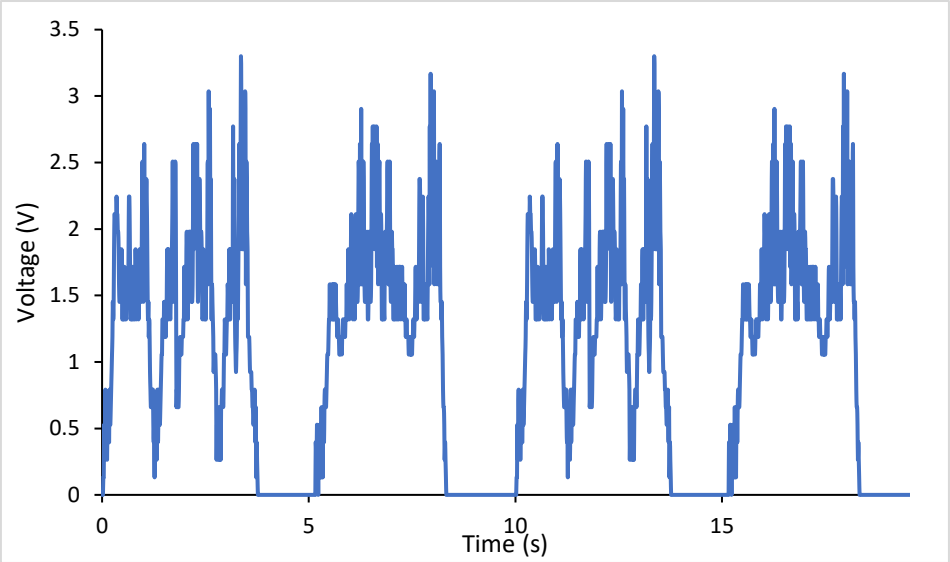

Figure 5.5: Voltage- time of the harvester under loading speed of 3.34 mm/s and displacement of 16 mm- Spring stiffness 25.2 N/mm

Considering the motion analysis of the system, the maximum angular speed of the crank in this loading scenario is 18 deg/s, corresponding to 0.05 rps. As a result of the gearbox, the generator is rotating at 5 rps. If the electrical constant of the generator and the effect of the rectifier is considered, the maximum theoretical voltage from the generator is equal to 4.54 V. The experimental peak voltage is 3.3 V, equal to 73% of the theoretical value. This proportion indicates the efficiency of the harvester under this loading scenario. The deviation is caused by the energy dissipating factors in the assembly, such as the friction between the components.

The voltage around the external resistor is measured, and the power is calculated following the ohm's law to evaluate the system's output power. Figure 5.6 shows the respective diagrams of the voltage and power.

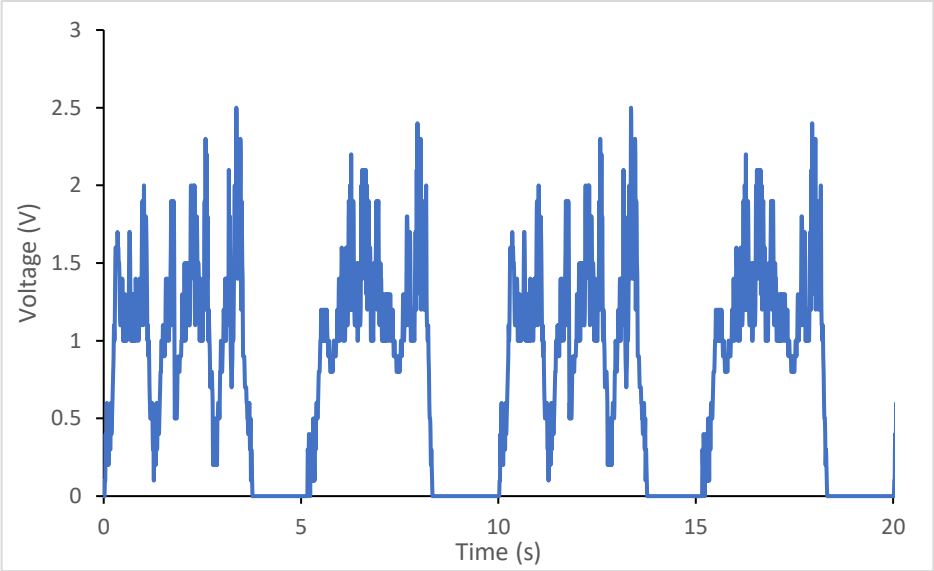

a

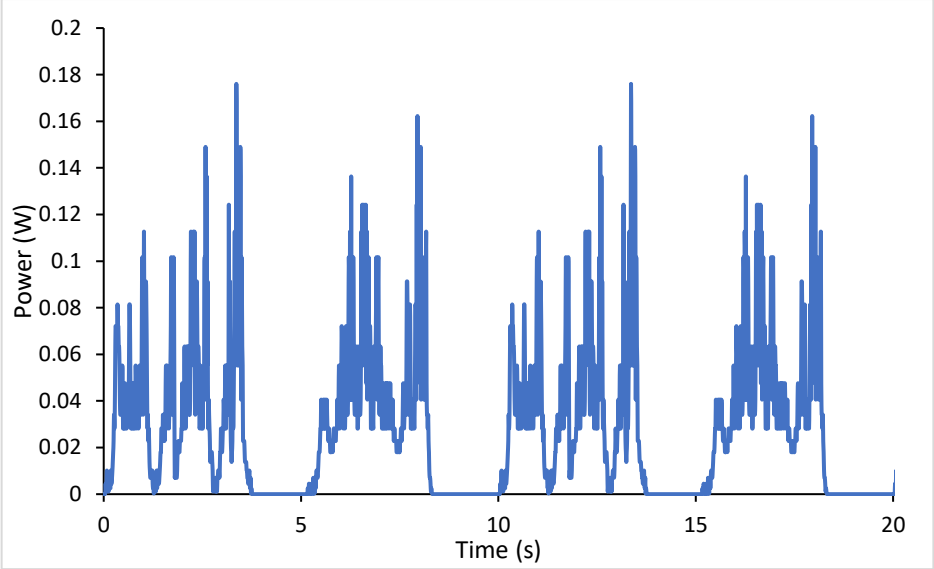

b

Figure 5.6: System's response under 3.34 mm/s and 16 mm displacement- spring stiffness 25.2 N/mm.

a) Voltage-time around the 35.5 ohms, b) Power-time

Voltage values around the external resistances are lower than the raw rectified voltage. The loading and unloading cycles generate voltages and power pulses with maximum values of 2.5 V and 0.18 W and 2.4 V and 0.165 W, respectively. The average voltage is 0.9 V, and the average power is 0.033 W in this loading scenario.

5.2.1.2 Loading Speed of 9 mm/s and Displacement Of 25 mm

Force time diagram of testing the crank harvester under the displacement of 25 mm and the loading speed of 9 mm/s is plotted in Figure 5.7. The force diagram increases as the loading

starts and gradually reaches a maximum of 3 KN, which in the first cycle happens around 2.5 seconds. After this peak, unloading starts, and force drops to zero over almost 2.2 seconds. The remaining cycles also repeat in the same trend.

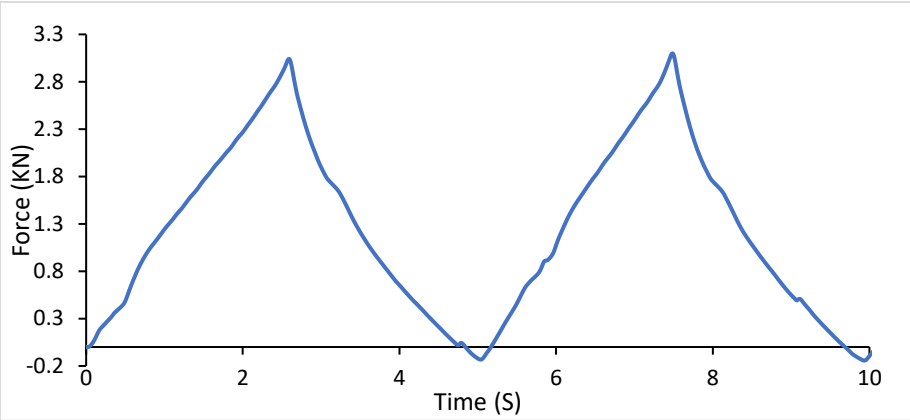

Figure 5.7: Force-time diagram of the harvester under 9 mm/s and Displacement Of 25 mm- 25.2 N spring stiffness

Figure 5.8 shows the voltage-time diagram logged from the rectifier under the loading scenario of 9 mm/s speed and displacement of 25 mm.

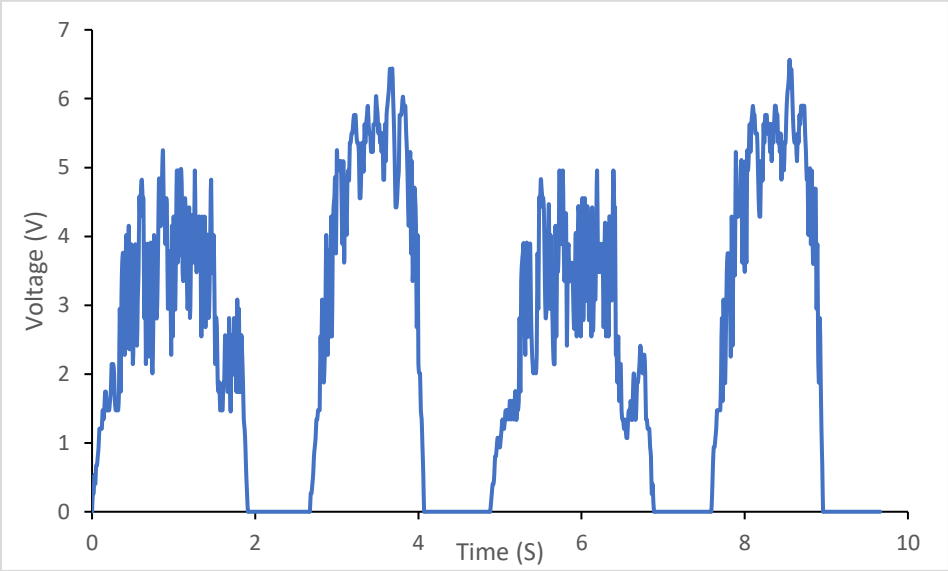

Figure 5.8: Voltage- time of the harvester under loading speed of 9 mm/s and displacement of 25 mm- Spring stiffness 25.2 N/mm

As the displacement is applied, the crank starts revolving and the plot increases until a peak of 5.3 V in loading, and as the spinning stops, the voltage drops to zero around 2 seconds. When

the unloading starts, the voltage increases again and reaches the maximum of about 6.6 V at the peak.

The maximum crank speed is 0.128 rps, and when conveyed to the generator, it revolves at 12.8 rps. Considering the influences of the generator and rectifier, the maximum theoretical voltage from this revolution speed is 11.63 V. Comparing the average of the experimental peak voltages (6.6 V and 5.3 V), they are almost 51% of the theoretical value, and the absolute maximum of the experimental voltage (6.6 V) is 57% of the theoretical voltage, which are indicating an estimation of the system's efficiency.

The difference between the peak voltage of loading and unloading is worth noting. It is caused by the slight difference between the loading speed (applied by the testing machine) and the unloading speed (affected by springs and their compression level). As the rebounding speed of the spring also depends on its compression level, this difference is more pronounced when the loading displacement is either minimum or maximum.

The voltage and power outcomes of the harvesting circuit are plotted in Figure 5.9.

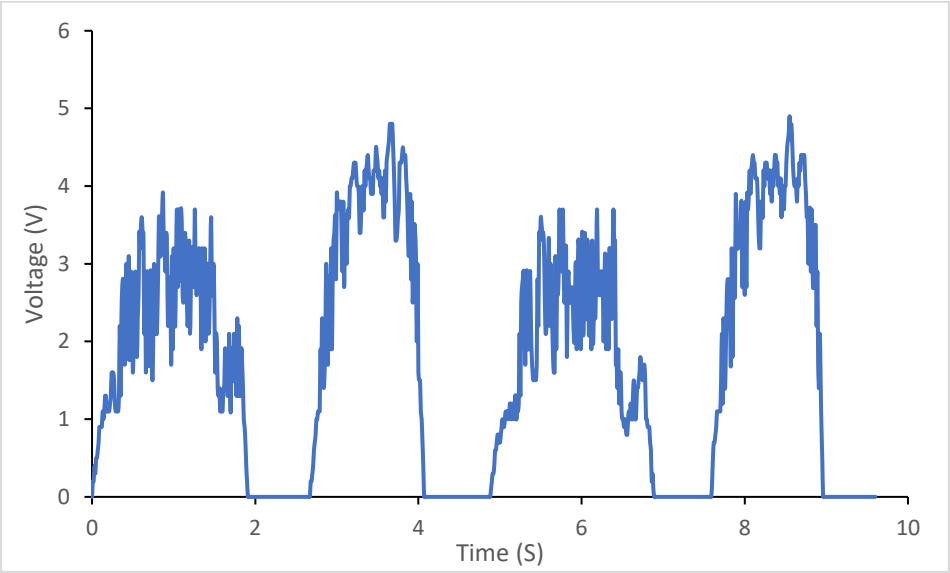

a

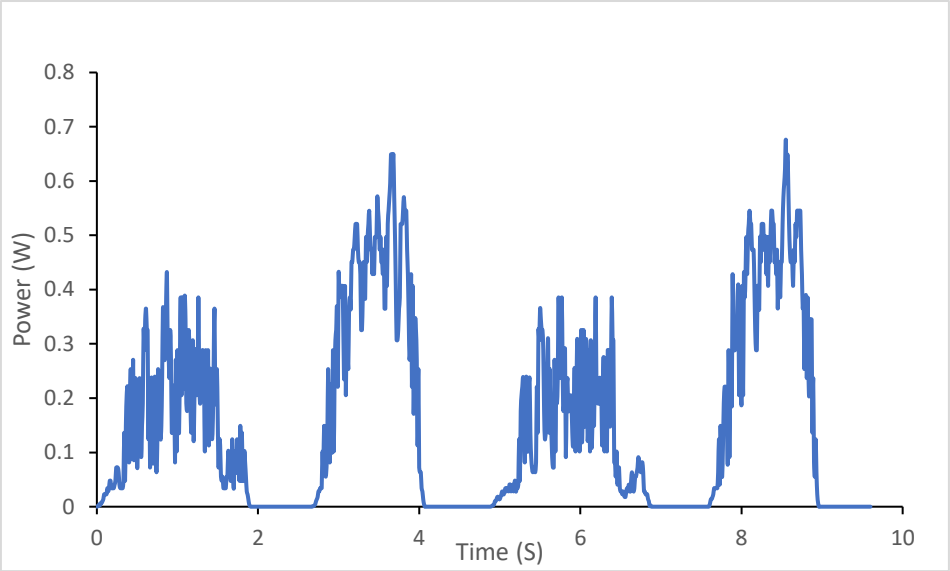

b

Figure 5.9: System's response under 9 mm/s and 25 mm displacement- spring stiffness 25.2 N/mm. a) Voltage-time around the 35.5 ohms, b) Power-time

According to Figure 5.9, the maximum voltage around the resistor is 4.9 V, corresponding to the peak power of 0.7 W. Also, the peak values of voltage and power over the loading periods (the first and the third peaks) are 4 V and 0.43 W, respectively. Over the one cycle of loading and unloading, the average voltage is 2.11 V, and the average power is 0.19 W.

5.2.1.3 Loading Spped of 13 mm/s and Displacement Of 10 mm

Force time diagram of two cycles of loading and unloading is presented in Figure 5.10.

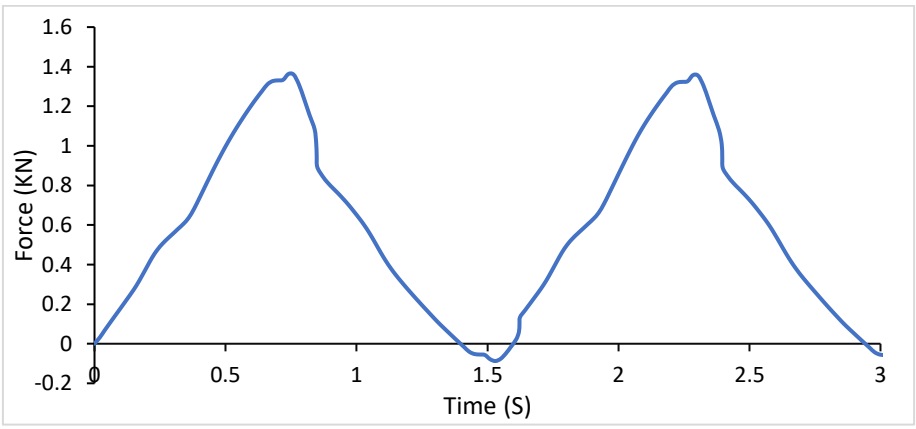

Figure 5.10: Force-time diagram of the harvester under 13 mm/s and Displacement Of 10 mm- 25.2 N spring stiffness

The applied force on the system begins to raise when the loading starts and within 0.7 seconds reaches a peak of 1.37 KN. After a short pause, the unloading starts and the force reaches almost

zero again around the time 1.5 seconds. The following cycles also follow a similar pattern with identical peaks and durations.

Figure 5.11 shows the rectified voltage-time diagram of the system under the current loading condition.

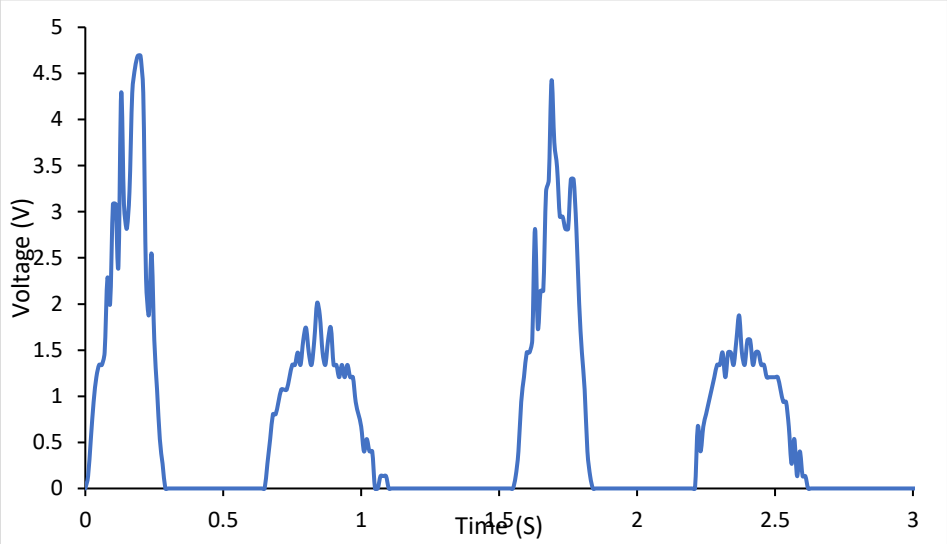

Figure 5.11: Voltage- time of the harvester under loading speed of 13 mm/s and displacement of 10 mm- Spring stiffness 25.2 N/mm

The diagram consists of 4 loading (the first and the third) and unloading (the second and the fourth) peaks over 3 seconds. The loading voltages are higher than the unloading voltages, which is related to the fact that the spring was the least compressed in this scenario which affects the recovery speed, generating a lower angular speed in the crank as coming back to the original state. As the loading starts, the voltage rises to a maximum of 4.7 V, followed by a drop as the loading ends. Once the unloading starts, the voltage rises again, forming the unloading half-cycle, with the peak value of 2 V.

Based on the motion analysis, the maximum angular speed of the crank in this scenario is 0.225 rps, which means that the maximum angular speed of the generator is 22.5 rps. The theoretical maximum voltage output is 20.44 V, considering the generator's electrical constant and the effect of the rectifier. The peak experimental voltage is 4.7 V, 23% of the theoretical value.

This percentage indicates the system's efficiency and is caused by the energy dissipation in the components of the system in this testing scenario.

The outputs of the power harvesting circuit are plotted in Figure 5.12.

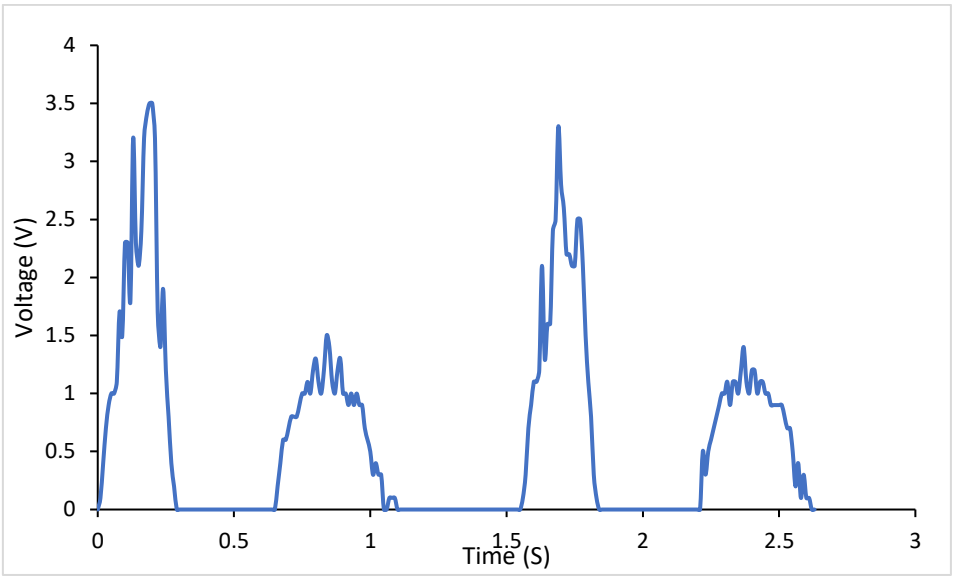

a

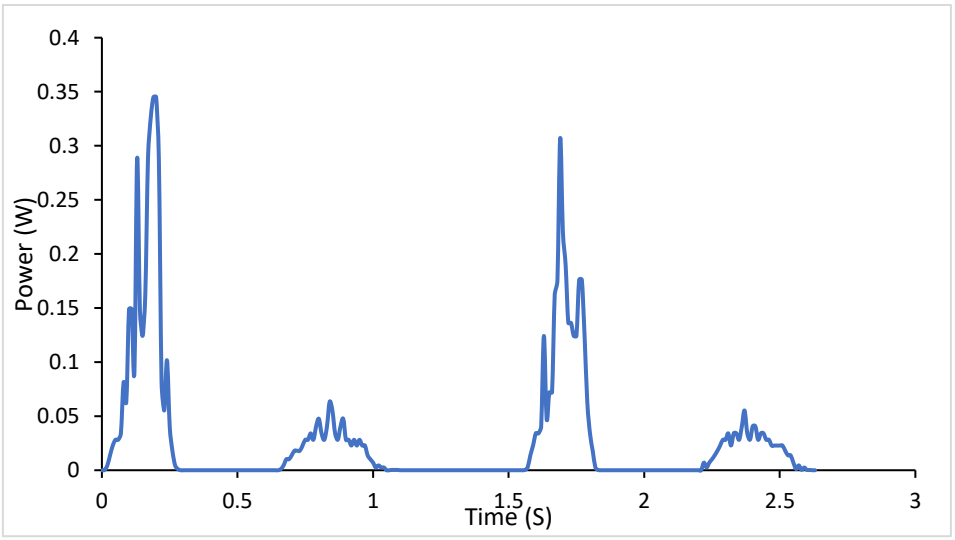

b

Figure 5.12:System's response under 13 mm/s and 10 mm displacement- spring stiffness 25.2 N/mm.

a) Voltage-time around the 35.5 ohms, b) Power-time

According to the voltage-time diagram, the maximum voltage around the resistor equals 3.5 V, which also corresponds to the peak power of 0.35 W. The maximum voltage and power during unloading are also equal to 1.5 V, and 0.06 W. Furthermore, the average voltage and power in one cycle of loading and unloading are 0.76 V and 0.038 W.

5.2.1.4 Loading Speed of 14.67 mm/s and Displacement Of 25 mm

The load time diagram of the harvester under this loading scenario is plotted in Figure 5.13.

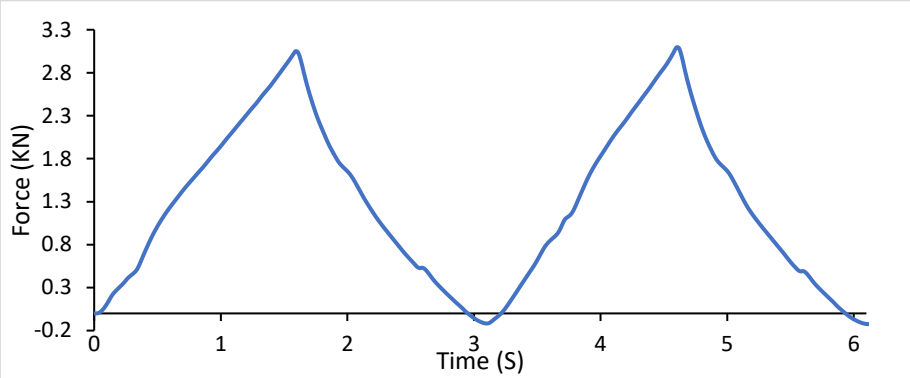

Figure 5.13: Force-time diagram of the harvester under 14.67 mm/s and Displacement Of 25 mm- 25.2 N spring stiffness

Force values increase as the loading starts and reach a maximum of about 3.1 KN at 1.5 s. afterwards, as the unloading starts, the forces decrease until the system recovers and force returns to almost zero at 3.15 s. The remaining loading and unloading cycles also occur with the same trend.

Rectified voltage-time diagram of the harvester under this loading scenario is plotted in Figure 5.14. As the loading starts, the voltage gradually increases and reaches a maximum of almost 5.3 V at 0.81s. Once the unloading starts, the system quickly recovers back, and a sharp half-cycle is generated with a maximum of 8.4 V.

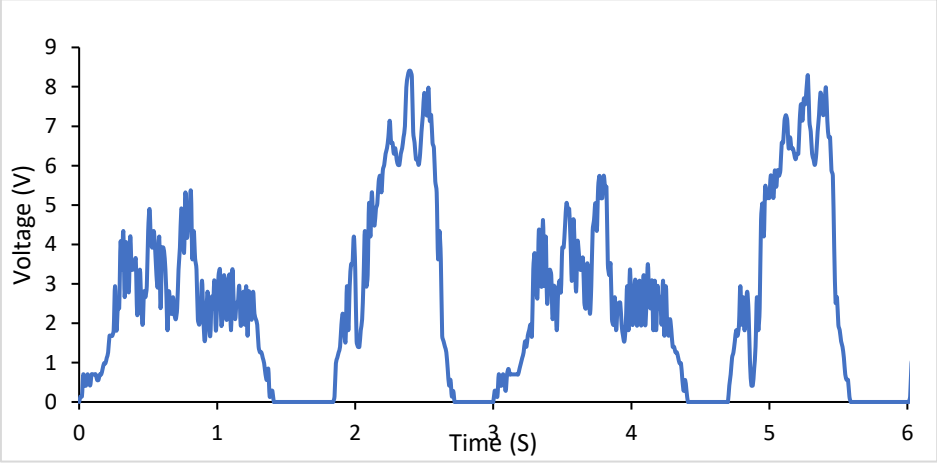

Figure 5.14: Voltage- time of the harvester under loading speed of 14.67 mm/s and displacement of 25 mm- Spring stiffness 25.2 N/mm

According to the motion analysis, the maximum angular speed of the generator in this loading scenario equals 20.6 rps. Hence, the theoretical maximum voltage is 18.71 V. The experimental peak voltage is around 8.4 V, which is 45% of the theoretical value, denoting the system's efficiency, caused by the efficiency of the components and loss of energy during the performance.

Figure 5.15 shows the voltage and the power outputs of the power harvesting circuit.

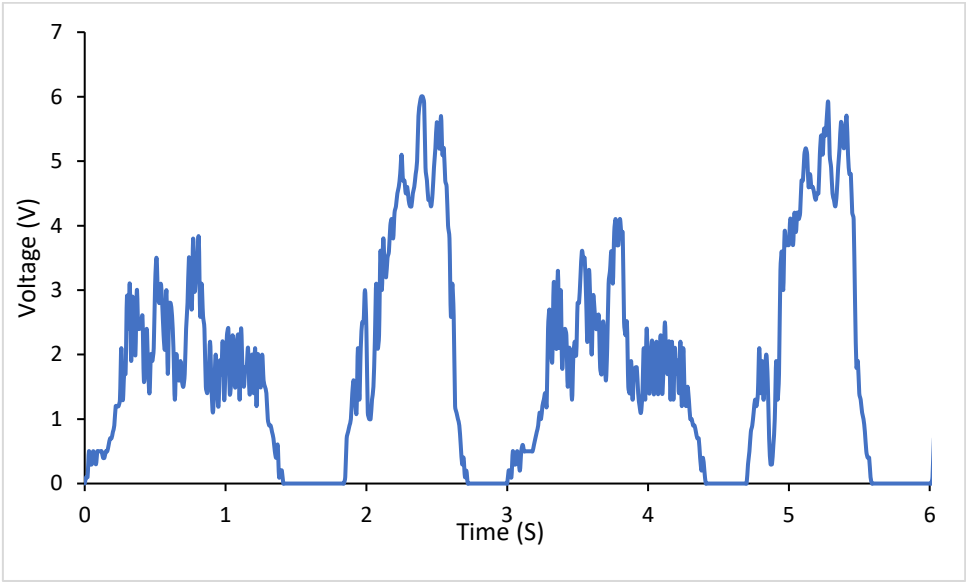

a

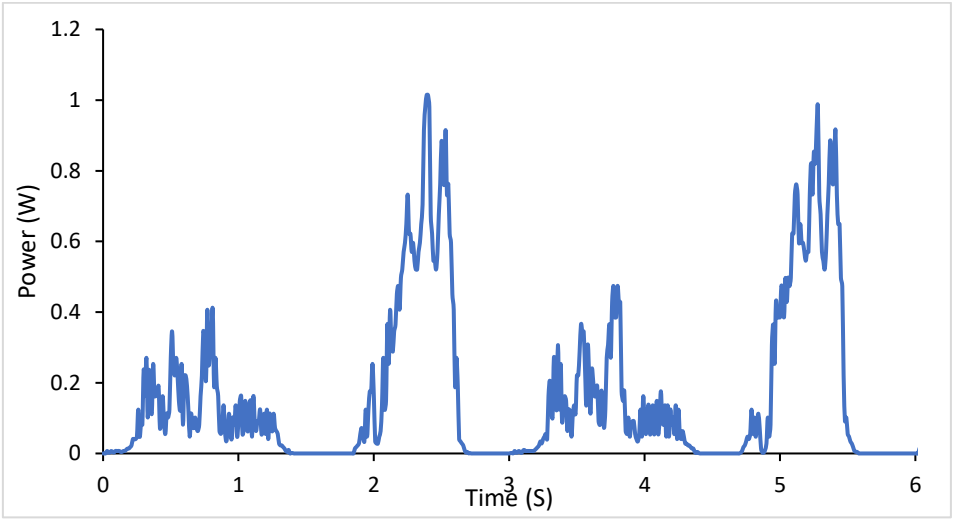

b

Figure 5.15: System's response under 14.67 mm/s and 25 mm displacement- spring stiffness 25.2 N/mm. a) Voltage-time around the 35.5 ohms, b) Power-time

According to the diagrams, the maximum harvested voltage around the resistor of 35.5 ohms is about 6 V, corresponding to the maximum power of 1.01 W. The average voltage and the power in one loading and unloading cycle are 1.94 V and 0.178 W, respectively.

In the previous section, the response of the harvester unit was evaluated under various loading scenarios. As shown previously through analyses, both loading speed and displacement affect the electrical output of the harvester. Hence, these factors were studied experimentally through different testing scenarios on the harvester using the spring set of 25.2 N/mm, and the results were presented in separate sections.

In the following sections, the experimental results obtained from the harvester with the spring set of 29.77 N/mm (S2) are discussed.

5.2.2 Results of Spring Set of 29.77 N/mm

This section discusses the results of the harvester assembled with the spring set of S2, 29.77 N/mm stiffness. Similar to the previous section, first, the results of the optimal external resistor are presented, followed by the responses of the system, under different mechanical conditions.

Different resistors ranging from 8.5 to 270 ohms were connected to the output of the rectifier, and the voltage around them was measured under a constant mechanical loading scenario to measure the optimal external resistor. Following Ohm's law, the power is calculated and finally, the optimal resistor is found by plotting the average power against the external resistors. Figure 5.16 shows the voltage-time around the resistor of 8, 100, 180 and 270 ohms.

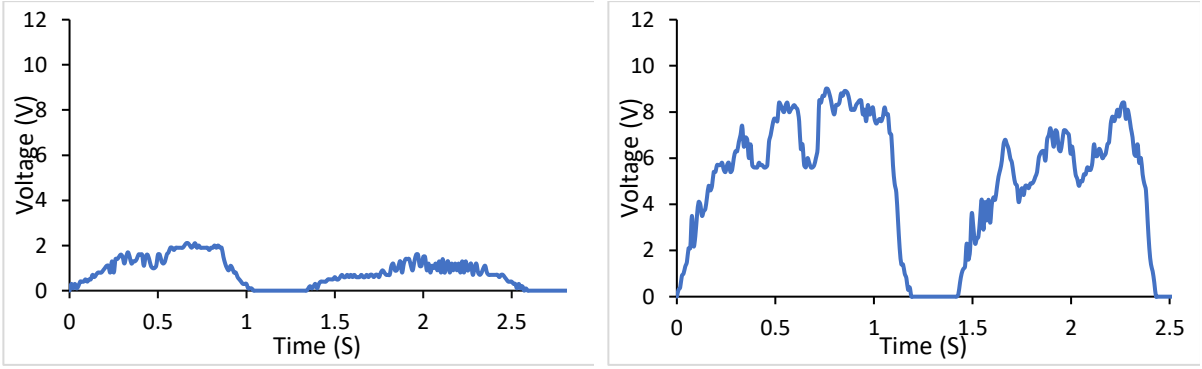

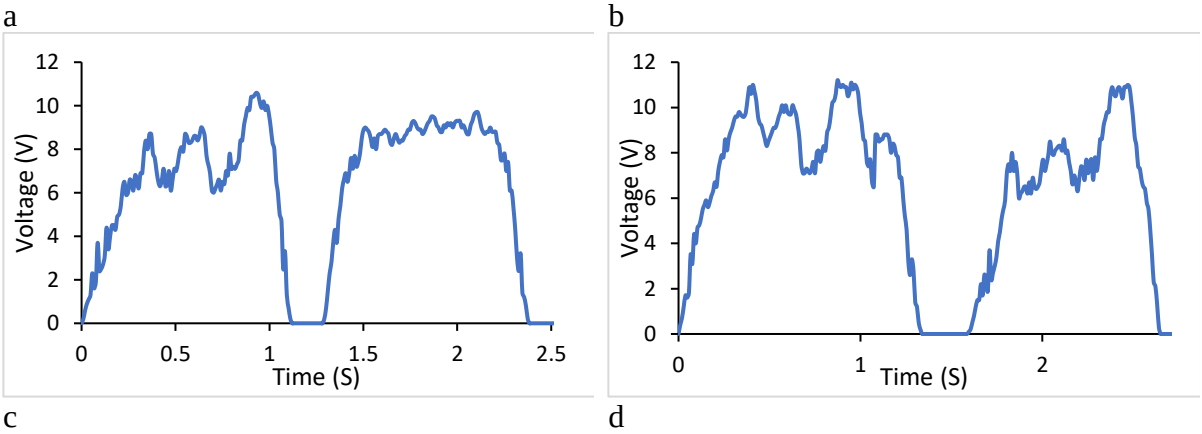

Figure 5.16: Voltage-time diagrams of the harvester with the spring set of 29.77 N/mm^2, the voltage around the resistors of a) 8 ohms, b) 100 ohms, c) 180 ohms and d) 270 ohms

As it can be seen, the voltage output increases by the increase in the resistor and eventually stabilizes. Figure 5.17 shows the power resistance diagram of the harvester with springs set of 29.77 N/mm stiffness under the constant mechanical testing scenario of 18 mm displacement and 13 mm/s loading speed. The power is the average power recorded from the two pairs of the output of the generator.

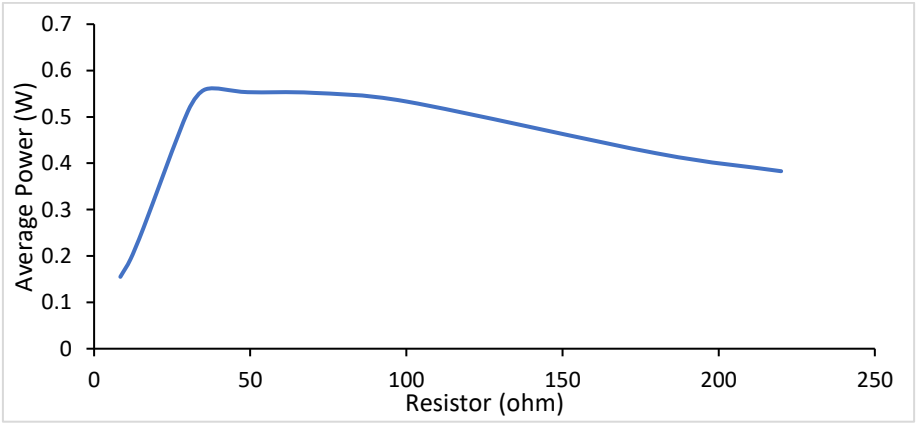

Figure 5.17: Power-resistance diagram- 29.77 N/mm spring stiffness

It is observed that the power optimizing resistor, according to Figure 5.17, is equal to 35.5 ohms, which is equal to the resistor obtained from the harvester with the spring sets of 25.2 N/mm and 19.12 N/mm.

The mechanical and electrical performance of the harvester with the spring set of 29.77 N/mm is detailed in the following sections, discussing 4 of the loading scenarios. The remaining results are available in the Appendix.

5.2.2.1 Loading Speed of 3.34 mm/s and Displacement Of 16 mm

The force-time diagram of the crank-based harvester under this loading scenario is plotted in Figure 5.18. as the loading starts, the force values increase gradually, until they maximize around 2.47 KN at the time of 5.1s. Afterwards, as the unloading starts, the force decreases, and over and over 5 seconds, it reaches zero.

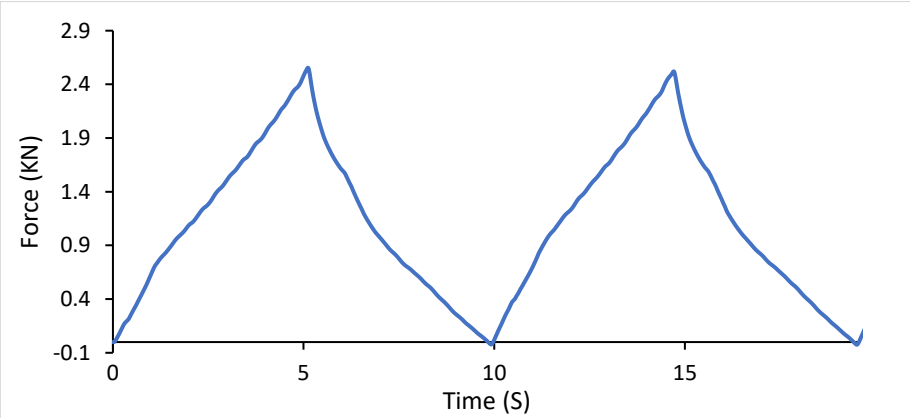

Figure 5.18: Force-time diagram of the harvester under 3.34 mm/s and Displacement Of 16 mm- 29.77 N/mm spring stiffness

Figure 5.19 shows the rectified voltage-time diagram logged directly from the rectifier under the testing scenario of 16 mm displacement and 3.34 mm/s loading speed. As shown, the loading and unloading half-cycles have similar trends and almost the same peak voltage.

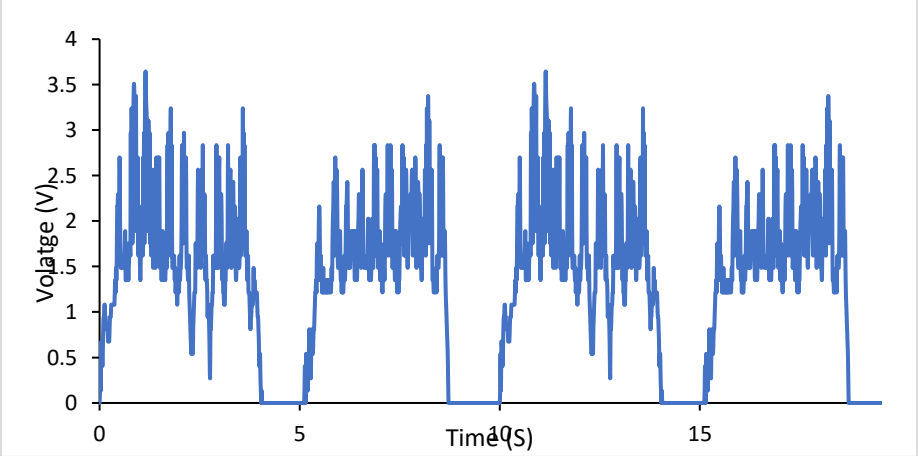

Figure 5.19: Voltage- time of the harvester under loading speed of 3.34 mm/s and displacement of 16 mm- Spring stiffness 29.77 N/mm

When the loading starts and the generator starts spinning, the voltage gradually increases and maximizes at 3.65 volts. The voltage generation continues for about 4.2 seconds, and as the loading stops, there is a sharp decrease in the voltage, reaching 0 within 5 seconds. However, as the unloading starts, voltage is generated again, the unloading half cycle is formed with a maximum of 3.4. Similar loading and unloading trends are also repeated in the rest of the cycles.

Based on the motion analysis, the theoretical maximum angular speed of the generator is equal to 5 rps, which is capable of generating a maximum theoretical voltage of 4.8 V, considering the effect of the rectifier and the electrical constant of the generator. The maximum experimental voltage (3.65 V) is 76% of the theoretical value, indicating the system's efficiency under this testing scenario. The energy dissipation is due to the friction between the mechanical components, the efficiency of the gearbox and generator.

Voltage and power-time diagrams logged from the harvester circuit are plotted in Figure 5.20. It can be observed that the voltage around the resistance is lower than the raw voltage around the rectifier. During the loading, the voltage increases and has a maximum of 2.7 V and then gradually decreases to zero over around 5 seconds. As there is a short pause, the voltage will be equal to zero, and once the unloading starts, the voltage again increases and reaches a maximum of 2.5 V, followed by a drop to zero as the system recovers to its original state.

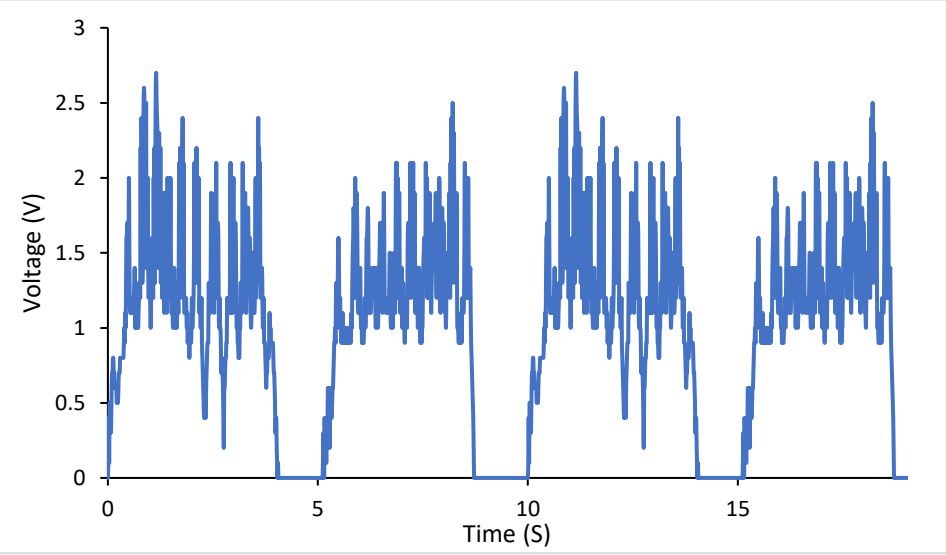

a

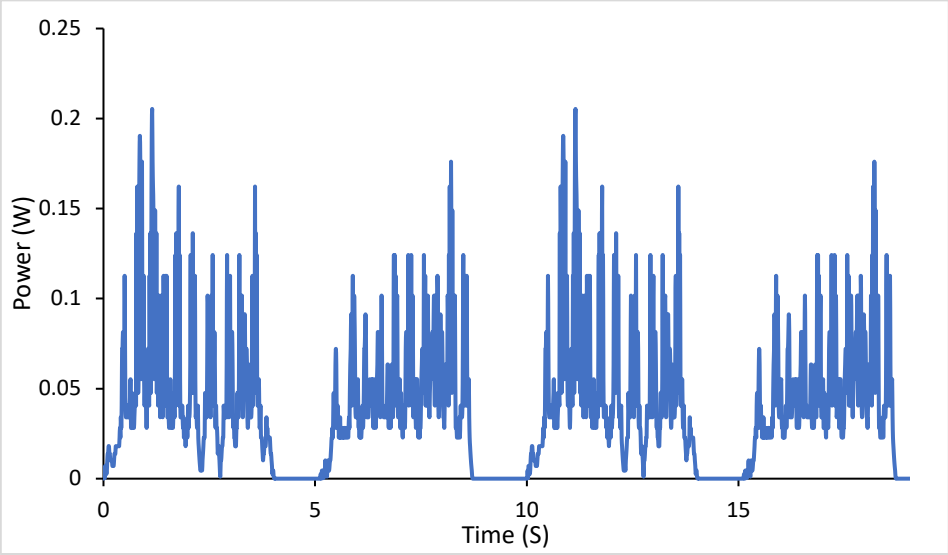

b

Figure 5.20: System's response under 3.34 mm/s and 16 mm displacement- Spring stiffness 29.77 N/mm a) Voltage-time around the 35.5 ohms, b) Power-time

Moreover, according to the data, the average voltage around the resistor and the average power in one loading and unloading cycle is 1.085 V and 0.043 W.

5.2.2.2 Loading Speed of 9 mm/s and Displacement Of 25 mm

In this section, the outputs of the harvester under the loading scenario of 25 mm displacement and 9 mm/s loading speed are discussed. Figure 5.21 shows the force-time response of the harvester. The force values increase as the loading starts, and after a peak value of 3.3 KN at 2.61 s, the unloading process starts, in which the compressed system is fully recovered over 2.54 seconds. The following cycles of loading and unloading keep the same pattern.

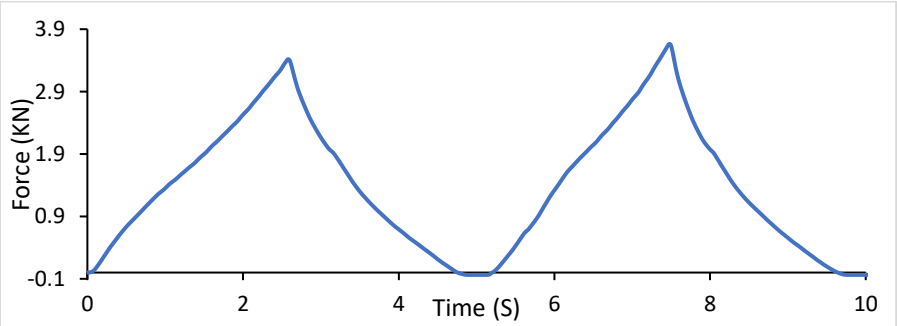

Figure 5.21: Force-time diagram of the harvester under 9 mm/s and displacement of 25 mm- Spring stiffness 29.77 N/mm

Figure 5.22 illustrates the rectified voltage-time diagram of the harvester under the current loading scenario. It shows that the voltage increases as the loading start, and after a peak of 7.25 V, as the loading approaches an end, the voltage drops to zero. As the unloading starts, another voltage curve is formed, with a peak of 7.4 V.

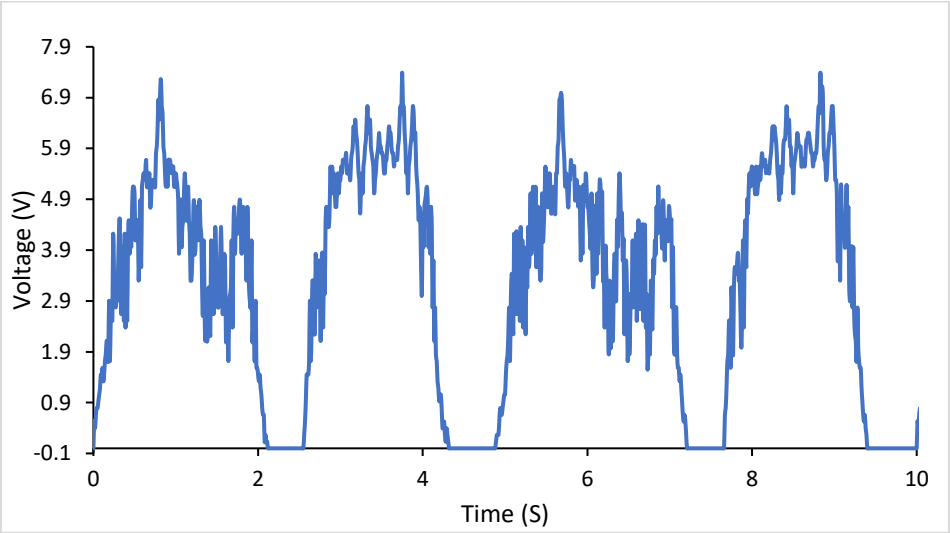

Figure 5.22: Voltage-time of the harvester under 25 mm of displacement and the speed of 9 mm/s-Spring stiffness 29.77 N/mm

Moreover, according to the motion analysis, the maximum angular speed of the generator in this loading scenario is 12.8 rps, which considering the electrical constant of the generator and the rectifier's effect, can generate a maximum theoretical voltage of 11.63 V. By comparison, the experimental peak voltage (7.4 V) is 64% of the theoretical value, which is caused by the loss of energy in the system and indicates the efficiency under this loading scenario.

Figure 5.23 shows the voltage and power output of the power harvesting circuit. Following a similar trend to Figure 5.22, the voltage-time diagram around the external resistor has slightly lower voltage peak values in loading and unloading, equal to 5.5 V and 5.6 V, respectively, corresponding to the peak power of 0.89 W. Moreover, the average voltage and power of the circuit over one loading and unloading cycle are 2.78 V and 0.29 W.

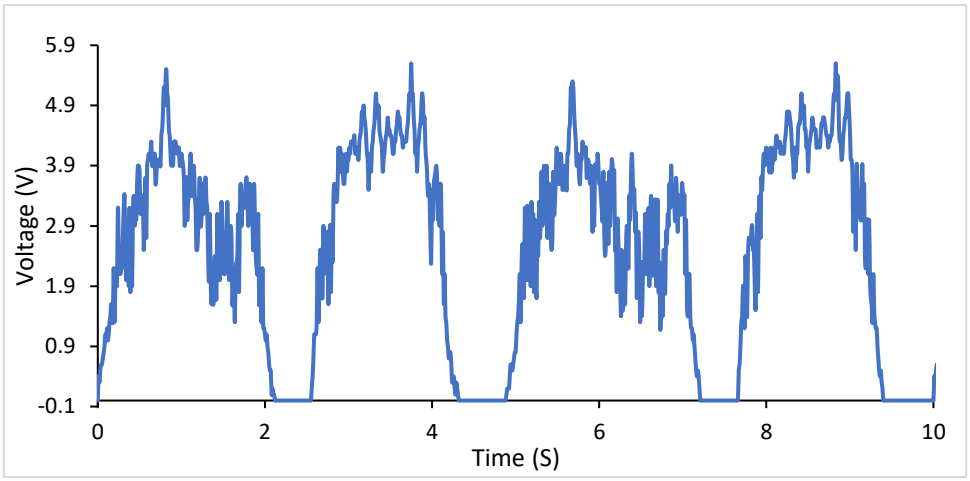

a

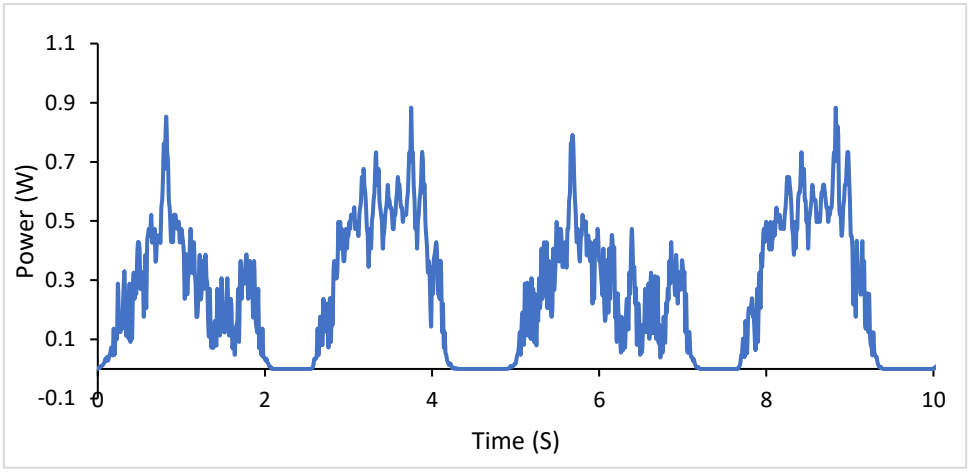

b

Figure 5.23: System's response under 9 mm/s and 25 mm displacement- Spring stiffness 29.77 N/mm

a) Voltage-time around the 35.5 ohms, b) Power-time

5.2.2.3 Loading Speed of 13 mm/s and Displacement Of 10 mm

Force time diagram of the harvester under the loading scenario of 13 mm/s loading speed and 10mm displacement is plotted and shown in Figure 5.24.

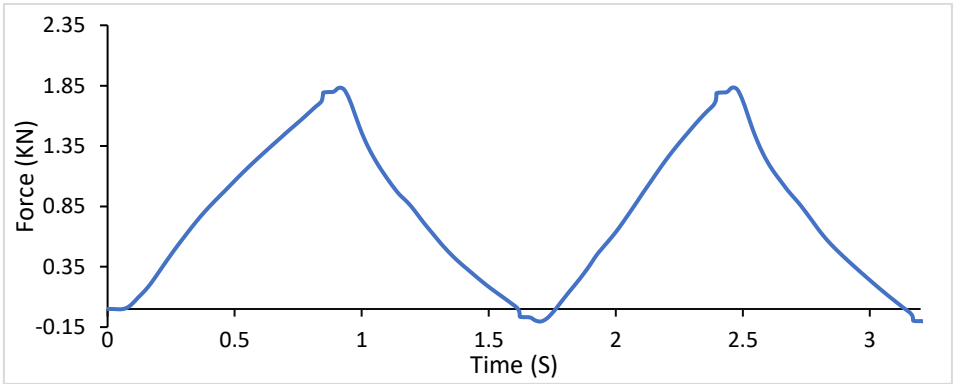

Figure 5.24: Force-time diagram of the harvester under 13 mm/s and Displacement Of 10 mm- Spring stiffness 29.77 N/mm

Accordingly, as the loading starts, the force increases and after 1.8 s, it reaches a peak of 1.85 KN at about 0.96 s, followed by the unloading period of about 0.76s, in which the harvester recovers to the original state. The rest of the loading and unloading cycles also repeat with a similar trend.

The voltage-time diagram of the harvester under the current loading scenario and logged from the rectifier is plotted in Figure 5.25.

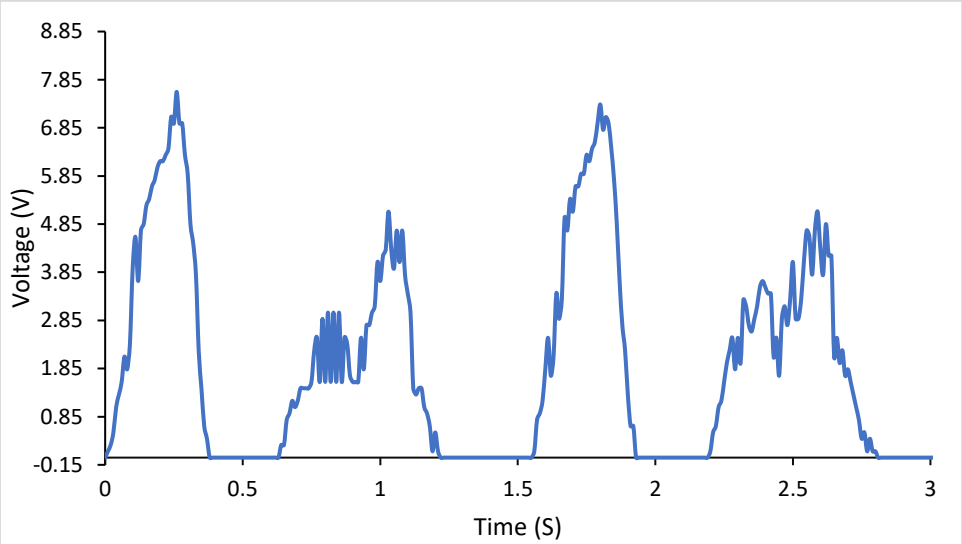

Figure 5.25: Voltage-time of the harvester under 10 mm of displacement and the speed of 13 mm/s- Spring stiffness 29.77 N/mm

In the diagram, once the loading starts, the voltage increases with a sharp peak of 7.6 V at 0.26 s, followed by a drop, as the loading finishes and the generator stops spinning. This pause is followed by another peak over the unloading, which takes a slightly longer process (0.92s as opposed to 0.62s) and has a lower peak of 5.1 V.

According to the motion analysis, the peak angular speed of the generator in this loading scenario is 22.5 rps, which is capable of generating 20.44 V, considering the electrical constant of the generator and the rectifier. Comparing the experimental and the theoretical values, the experimental peak voltage (7.6 V) is 37% of the theoretical value, which is caused by the energy dissipation in the mechanical components of the system under the current mechanical conditions.

Figure 5.26 shows the voltage and the power response of the energy harvesting circuit.

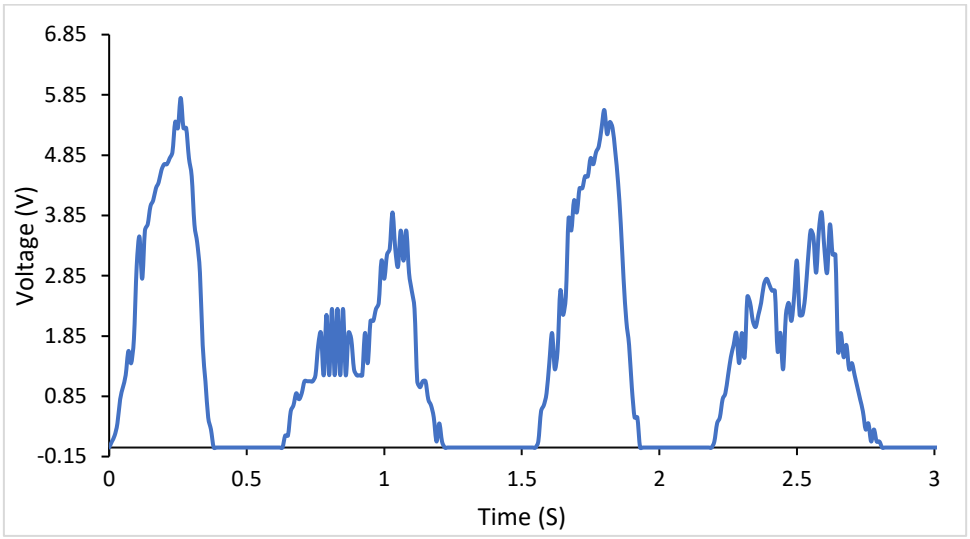

a

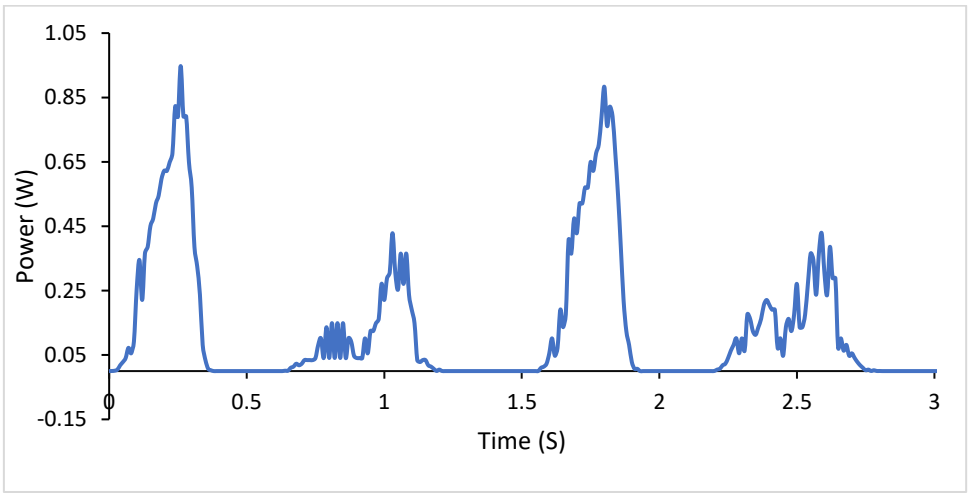

b

Figure 5.26: System's response under 13 mm/s and 10 mm displacement - Spring stiffness 29.77 N/mm a) Voltage-time around the 35.5 ohms, b) Power-time

According to Figure 5.26a, the voltage diagram follows the same trend as the rectified voltage-time diagram, plotted in Figure 5.25, and only the peak voltage values are lower, i.e., 5.8 V, vs 7.6 V. The peak values of the voltage in loading and unloading correspond to the peak values of the power, 0.95 W and 0.43 W, respectively. The average values of the voltage and power for one cycle of loading and unloading are 1.73 V and 0.16W, respectively.

5.2.2.4 Loading Speed of 14.67 mm/s and Displacement Of 25 mm

Figure 5.27 shows the force-time diagram of the harvester under the testing scenario of 14.67 mm/s loading speed and 25 mm displacement. According to the diagram, the peak force occurs

at the ultimate stage of the loading and is equal to 3.8 KN occurring at the time of 1.71 s in the first cycle, followed by the unloading process in which the system recovers over 1.6 seconds. The following cycles also repeat in a similar trend.

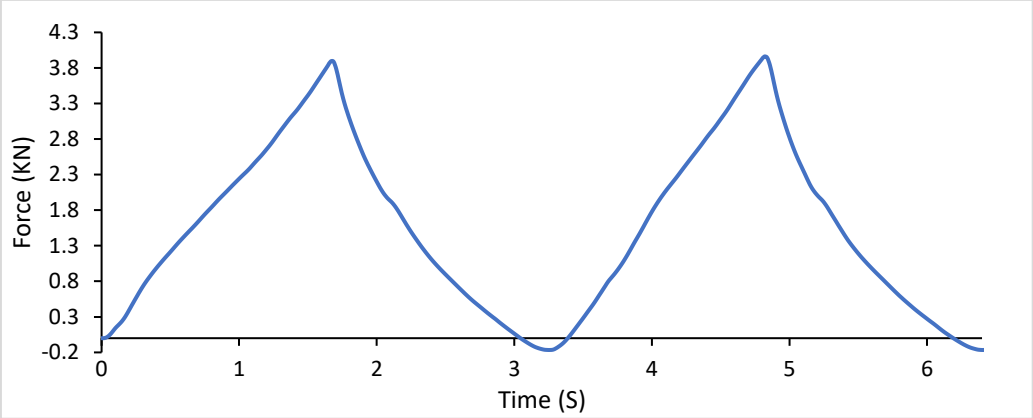

Figure 5.27: Force-time diagram of the harvester under 14.67 mm/s and Displacement Of 25 mm- Spring stiffness 29.77 N/mm

Figure 5.28 plots the voltage-time diagram of two cycles of loading and unloading of the harvester directly recorded from the rectifier.

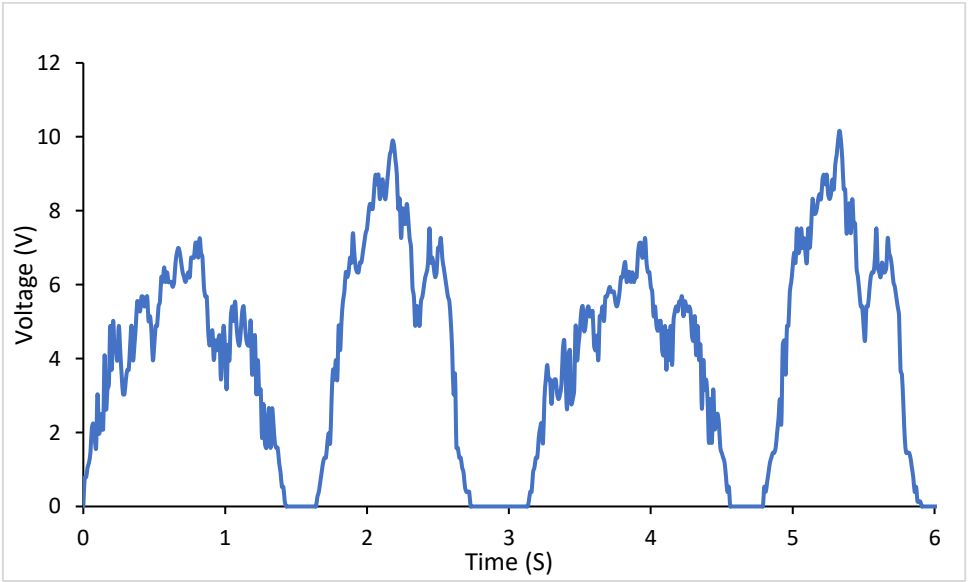

Figure 5.28: Voltage- time of the harvester under loading speed of 14.67 mm/s and displacement of 25 mm- Spring stiffness 29.77 N/mm

According to the illustration, the voltage increases as the loading starts and peaks at 6.87 V during the loading process. However, once the loading is finished, the unloading is started with

a sharp increase in the voltage as the harvester bounces back to its original state. Hence, the unloading peak is higher than the loading and is equal to 10 V.

According to the motion analysis, the maximum angular speed of the generator in this testing scenario is 20.6 rps, capable of generating a maximum theoretical voltage of 18.71V. By comparison, the maximum experimental voltages during the loading and unloading are 37% and 53% of the theoretical value, respectively. Thus, on average, the experimental output is 45% of the theoretical peak voltage, indicating the system's average efficiency in this loading scenario.

Figure 5.29 shows the voltage and power outputs of the energy harvesting circuit. According to Figure 5.29a, the voltage around the resistor has the same pattern as the rectified voltage diagram, with lower peak values of 5.5 V and 7.6 V in loading and unloading, respectively.

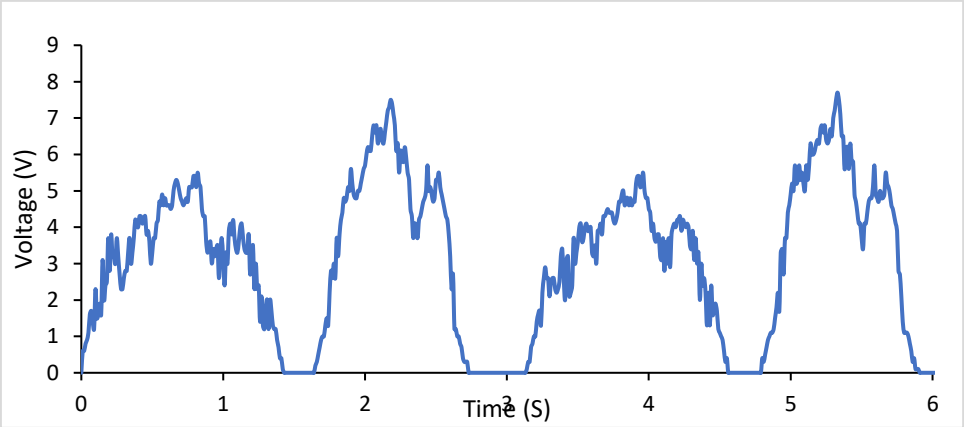

a

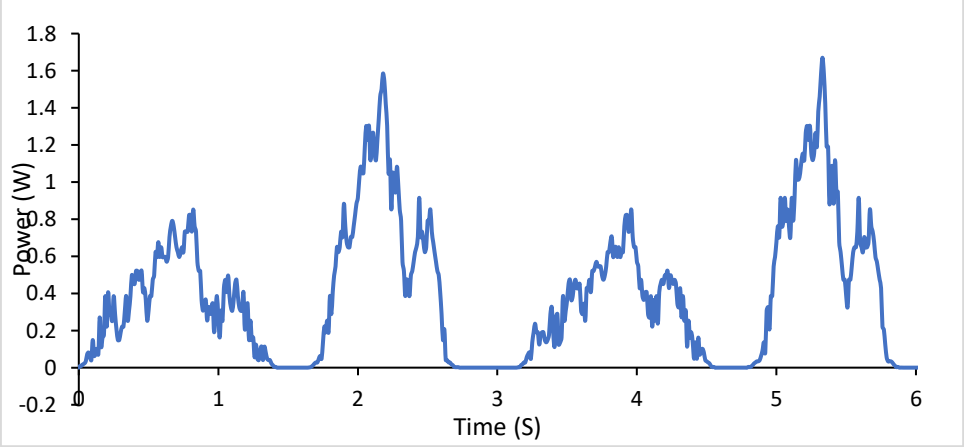

b

Figure 5.29: System's response under 14.67 mm/s and 25 mm displacement- spring stiffness 29.77 N/mm. a) Voltage-time around the 35.5 ohms, b) Power-time

These peak voltages also correspond to the power peaks of 0.85 W, and 1.6 W. Furthermore, the average voltage and power of the system over one cycle of loading and unloading are 3.4 V and 0.433 W, respectively.

In the previous sections, the mechanical and electrical results of the harvester assembled with the spring set of 29.77 N/mm (S2) was discussed. Similar to the previous parts, the responses were evaluated under various mechanical testing scenarios, with the loading speed and displacement as the variables. It is worth noting that the loading scenarios are decided so to represent the real application conditions, where passing vehicles with different curb weights apply forces (displacements) with various speeds. As observed, the output voltage, power, and efficiency of the system depend on the scenario.

In order to study the harvester's responses, another set of springs with higher stiffness (37.88 N/mm) were assembled in the harvester. The results are presented in the following section.

5.2.3 Results of Spring Set of 37.88 N/mm

To investigate the harvester's response with the spring set of 37.88 N/mm, first, the optimizing external resistor is measured by installing various resistors in the power harvesting circuit and measuring the voltage around the resistor, while the harvester is under a constant mechanical loading scenario of 18 mm displacement and 13 mm/s loading speed. Figure 5.30 shows the voltage-time diagrams around two different resistors.

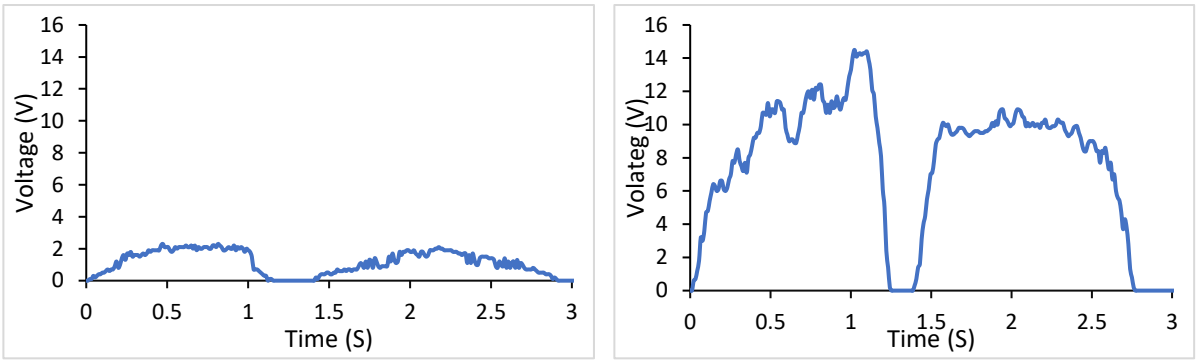

a b

Figure 5.30: Voltage-time diagrams of the harvester with the spring set of 38.77 N/mm, around the resistors of a) 8 ohms, b) 270 ohms

Similar to the previous corresponding cases, the output voltage and power are dependants on the external resistor. Figure 5.31 shows the output power of the harvester against the various external resistors. The power values are the average of one loading and unloading cycle. As it is shown, the optimizing resistor of the harvester circuit in this testing scenario is also 35.5 ohms.

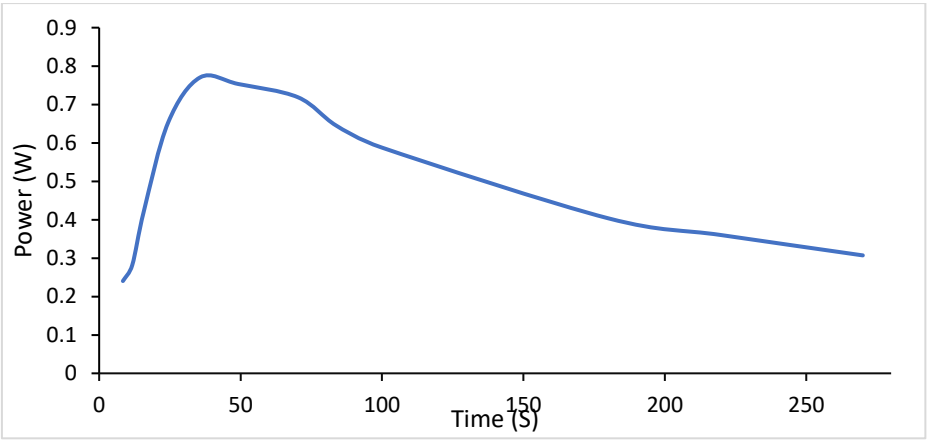

Figure 5.31: Power-resistance diagram- 37.88 N/mm spring stiffness

The mechanical performance of the harvester is detailed in the following sections.

5.2.3.1 Loading Speed of 3.34 mm/s and Displacement Of 16 mm

The force-time diagram of the harvester under this mechanical condition is plotted in Figure 5.32. Two cycles of loading and unloading are applied over 20 seconds. The ultimate force applied on the harvester in this scenario is 2.9 KN.

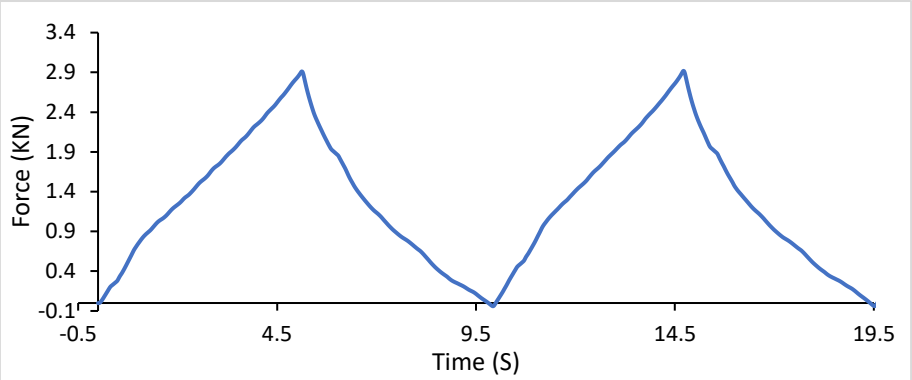

Figure 5.32: Force-time diagram of the harvester under 3.34 mm/s and Displacement Of 16 mm- 37.88 N/mm spring stiffness

Figure 5.33 shows the voltage-time diagram of the harvester logged directly from the rectifier.

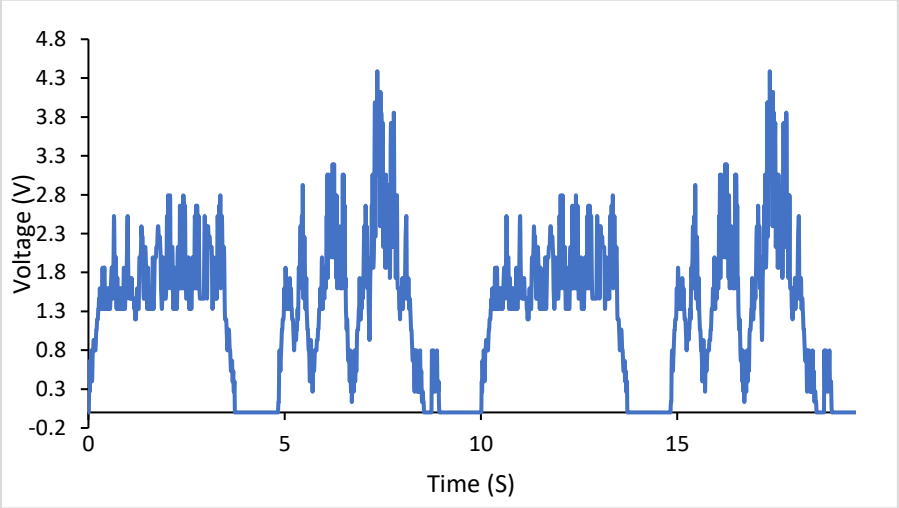

Figure 5.33: Voltage- time of the harvester under loading speed of 3.34 mm/s and displacement of 16 mm- Spring stiffness 37.88 N/mm

As illustrated, the maximum voltages during the loading and unloading are 2.7 V and 4.4 V. Due to the high stiffness of the harvester, as the unloading starts, the system quickly bounces back to the original state, generating sharp peaks of voltage.

The maximum theoretical output voltage in this testing scenario is 4.8 V. The average maximum voltage from the experiments (in loading and unloading) is 3.55 V, which is 74% of the theoretical estimation, indicating the system's generation efficiency in this loading scenario.

Figure 5.34 shows the power time diagram of the system, recorded from the power harvesting circuit with an external resistor of 35.5 ohms, which is the optimizing resistor.

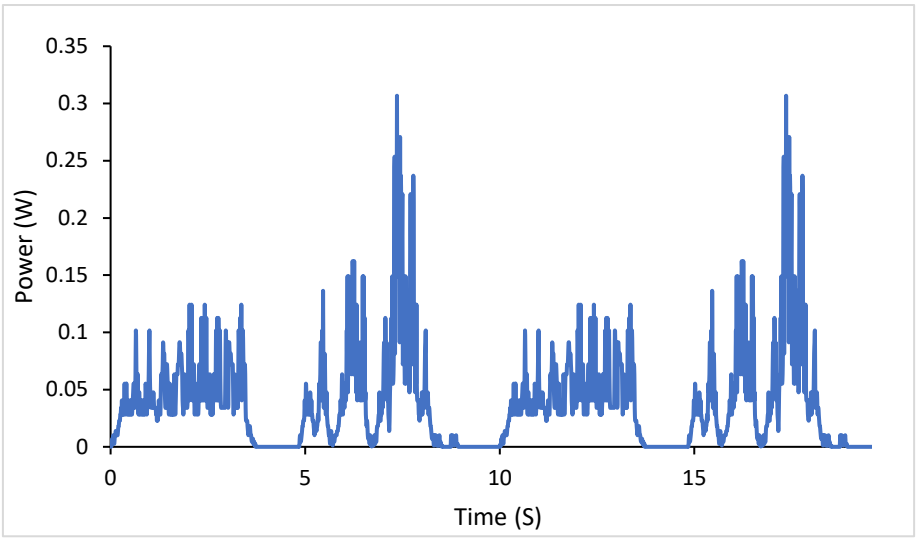

Figure 5.34: Power time diagram of the harvester with the springs' stiffness of 37.88 N/mm, under the loading scenario of 3.34 mm/s loading speed and 16 mm displacement

As shown, the maximum harvested power during the loading and unloading is 0.125 W and 0.31 W, which correspond to the maximum voltage values of 2.1 V and 3.3 V, respectively. The average power of one cycle of loading and unloading is 0.044 W.

5.2.3.2 Loading Speed of 9 mm/s and Displacement Of 25 mm

Force time diagram of the two loading and unloading cycles in this scenario are plotted in Figure 5.35. It can be seen that both cycles are similar in their durations and their peak force values, which is equal to 4.38 KN at the ultimate point of loading.

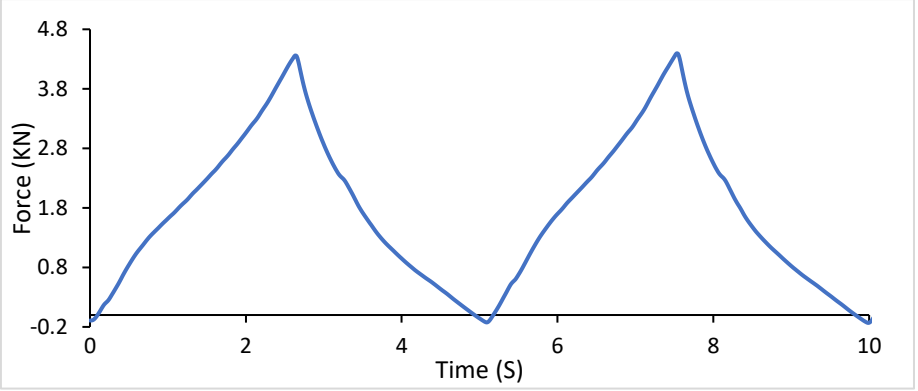

Figure 5.35: Force-time diagram of the harvester under 9 mm/s and Displacement Of 25 mm- 37.88 N/mm spring stiffness

Figure 5.36 is the voltage-time diagram recorded directly from the rectifier. The maximum voltages of loading and unloading are 7.5 V and 8.6 V, respectively. Moreover, the theoretical

peak voltage of this loading scenario (from the motion analysis) is 11.63 V. The average experimental voltage is equal to 8.05V, which is 69% of the theoretical value, indicating the efficiency of the harvester under the current loading scenario.

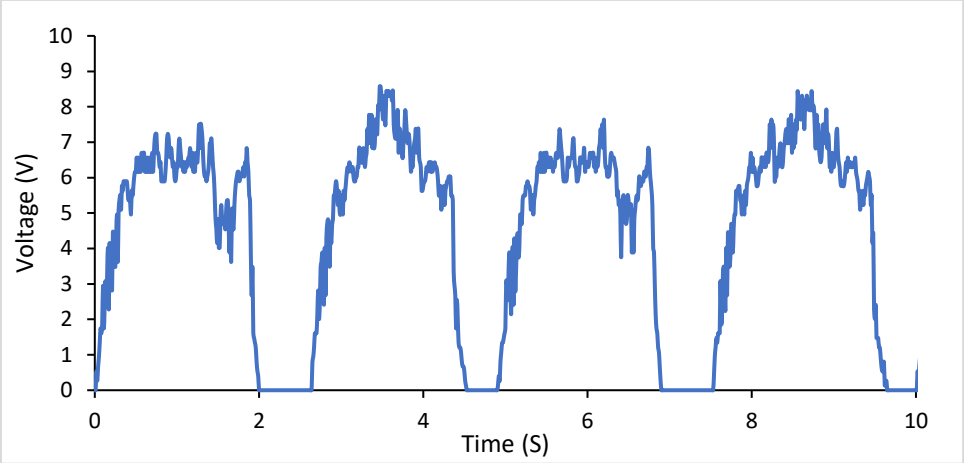

Figure 5.36: Voltage- time of the harvester under loading speed of 9 mm/s and displacement of 25 mm- Spring stiffness 37.88 N/mm

The power time diagram of the harvester under the current mechanical loads is plotted in Figure 5.37.

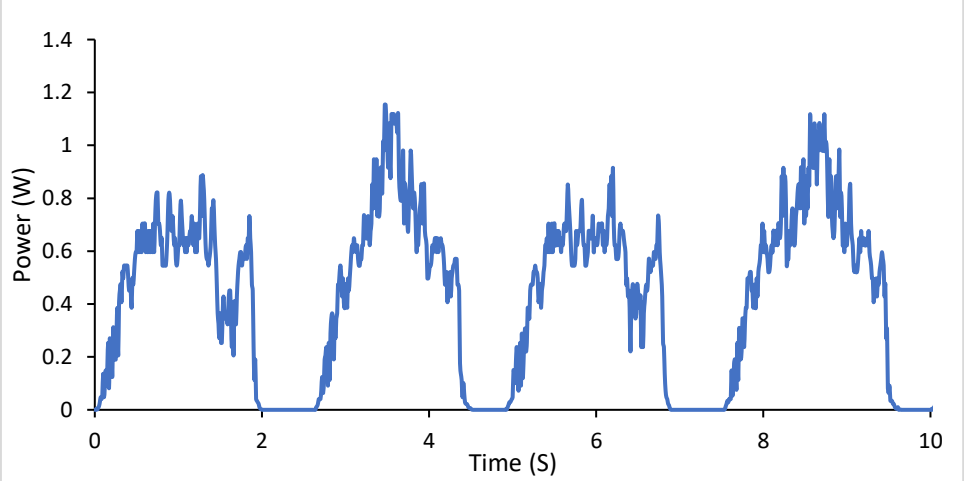

Figure 5.37: Power time diagram of the harvester with the springs' stiffness of 37.88 N/mm, under the loading scenario of 9 mm/s loading speed and 25 mm displacement

According to the diagram, the peak powers in loading and unloading are 0.85 W and 1.15 W, corresponding to the peak voltages of 5.6 V and 6.4 V, respectively. The average power of one cycle of loading and unloading in this loading scenario is 0.45 W.

5.2.3.3 Loading Speed of 13 mm/s and Displacement Of 10 mm

The force-time diagram of the harvester under the mechanical load of 10 mm displacement applied at the loading speed of 13 mm/s is plotted in Figure 5.38. As it can be seen, the two cycles of loading and unloading have identical features of duration and the peak force value of 2.15 KN.

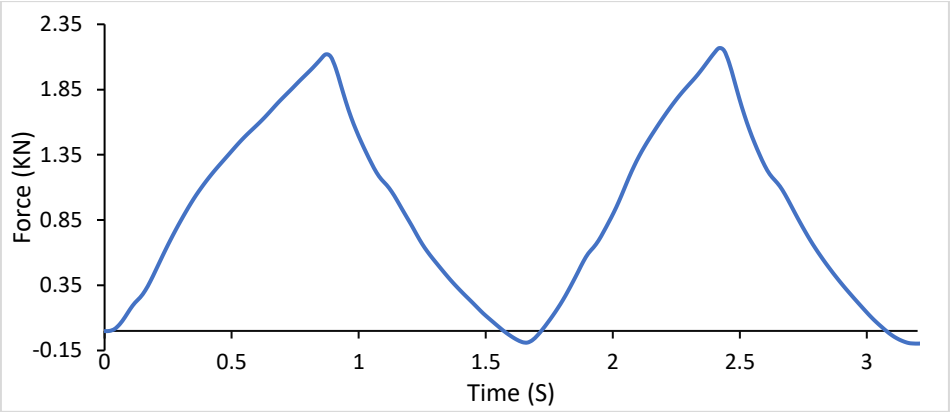

Figure 5.38: Force-time diagram of the harvester under 13 mm/s and Displacement Of 10 mm- 37.88 N/mm spring stiffness

Figure 5.39 shows the voltage-time data of the harvester under this loading scenario, directly logged from the rectifier.

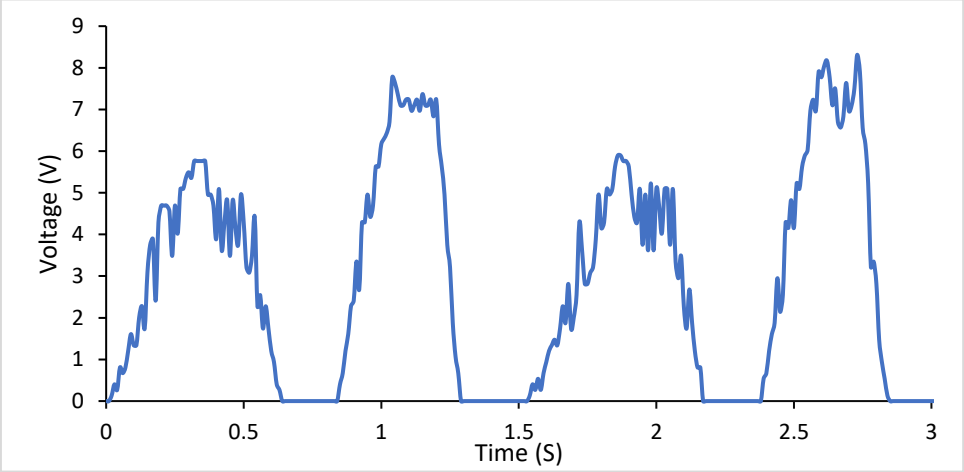

Figure 5.39: Voltage- time of the harvester under loading speed of 13 mm/s and displacement of 10 mm- Spring stiffness 37.88 N/mm

The maximum voltages of loading and unloading are 5.8 V and 8 V. The maximum theoretical voltage, estimated from the motion analysis in this loading scenario, is 20.44 V, generated by

the angular speed of 22.5 rps. The average experimental output voltage is 6.9 V, which is 34%, which implies the system's generation efficiency at this mechanical condition.

The power time diagram of the harvester is plotted in Figure 5.40.

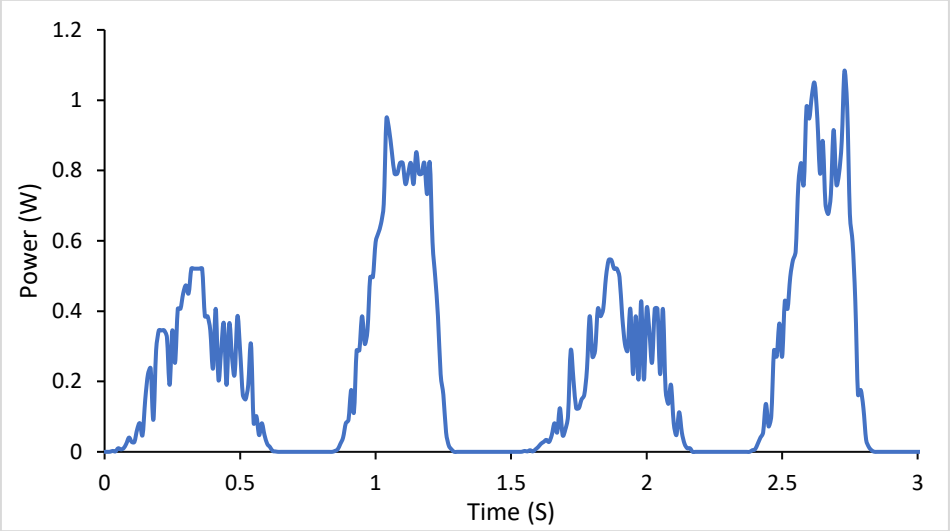

Figure 5.40: Power time diagram of the harvester with the springs' stiffness of 37.88 N/mm, under the loading scenario of 13 mm/s loading speed and 10 mm displacement

The power values maximise at around 0.5 W and 1 W during the loading and unloading periods, equivalent to the peak voltage values of 4.3 V and 6 V, respectively. Moreover, the average power of one loading and unloading cycle is 0.3 W.

5.2.3.4 Loading Speed of 14.67 mm/s and Displacement Of 25 mm

The force-time output of the harvester assembled with the spring set of 37.88 N/mm is illustrated in Figure 5.41. The plotted two cycles are similar in shape, with equal durations and peak values. The maximum force applied in this scenario is 4.23 KN.

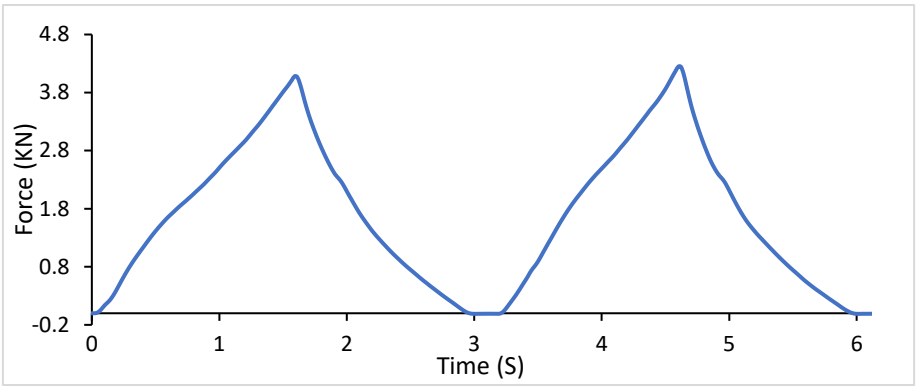

Figure 5.41: Force-time diagram of the harvester under 14.67 mm/s and Displacement Of 25 mm- 37.88 N/mm spring stiffness

Figure 5.42 shows the rectified voltage-time diagram of the harvester tested using the current setup. It can be seen that the loading and unloading curves have the same period and a similar peak voltage of around 11.3 V.

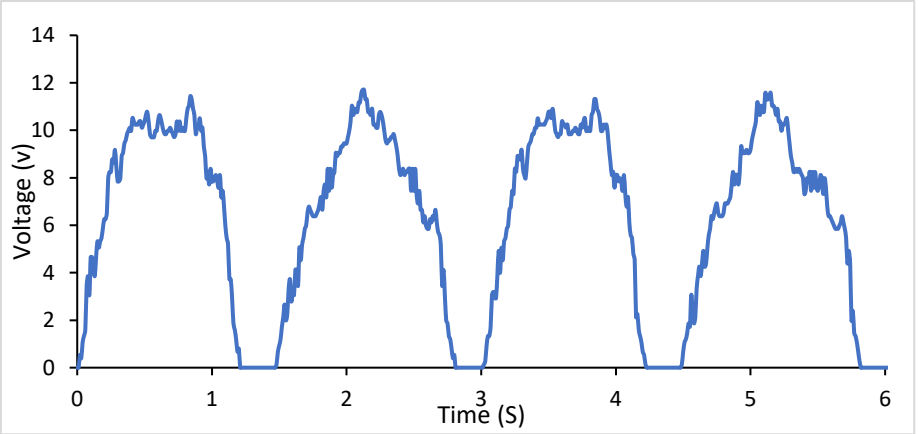

Figure 5.42: Voltage- time of the harvester under loading speed of 14.67 mm/s and displacement of 25 mm- Spring stiffness 37.88 N/mm

Theoretically, it can be estimated that the attainable peak voltage from the harvester under the current testing scenario is 18.7 V, corresponding to the generator's maximum angular speed of 20.6 rps. The experimental peak value (11.3 V) is 60% of the theoretical value, referring to the efficiency of this system under the current loading condition.

Two cycles of power time output of the harvester under this scenario are plotted in Figure 5.43.

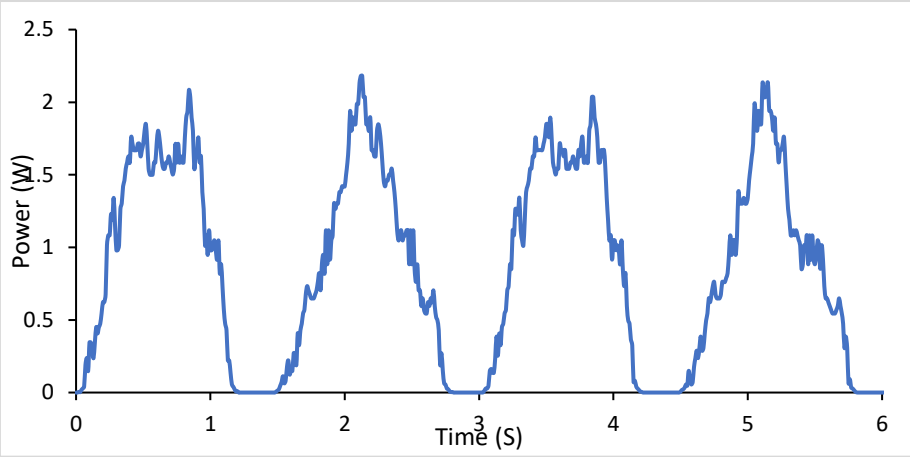

Figure 5.43: Power time diagram of the harvester with the springs' stiffness of 37.88 N/mm, under the loading scenario of 14.67 mm/s loading speed and 25 mm displacement

It can be seen that in this loading setup, pulses of power reach a maximum of 2.2 W, corresponding to the peak voltage of 8.84 V. Moreover, the average output power of the system during one cycle of loading and unloading is 0.94 W.

In the previous sections, the responses of the crank-based road energy harvester incorporating the spring set with the stiffness of 37.88 N/mm are discussed in separate parts for 9 different testing scenarios. As a brief comparison to the previous results from the spring sets with lower stiffness, the average efficiency of the system is higher as the stiffness of the springs increase. Hence, to have a broader investigation, another set of springs with higher stiffness is used to assemble the harvester, which was then tested in various mechanical conditions. The results are presented in the following sections.

5.2.4 Results of Spring Set of 43.54 N/mm

This section presents the results of the experiments on the harvester with the spring set of 43.54 N/mm stiffness. The harvester is tested in the same scenarios as the rest of the experimental plans. First, the optimal external resistor is measured using various resistors installed in the power harvesting circuit. Afterwards, using the optimal resistor, the electrical and mechanical output of the harvester is calculated under different mechanical loads. In the following sections, the results of the optimal resistor and 4 testing scenarios are presented.

Figure 5.44 is the voltage-time diagram around two external resistors tested under 18 mm of displacement and 13 mm/s loading speed. It is observed that the voltage around the resistor (hence the power) depends on the resistance.

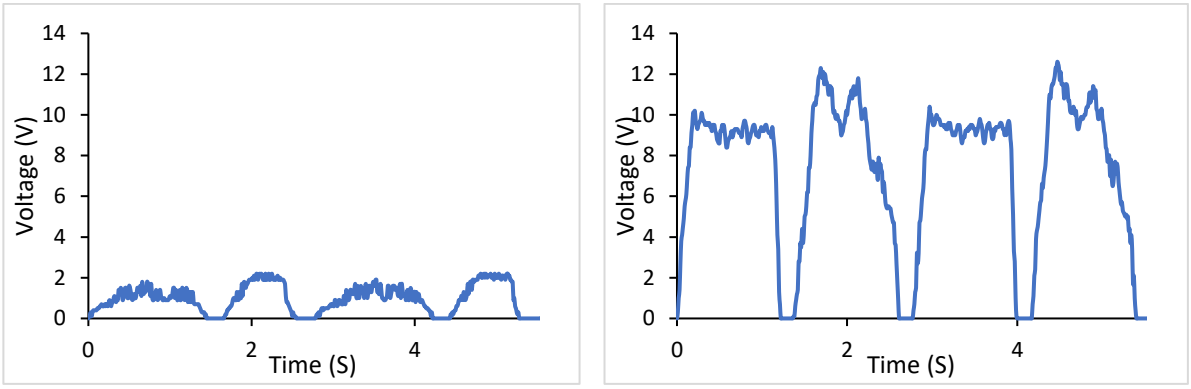

a b

Figure 5.44: Voltage-time diagrams of the harvester with the spring set of 43.54 N/mm, around the resistors of a) 8 ohms, b) 270 ohms

Figure 5.45 shows the average power-resistance diagram for various resistors under a constant mechanical condition. The average was calculated from one cycle of loading and unloading. Similar to the previous sections, the average power maximizes when the resistor of 35.5 ohms is installed in the circuit. Therefore, this resistor is the optimizing one and is employed for the mechanical and electrical evaluation of the system.

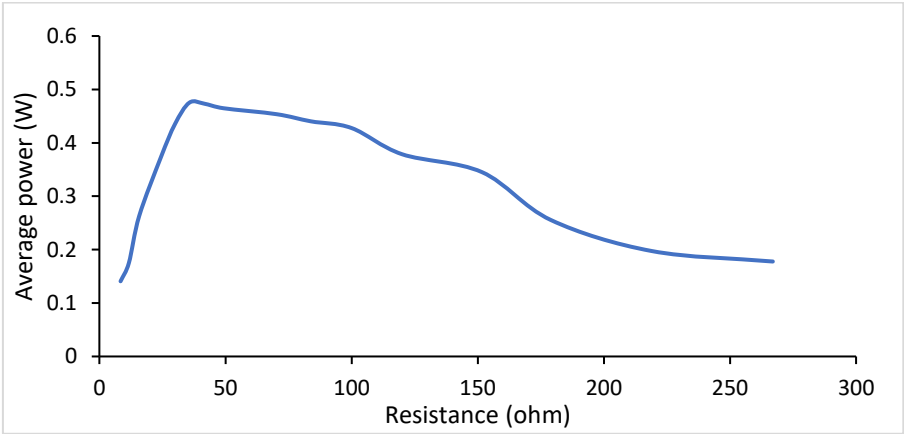

Figure 5.45: Power-resistance diagram- 43.54 N/mm spring stiffness

5.2.4.1 Loading Speed of 3.34 mm/s and Displacement Of 16 mm

The Force time diagram of the harvester with the spring set of 43.54 N/mm is illustrated in Figure 5.46.

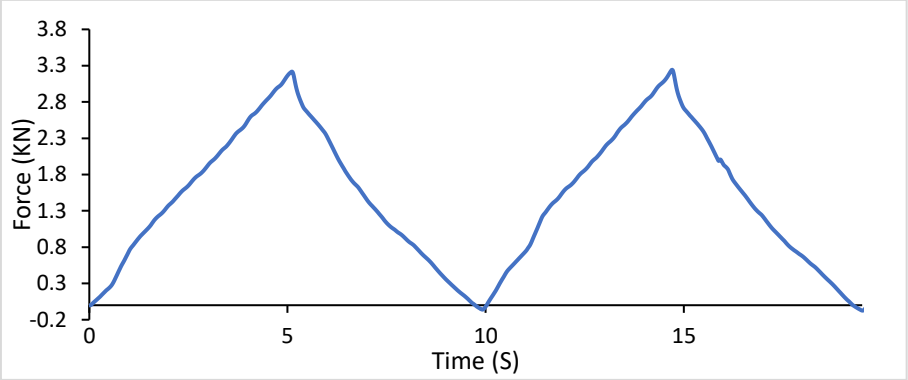

Figure 5.46: Force-time diagram of the harvester under 3.36 mm/s and Displacement Of 16 mm- 43.54 N/mm spring stiffness

According to the diagram, the two cycles occur in equal durations of around 10 seconds, with the same peak force value of 3.12 KN.

Figure 5.47 shows the rectified voltage-time diagram of the harvester, logged directly from the rectifier. According to the diagram, the peak voltages of the harvester in loading and unloading are 3.2 and 4 V, respectively. The difference is caused by the slow loading period, followed by a sharp recovery of the system in unloading.

The maximum achievable theoretical voltage from the harvester in this mechanical loading is 4.8 V. The average peak voltage from the experiment is 3.6 V, equal to 75% of the theoretical estimation, which refers to the efficiency of the system under these applied loads.

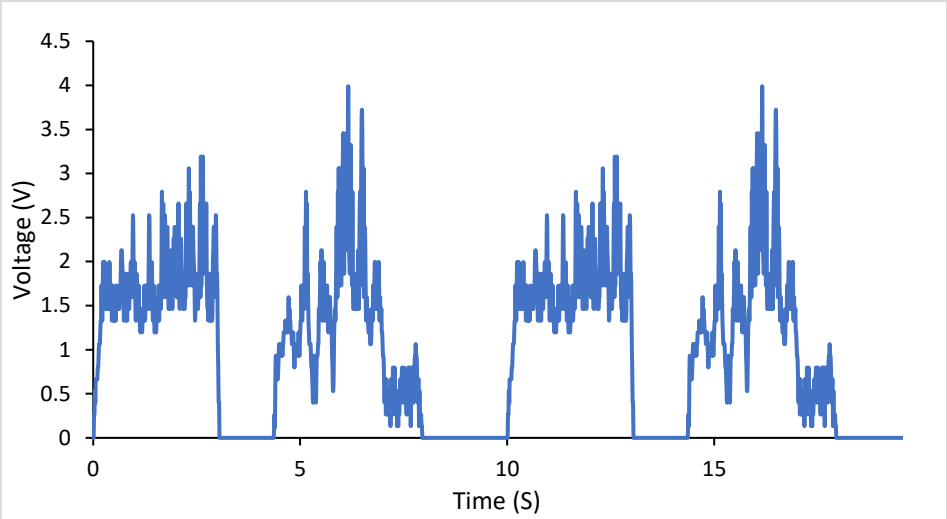

Figure 5.47: Voltage- time of the harvester under loading speed of 3.34 mm/s and displacement of 16 mm- Spring stiffness 43.54 N/mm

Figure 5.48 shows the power time results recorded from the power harvesting diagram, with the resistor of 35.5 ohms (the optimizing resistance).

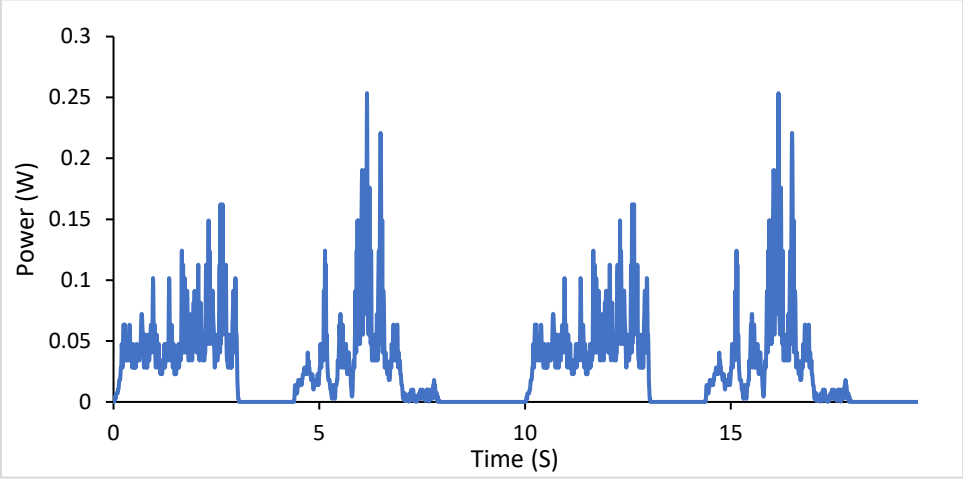

Figure 5.48: Power time diagram of the harvester with the springs' stiffness of 43.54 N/mm, under the loading scenario of 3.34 mm/s loading speed and 16 mm displacement

According to the diagram, the loading and unloading power pulses have different peak values of 0.16 W and 0.26 W, corresponding to 2.4 V and 3 V, respectively. The average power of one cycle of loading and unloading under this mechanical loading is 0.035 W.

5.2.4.2 Loading Speed of 9 mm/s and Displacement Of 25 mm

The force-time diagram of the harvester is plotted in Figure 5.49. The cycles have equal durations of loading and unloading and equal peak forces of 5 seconds and 4.6 KN, respectively.

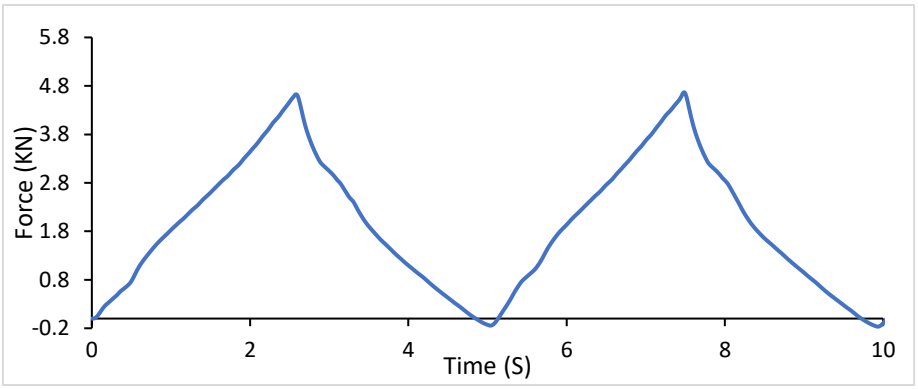

Figure 5.49: Force-time diagram of the harvester under 9 mm/s and Displacement Of 25 mm- 43.54 N/mm spring stiffness

Figure 5.50 shows the voltage-time diagram of the harvester at this testing set up, logged directly from the rectifier. It can be seen that the loading and unloading maximum voltages and the durations are close to each other, almost equal to 8 V and 2.5 seconds, respectively. In theory, in this testing scenario, the harvester is capable of generating a maximum voltage of 11.63 V. Comparing these two voltages, the experimental peak voltage is 69% of the theoretical estimation, which refers to the efficiency of the system under this loading set-up.

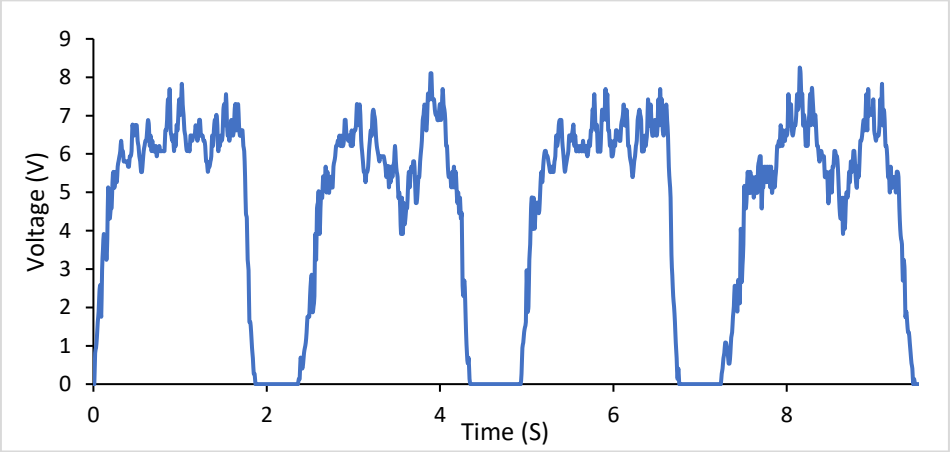

Figure 5.50: Voltage- time of the harvester under loading speed of 9 mm/s and displacement of 25 mm- Spring stiffness 43.54 N/mm

Figure 5.51 is the power output of the system, logged from the power harvesting circuit. It can be observed that the maximum power pulse is around 1 W and is almost equal in loading and unloading curves. Moreover, the average power output in this testing scenario is 0.46 W.

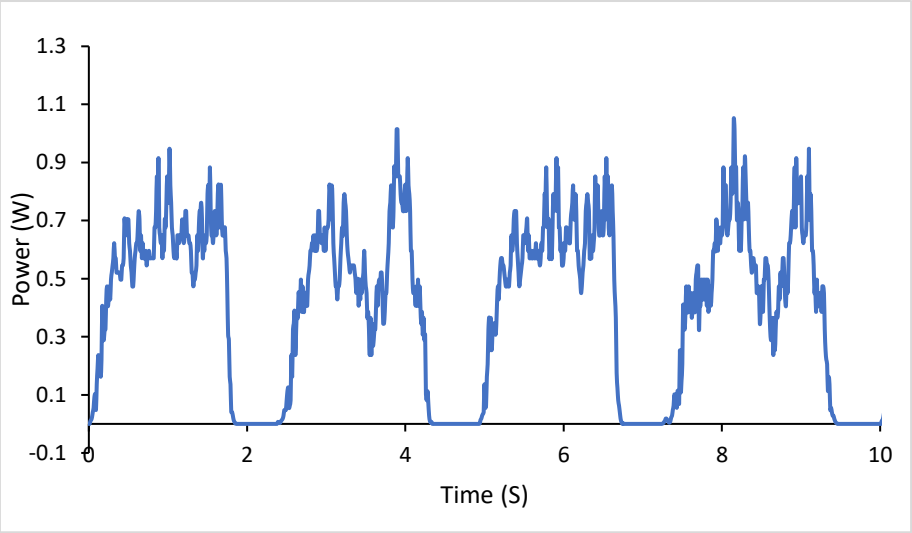

Figure 5.51: Power time diagram of the harvester with the springs' stiffness of 43.54 N/mm, under the loading scenario of 9 mm/s loading speed and 25 mm displacement

5.2.4.3 Loading Speed of 13 mm/s and Displacement Of 10 mm

The force-time diagram of the harvester under the testing scenario of 13 mm/s loading speed and 10 mm displacement is plotted in Figure 5.52.

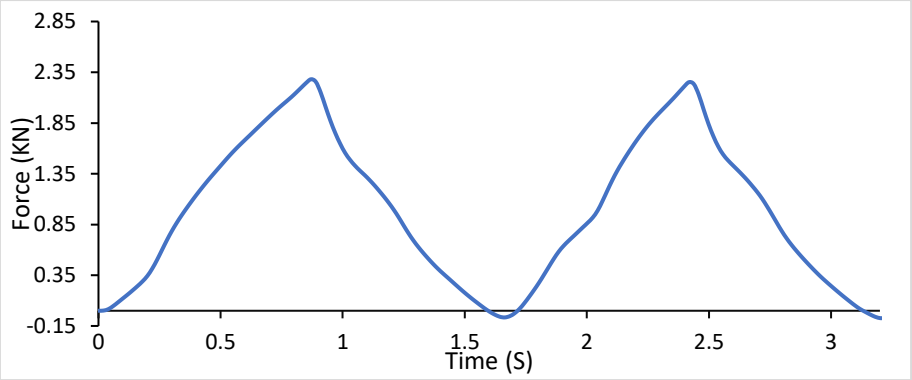

Figure 5.52: Force-time diagram of the harvester under 13 mm/s and Displacement Of 10 mm- 43.54 N/mm spring stiffness

Two cycles are consistent, taking place over an equal time duration of around 1.54 seconds, and have a peak force of 2.26 KN.

Figure 5.53 shows the voltage-time diagram of the harvester, logged directly from the rectifier. It can be seen that the peak voltages of loading and unloading are slightly different, equal to 8.2 V and 5.56 V, respectively. Hence, the average maximum voltage is 7.19 V.

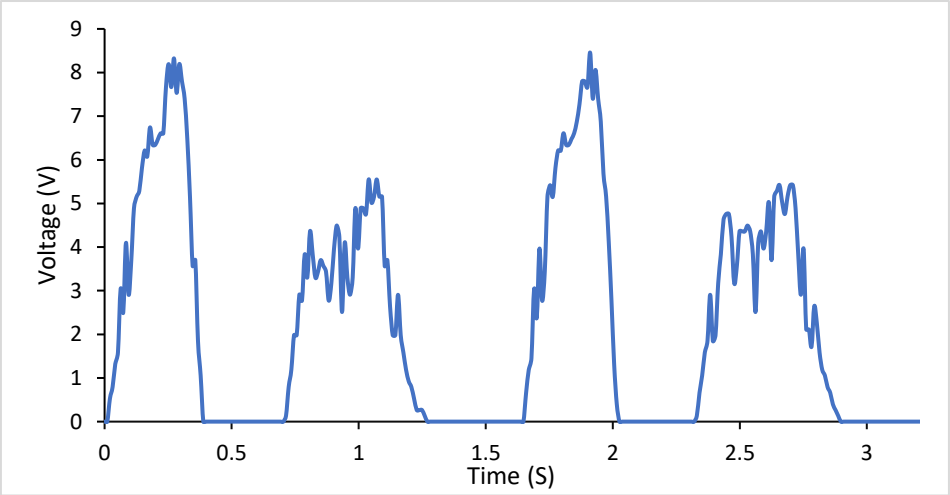

Figure 5.53: Voltage- time of the harvester under loading speed of 13 mm/s and displacement of 10 mm- Spring stiffness 43.54 N/mm

However, the theoretical maximum voltage estimated from the motion analysis is 20.44 V in this loading scenario. The obtained experimental voltage is 35% of the theoretical peak voltage, which indicates the efficiency of the harvester under this loading scenario.

Figure 5.54 is the power time diagram of the system, logged from the power harvesting circuit.

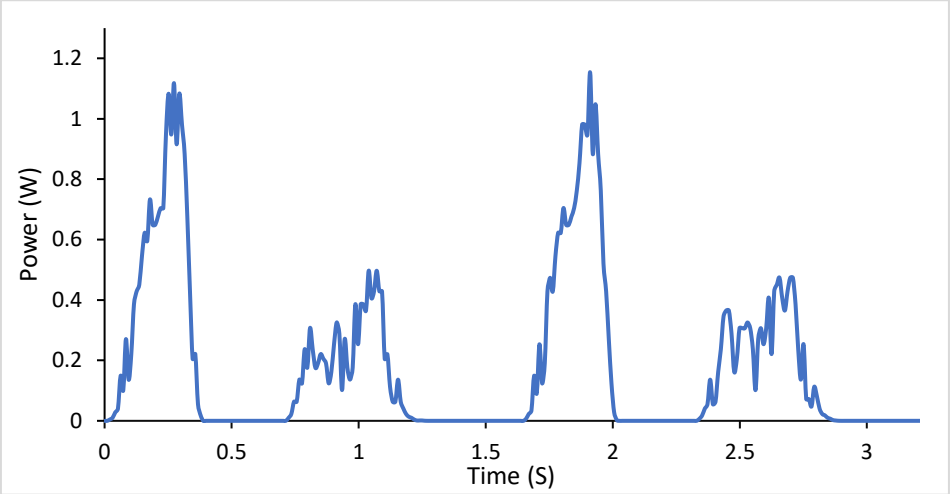

Figure 5.54: Power time diagram of the harvester with the springs' stiffness of 43.54 N/mm, under the loading scenario of 13 mm/s loading speed and 10 mm displacement

The maximum power values reach 1.12 W and 0.5 W in loading and unloading, equivalent to the peak voltages of 6.2 and 4.3 V, respectively. Moreover, the average voltage of one loading and unloading cycle at the current testing scenario is 0.23 W.

5.2.4.4 Loading Speed of 14.67 mm/s and Displacement of 25 mm

The force-time diagram of the harvester under the testing scenario of 25 mm displacement and 14.67 mm/s loading speed is plotted in Figure 5.55. The diagram shows two cycles of loading and unloading that have an equal duration of 3.15 seconds and equal peak force magnitudes of 4.44 KN.

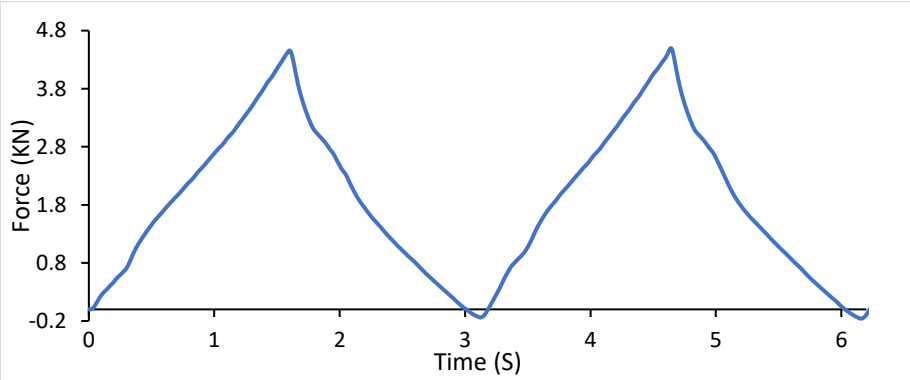

Figure 5.55: Force-time diagram of the harvester under 14.67 mm/s and Displacement Of 25 mm-43.54 N/mm spring stiffness

The voltage-time diagram of the harvester under this testing scenario logged directly from the rectifier is plotted in Figure 5.56. The diagram shows that the peak voltages obtained from loading and unloading are the same and equal to 10.3 V. According to motion analysis, the theoretical voltage achieved from this scenario can have a maximum of 18.71 V. Comparing these two voltages, the maximum experimental voltage is 55% of the theoretical value, indicating the harvester's efficiency under this mechanical loads.

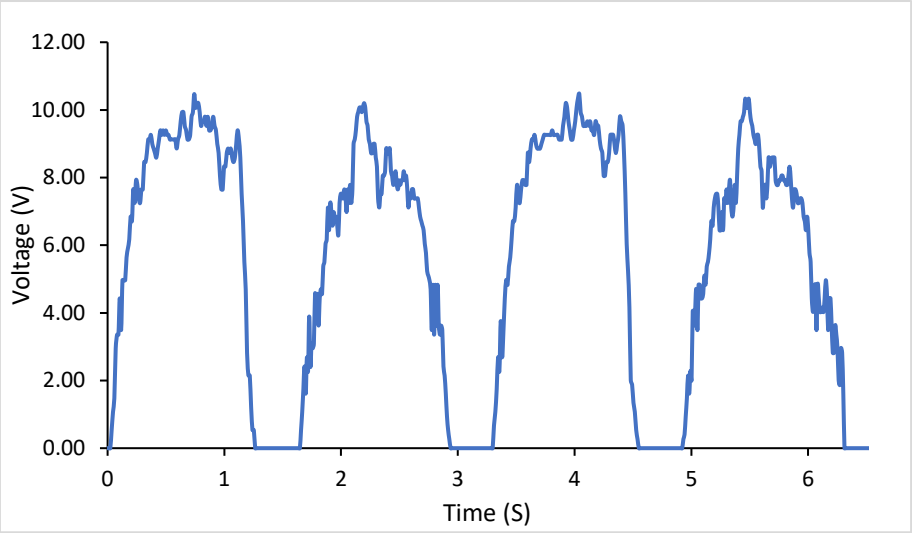

Figure 5.56: Voltage- time of the harvester under loading speed of 14.67 mm/s and displacement of 25 mm- Spring stiffness 43.54 N/mm

Figure 5.57 is the power time diagram of the harvester under the current testing scenario. The power pulses reach a maximum value of 1.7 W, corresponding to the peak voltage of 7.6 V. Moreover, the average power of one loading and unloading is 0.76 W.

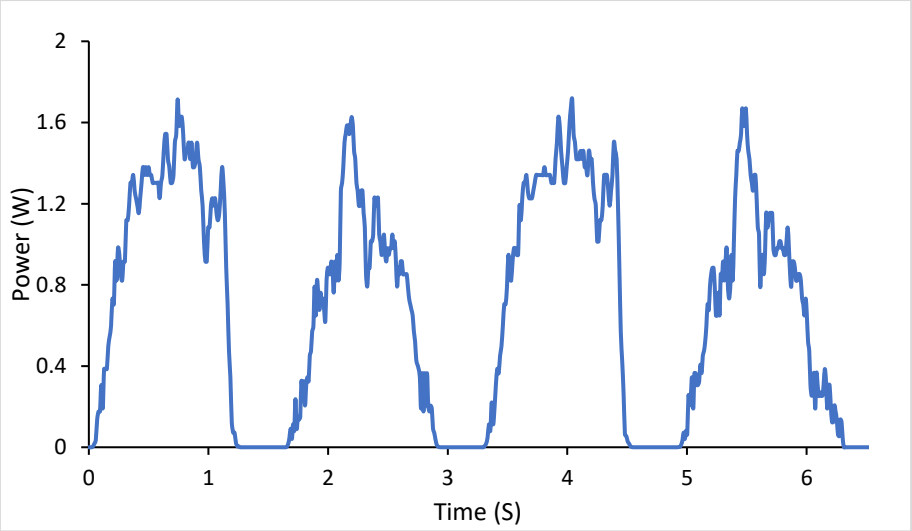

Figure 5.57: Power time diagram of the harvester with the springs' stiffness of 43.54 N/mm, under the loading scenario of 14.67 mm/s loading speed and 25 mm displacement

Previously, the mechanical and electrical output of the crank-based harvester under different loading scenarios of the combination of loading speed and displacement were presented.

In the following section, the mechanical and electrical results of maximum force, the average output power, the peak power, and the system's efficiency obtained from different spring sets and scenarios are compared with each other.

5.3 Comparison of the Mechanical and Electrical Results

In the following parts, comparisons are made on the different results achieved from the harvester with different springs.

5.3.1 Maximum Applied Load

The maximum applied load is an essential function in this study, as it indicates the harvester's performance in terms of the mechanical loads applied on it. Since the harvester is designed within the concept of speed bumps, or road rumbles, the mechanical loads are directly a function of the type and speed of the passing cars. Therefore, to understand the behaviour of the harvester in the real application, this parameter has to be discussed. Figure 5.58 shows the contour diagrams of maximum load applied on the top plate of the harvester, in terms of the loading speed and displacement, for different sets of springs.

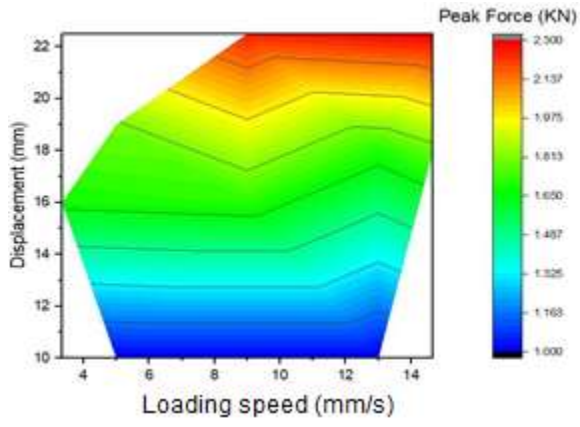

a

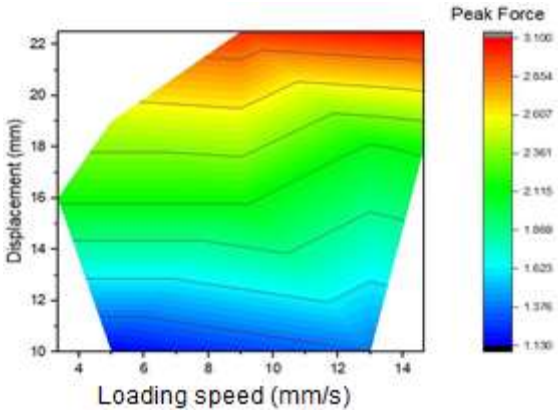

b

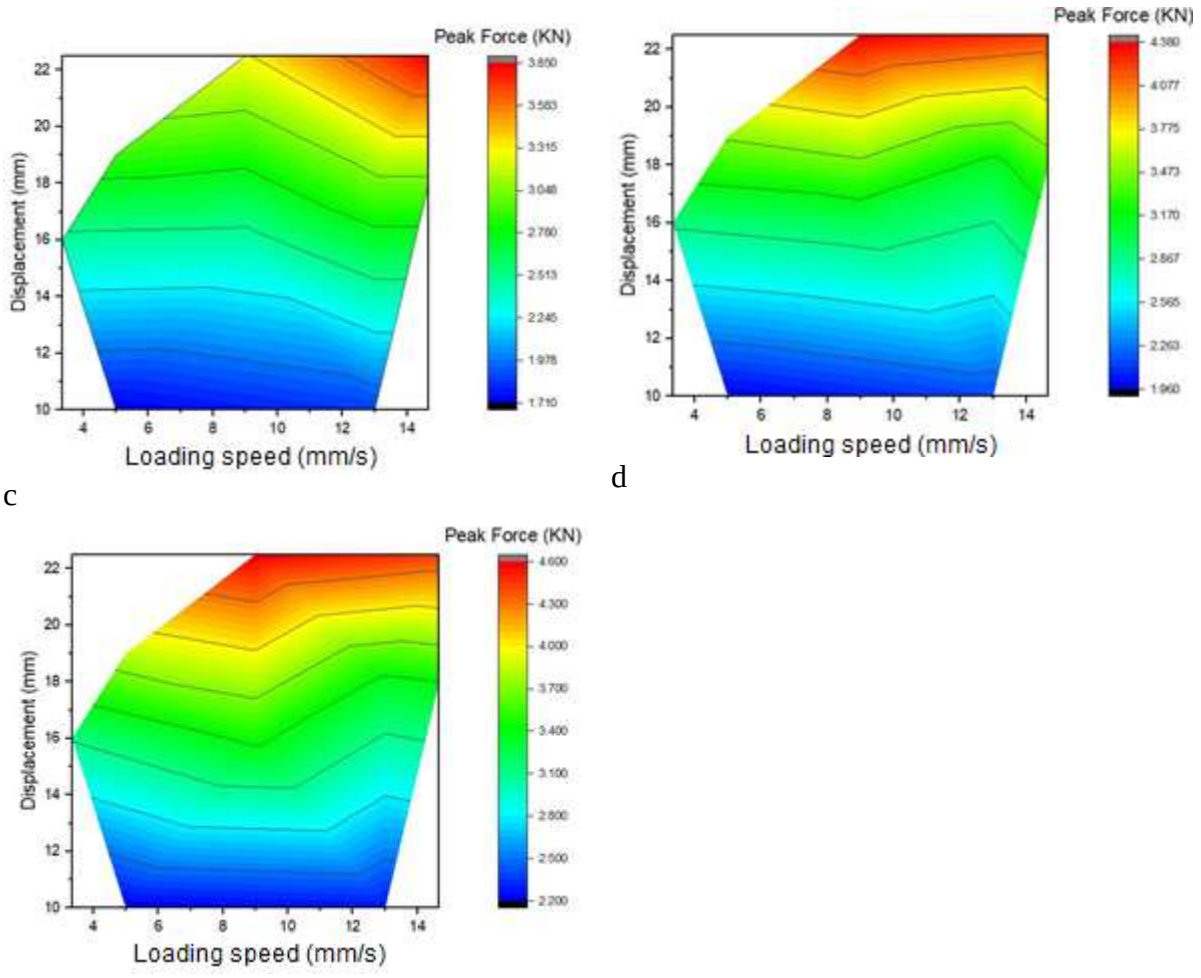

Figure 5.58: Contour diagram of the peak force applied on the harvester with the spring set of a) 19.12 N/mm, b) 25.2 N/mm, c) 29.8 N/mm, d) 37.88 N/mm and e) 43.54 N/mm

It is observed that by increasing the spring stiffness, the maximum applied force also increases. The highest applied force is equal to 4.6 KN, which is applied on the harvester with the spring set of 43.54 N/mm stiffness when the maximum displacement is equal to 25 mm. The lowest applied load is 1 KN, applied on the harvester with the spring set of 19.12 N/mm when the maximum displacement is 10 mm. In all cases, comparing the two independent variables, the factor of displacement magnitude affects the response (peak force) stronger than the loading speed. It is observed that in all the diagrams, in a constant displacement, increasing the loading speed has a minimal effect on the peak force magnitude, while in a constant speed, increasing the displacement increases the peak force significantly.

As the peak applied force ranges between 1 KN to 4.6 KN, depending on the utilised spring stiffness, it can be concluded that this harvester is compatible with various types of urban vehicles having different curb weights. Table 5.3 summarises the average weight of a few urban cars. It is worth noting that this harvester has compact dimensions and is designed such that the vehicle's load is applied by one tyre at a time. The load on the harvester is calculated assuming all the forces from the wheel's weight share is applied on the harvester's cap. Hence the applied load is caused by one-fourth of the car's weight in each passing incident. According to Table 5.3, each vehicle's loads applied on the harvester are in the range of the peak forces applied in the experiments. However, from the employed spring stiffnesses, 38.77 N/mm and 43.54 N/mm are more suitable for these cars. The rest of the springs are more suitable for lighter types of vehicles, such as motorbikes. In other words, the harvester can be tailormade, depending on the average weight of the vehicle passing from the lane in which the harvester is installed.

Table 5.3: Average mass of some regular cars and their corresponding load applied on the harvester [140]

Vehicle	Average mass (Kg)	Load on the harvester (KN)
Suzuki Motor Corporation	1000	2.45
Automobile Dacia SA	1150	2.82
Renault SAS	1350	3.31
Volkswagen AG	1450	3.6
Audi AG	1550	3.8

5.3.2 Average Output Power

Another set of results worth comparing is the average electrical power obtained from each testing scenario and set of springs. Average power indicates the system's electrical performance, under loading and unloading cyclic loads applied by passing cars, giving an understanding of how much electrical power can be expected on average from this harvester. In addition, as the

maximum power and voltage are affected by both loading speed and displacement, taking an average of the output is helpful to understand the overall performance of the harvester.

Figure 5.59 shows the contour diagram of the average power obtained from each testing scenario for different spring stiffnesses. In these diagrams, the average power from each scenario is the total output of the generator from its two pairs of outputs. Hence, the values are double the average power values presented in the previous sections.

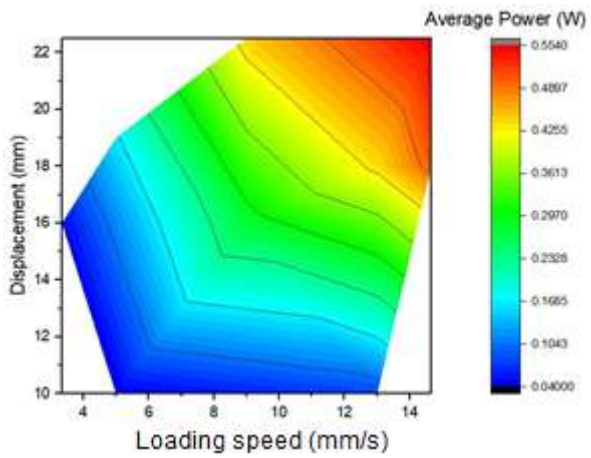

a

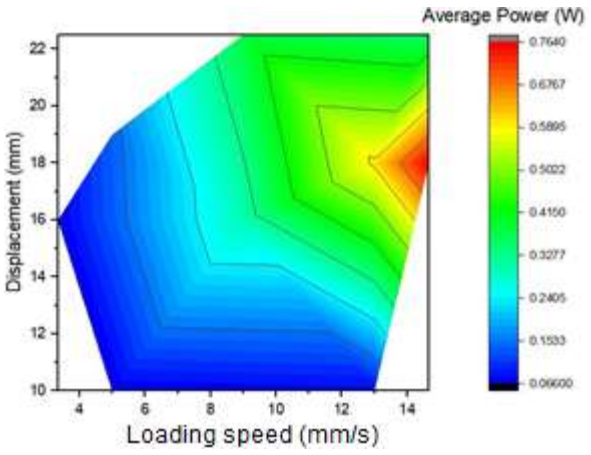

b

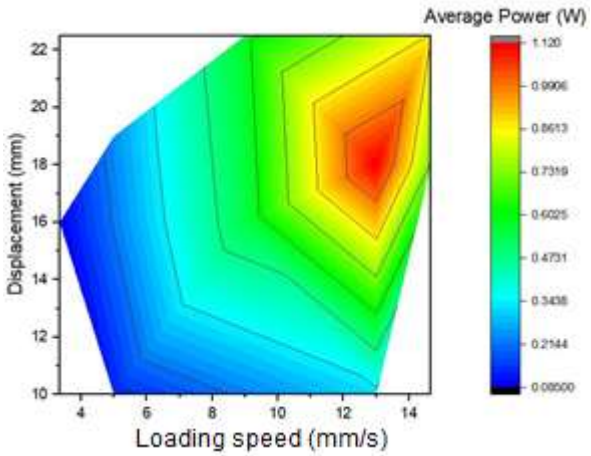

c

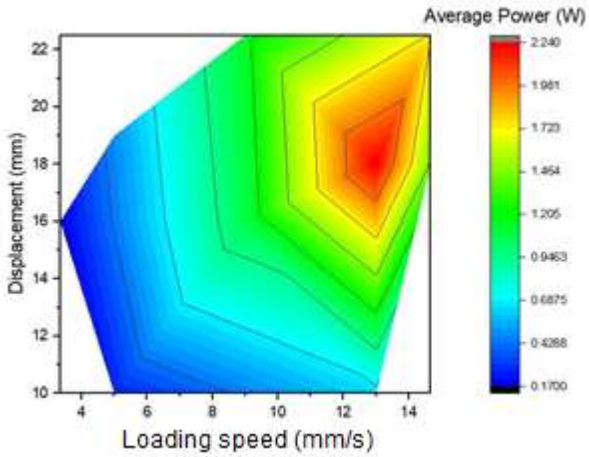

d

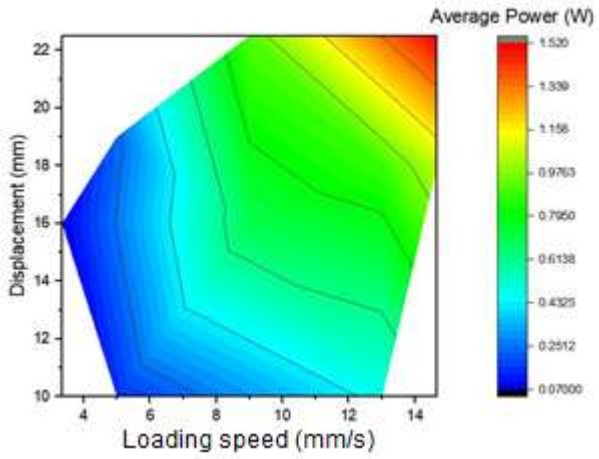

e

Figure 5.59: Contour diagram of the average power achieved from the harvester with the spring set of a) 19.12 N/mm, b) 25.2 N/mm, c) 29.8 N/mm, d) 37.88 N/mm and e) 43.54 N/mm

According to the contour diagrams, the average power maximises when the loading speed and displacement are maximum or close to maximum. Moreover, to compare the maximum voltages obtained from each spring stiffness, Figure 5.60 is plotted.

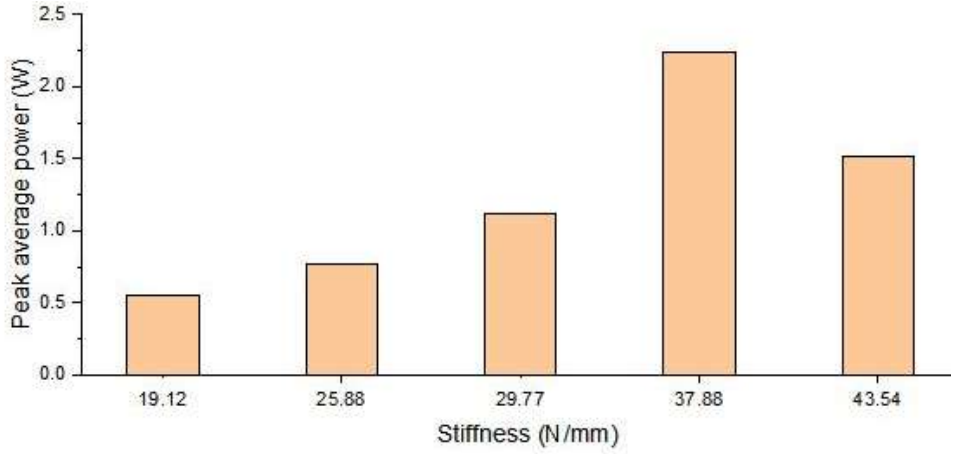

Figure 5.60: Peak average power achieved from each spring stiffness

It can be seen that the average power obtained from the harvester increases by increasing the spring stiffness. Among the tested springs, the peak average power recorded from the spring sets of 37.88 N/mm and 43.54 N/mm are higher than the values obtained from the spring sets of 19.12, 25.88 and 29.77 N/mm. The observations are in agreement with the previous findings [16], [21], [67], [68], [136].

5.3.3 Maximum Output Power

Maximum output power is obtained from the highest pulse of voltage around the external resistor, and unlike the average power, it does not depend on the output of both unloading and unloading. Nevertheless, it is essential to study, as it indicates the highest potential of the harvester in each case and shows in which scenario the maximum voltage and power have occurred. Figure 5.61 shows the contour diagram of the maximum power in terms of loading speed, displacement, and different spring stiffnesses.

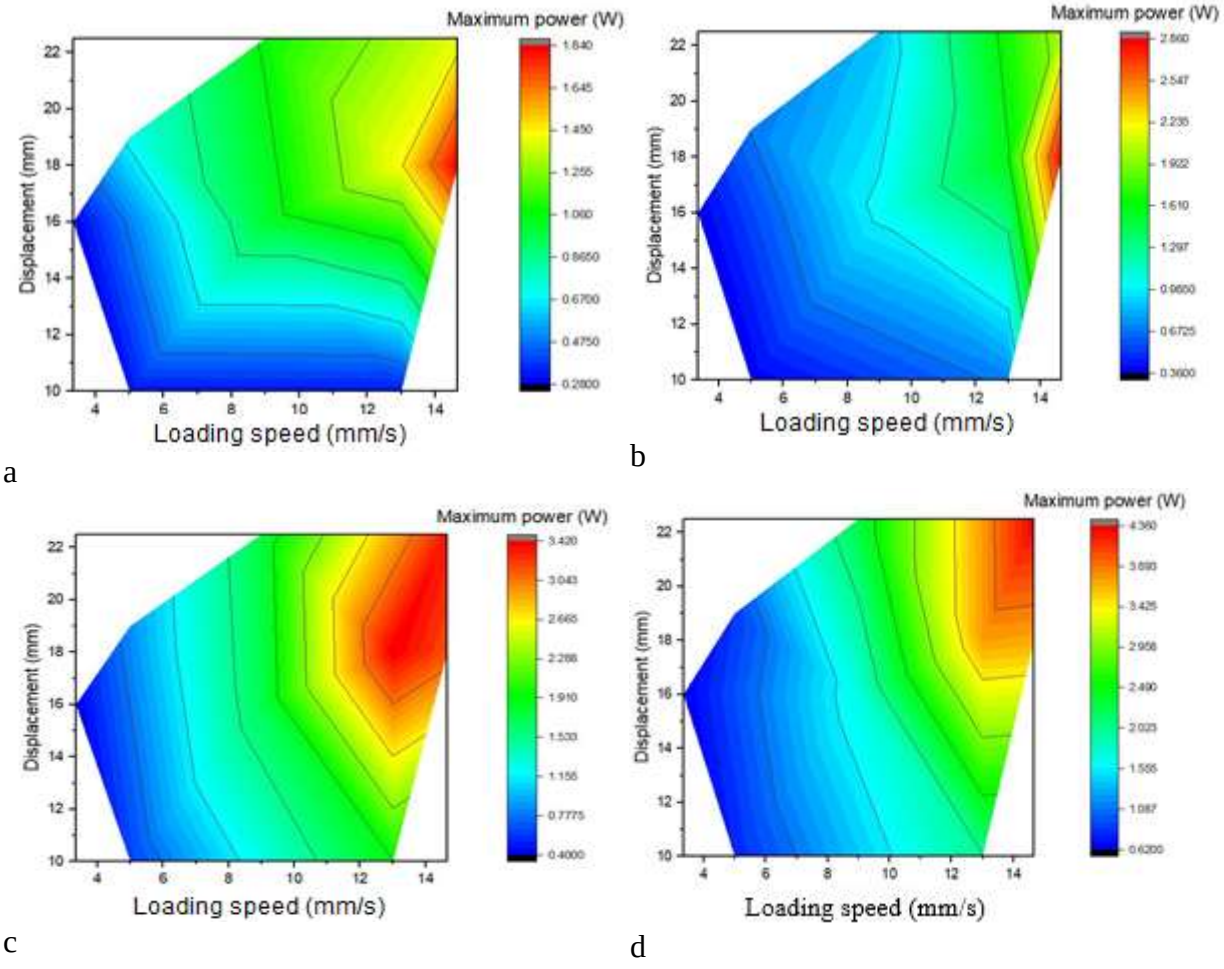

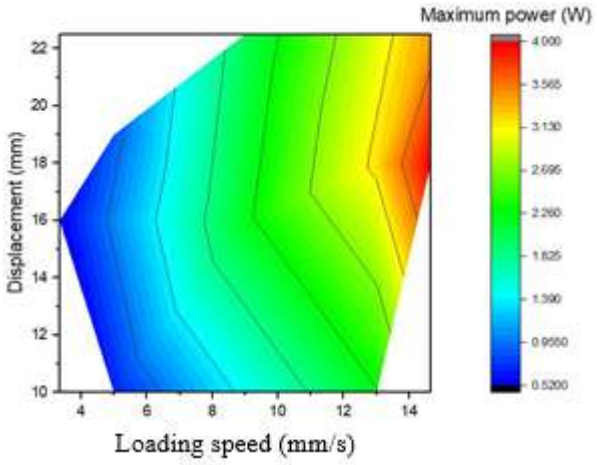

e

Figure 5.61: Contour diagram of the maximum power achieved from the harvester with the spring set of a) 19.12 N/mm, b) 25.2 N/mm, c) 29.8 N/mm, d) 37.88 N/mm, and e) 43.54 N/mm

In all cases, the maximum power is the highest when the loading speed is maximum and the displacement is above average (16 mm). The highest output power among all the scenarios and spring stiffness equals 4.36 W achieved when the harvester has the springs with the stiffness of 38.77 N/mm, the loading speed is 14.67 (maximum), and the displacement is 25 mm (maximum).

Figure 5.62 is plotted to show the maximum output powers achieved from each set of spring stiffness. It can be seen that the spring sets of 43.54 and 37.88 N/mm have given the highest peak power values among all the tested spring sets.

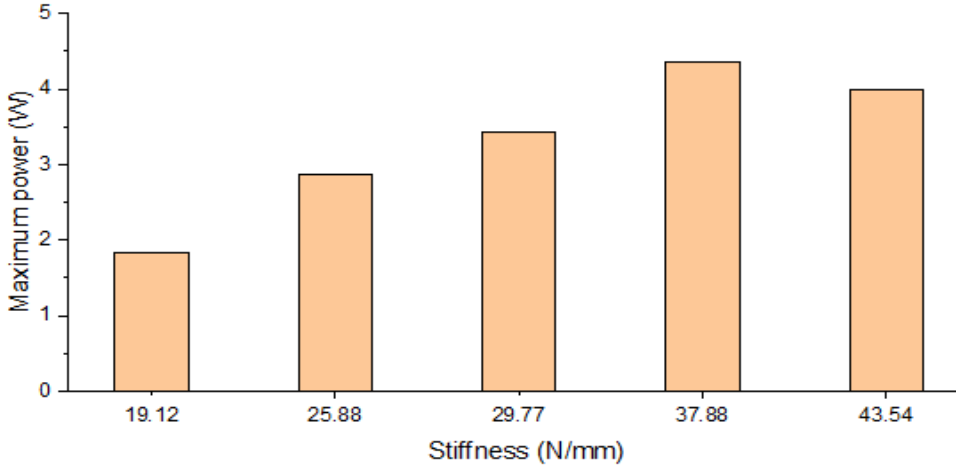

Figure 5.62: Maximum power achieved from each spring stiffness

These observations are also consistent with the previous findings of [16], [21], [68], [141].

5.3.4 Generation Efficiency of The Harvester

The generation efficiency of the harvester (also referred to as “efficiency”) is defined as a comparison of the theoretical and experimental voltage output. First, the theoretical maximum voltage is calculated and compared to the maximum experimental voltage obtained at each condition. Then, the percentage of the experimental output respecting the theoretical peak is calculated and indicated as the generation’s efficiency. It is essential to study this variable to understand how much energy is dissipated in the mechanism and in which scenario the loss is significant. Furthermore, as observed before, the generation’s efficiency also depends on the testing scenario. Hence, contour diagrams of efficiency are plotted in Figure 5.63 regarding the loading speed and displacement for each spring stiffness.

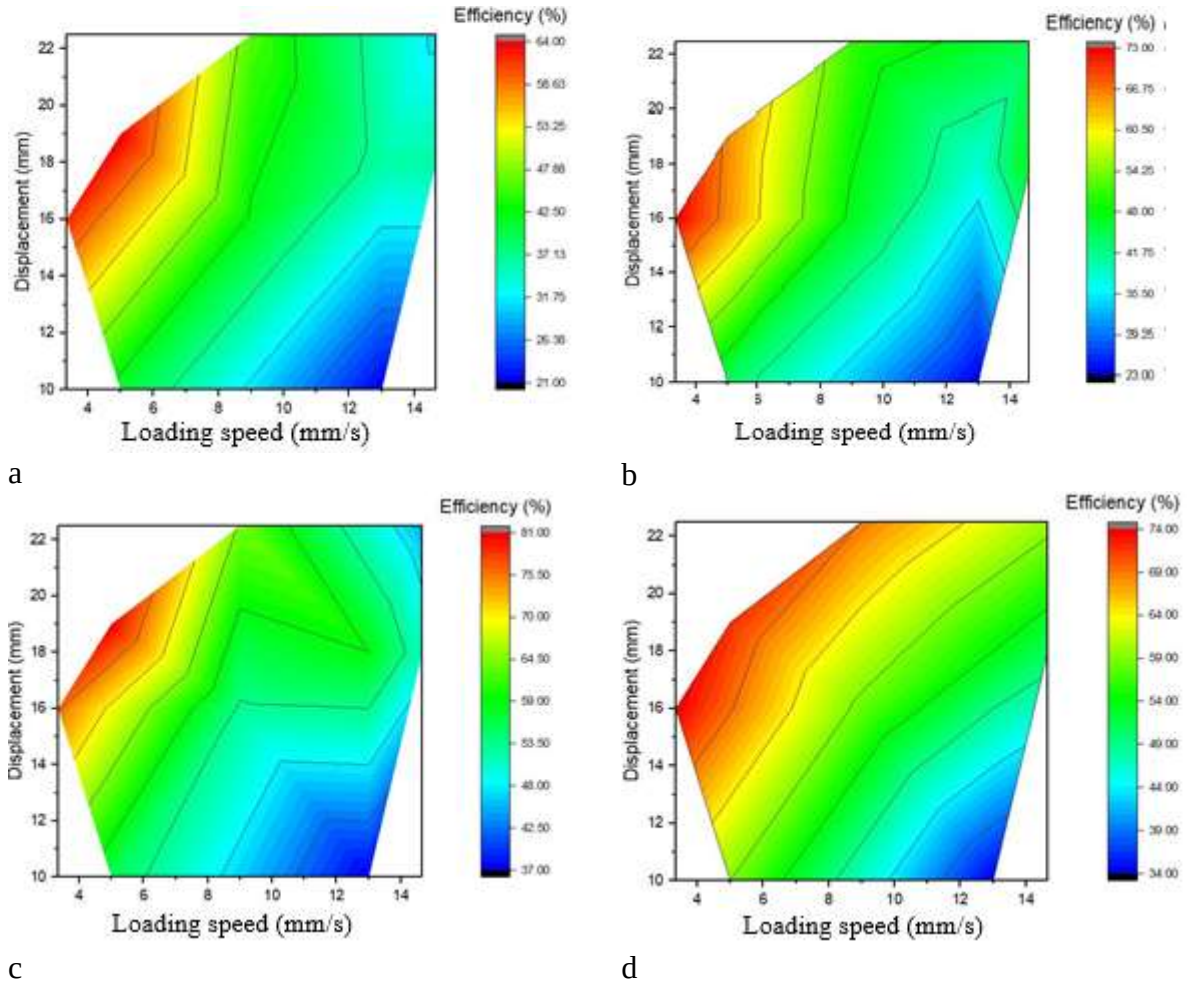

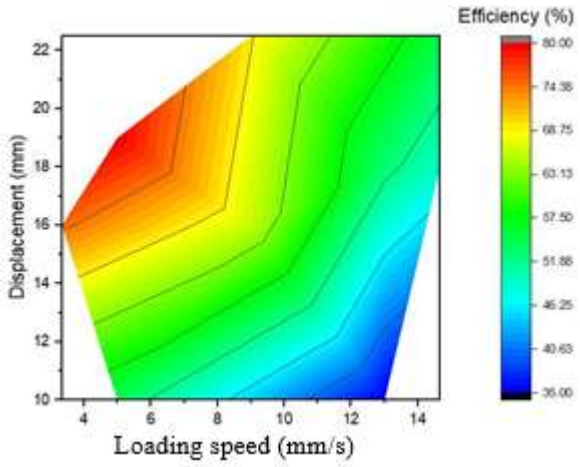

e

Figure 5.63: Contour diagram of the efficiency of the harvester with the spring set of a) 19.12 N/mm, b) 25.2 N/mm, c) 29.8 N/mm, d) 37.88 N/mm, and e) 43.54 N/mm

According to Figure 5.63, regardless of the spring stiffness, the efficiency maximizes when the loading speed is low (around 5 to 8 mm/s). On the other hand, the efficiency is minimum when the loading speed is maximum and the displacement is minimum. The efficiency varies between 40 to 70% in the middle scenarios, depending on the harvester's spring stiffness. It is worth noting that by increasing the stiffness, the efficiency of the harvester in each scenario increases. Hence, the spring stiffnesses suitable for urban roads under the regular passenger cars (37.88 N/mm and 43.54 N/mm) are more efficient than those with lower spring stiffness. Figure 5.64 shows the column chart of the maximum efficiency achieved for each stiffness.

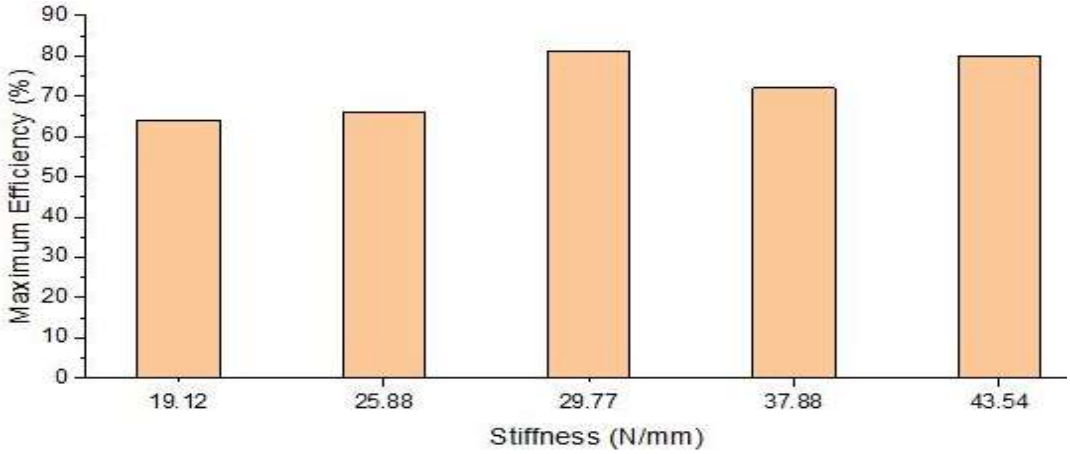

Figure 5.64: Maximum efficiency achieved from each spring stiffness

Since the patterns are the same, another contour diagram is plotted in Figure 5.65, showing the average efficiency of all the harvester's stiffnesses for each testing scenario.

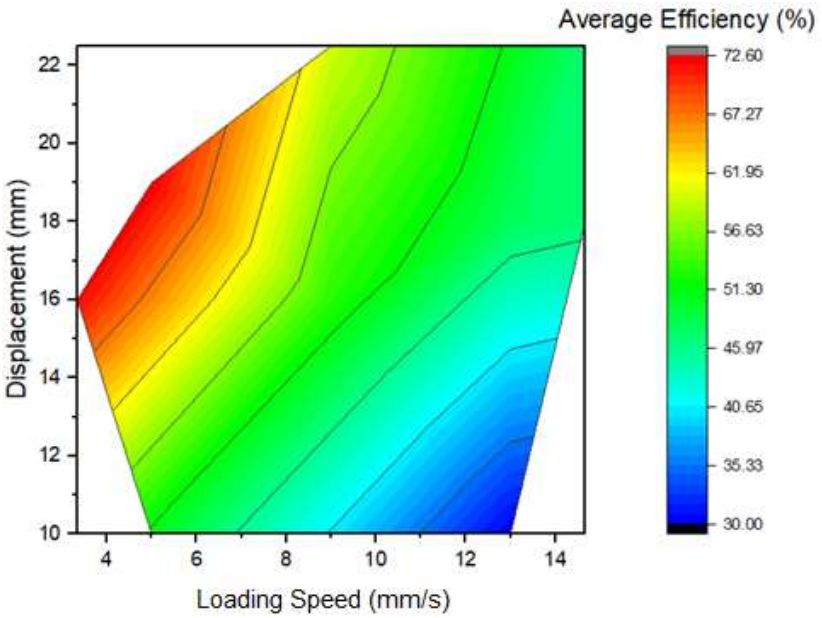

Figure 5.65: Average efficiency obtained from each scenario

According to Figure 5.65, the average efficiency of the harvester at high loading speeds and displacements is around 51.30%. It can be reasoned that when the harvester is in a real application, with the loads are applied from the vehicles passing at various speeds, the energy generation efficiency of the harvester is around 51.3%. A similar observation was made in a previous study [141].

5.3.5 Applications of the Crank-Based Road Harvester

As discussed, this harvester is designed as a road rumble or smooth speed bump to generate sustainable energy for low-power devices of smart cities, such as the sensors and IoT. Having a maximum displacement of 25 mm fulfils this target. In addition, the load-bearing capacity of this harvester can be altered by changing the stiffness of the supporting springs and adjusting the maximum force applied by the vehicles in a travel lane. Hence, the installation location of this harvester is versatile, from biking lanes to highways.

Figure 5.66 illustrates the harvester illuminating two LED bulbs upon loading and unloading. The loading condition for this illustration is 18 mm displacement, 14.67 mm/s loading speed, and the spring stiffness is 25.77 N/mm. The LED bulbs have a power rating of 2 W and a voltage rating of 12 V. This illustration shows the competence of the harvester to fulfil the targets of the study.

a b

Figure 5.66: Light bulb illumination- 18 mm displacement and 14.67 mm/s loading speed- spring stiffness 25.2 N/mm

In the following section, the main concluding points that summarize this chapter are listed.

5.4 Conclusions

This chapter tests the performance of the crank-based energy harvester with various springs sets (different stiffnesses) under various mechanical loads. The performance is evaluated based on the maximum applied force, average power, peak power, and efficiency. In this section, a summary of the discussions is brought.

1. The maximum force applied on the harvester depends on the stiffness of the unit and, in particular, the stiffness of the springs supporting it. As the spring stiffnesses increase, the maximum force to induce a certain displacement also increases. Moreover, it was observed that the loading speed plays a minor role in the magnitude of the peak load as opposed to the

significant role of the displacement magnitude. The highest load carried by the harvester was 4.6 KN, which was applied at the displacement of 25 mm and the loading speed of 14.67 mm/s. The other significant loads are 4.3 KN and 3.8 KN, applied at the same loading scenario, on the harvester with the spring stiffnesses of 37.88 N/mm and 29.77 N/mm, respectively. Considering the dimensions of the harvester, the peak loads represent one-fourth of a passing car (one wheel). According to Table 4, these maximum loads are almost equal to one-fourth of the forces applied by the weight of an average Renault SAS, Volkswagen AG, or Audi AG car. Moreover, since the maximum forces of the other sets of springs are lower, it can be deduced that the current harvester can be tailormade and adjusted to its installation location. The lower stiffness springs can be used for biking lanes and even pedestrians.

2. The factor of average power is the average of the output power pulses generated in one cycle under each mechanical loading condition, and it provides an overall understanding of the generation capacity of the harvester system. It was observed that the average output power depended on the testing scenario and the spring stiffness of the system. In most cases, the average power is the highest when the loading speed is 13 mm/s, and the displacement is 18 mm. However, when the spring stiffness was 19.12 N/mm and 43.54 N/mm, the average power maximised at 25 mm displacement and 14.67 mm/s. The average power has an overall peak of 2.46 W when the displacement is 18 mm, and the loading speed is 13 mm/s, from the harvester with the spring stiffness of 37.88 N/mm. The rest of the peaks are 0.55 W, 0.76 W, 1.12 W, 1.54 W, for the spring stiffnesses of 19.12 N/mm, 25.77 N/mm, 29.77 N/mm and 43.54 N/mm, respectively.

3. Peak power is the highest power pulse achieved from the harvester, and it is worth investigating as it indicates the maximum capability of the harvester in terms of power. Similar to the average power, maximum power is also a function of loading speed, displacement, and spring stiffness. The recorded power pulse is from the harvester is equal to 4.36 W, obtained under the loading speed of 14.67 mm/s and the displacement of 25 mm, and with the spring

stiffness of 37.88 N/mm. The other peak power values are 1.84 W, 2.86 W, 3.46 W and 4 W, for the spring stiffnesses of 19.12 N/mm, 25.77 N/mm, 29.77 N/mm and 43.54 N/mm, respectively.

4. The efficiency of the system is another important parameter that indicates the difference between the experimental outcomes and the theoretical output capacity of the system, calculated by solving the analytical equation of motion. It was observed that the efficiency of the system also changes by its stiffness and the testing scenario. Unlike the previous parameters, efficiency is higher when the loading speed is relatively slow and the displacement is high. However, there is also a steady increase between the system's stiffness and the maximum efficiency. The highest efficiency of the system is 81%, observed when the testing scenario is 5mm/s loading speed and 19 mm displacement and the spring stiffness is 29.77 N/mm, followed by the efficiencies of 80% and 72%, under the same testing scenarios but with the spring stiffnesses of 43.54 N/mm and 38.77 N/mm, respectively.

6 Feasibility Analysis of the Crank Road Harvester

6.1 Introduction

This chapter discusses the feasibility of employing the new crank-based road harvester in the roads as a new energy harvesting method. The discussion is made from different points of the potential applications, field installation, challenges (technical feasibility), and cost-effectiveness (financial feasibility).

6.2 Technical Feasibility of the Crank-Based Road Harvester

This harvester was designed and manufactured aiming to have a sustainable energy harvesting source for low-power applications of smart cities. As it was shown in the previous chapter, the power output and the mechanical capacity of this design fulfil this aim.

Moreover, it is possible to connect the rectifier output to a rechargeable battery for storage purposes and save the generated electrical potential for further use. The employed rectifier is suitable for recharging batteries, and therefore, it gives a significant potential to the harvester to generate power for later usage. Figure 6.1 shows a schematic plan of the harvester's road installation as road rumbles, power storage and its future use, as road illumination, signals, sensors and IoT powering.

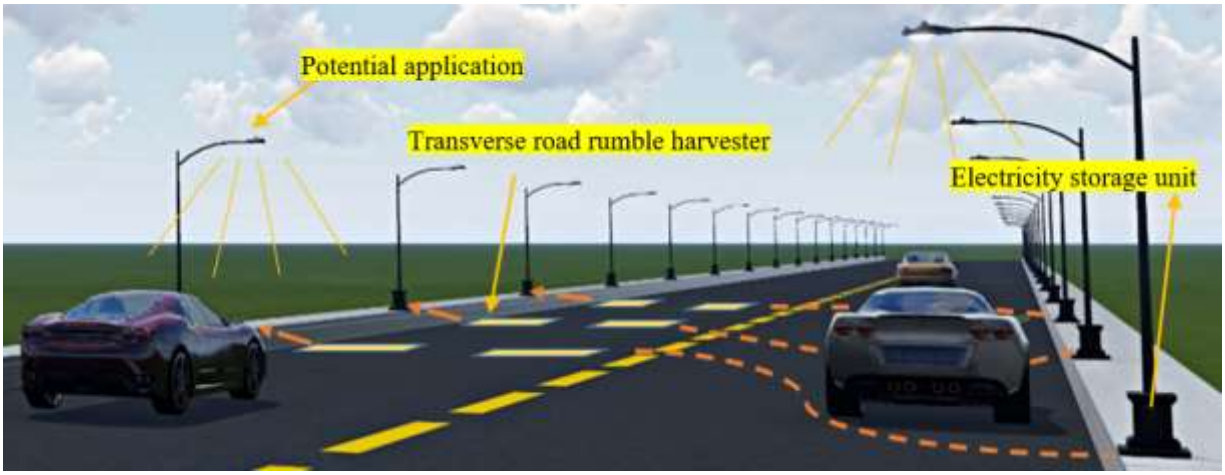

Figure 6.1: Energy storage and potential use of the stored energy for illumination (not scaled)

Low power applications of the smart cities could potentially be provided off-grid by installing a sufficient number of harvesters in suitable locations and storing the generated potential. Further discussions on the potentials of the harvester are given in the cost-effectiveness analysis section.

6.2.1 Field Installation Recommendations

This harvester is capable of withstanding the dynamic loads applied from various types of vehicles, and it is an ideal choice of a sustainable energy source in smart cities. Based on the analysis and the experimental results, the following zones are examples of suitable options for field installation:

- Road rumble strips along the roads and highways
- Transverse road rumbles in streets and highways
- A smooth speed bump at junctions, crosswalks, and parking lots

As this harvester operates with a minimal vertical displacement, unlike the current electromagnetic harvesters, it is also compatible with areas of higher speeds, such as highways.

6.3 Financial Feasibility: A Case Study of Lancashire, UK

In this section, the feasibility of the newly developed harvesting method is assessed. This assessment is done from different aspects of cost-effectiveness, carbon offset, financial gain and technology readiness level (TRL).

6.3.1 Cost Analysis

Cost analysis of this energy harvesting technology is conducted to estimate the cost of the technology and compare it to the other road energy harvesting methods, such as photovoltaic cells, piezoelectric and thermoelectric harvesters, and the regular energy power plants in terms of their cost. Moreover, the potential gain from installing a sufficient number of harvesters in a road lane is evaluated.

Building a prototype of a crank-based road harvester costs about £500, for laboratory testing purposes. It is estimated that, if made commercially, the manufacturing price would rise to around £700, and including the excavation and preparation, the final cost is assumed to be about £1500. Table 6.1 summarises these costs of one unit of harvester when built commercially.

Table 6.1: Cost analysis details

Building stage	Cost details
Laboratory prototype	Sets of springs: £170 Gearbox and generator: £300 Top and Bottom plate, crank components, and bolts: £30 Sum: £500
Commercially building	Sets of springs: £150 Gearbox and generator: £300 Top and Bottom plate, crank components, and bolts: £250 Sum: £700
Building and installation cost	Cost of the harvester: £700 Cost of the cords, wall box and waterproofing: £100 Cost of excavation: £300 Cost of installation (incl. the concrete walls): £400 Sum: £1500

The average output power generated by the harvester can reach 2.25 W over 2.76 seconds in one loading and unloading cycle, projecting one tyre (one axle) of a passing car. Hence the generated electrical energy from one passing car is 6.2 J. If the harvester is placed in a roadway of 200 cars per hour, 1240 J., equal to 0.34 Wh energy is generated per hour from one harvester. Figure 6.2 shows the primary roads network in Lancashire county in the UK. Based on the collected data, the average annual daily flow of Lancashire county in both directions (on an average day) is around 9766 cars [142].

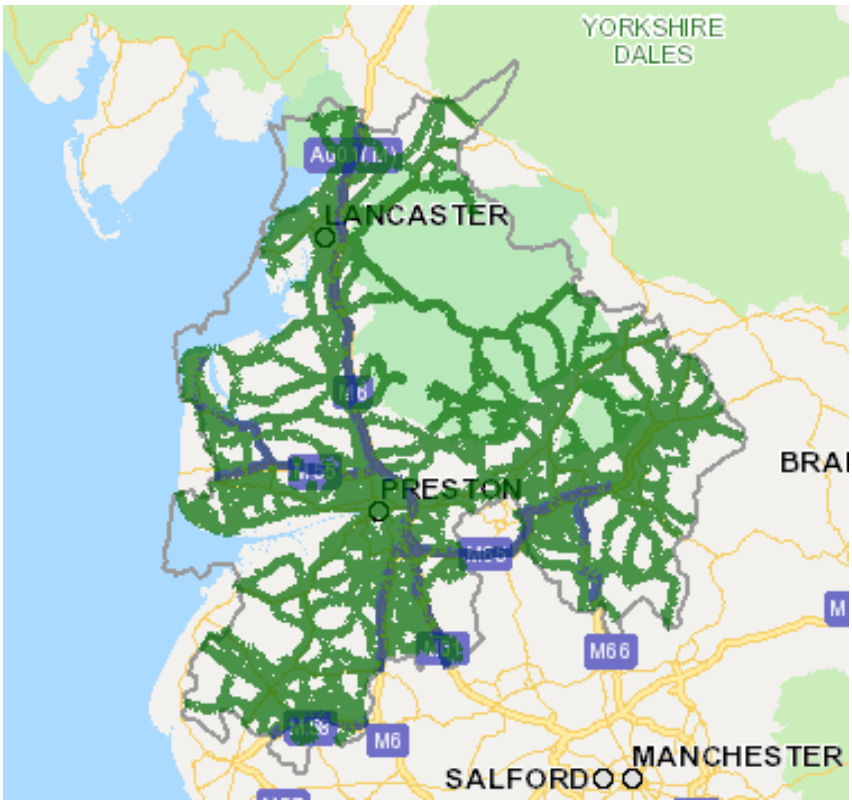

Figure 6.2: Map of primary roads in Lancashire county [143]

Assuming that from this traffic, almost 1600 cars (almost one-sixth) pass on one harvester, the harvester can produce average energy of 5.51 Wh per day, which results in 2 KWh per year and 20 KWh over 10 years (service life). Table 6.2 shows the described calculations in steps.

Table 6.2: lifetime energy-generating analysis of one harvester, according to the traffic data in Lancashire country

Step	Generated energy
The average power of one cycle, over 2.76 s	2.25 x 2.76= 6.21 J
One passing car (two cycles)	6.21 J x 2= 12.42 J
1600 cars in one day	1600 x 12.42 = 19872 J= 5.52 W.h.
In one year	$5.52 \times 365 \cong 2.015 KWh$
In 10 years of service life	$2.015 \text{ KWh} \times 10 = 20.2 \text{ KWh}$

As the cost of each harvester is £1500, the cost of generating each Kilowatt-hour of energy from one unit of the harvester is

$£1500 \div 20.2 = £74.26/\text{KWh}$

According to the local authorities, the cost of electricity generation per KWh from the conventional fossil fuel power plants is about 17.2 p [144]. By comparison, the crank-based energy harvester generation cost is higher. However, it is believed that by improving the design, such as employing a more efficient generator and optimizing the design, the system's output will be improved. Moreover, considering the environmental impact of fossil fuel power plants, having a clean and sustainable energy harvester that can be placed in versatile locations is a positive shift towards more sustainable infrastructures in smart cities.

Assuming that each streetlamp consumes around 150 W, in 10 hours of lighting, their energy consumption is 1.5 KWh. According to the calculations in Table 6.3, 90 units of the harvester is required to generate this amount of energy. Table 3 shows the details of these calculations.

Table 6.3: Sufficient number of harvesters for powering one streetlamp for 10 hours in Lancashire-UK

Energy consumption of one streetlamp in one hour	$150 \times 1 = 150$ Wh
In 10 hours of illumination (one day)	$150 \times 10 = 1500\ Wh = 1.5$ KW. h
One harvester's generation per car (4 tyres when the harvesters are placed consecutively)	12.4 J
Generation per day in Lancashire (in one direction): The harvesters are placed consecutively, allowing all the cars to pass over them	$4883 \times 12.4 = 60549.2$ J = 16.82 Wh
Number of required harvesters	$1500 \div 16.82 \cong 90$
As rumbles: Installing nine harvesters in a three-lane road (four in each lane)	$180 \div 12 = 8$ rows of transverse rumbles

According to the calculations, if the output energy of a total number of 90 harvesters per direction is stored for one day, a sufficient amount of energy will be available to run one streetlamp for one working day. These harvesters can be placed as 8 rows of transverse road rumbles, given that in each row, 12 harvesters are placed. A schematic illustration is shown in Figure 6.3.

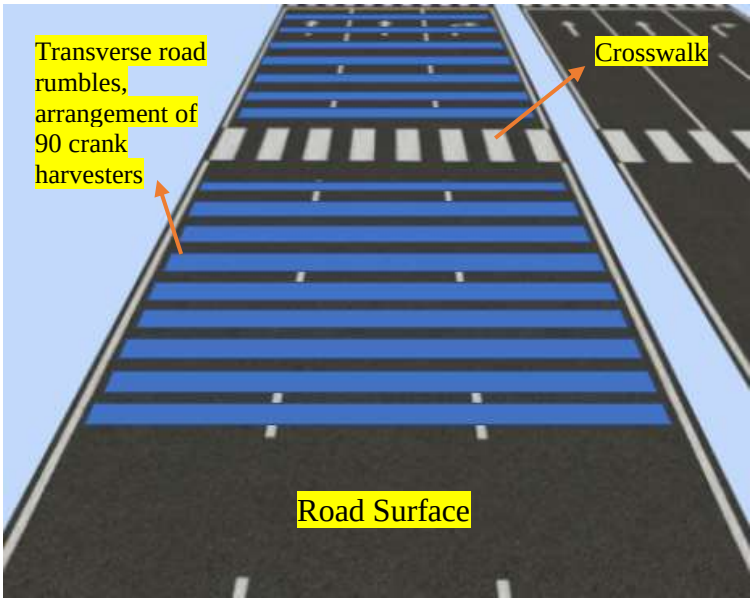

Figure 6.3: Schematic illustration of installing 16 rows of rumbles before crosswalks, sufficient to power 2 streetlamps for one day

It must be highlighted that streetlamps are relatively high consuming facilities. Aiming to power the low-power facilities of smart cities, like sensors and IoT, this harvester is sufficiently capable of powering them in real-time or with minimal storage. As an example, the nodes of IoT, the regular air quality measurers suitable for smart cities, consume around 1 W or within milliwatts [145]–[148], which can easily be powered by one harvester in real-time.

6.3.2 Carbon Offset

In the UK, it is reported that for each KWh electricity generation in a fossil fuel power plant, around 850, 450 and 200 grams of CO_2 is emitted for the plant types of coal, natural gas, and carbon capture and storage (CCS), respectively [149]. Hence, by generating 2 kWh of energy each year, potentially, 1.7 Kg CO_2 emission is reduced each year. However, it is essential to

mention that this is only for 1 unit of the harvester, and the level of carbon offset can be scaled up by building and placing more harvesters in suitable locations. By installing 90 units of the harvester, in addition to providing off-grid power to one streetlamp, 153 Kg of CO_2 emission is reduced every year.

6.3.3 Technology Readiness Level (TRL)

In terms of technology readiness level analysis (TRL), the system is currently designed, and its performance is approved in the laboratory under mechanical conditions matching the real field loads. Its performance is approved by powering the LED bulbs under loading conditions similar to the operation environment. Therefore, it has a TRL of 5.

Table 6.4 summarises the current crank-based harvester's financial feasibility features and compares it to the previously studied systems.

Table 6.4: Comparison of the current study to the other road energy harvesting alternatives

Mechanism	Reference	TRL	Cost-Benefit (£/KWh)
Piezoelectric	[46]	4	~136
	[41]	5	174
	[150]	3	42
Thermoelectric	[11]	3	0.7
	[30]	3	1.7
Photovoltaic	[25]	4	14.5
	[113]	9	Not available
Electromagnetic	[151]	5	152
	Current system	5	74.62

According to Table 6.4, the cost of this system is less than the similar electromagnetic road harvester, while it is mechanically more stable, as all the parts are linked together. It is noteworthy that in the largescale application stage, the cost of excavation and installation will also decrease.

6.4 Conclusion

In this chapter, the feasibility analysis of the crank road energy harvester was conducted from two major aspects of technology and finance. The following points summarise the main results of the analyses.

1. Based on experiments, the crank road energy harvester can withstand mechanical loads matching the real field conditions and power LED lights. Hence, for real-scale applications, it is possible to install it in versatile conditions such as road rumble strips, transverse road rumbles, and crosswalks to generate sustainable energy, especially for low-power facilities of smart cities.

2. In the financial feasibility, the cost analysis shows that the crank road energy harvester is relatively cheaper than the previous similar systems, and because of its unique design, there is minimal risk of mechanical failures due to parts mismatch and backlash. Although it is still more expensive than the conventional power generation methods of fossil fuels powerplants, the carbon offset analysis shows that each unit of the crank-based harvester, with the current design, can prevent around 1.7 Kg of CO_2 emission each year. It is believed that with an improvement in the design and implementation of this unit in suitable locations on a large scale, the carbon offset potentials of this harvester are remarkable.

3. For powering a 150-watts streetlamp, the energy generated by 90 harvesters in one day is sufficient. In addition to off-grid powering, they reduce the annual carbon emissions by 153 Kg. Considering the fact that the conventional speed bumps and rumbles are generally considered to increase fuel consumption, using crank-based energy harvesters instead of conventional systems is a significant shift towards having more sustainable infrastructures.

7 Conclusions and Future Works Recommendations

This research focuses on generating energy from kinetic energy on roads by designing and testing a novel electromagnetic harvester, which is capable of generating power, especially for low power facilities of smart cities.

The other potential of energy harvesting from roads is the thermal form of energy. It was discussed through the literature review that the thermal energy road harvesters' performance is highly dependant on environmental factors, such as the time of the day and the regions climate. Besides, solar panel road harvesters are brittle, and even though they are implemented in some large-scale projects, significant improvements are still required to adapt them to the road mechanical demands and prevent them from failures such as cracking and irreparable damages. Therefore, kinetic energy road harvesters are more reliable technologies, and among them, electromagnetic road energy harvesters have a better capacity for power generation and require minimal maintenance.

The significant part of this work is on building and evaluating a crank-based electromagnetic road energy harvester with a novel design that can be utilised as rumble strips, and transverse road rumbles in roads and highways and smooth speed bumps in low-speed traffic zones. Speed bumps and rumbles are essential for increasing the roadway's safety. In the following sections, the main contributions and outcomes of this study are summarised, followed by some recommendations for future works in this field.

7.1 Conclusion points

1. Analytical evaluation of the crank system showed that the output of the energy harvester depends on both the displacement magnitude and the displacement speed of the top plate. The external resistor of the power harvesting circuit was the other important factor affecting the system's output. Motion analysis of the system was conducted and verified, and it was shown

that the maximum feasible displacement of the top plate is 25 mm, which makes the harvester a suitable choice to be employed as smooth speed bumps or rumbles in roads and highways.

2. The mechanical performance of the system was also evaluated through finite element analysis (FEA) and verified in the laboratory. It was observed through FEA that none of the critical zones had stress values exceeding the yield strength of aluminium which is the material used to build the prototype, and hence, the harvester's initial prototype is mechanically stable.

3. The harvester's prototype was built for laboratory testing. The crank's components were made of aluminium and were bolted together. All the components of this study are bolted to each other, minimizing any risk of backlash and mismatch. In addition, a planetary gearbox, an electromagnetic generator, and a full bridge rectifier are the other components of the harvester unit. The top plate was mechanically supported by 4 springs in the corners of the harvester case. The initial prototype was made using the springs with stiffness of 19.12 N/mm. The experimental phase was done using an INSTRON device, with a maximum displacement speed limit of 14.67 mm/s.

4. The experimental study was planned based on the simulation results, and the harvester's prototype was tested under different testing scenarios of the external resistor, displacement magnitude and speed of the top plate. The harvester's output was logged using a NIDAQ instrument, recording the raw output voltage and the voltage around the external resistor. The output power of the system was calculated using the voltage around the resistor. Moreover, by comparing the raw and rectified voltage, the generator's efficiency was calculated in each scenario and used for comparison.

5. The optimum external resistor of the first prototype of the harvester was equal to 35.5 ohms, at which the output voltage maximizes, resulting in the highest output power. The maximum output raw voltage of the harvester was 6.9 V recorded at the displacement of 18 mm and the displacement speed of 14.67 mm/s.

6. In the first prototype (with the springs of 19.12 N/mm), the highest power pulse was recorded at the displacement of 18 mm and the speed of 14.67 mm/s, equal to 1.84 W. Moreover, the average output power was also calculated by taking the average of the power pulses in one loading and unloading cycle. The highest average power of one cycle was equal to 0.55 W, recorded when the displacement was 25 mm, and the displacement speed was 14.67 m/s. It is worth noting that both voltage and power maximize when the loading speed peaks.

7. Comparing The generation efficiency of the first prototype was found that, unlike the voltage and power, the generation efficiency maximizes in low displacement speeds. The highest generation efficiency of this prototype was equal to 64% obtained when the displacement was 19 mm and the displacement speed of 5 mm/s.

8. The maximum load applied on the first harvester prototype was equal to 2.3 KN, recorded at the displacement of 25 mm and the displacement speed of 14.67 N.mm.

9. In further steps, the performance of the harvester was evaluated using different sets of springs. Four different sets of springs were chosen as the supporting system of the harvester, with stiffnesses of 25.20 N/mm, 29.77 N/mm, 37.88 N/mm, and 43.54 N/mm. The same experimental testing scenarios were conducted using these springs, and the performance of the harvester was evaluated.

10. As an expected outcome, the loading capacity of the energy harvester increased by using springs with higher stiffness. The maximum recorded force on the harvester increased to 3.1 KN, 3.85 KN, 4.38 KN and 4.6 KN, for the springs of 25.20 N/mm, 29.77 N/mm, 37.88 N/mm, and 43.54 N/mm, respectively. Considering the fact that the loading capacity indicates the forces applied by the passing vehicles, having a higher loading capacity means that the harvester can be employed on roads where heavier cars pass. In other words, the loading capacity of the harvester can be tailor-made depending on the heaviest passing vehicle from each road.

11. The optimizing external resistor of the harvester does not change when employing different springs. In all cases of springs, the optimizing external resistor was equal to 35.5 ohms, at which the output voltage and, therefore, the power maximizes.

12. In all cases, the highest power peak was obtained when the displacement speed was maximum, and the displacement was equal to or more than 18 mm. The peak power was 1.84 W, 2.86 W, 3.42 W, 4.36 W and 4 W for spring stiffnesses of 19.12 N/mm, 25.20 N/mm, 29.77 N/mm, 37.88 N/mm, and 43.54 N/mm, respectively.

13. The average power of the harvester also occurs at the maximum displacement speed and magnitude and increases by increasing the stiffness of the springs. For springs with the stiffness of 25.20 N/mm, 29.77 N/mm, 37.88 N/mm and 43.54 N/mm, the average power of one loading and unloading cycle is 0.76 W, 1.12 W, 2.24 W and 1.52 W.

14. The generation efficiency of the harvester shows a general increase by using springs with higher stiffness. Like the initial prototype, the highest generation efficiency occurs when the displacement speed is low, around 5 mm/s, and the displacement is equal to or higher than 16 mm. A generation efficiency of 81% and 80% was obtained when the displacement speed was 5 mm/s and displacement was 19 mm, with spring stiffnesses of 29.8 N/mm and 43.54 N/mm.

15. The feasibility analysis of the harvester shows that it is suitable for being employed in urban roads and highways as it can withstand the vehicles' applied forces. Moreover, one unit of the current harvester can reduce 1.7 Kg of CO_2 emissions. An arrangement of 90 harvesters in the road (as transverse road rumbles) can provide enough power for one stress lamp in one day, as well as reduce 153 Kg of CO_2 emissions in one year.

7.2 Future works recommendations

In this research, a new electromagnetic road energy harvester was designed and modelled, and its prototype's performance was approved through laboratory testing. The following points can be recommended for future investigations to improve the performance of this harvester:

1. Employing a more efficient generator can increase the overall efficiency of this system. In the built prototype, the employed generator is a commercially available NEMA 17 stepper motor. It is recommended to examine the output of the harvester by employing a bigger NEMA 23, or a more efficient electromagnetic generator, improving the power output and increase the efficiency.

2. It is possible to make further improvements by optimizing the dimensions of the crank's components and investigating its effects on the output of the harvester.

3. Conducting field tests will give a better understanding of the system's performance in a real field, and verify the estimated output of the harvester, which was done by simulation. In order to test the harvester in the real field, it is essential to ensure its waterproofness and mechanical supports.

4. Conducting studies to evaluate fatigue and the creep of the springs over time. Moreover, to study the harvester's effect on the fuel consumption of the vehicles, compared to the regular road rumbles, transverse road rumbles and smooth speed bumps.

5. Studying the interaction between the drivers and the harvester in real field, and the comfort of the drivers.

6. It is possible to adapt the harvester's springs stiffness according to the maximum expected mechanical loads. Therefore, an interesting study can be incorporating various springs as the support system of the harvester and classify them for their potential employment areas through laboratory testing. For example, employing the spring set of 10 N/mm is not suitable for urban road applications; however, it may be used for harvesting energy from pedestrian lanes.

8 References

[1] Smart Energy IP, “Creating a Smart City Roadmap For Public Power Utilities,” *Am. Public Power Assoc.*, pp. 1–18, 2018.

[2] H.-P. Lu, C.-S. Chen, and H. Yu, “Technology roadmap for building a smart city: An exploring study on methodology,” *Futur. Gener. Comput. Syst.*, vol. 97, pp. 727–742, 2019, doi: https://doi.org/10.1016/j.future.2019.03.014.

[3] M. Batty *et al.*, “Smart cities of the future,” *Eur. Phys. J. Spec. Top.*, vol. 214, no. 1, pp. 481–518, 2012, doi: 10.1140/epjst/e2012-01703-3.

[4] Department for Business Energy & Industrial Strategy, “Digest of UK Energy Statistics Annual data for UK, 2020,” no. July, 2021.

[5] Department for Business Energy and Industrial Strategy, “Digest of UK Energy Statistics 2019,” *Dukes 2019*, no. July, pp. 1–11, 2019.

[6] T. Sujjaviriyasup and K. Pitiruek, “A comparison between MODWT-SVM-DE hybrid model and ARIMA model in forecasting primary energy consumptions,” *IEEE Int. Conf. Ind. Eng. Eng. Manag.*, vol. 2017-Decem, no. 1, pp. 799–802, 2018, doi: 10.1109/IEEM.2017.8290001.

[7] Department for Business Energy & Industrial Strategy, “Energy Consumption in the UK 2020,” *Dep. Business, Energy Ind. Strateg.*, no. October, pp. 4–7, 2020.

[8] F. Duarte and A. Ferreira, “Energy harvesting on road pavements: State of the art,” *Proc. Inst. Civ. Eng. Energy*, vol. 169, no. 2, pp. 79–90, 2016, doi: 10.1680/jener.15.00005.

[9] S. A. Tahami, M. Gholikhani, and S. Dessouky, “Thermoelectric Energy Harvesting System for Roadway Sustainability,” *Transp. Res. Rec.*, vol. 2674, no. 2, pp. 135–145, 2020, doi: 10.1177/0361198120905575.

[10] M. Gholikhani, H. Roshani, S. Dessouky, and A. T. Papagiannakis, “A critical review of roadway energy harvesting technologies,” *Appl. Energy*, vol. 261, no. December 2019, p. 114388, 2020, doi: 10.1016/j.apenergy.2019.114388.

[11] U. Datta, S. Dessouky, and A. T. Papagiannakis, “Harvesting thermoelectric energy from asphalt pavements,” *Transp. Res. Rec.*, vol. 2628, pp. 12–22, 2017, doi: 10.3141/2628-02.

[12] F. J. A. Duarte, “Pavement Energy Harvesting System to Convert Vehicles Kinetic Energy into Electricity,” 2018.

[13] S. D. Brusaw and J. A. Brusaw, “Solar roadway panel.” Google Patents, 09-Sep-2014.

[14] H. Roshani, “Feasibility Study of Piezoelectric Energy Harvesting From.”

[15] P. Pan, S. Wu, Y. Xiao, and G. Liu, “A review on hydronic asphalt pavement for energy harvesting and snow melting,” *Renew. Sustain. Energy Rev.*, vol. 48, pp. 624–634, 2015, doi: 10.1016/j.rser.2015.04.029.

[16] M. GHOLIKHANI, “A COMPREHENSIVE STUDY OF THE ELECTROMAGNETIC ENERGY HARVESTING TECHNOLOGY FROM ROADWAYS SYSTEMS,” 2019.

[17] F. J. A. Duarte, A. J. L. FERREIRA, and P. M. O. FAEL, “US20200007006A1.pdf,” 02-

Jan-2020.

[18] K. M. Ullah, K. M. Ahsan-Uz-zaman, S. Hosen, R. H. Khan, and S. Parvin, “Electrical power generation through speed breaker,” *Proc. 9th Int. Conf. Electr. Comput. Eng. ICECE 2016*, pp. 30–33, 2017, doi: 10.1109/ICECE.2016.7853848.

[19] N. Zabihi and M. Saafi, “Recent Developments in the Energy Harvesting Systems from Road Infrastructures,” *Sustain.*, 2020.

[20] M. Gholikhani, S. Y. Beheshti Shirazi, G. M. Mabrouk, and S. Dessouky, “Dual electromagnetic energy harvesting technology for sustainable transportation systems,” *Energy Convers. Manag.*, vol. 230, no. October 2020, p. 113804, 2021, doi: 10.1016/j.enconman.2020.113804.

[21] P. Todaria, “Design, Modelling, and Test of an Electromagnetic Speed Bump Energy Harvester,” pp. 1–89, 2016.

[22] A. S. Dezfooli, F. M. Nejad, H. Zakeri, and S. Kazemifard, “Solar pavement: A new emerging technology,” *Sol. Energy*, vol. 149, pp. 272–284, 2017, doi: 10.1016/j.solener.2017.04.016.

[23] X. Zhu, Y. Yu, and F. Li, “A review on thermoelectric energy harvesting from asphalt pavement: Configuration, performance and future,” *Constr. Build. Mater.*, vol. 228, p. 116818, 2019, doi: 10.1016/j.conbuildmat.2019.116818.

[24] A. Northmore and S. Tighe, “Innovative pavement design: Are solar roads feasible,” *2012 TAC Conf. Exhib. - Transp. Innov. Oppor. TAC/ATC 2012*, 2012.

[25] M. F. T. Hossain and S. Dessouky, “Development of a Solar Prototype for Roadway,” *MATEC Web Conf.*, vol. 271, p. 08007, 2019, doi: 10.1051/matecconf/201927108007.

[26] T. R. Oke, “The energetic basis of the urban heat island,” *Q. J. R. Meteorol. Soc.*, vol. 108, no. 455, pp. 1–24, 1982.

[27] A. M. Rizwan, L. Y. C. Dennis, and L. I. U. Chunho, “A review on the generation, determination and mitigation of Urban Heat Island,” *J. Environ. Sci.*, vol. 20, no. 1, pp. 120–128, 2008.

[28] Y. Song *et al.*, “Road energy harvester designed as a macro-power source using the piezoelectric effect,” *Int. J. Hydrogen Energy*, vol. 41, no. 29, pp. 12563–12568, 2016, doi: 10.1016/j.ijhydene.2016.04.149.

[29] X. Jiang, Y. Li, J. Li, J. Wang, and J. Yao, “Piezoelectric energy harvesting from traffic-induced pavement vibrations,” *J. Renew. Sustain. Energy*, vol. 6, no. 4, 2014, doi: 10.1063/1.4891169.

[30] L. Guo and Q. Lu, “Potentials of piezoelectric and thermoelectric technologies for harvesting energy from pavements,” *Renew. Sustain. Energy Rev.*, vol. 72, no. November 2016, pp. 761–773, 2017, doi: 10.1016/j.rser.2017.01.090.

[31] J. Walsh, T. Muneer, and A. N. Celik, “Design and analysis of kinetic energy recovery system for automobiles: Case study for commuters in Edinburgh,” *J. Renew. Sustain. energy*, vol. 3, no. 1, p. 13105, 2011.

[32] E. Hellström, J. Åslund, and L. Nielsen, “Management of kinetic and electric energy in heavy trucks,” *SAE Tech. Pap.*, vol. 3, no. 1, pp. 1152–1163, 2010, doi: 10.4271/2010-01-1314.

[33] A. Erturk and D. J. Inman, *Piezoelectric energy harvesting*. John Wiley & Sons, 2011.

[34] R. S. Dahiya and M. Valle, “Appendix A Fundamentals of Piezoelectricity,” in *Robotic Tactile Sensing: Technologies and System*, vol. 9789400705, 2014, pp. 1–245.

[35] Z. L. Wang and W. Wu, “Piezotronics and piezo-phototronics: Fundamentals and applications,” *Natl. Sci. Rev.*, vol. 1, no. 1, pp. 62–90, 2014, doi: 10.1093/nsr/nwt002.

[36] P. J. Szary, A. Maher, R. K. Panda, and A. Safari, “Implementation of advanced fiber optic and piezoelectric sensors: fabrication and laboratory testing of piezoelectric ceramic-polymer composite sensors for weigh-in-motion systems.,” New Jersey. Dept. of Transportation, 1999.

[37] S. W. Arms, C. P. Townsend, D. L. Churchill, J. H. Galbreath, and S. W. Mundell, “Power Management for Energy Harvesting Wireless Sensors,” *SPIE Int’l Symp. Smart Struct. Smart Mater.*, vol. 10, no. March, p. 415, 2005.

[38] H. Zhao, Y. Tao, Y. Niu, and J. Ling, “Harvesting energy from asphalt pavement by piezoelectric generator,” *J. Wuhan Univ. Technol. Mater. Sci. Ed.*, vol. 29, no. 5, pp. 933–937, 2014, doi: 10.1007/s11595-014-1023-3.

[39] H. Zhao, J. Yu, and J. Ling, “Finite element analysis of Cymbal piezoelectric transducers for harvesting energy from asphalt pavement,” *J. Ceram. Soc. Japan*, vol. 118, no. 1382, pp. 909–915, 2010, doi: 10.2109/jcersj2.118.909.

[40] H. ZHAO, L. QIN, and J. LING, “Test and Analysis of Bridge Transducers for Harvesting Energy from Asphalt Pavement,” *Int. J. Transp. Sci. Technol.*, 2015, doi: 10.1260/2046-0430.4.1.17.

[41] H. Xiong and E. Weaver, “Piezoelectric Energy Harvesting on Public Roadways,” *Int. J. Pavement Res. Technol.*, vol. 5, no. 5, pp. 331–337, 2013.

[42] A. F. Jasim, H. Wang, G. Yesner, A. Safari, and P. Szary, “Performance Analysis of Piezoelectric Energy Harvesting in Pavement: Laboratory Testing and Field Simulation,” *Transp. Res. Rec.*, vol. 2673, no. 3, pp. 115–124, 2019, doi: 10.1177/0361198119830308.

[43] X. Liu and J. Wang, “Performance Exploration of A Radially Layered Cymbal Piezoelectric Energy Harvester under Road Traffic Induced Low Frequency Vibration,” *IOP Conf. Ser. Mater. Sci. Eng.*, vol. 542, no. 1, p. 012075, Jul. 2019, doi: 10.1088/1757-899X/542/1/012075.

[44] H. Xiong and L. Wang, “Piezoelectric energy harvester for public roadway: On-site installation and evaluation,” *Appl. Energy*, vol. 174, pp. 101–107, 2016, doi: 10.1016/j.apenergy.2016.04.031.

[45] H. Roshani, P. Jagtap, S. Dessouky, A. Montoya, and A. T. Papagiannakis, “Theoretical and experimental evaluation of two roadway piezoelectric-based energy harvesting prototypes,” *J. Mater. Civ. Eng.*, vol. 30, no. 2, 2018, doi: 10.1061/(ASCE)MT.1943-5533.0002112.

[46] H. Roshani, S. Dessouky, A. Montoya, and A. T. Papagiannakis, “Energy harvesting from asphalt pavement roadways vehicle-induced stresses: A feasibility study,” *Appl. Energy*, vol. 182, pp. 210–218, 2016, doi: 10.1016/j.apenergy.2016.08.116.

[47] C. Wang, Z. Song, Z. Gao, G. Yu, and S. Wang, “Preparation and performance research of stacked piezoelectric energy-harvesting units for pavements,” *Energy Build.*, vol. 183, pp. 581–591, 2019, doi: 10.1016/j.enbuild.2018.11.042.

[48] M. Khalili, A. B. Biten, G. Vishwakarma, S. Ahmed, and A. T. Papagiannakis, “Electro-mechanical characterization of a piezoelectric energy harvester,” *Appl. Energy*, vol. 253,

no. April, p. 113585, 2019, doi: 10.1016/j.apenergy.2019.113585.

[49] M. Khalili, G. Vishwakarma, S. Ahmed, and A. T. Papagiannakis, “Development of a low-power weigh-in-motion system using cylindrical piezoelectric elements,” *Int. J. Transp. Sci. Technol.*, no. xxxx, 2021, doi: 10.1016/j.ijtst.2021.06.004.

[50] C. Chen, T. B. Xu, A. Yazdani, and J. Q. Sun, “A high density piezoelectric energy harvesting device from highway traffic — System design and road test,” *Appl. Energy*, vol. 299, no. January, p. 117331, 2021, doi: 10.1016/j.apenergy.2021.117331.

[51] C. H. Yang *et al.*, “Feasibility study of impact-based piezoelectric road energy harvester for wireless sensor networks in smart highways,” *Sensors Actuators, A Phys.*, vol. 261, pp. 317–324, 2017, doi: 10.1016/j.sna.2017.04.025.

[52] L. Guo and Q. Lu, “Modeling a new energy harvesting pavement system with experimental verification,” *Appl. Energy*, vol. 208, no. March, pp. 1071–1082, 2017, doi: 10.1016/j.apenergy.2017.09.045.

[53] A. Chalmers, “Maxwell, Mechanism, and the Nature of Electricity,” *Phys. Perspect.*, vol. 3, no. 4, pp. 425–438, 2001, doi: 10.1007/PL00000539.

[54] M. Gholikhani, M. Sharzehee, S. A. Tahami, F. Martinez, S. Dessouky, and L. F. Walubita, “Effect of electromagnetic energy harvesting technology on safety and low power generation in sustainable transportation: a feasibility study,” *Int. J. Sustain. Eng.*, vol. 00, no. 00, pp. 1–14, 2019, doi: 10.1080/19397038.2019.1688890.

[55] H. Hadi Obeid, A. K. Jaleel, and N. Aubays Hassan, “Design and Motion Modeling of an Electromagnetic Hydraulic Power Hump Harvester,” *Adv. Mech. Eng.*, vol. 2014, 2014, doi: 10.1155/2014/150293.

[56] J. Wickert and K. Lewis, *An introduction to mechanical engineering*. Cengage Learning, 2020.

[57] A. D. Dimarogonas and G. Lewis, “Machine design: a CAD approach,” *Appl. Mech. Rev.*, vol. 54, no. 4, pp. B65–B68, 2001.

[58] R. G. Budynas and J. K. Nisbett, *Shigley’s mechanical engineering design*. Mc Graw Hill, 2015.

[59] A. V. da Rosa and J. C. Ordóñez, “Chapter 3 - Mechanical Heat Engines,” A. V. da Rosa and J. C. B. T.-F. of R. E. P. (Fourth E. Ordóñez, Eds. Oxford: Academic Press, 2022, pp. 105–160.

[60] K. Sotoodeh, “Chapter 2 - Introduction to actuators,” K. B. T.-P. of A. E. in the O. and G. I. Sotoodeh, Ed. Gulf Professional Publishing, 2021, pp. 27–58.

[61] N. CRACIUNOIU and B. O. CIOCIRLAN, “8 - Fluid Dynamics,” in *Academic Press Series in Engineering*, D. B. B. T.-M. E. H. Marghitu, Ed. San Diego: Academic Press, 2001, pp. 559–610.

[62] K.-H. Chang, *Motion Analysis*. 2013.

[63] Duomotiva, “Rack & Pinion In this presentation.” .

[64] F. Duarte, F. Casimiro, D. Correia, R. Mendes, and A. Ferreira, “A new pavement energy harvest system,” *Proc. 2013 Int. Renew. Sustain. Energy Conf. IRSEC 2013*, pp. 408–413, 2013, doi: 10.1109/IRSEC.2013.6529704.

[65] F. J. A. Duarte, A. J. L. FERREIRA, and P. M. O. FAEL, “Device for applying in a pavement for collecting mechanical energy from vehicles passing over for generating

electricity," 02-Jan-2020.

[66] F. Duarte, A. Ferreira, and J. P. Champalimaud, "Waynergy People - application in an operational environment," *Proc. Inst. Civ. Eng. Energy*, vol. 171, no. 2, pp. 82–89, 2018, doi: 10.1680/jener.16.00010.

[67] P. Todaria *et al.*, "Design, modeling and test of a novel speed bump energy harvester," *Sensors Smart Struct. Technol. Civil, Mech. Aerosp. Syst. 2015*, vol. 9435, p. 943506, 2015, doi: 10.1117/12.2084371.

[68] L. Wang, P. Todaria, A. Pandey, J. Oconnor, B. Chernow, and L. Zuo, "An electromagnetic speed bump energy harvester and its interactions with vehicles," *IEEE/ASME Trans. Mechatronics*, vol. 21, no. 4, pp. 1985–1994, 2016, doi: 10.1109/TMECH.2016.2546179.

[69] A. Pirisi, M. Mussetta, F. Grimaccia, and R. E. Zich, "Novel speed-bump design and optimization for energy harvesting from traffic," *IEEE Trans. Intell. Transp. Syst.*, vol. 14, no. 4, pp. 1983–1991, 2013, doi: 10.1109/TITS.2013.2272650.

[70] N. N. Ghuge, A. Sathe, V. Patil, and A. Warankar, "Every Speed Breaker Is A Source Of Power," vol. 4, no. 3, pp. 1–5, 2014.

[71] B. S. Sarma, V. Jyothi, and D. Sudhir, "Design of Power Generation Unit Using Roller Mechanism," *IOSR J. Electr. Electron. Eng.*, vol. 9, no. 3, pp. 55–60, 2014, doi: 10.9790/1676-09315560.

[72] C. C. Ting, D. Y. Tsai, and C. C. Hsiao, "Developing a mechanical roadway system for waste energy capture of vehicles and electric generation," *Appl. Energy*, vol. 92, pp. 1–8, 2012, doi: 10.1016/j.apenergy.2011.10.006.

[73] X. Zhang, Z. Zhang, G. Meng, and D. Luo, "Design, modeling, simulation of a novel mechanical road tunnel energy harvesting system with hydraulic transaction," *2015 IEEE Int. Conf. Inf. Autom. ICIA 2015 - conjunction with 2015 IEEE Int. Conf. Autom. Logist.*, no. August, pp. 726–730, 2015, doi: 10.1109/ICInfA.2015.7279380.

[74] D. Goodey *et al.*, "A Pneumatic Multi-Dome Active Energy Harvesting System," in *ASME International Mechanical Engineering Congress and Exposition*, 2016, vol. 50664, p. V012T16A026.

[75] C. Li and P. W. Tse, "Fabrication and testing of an energy-harvesting hydraulic damper," *Smart Mater. Struct.*, vol. 22, no. 6, 2013, doi: 10.1088/0964-1726/22/6/065024.

[76] V. Bobes-Jesus, P. Pascual-Muñoz, D. Castro-Fresno, and J. Rodriguez-Hernandez, "Asphalt solar collectors: A literature review," *Appl. Energy*, vol. 102, pp. 962–970, 2013, doi: 10.1016/j.apenergy.2012.08.050.

[77] J. W. Lund *et al.*, "Industrial uses of geothermal energy," *Geothermics*, vol. 21, no. 5–6, pp. 587–588, 1992, doi: 10.1016/0375-6505(92)90010-7.

[78] A. Balbay and M. Esen, "Experimental investigation of using ground source heat pump system for snow melting on pavements and bridge decks," *Sci. Res. Essays*, vol. 5, no. 24, pp. 3955–3966, 2010.

[79] Q. Gao, Y. Huang, M. Li, Y. Liu, and Y. Y. Yan, "Experimental study of slab solar collection on the hydronic system of road," *Sol. Energy*, vol. 84, no. 12, pp. 2096–2102, 2010, doi: 10.1016/j.solener.2010.09.008.

[80] R. B. Mallick, B.-L. Chen, S. Bhowmick, and M. Hulen, "Capturing solar energy from asphalt pavements," in *International symposium on asphalt pavements and environment,*

international society for asphalt pavements, Zurich, Switzerland, 2008, pp. 161–172.

[81] W. He, X. Hong, B. Luo, H. Chen, and J. Ji, "CFD and comparative study on the dual-function solar collectors with and without tile-shaped covers in water heating mode," *Renew. Energy*, vol. 86, pp. 1205–1214, 2016, doi: 10.1016/j.renene.2015.09.053.

[82] A. Alonso-Estébanez, P. Pascual-Muñoz, J. L. Sampedro-García, and D. Castro-Fresno, "3D numerical modelling and experimental validation of an asphalt solar collector," *Appl. Therm. Eng.*, vol. 126, pp. 678–688, 2017, doi: 10.1016/j.applthermaleng.2017.07.127.

[83] A. P. Masoumi, E. Tajalli-Ardekani, and A. A. Golneshan, "Investigation on performance of an asphalt solar collector: CFD analysis, experimental validation and neural network modeling," *Sol. Energy*, vol. 207, no. April, pp. 703–719, 2020, doi: 10.1016/j.solener.2020.06.045.

[84] H. Farzan, E. H. Zaim, M. Ameri, and T. Amiri, "Study on effects of wind velocity on thermal efficiency and heat dynamics of pavement solar collectors: An experimental and numerical study," *Renew. Energy*, vol. 163, pp. 1718–1728, 2021, doi: 10.1016/j.renene.2020.10.087.

[85] A. Chiarelli, A. Dawson, and A. García, "Mitigation of asphalt pavement temperatures by means of natural air convection," in *Functional Pavement Design*, CRC Press, 2016, pp. 1269–1277.

[86] A. Chiarelli, A. Dawson, and A. Garcia, "Analysis of the performance of an air-powered energy-harvesting pavement," *Transp. Res. Rec.*, vol. 2523, pp. 156–163, 2015, doi: 10.3141/2523-17.

[87] A. García and M. N. Partl, "How to transform an asphalt concrete pavement into a solar turbine," *Appl. Energy*, vol. 119, pp. 431–437, 2014, doi: 10.1016/j.apenergy.2014.01.006.

[88] A. Majumdar, "Thermoelectricity in semiconductor nanostructures," *Science (80-.).*, vol. 303, no. 5659, pp. 777–778, 2004.

[89] D. K. C. MacDonald, *Thermoelectricity: an introduction to the principles*. Courier Corporation, 2006.

[90] R. A. Kishore and S. Priya, "A Review on low-grade thermal energy harvesting: Materials, methods and devices," *Materials (Basel).*, vol. 11, no. 8, 2018, doi: 10.3390/ma11081433.

[91] D. M. Rowe, *THERMOELECTRICS HANDBOOK*. 2006.

[92] T. M. Tritt and M. A. Subramanian, "T hermoelectric Materials , Phenomena , and Applications : A Bird ' s Eye View," vol. 31, no. March 2006, 2019.

[93] A. F. Bissada, "Asphalt Pavement Temperatures Related To Kuwait Climate.," *Highw Res Rec*, no. 40, pp. 71–85, 1972.

[94] W. Jiang, J. Xiao, D. Yuan, H. Lu, S. Xu, and Y. Huang, "Design and experiment of thermoelectric asphalt pavements with power-generation and temperature-reduction functions," *Energy Build.*, vol. 169, pp. 39–47, 2018, doi: 10.1016/j.enbuild.2018.03.049.

[95] W. Jiang *et al.*, "Energy harvesting from asphalt pavement using thermoelectric technology," *Appl. Energy*, vol. 205, no. June, pp. 941–950, 2017, doi: 10.1016/j.apenergy.2017.08.091.

[96] S. A. Tahami, M. Gholikhani, R. Nasouri, and S. Dessouky, “Evaluation of a Novel Road Thermoelectric Generator System,” *MATEC Web Conf.*, vol. 271, p. 08002, 2019, doi: 10.1051/matecconf/201927108002.

[97] M. Hasebe, Y. Kamikawa, and S. Meiarashi, “Thermoelectric generators using solar thermal energy in heated road pavement,” *Int. Conf. Thermoelectr. ICT, Proc.*, pp. 697–700, 2006, doi: 10.1109/ICT.2006.331237.

[98] K. N. Khamil, M. F. Mohd Sabri, and A. M. Yusop, “Thermoelectric energy harvesting system (TEHs) at asphalt pavement with a subterranean cooling method,” *Energy Sources, Part A Recover. Util. Environ. Eff.*, vol. 00, no. 00, pp. 1–17, 2020, doi: 10.1080/15567036.2020.1785057.

[99] M. S. Sharuddin, A. Yusop, A. Sadhiqin, M. Isira, and K. N. Khamil, “Effect of Different Condition on Voltage Generation and Thermal Gradient from Road Pavement Using Thermoelectric Generator,” *J. Eng.*, vol. 32, no. 3, pp. 415–422, 2020, doi: 10.17576/jkukm-2020-32(3)-06.

[100] P. Park, G. S. Choi, E. Rohani, and I. Song, “Optimization of thermoelectric system for pavement energy harvesting,” *Asph. Pavements - Proc. Int. Conf. Asph. Pavements, ISAP 2014*, vol. 2, no. February 2019, pp. 1827–1838, 2014, doi: 10.1201/b17219-220.

[101] H. Lee, H. Jang, J. Park, S. Jeong, T. Park, and S. Choi, “Design of a Piezoelectric Energy-Harvesting shock absorber system for a vehicle,” *Integr. Ferroelectr.*, vol. 141, no. 1, pp. 32–44, 2013, doi: 10.1080/10584587.2013.778724.

[102] J. J. Lee, D. H. Kim, S. T. Lee, and J. K. Lim, “Fundamental study of energy harvesting using thermoelectric effect on concrete structure in road,” *Adv. Mater. Res.*, vol. 1044–1045, pp. 332–337, 2014, doi: 10.4028/www.scientific.net/AMR.1044-1045.332.

[103] G. Wu and X. Yu, “Thermal Energy Harvesting System to Harvest Thermal Energy Across Pavement Structure.,” *Int. J. Pavement Res. Technol.*, vol. 5, no. 5, 2012.

[104] Y. Mona, P. Jitsangiam, and K. Punyawudho, “A comparison of energy harvesting from cement and asphalt on road pavement using thermoelectric module,” *Energy Reports*, vol. 7, pp. 225–229, 2021, doi: https://doi.org/10.1016/j.egyr.2021.06.038.

[105] L. M. Fraas and L. D. Partain, *Solar cells and their applications*, vol. 236. John Wiley & Sons, 2010.

[106] L. F. Llin and D. J. Paul, “Thermoelectrics, Photovoltaics and Thermal Photovoltaics for Powering ICT Devices and Systems,” *ICT-Energy Concepts Energy Effic. Sustain.*, p. 215, 2017.

[107] R. Hantula, *How Do Solar Panels Work?* Infobase Publishing, 2009.

[108] A. M. Bagher, M. M. A. Vahid, and M. Mohsen, “Types of solar cells and application,” *Am. J. Opt. Photonics*, vol. 3, no. 5, pp. 94–113, 2015.

[109] C. Efthymiou, M. Santamouris, D. Kolokotsa, and A. Koras, “Development and testing of photovoltaic pavement for heat island mitigation,” *Sol. Energy*, vol. 130, pp. 148–160, 2016, doi: 10.1016/j.solener.2016.01.054.

[110] J. H. Nussbaum, R. A. Lake, and R. A. Coutu, “Standardized testing of non-standard photovoltaic pavement surfaces,” *Proc. IEEE Natl. Aerosp. Electron. Conf. NAECON*, vol. 0, pp. 1–8, 2016, doi: 10.1109/NAECON.2016.7856766.

[111] A. Shekhar *et al.*, “Harvesting roadway solar energy-performance of the installed infrastructure integrated pv bike path,” *IEEE J. Photovoltaics*, vol. 8, no. 4, pp. 1066–

1073, 2018, doi: 10.1109/JPHOTOV.2018.2820998.

[112] R. A. Coutu, D. Newman, M. Munna, J. H. Tschida, and S. Brusaw, “Engineering Tests to Evaluate the Feasibility of an Emerging Solar Pavement Technology for Public Roads and Highways,” *Technologies*, vol. 8, no. 1, p. 9, 2020, doi: 10.3390/technologies8010009.

[113] SolaRoad, “SolaRoad , the road that converts sunlight into electricity SolaRoad is a pioneering innovation in the field of energy harvesting . It is a unique concept , which converts sunlight on the road surface into electricity : the road network works as an inexha.”

[114] S. Magazine, “SolarMagazine-Jun20-SolaRoad-nieuwe-generatie-zonnefietspaden.pdf,” 2020. [Online]. Available: https://www.solaroad.nl/wp-content/uploads/2020/09/SolarMagazine-Jun20-SolaRoad-nieuwe-generatie-zonnefietspaden.pdf.

[115] B. Zhou, J. Pei, J. K. Calautit, J. Zhang, and F. Guo, “Solar self-powered wireless charging pavement—a review on photovoltaic pavement and wireless charging for electric vehicles,” *Sustain. Energy Fuels*, vol. 5, no. 20, pp. 5139–5159, 2021, doi: 10.1039/d1se00739d.

[116] T. Pultarova, “Welcome To the World ’ S First Solar Road,” *Eng. Technol.*, no. February, p. 1, 2017.

[117] B. Zhou, J. Pei, D. M. Nasir, and J. Zhang, “A review on solar pavement and photovoltaic/thermal (PV/T) system,” *Transp. Res. Part D Transp. Environ.*, vol. 93, no. March, p. 102753, 2021, doi: 10.1016/j.trd.2021.102753.

[118] H. Hu, D. Vizzari, X. Zha, and R. Roberts, “Solar pavements: A critical review,” *Renew. Sustain. Energy Rev.*, vol. 152, no. May, p. 111712, 2021, doi: 10.1016/j.rser.2021.111712.

[119] Wattways, “Technical Datasheet of,” pp. 3700–3700, 2000.

[120] S. Roadways, “Solar Roadways – Solar Panels For Every Walking And Driving Surface.” [Online]. Available: https://solarroadways.com/.

[121] J. C. Mankins, “Technology readiness levels,” *White Pap. April*, vol. 6, no. 1995, p. 1995, 1995.

[122] B. Hicks, A. Larsson, S. Culley, and T. Larsson, “A methodology for evaluating technology readiness during product development,” in *17th International Conference on Engineering Design (ICED’09) Design has never been this cool, Stanford University, California, USA*, 2009.

[123] European Commission, “HORIZON 2020 - WORK PROGRAMME 2014-2015 General Annexes - Annex G . Technology readiness levels (TRL),” no. 2014, p. 4995, 2014.

[124] R. F. Fung, “Dynamic analysis of the flexible connecting rod of a slider-crank mechanism,” *J. Vib. Acoust. Trans. ASME*, vol. 118, no. 4, pp. 687–869, 1996, doi: 10.1115/1.2888353.

[125] C. M. DeStefano, Z. R. Killoy, and E. J. Brigham, “Slider-Crank Demonstration MQP,” 2013.

[126] Solidworks, “Understanding Motion Simulation,” 2008. [Online]. Available: https://www.solidworks.com/sw/images/content/Training/SIM_Motion_Understanding Motion_WP_ENG.pdf. [Accessed: 27-Jul-2021].

[127] K.-H. Chang, *Motion Simulation and Mechanism Design with SOLIDWORKS Motion 2021*. SDC publications, 2021.

[128] S. D. I. Software, “Simcenter 3D for motion simulation,” 2020. [Online]. Available: www.cardsplmsolutions.com/nl/producten/simcenter-3d.

[129] D. Nedelcu, M. D. Nedeloni, and D. Daia, “The kinematic and dynamic analysis of the crank mechanism with SolidWorks Motion,” *Recent Adv. Signal Process. Comput. Geom. Syst. Theory - ISCGAV’11, ISTASC’11*, no. January 2015, pp. 245–250, 2011.

[130] D. for T. Department, “Traffc Calming,” no. March, 2007.

[131] L. Johnson and a J. Nedzesky, “A Comparative Study of Speed Humps , Speed Slots and Speed Cushions,” *ITE Annu. Meet. Exhib.*, p. 14, 2004.

[132] H. Abdullahi, M. Z. Asmawi, A. Razak, and A. Aziz, “Department of Urban and Regional Planning, Kulliyyah of Architecture and Environmental Design, International Islamic University Malaysia. 2 City Universiti, Petaling Jaya, Selangor.,” vol. 8, no. 1, pp. 64–73, 2018.

[133] T. D. Homopolymer, Polypropylene, “Product information Product full identity : PPH | Sheet - Extruded,” pp. 4–5.

[134] S. Industrifjedre, “C19372073000M.” [Online]. Available: https://www.industrial-springs.com/c19372073000m. [Accessed: 06-Aug-2021].

[135] M. of C. of Seattle, “Roadway Pavement :: Seattle Streets Illustrated.” [Online]. Available: https://streetsillustrated.seattle.gov/design-standards/roadway-construction/roadway-pavement/.

[136] M. Gholikhani, R. Nasouri, S. A. Tahami, S. Legette, S. Dessouky, and A. Montoya, “Harvesting kinetic energy from roadway pavement through an electromagnetic speed bump,” *Appl. Energy*, vol. 250, no. April, pp. 503–511, 2019, doi: 10.1016/j.apenergy.2019.05.060.

[137] Vishay, “Vishay General Semiconductor Miniature Glass Passivated Single-Phase Bridge Rectifiers DF005M , DF01M , DF02M , DF04M , DF06M , DF08M , DF10M,” pp. 8–11, 2012.

[138] S. Zhao and A. Erturk, “Deterministic and band-limited stochastic energy harvesting from uniaxial excitation of a multilayer piezoelectric stack,” *Sensors Actuators, A Phys.*, vol. 214, pp. 58–65, 2014, doi: 10.1016/j.sna.2014.04.019.

[139] P. Gambier, S. R. Anton, N. Kong, A. Erturk, and D. J. Inman, “Piezoelectric, solar and thermal energy harvesting for hybrid low-power generator systems with thin-film batteries,” *Meas. Sci. Technol.*, vol. 23, no. 1, 2012, doi: 10.1088/0957-0233/23/1/015101.

[140] EEA, *Monitoring carbon dioxide emissions from passenger cars and vans in 2018*, no. 19. 2015.

[141] L. Qi *et al.*, “A high-efficiency road energy harvester based on a chessboard sliding plate using semi-metal friction materials for self-powered applications in road traffic,” *Energy Convers. Manag.*, vol. 165, no. April, pp. 748–760, 2018, doi: 10.1016/j.enconman.2018.04.003.

[142] L. L. Authority, “Road traffic statistics (TRA),” 2020.

[143] L. C. Council, “Gritting map -,” *Lancashire County Council*, 2021. [Online]. Available: https://www.lancashire.gov.uk/winter/gritting/gritting-map/.

[144] E. & I. S. Department for Business, “Statistical data set Annual domestic energy bills,” 2021. [Online]. Available: https://www.gov.uk/government/statistical-data-sets/annual-domestic-energy-price-statistics.

[145] D. E. Williams *et al.*, “Validation of low-cost ozone measurement instruments suitable for use in an air-quality monitoring network,” *Meas. Sci. Technol.*, vol. 24, no. 6, 2013, doi: 10.1088/0957-0233/24/6/065803.

[146] M. Penza, “New Sensing Technologies for Environmental Sustainability in Smart Cities,” 2014.

[147] D. Lesser, I. Katra, M. Dorman, H. Harari, and I. Kloog, “Validating and Comparing Highly Resolved Commercial ‘Off the Shelf’ PM Monitoring Sensors with Satellite Based Hybrid Models, for Improved Environmental Exposure Assessment,” *Sensors* , vol. 21, no. 1. 2021, doi: 10.3390/s21010063.

[148] A. Haenel, Y. Haddad, and Z. Zhang, “Lightweight Authentication Scheme for Internet of Things,” *2020 IEEE 17th Annu. Consum. Commun. Netw. Conf. CCNC 2020*, no. Id, pp. 1–2, 2020, doi: 10.1109/CCNC46108.2020.9045654.

[149] Parliamentery office of science and technology, “Carbon footprint of electricity gerenation,” *Carbon N. Y.*, no. 383, pp. 1–4, 2006.

[150] J. Zou, X. Guo, L. Xu, G. Tan, C. Zhang, and J. Zhang, “Design, Modeling, and Analysis of a Novel Hydraulic Energy-Regenerative Shock Absorber for Vehicle Suspension,” *Shock Vib.*, vol. 2017, 2017, doi: 10.1155/2017/3186584.

[151] M. Gholikhani, S. Amid Tahami, and S. Dessouky, “Harvesting Energy from Pavement – Electromagnetic Approach,” *MATEC Web Conf.*, vol. 271, p. 06001, 2019, doi: 10.1051/matecconf/201927106001.

Appendix: Complementary Experimental data of the crank road energy harvester

Spring set of 19.77 N/mm:

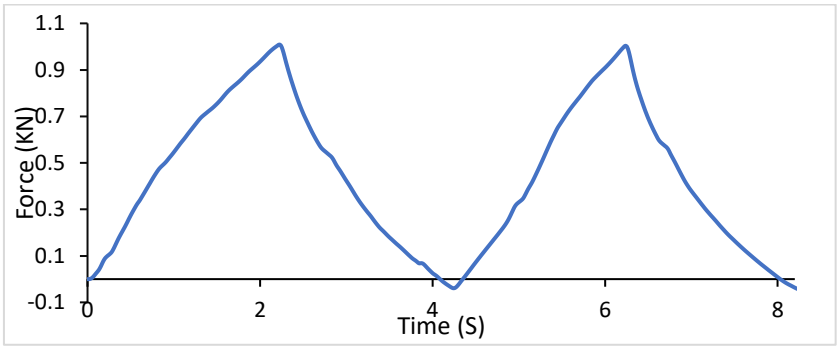

Figure 0.1: Force-time diagram of the harvester under 5 mm/s and Displacement Of 10 mm

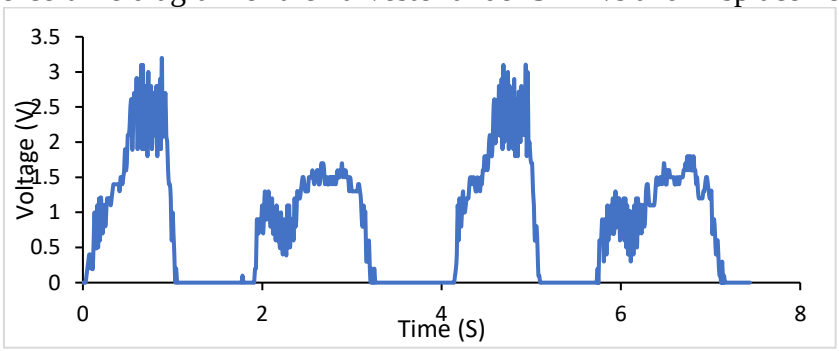

Figure 0.2: Voltage-time of the harvester under 10 mm of displacement and the speed of 5 mm/s

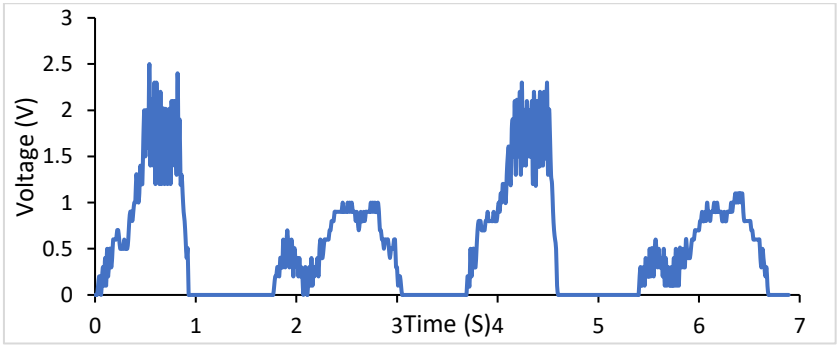

a

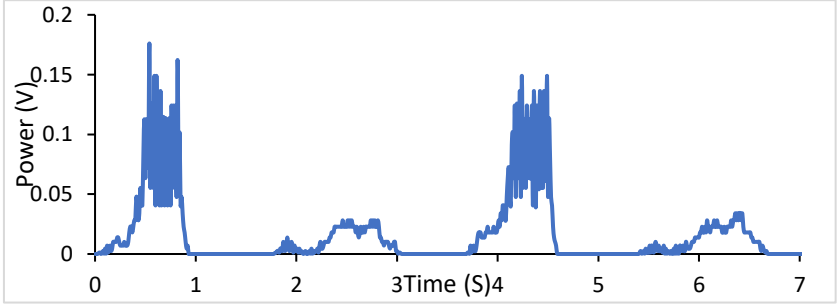

b

Figure 0.3: System's response under 5 mm/s and 10 mm displacement a) Voltage-time around the 35.5 ohms, b) Power-time

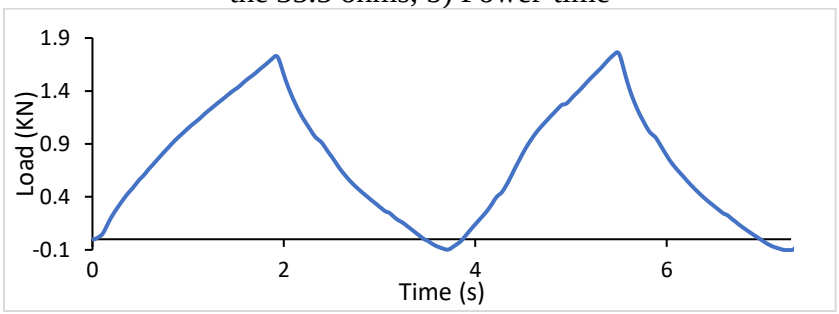

Figure 0.4: Force-time diagram of the harvester under 9 mm/s and Displacement Of 16 mm

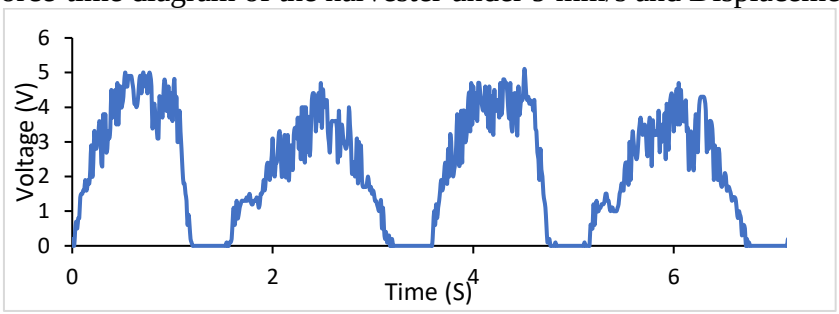

Figure 0.5: Voltage-time of the harvester under 16 mm of displacement and the speed of 9 mm/s

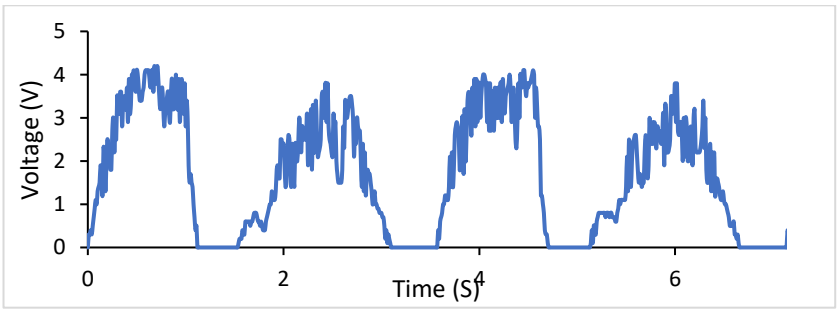

a

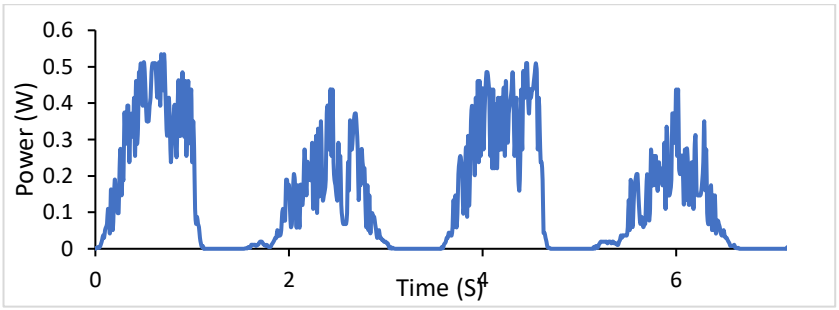

b

Figure 0.6: System's response under 9 mm/s and 16 mm displacement a) Voltage-time around the 35.5 ohms, b) Power-time

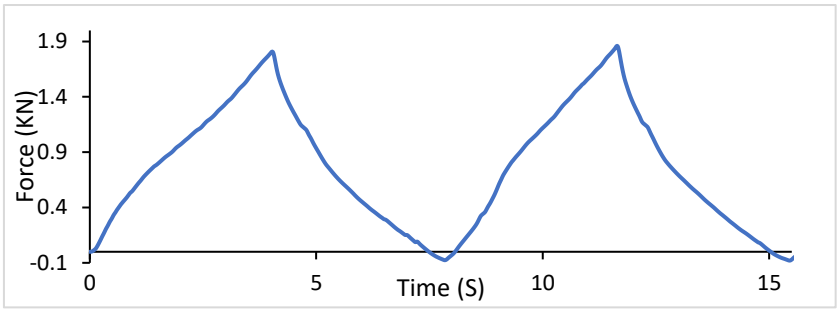

Figure 0.7: Force-time diagram of the harvester under 5 mm/s and Displacement Of 19 mm

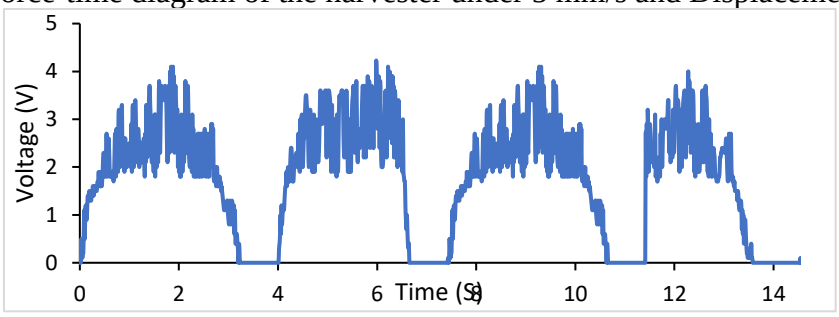

Figure 0.8: Voltage-time of the harvester under 19 mm of displacement and the speed of 5 mm/s

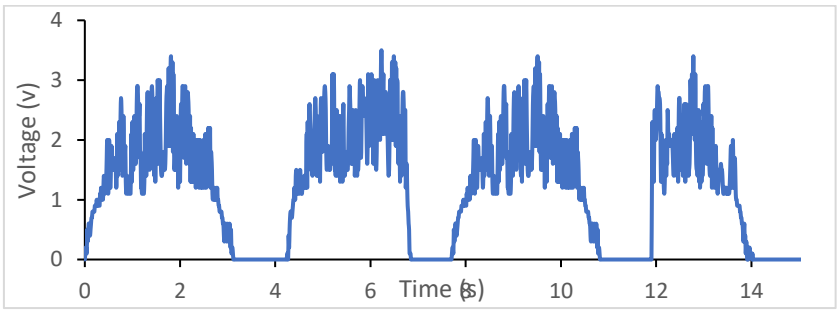

a

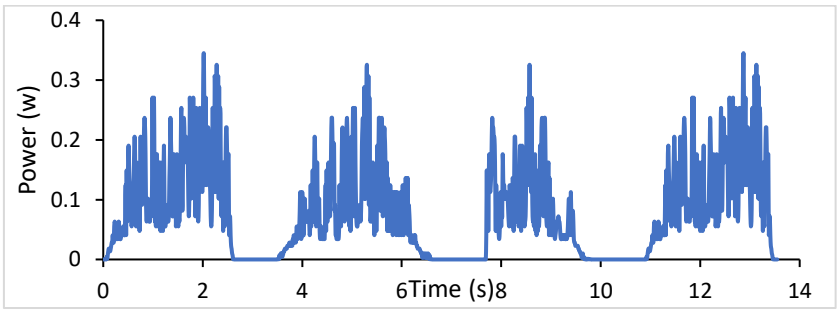

b

Figure 0.9: System's response under 5 mm/s and 19 mm displacement a) Voltage-time around the 35.5 ohms, b) Power-time

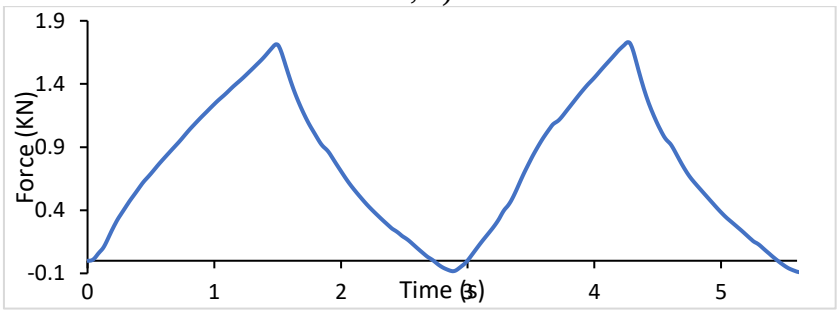

Figure 0.10: Force-time diagram of the harvester under 13 mm/s and Displacement Of 18 mm

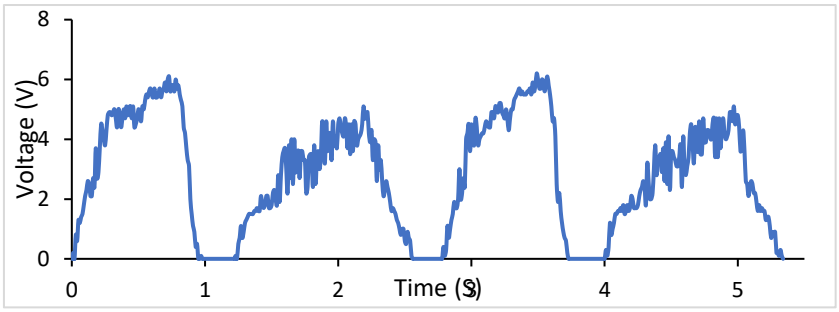

Figure 0.11: Voltage-time of the harvester under 18 mm of displacement and the speed of 13 mm/s

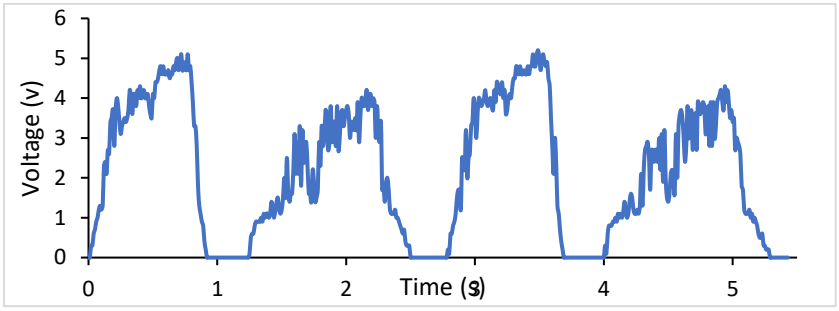

a

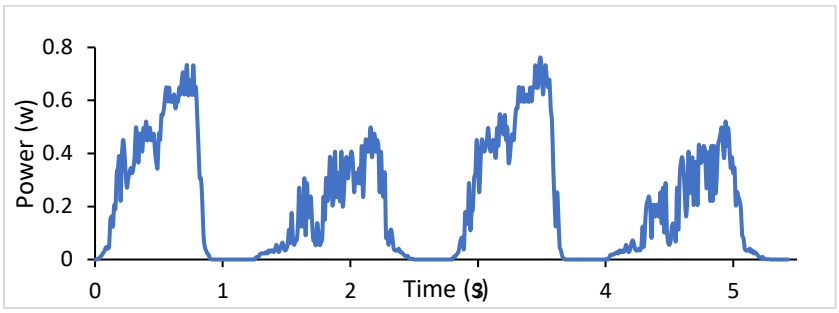

b

Figure 0.12: System's response under 13 mm/s and 18 mm displacement a) Voltage-time around the 35.5 ohms, b) Power-time

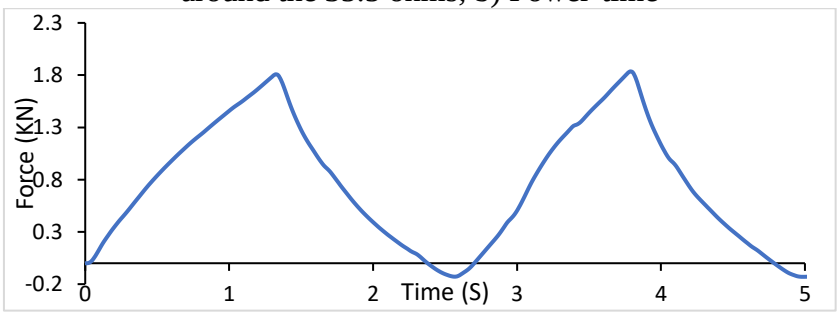

Figure 0.13: Force-time diagram of the harvester under 14.67 mm/s and Displacement Of 18 mm

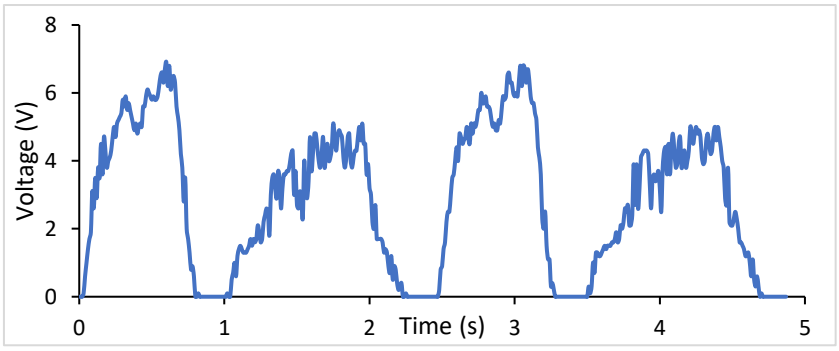

Figure 0.14:Voltage-time of the harvester under 18 mm of displacement and the speed of 14.67 mm/s

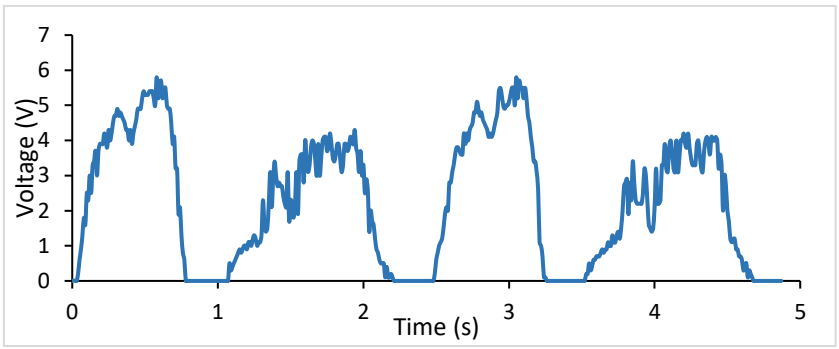

a

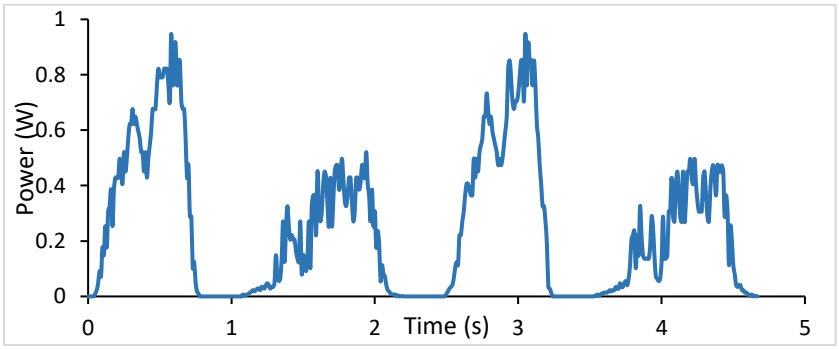

b

Figure 0.15: System's response under 14.67 mm/s and 18 mm displacement a) Voltage-time around the 35.5 ohms, b) Power-time

Spring set of 25.20 N/mm:

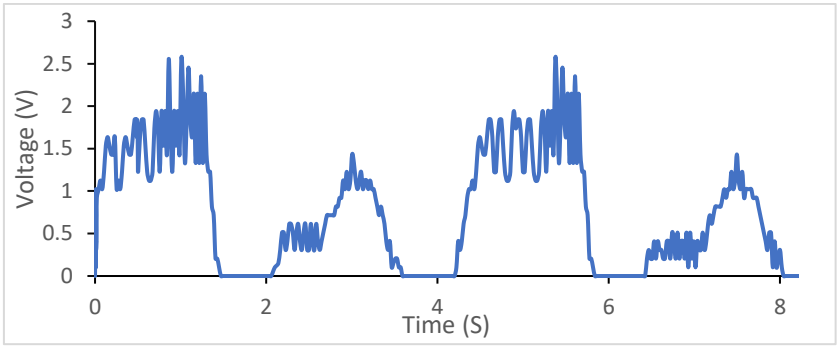

a

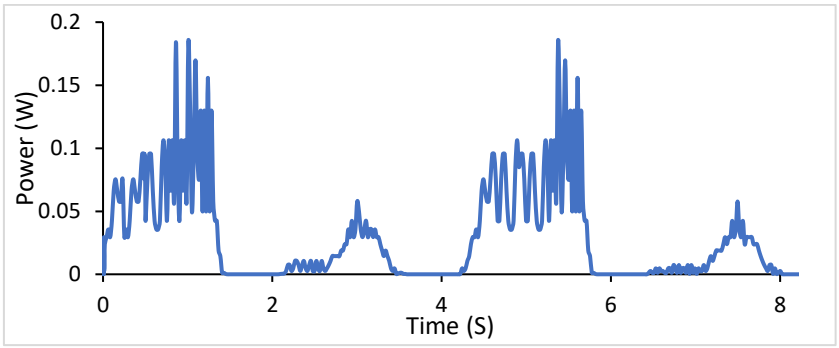

b

Figure 0.16: System's response under 5 mm/s and 10 mm displacement- spring stiffness 25.2 N/mm. a) Voltage-time around the 35.5 ohms, b) Power-time

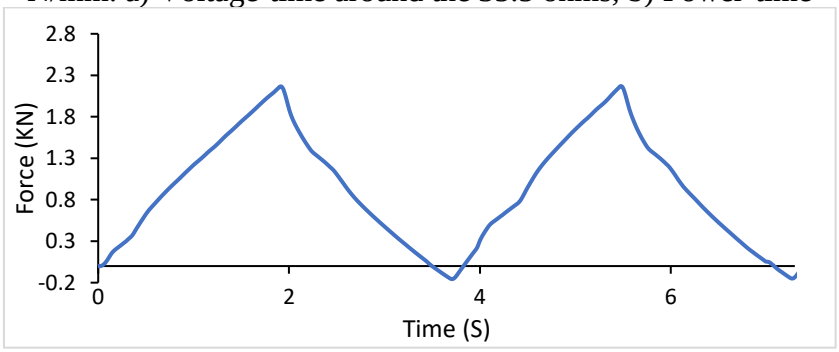

Figure 0.17: Force-time diagram of the harvester under 9 mm/s and Displacement Of 16 mm- 25.2 N spring stiffness

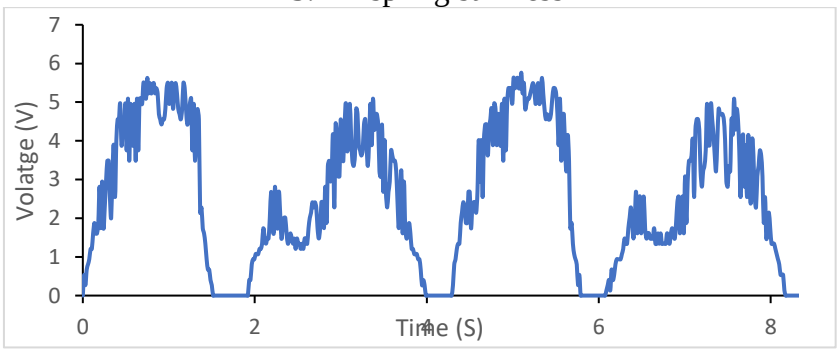

Figure 0.18: Voltage- time of the harvester under loading speed of 9 mm/s and displacement of 16 mm- Spring stiffness 25.2 N/mm

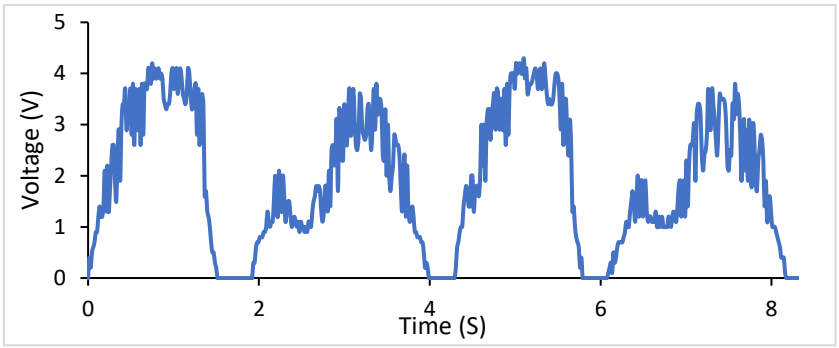

a

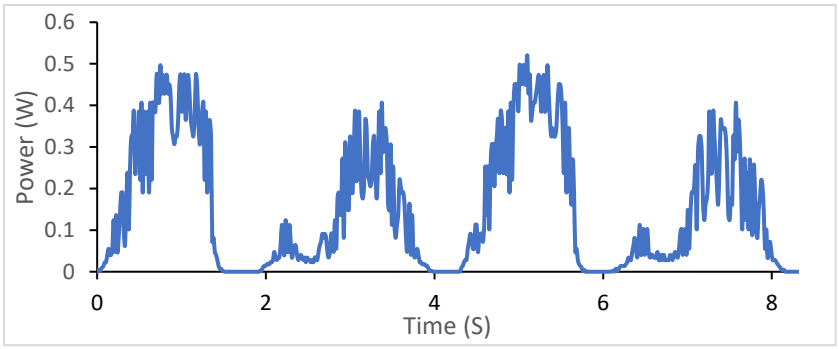

b

Figure 0.19: System's response under 9 mm/s and 16 mm displacement- spring stiffness 25.2 N/mm. a) Voltage-time around the 35.5 ohms, b) Power-time

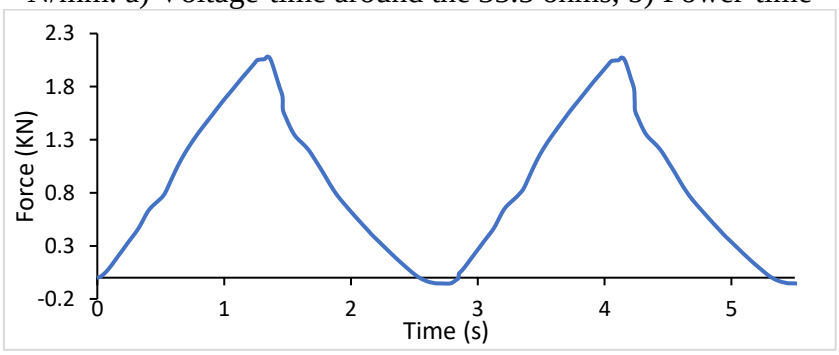

Figure 0.20: Force-time diagram of the harvester under 13 mm/s and Displacement Of 18 mm- 25.2 N spring stiffness

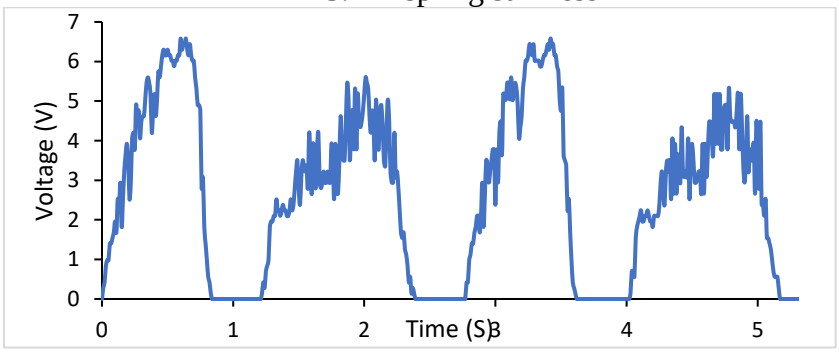

Figure 0.21: Voltage- time of the harvester under loading speed of 13 mm/s and displacement of 18 mm- Spring stiffness 25.2 N/mm

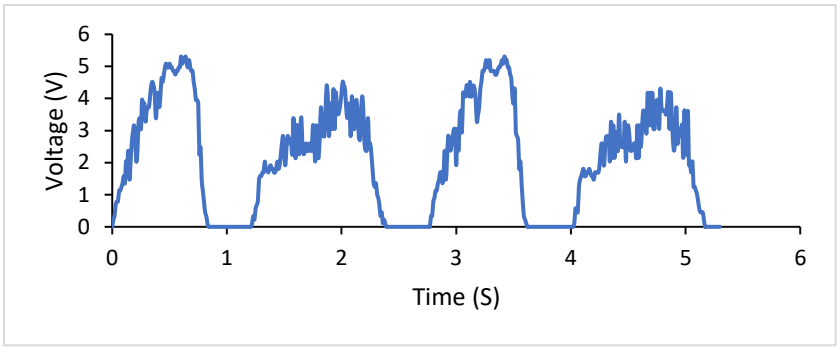

a

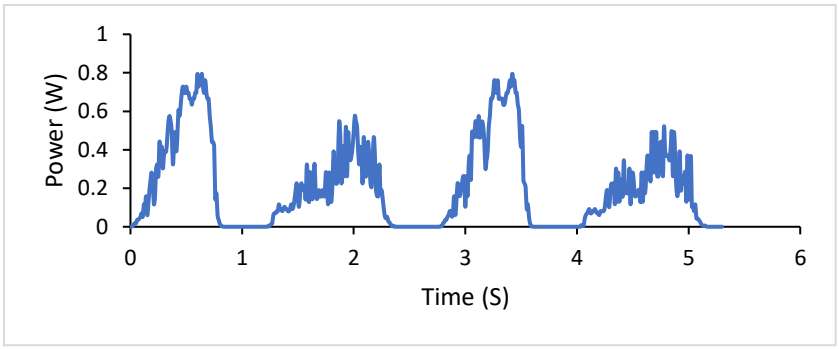

b

Figure 0.22: System's response under 13 mm/s and 18 mm displacement- spring stiffness 25.2 N/mm. a) Voltage-time around the 35.5 ohms, b) Power-time

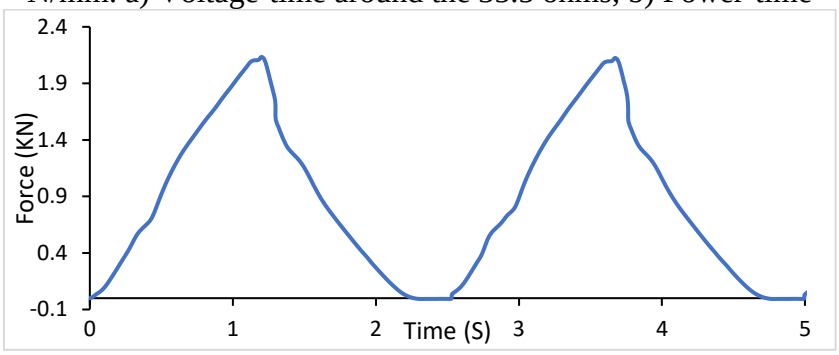

Figure 0.23: Force-time diagram of the harvester under 14.67 mm/s and Displacement Of 18 mm- 25.2 N spring stiffness

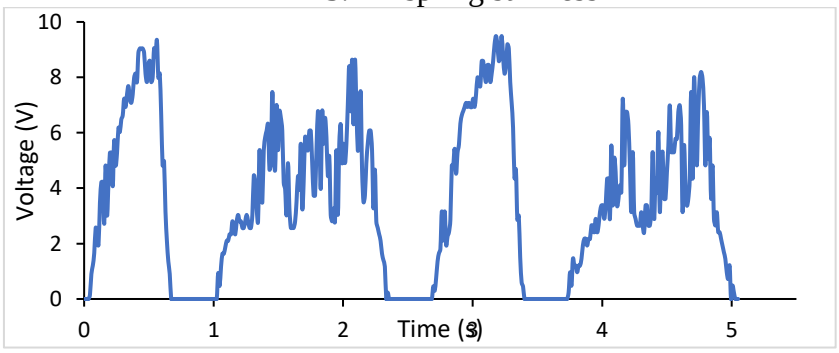

Figure 0.24: Voltage- time of the harvester under loading speed of 14.67 mm/s and displacement of 18 mm- Spring stiffness 25.2 N/mm

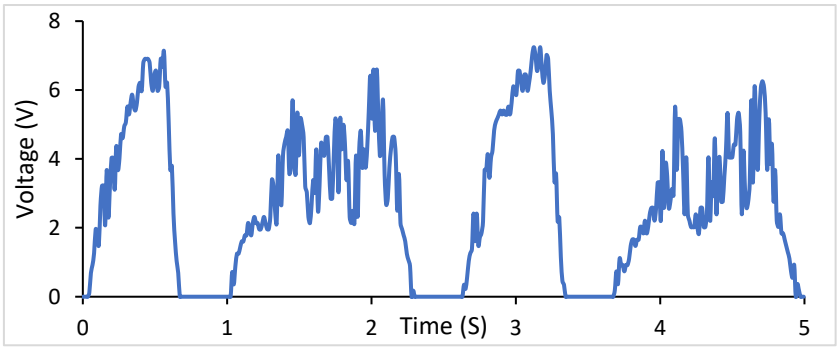

a

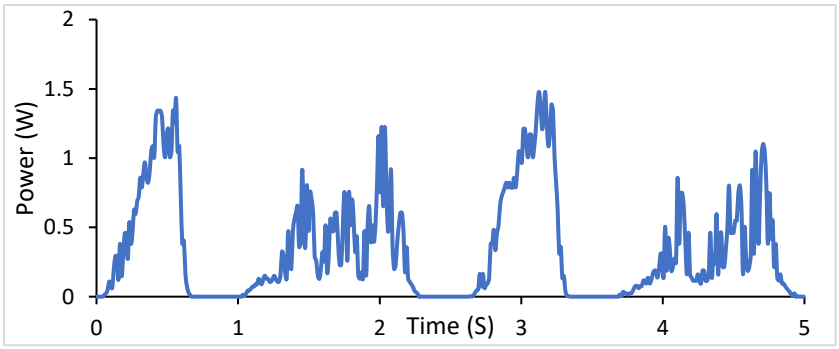

b

Figure 0.25: System's response under 14.67 mm/s and 18 mm displacement- spring stiffness 25.2 N/mm. a) Voltage-time around the 35.5 ohms, b) Power-time

Spring set of 29.77 N/mm:

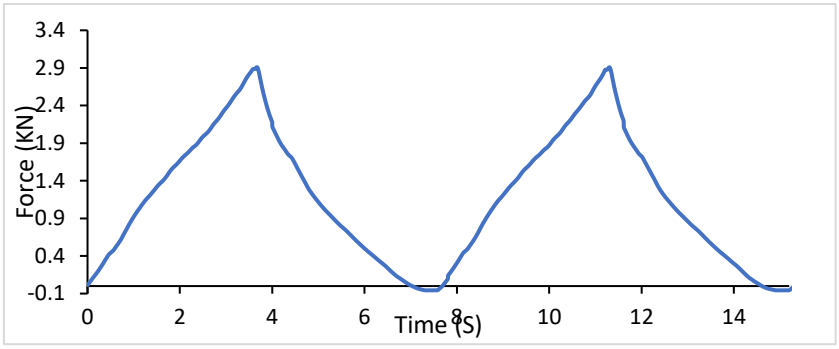

Figure 0.26: Force-time diagram of the harvester under 5 mm/s and Displacement Of 19 mm- Spring stiffness 29.77 N/mm

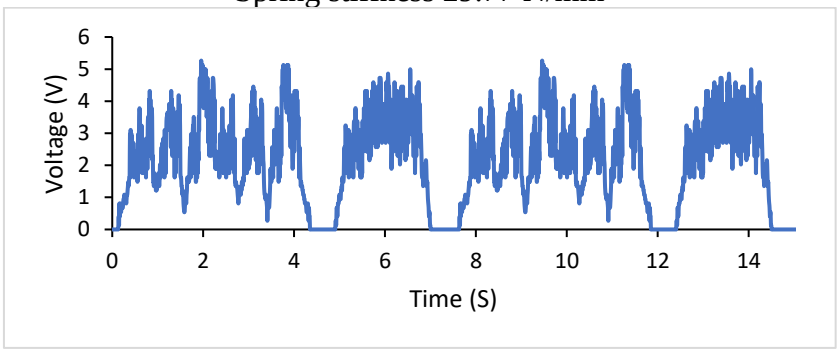

Figure 0.27: Voltage-time of the harvester under 19 mm of displacement and the speed of 5 mm/s- Spring stiffness 29.77 N/mm

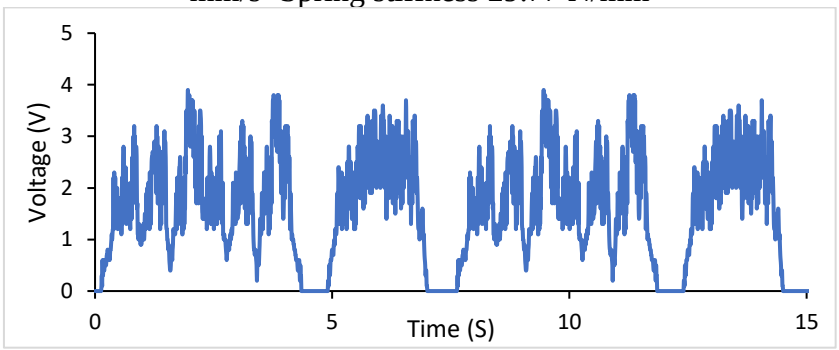

a

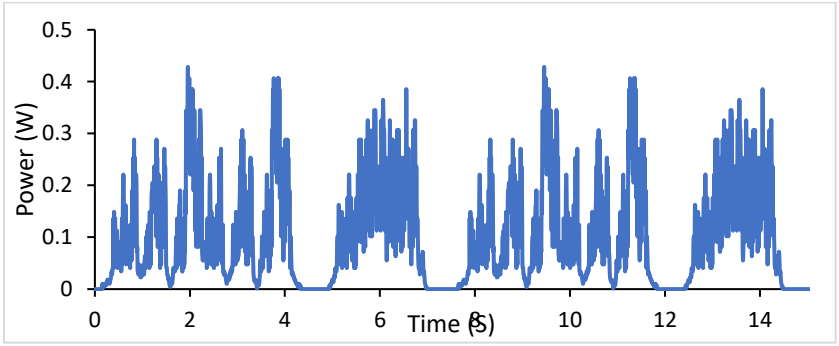

b

Figure 0.28: System's response under 5 mm/s and 19 mm displacement- Spring stiffness 29.77 N/mm a) Voltage-time around the 35.5 ohms, b) Power-time

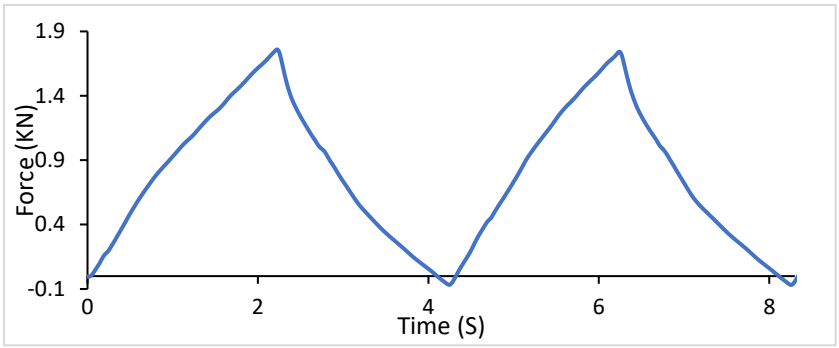

Figure 0.29: Force-time diagram of the harvester under 5 mm/s and Displacement Of 10 mm- Spring stiffness 29.77 N/mm

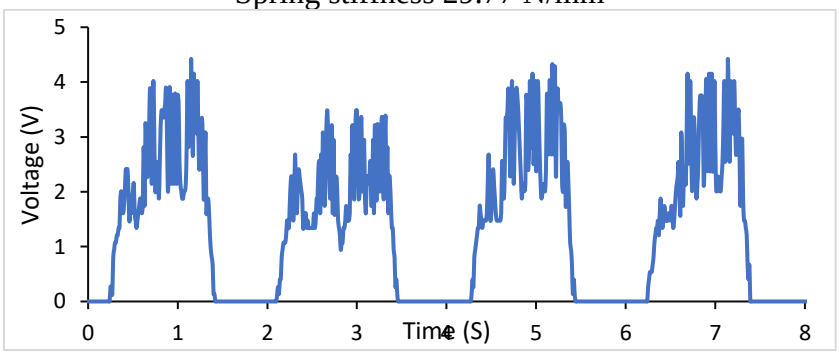

Figure 0.30: Voltage-time of the harvester under 10 mm of displacement and the speed of 5 mm/s- Spring stiffness 29.77 N/mm

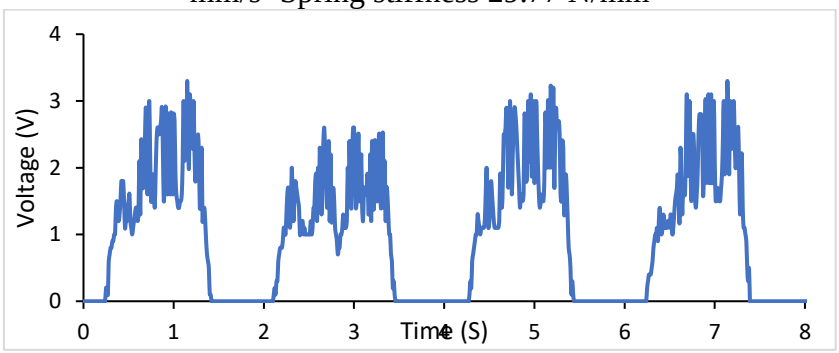

a

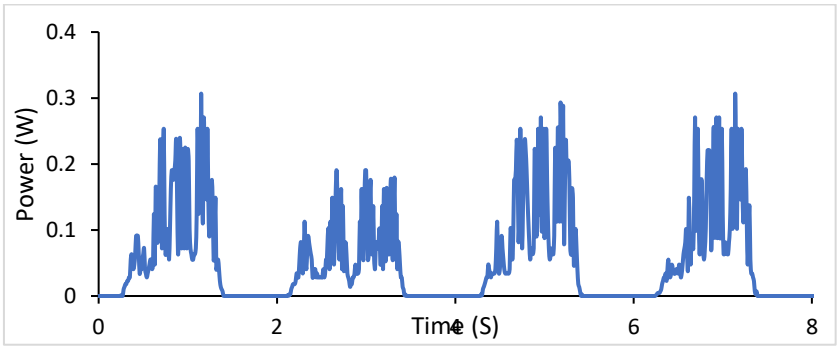

b

Figure 0.31: System's response under 5 mm/s and 10 mm displacement- Spring stiffness 29.77 N/mm a) Voltage-time around the 35.5 ohms, b) Power-time

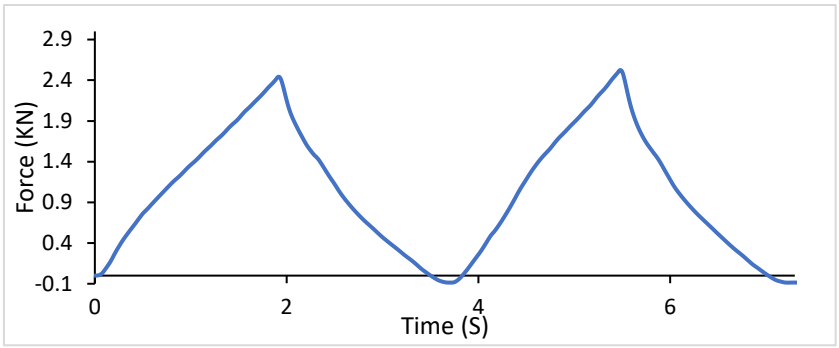

Figure 0.32: Force-time diagram of the harvester under 9 mm/s and Displacement Of 16 mm- Spring stiffness 29.77 N/mm

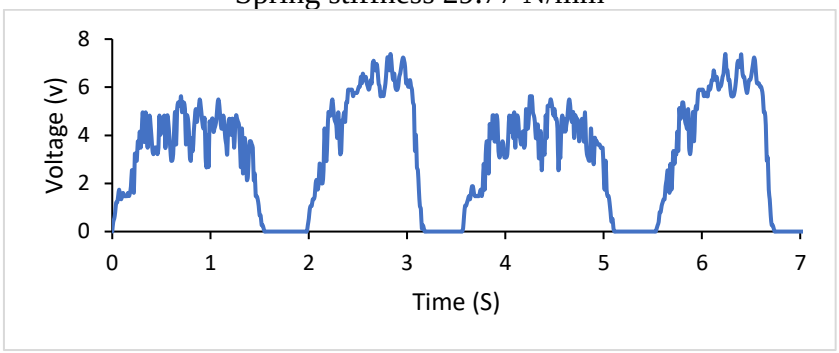

Figure 0.33: Voltage-time of the harvester under 16 mm of displacement and the speed of 9 mm/s- Spring stiffness 29.77 N/mm

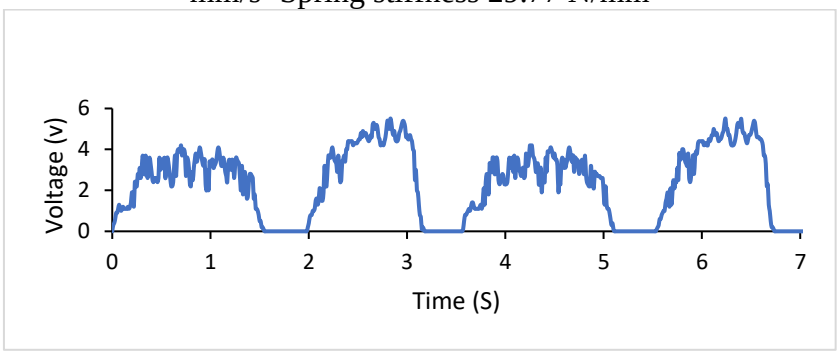

a

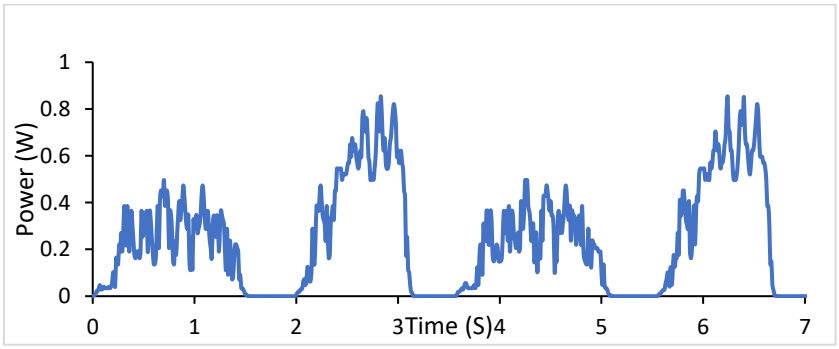

b

Figure 0.34: System's response under 9 mm/s and 16 mm displacement- Spring stiffness 29.77 N/mm a) Voltage-time around the 35.5 ohms, b) Power-time

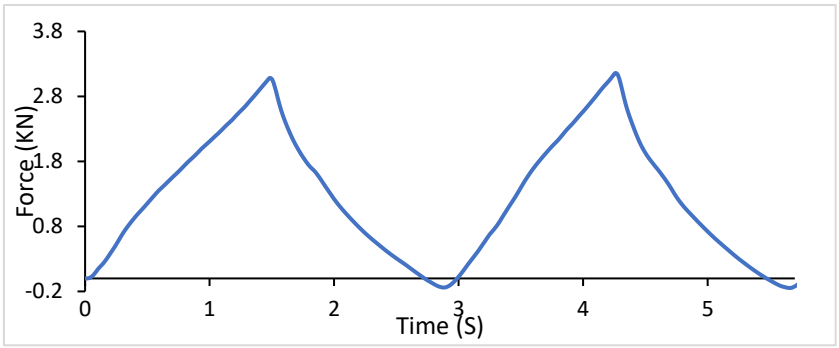

Figure 0.35: Force-time diagram of the harvester under 13 mm/s and Displacement Of 18 mm- Spring stiffness 29.77 N/mm

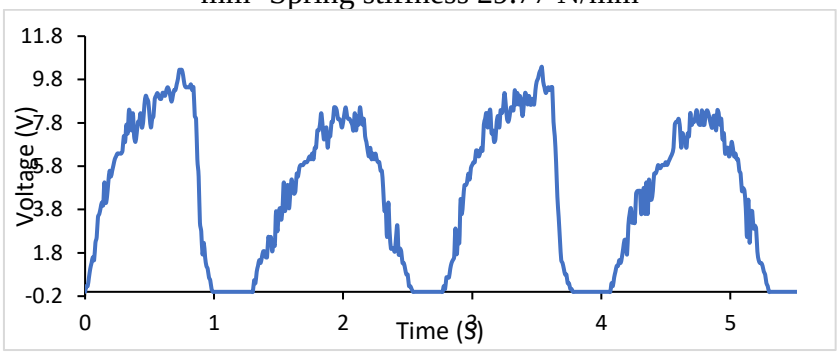

Figure 0.36: Voltage-time of the harvester under 18 mm of displacement and the speed of 13 mm/s- Spring stiffness 29.77 N/mm

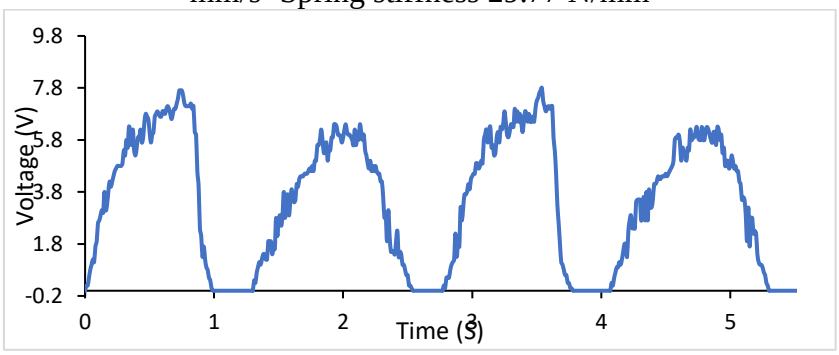

a

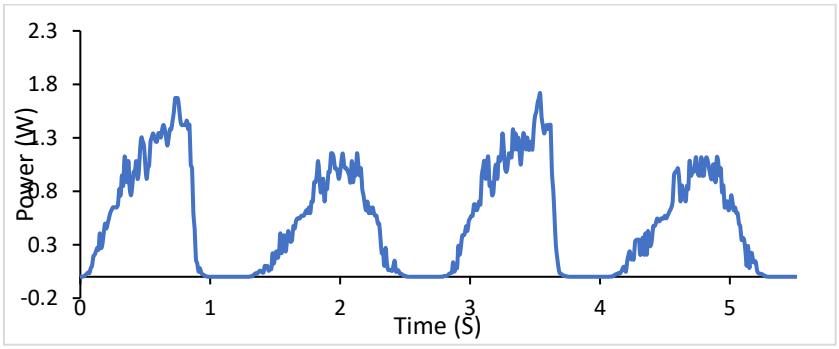

b

Figure 0.37: System's response under 13 mm/s and 18 mm displacement - Spring stiffness 29.77 N/mm a) Voltage-time around the 35.5 ohms, b) Power-time

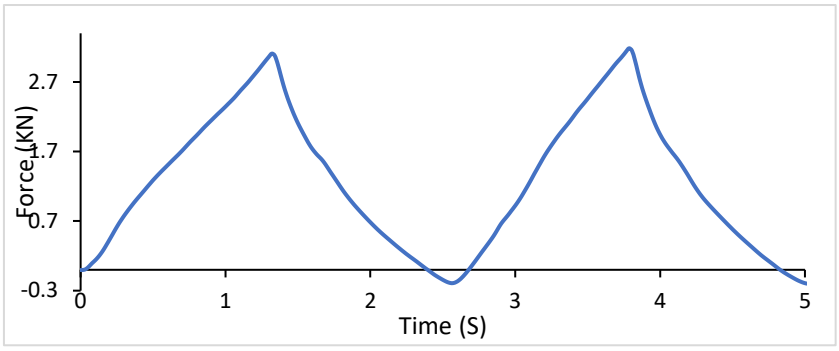

Figure 0.38: Force-time diagram of the harvester under 14.67 mm/s and Displacement Of 18 mm- Spring stiffness 29.77 N/mm

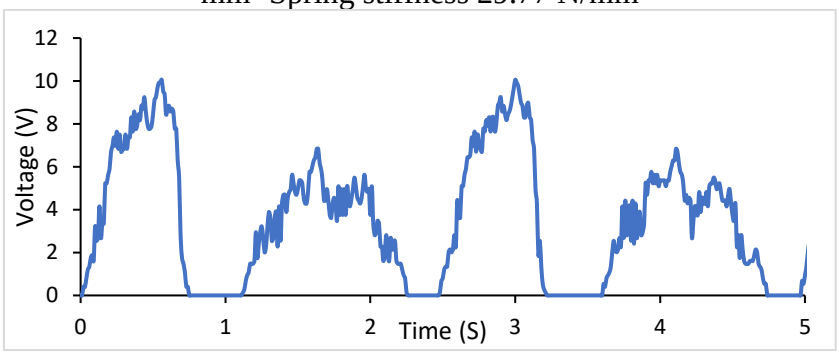

Figure 0.39: Voltage- time of the harvester under loading speed of 14.67 mm/s and displacement of 18 mm- Spring stiffness 29.77 N/mm

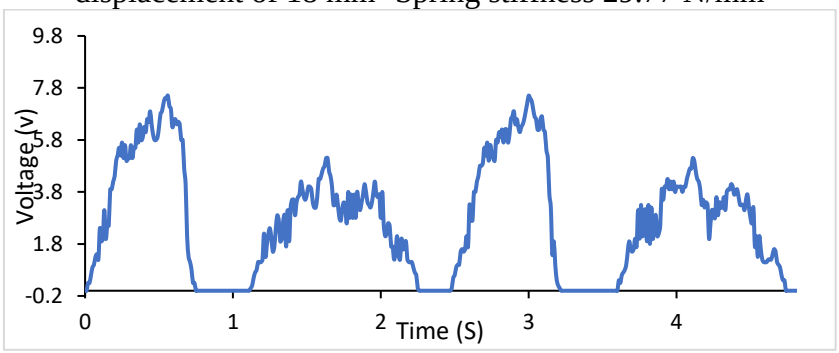

a

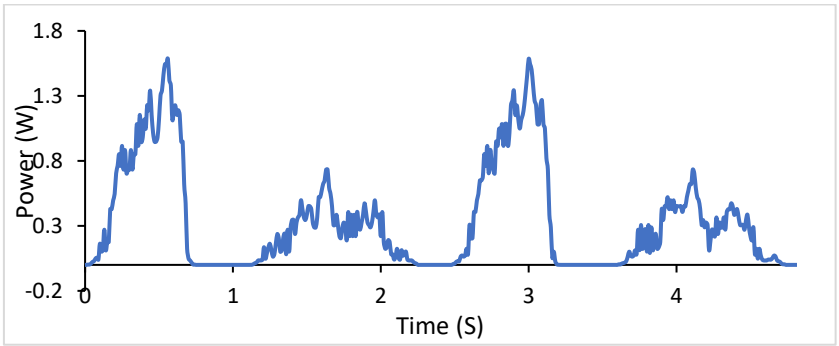

b

Figure 0.40: System's response under 14.67 mm/s and 18 mm displacement- spring stiffness 29.77 N/mm. a) Voltage-time around the 35.5 ohms, b) Power-time

37.88 N/mm

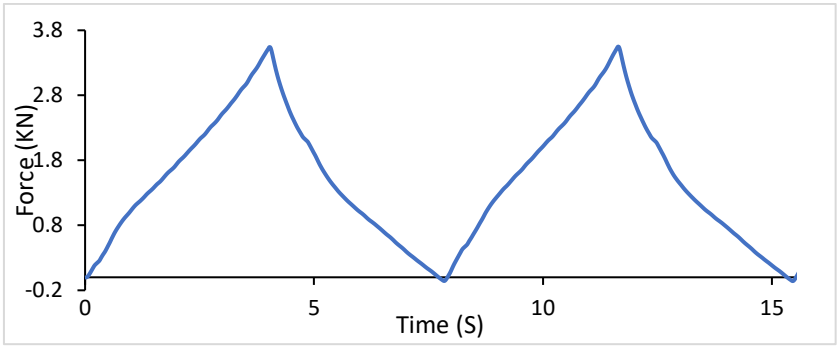

Figure 0.41: Force-time diagram of the harvester under 5 mm/s and Displacement Of 19 mm- 37.88 N/mm spring stiffness

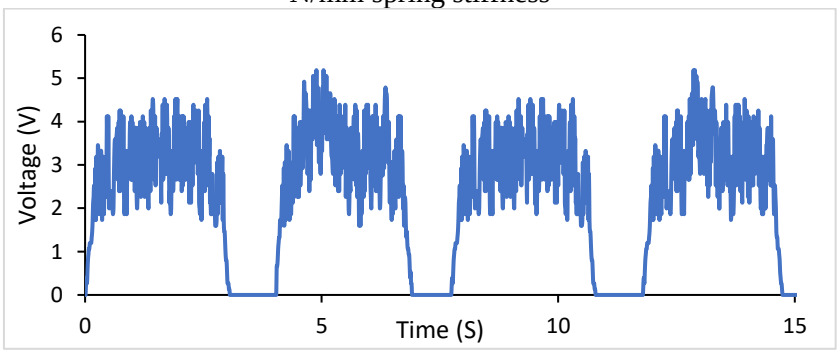

Figure 0.42: Voltage- time of the harvester under loading speed of 5 mm/s and displacement of 19 mm- Spring stiffness 37.88 N/mm

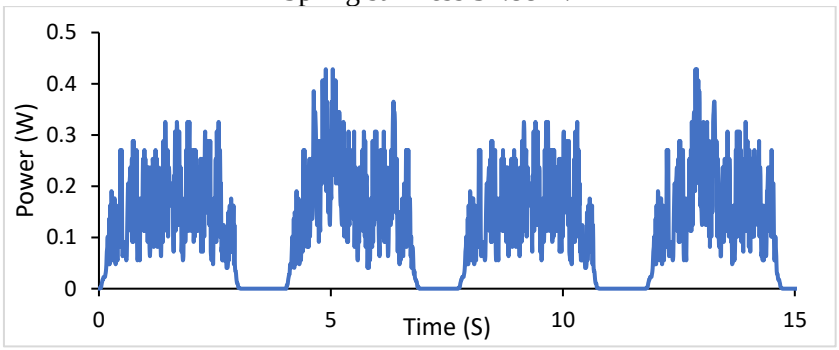

Figure 0.43: Power time diagram of the harvester with the springs' stiffness of 37.88 N/mm, under the loading scenario of 5 mm/s loading speed and 19 mm displacement

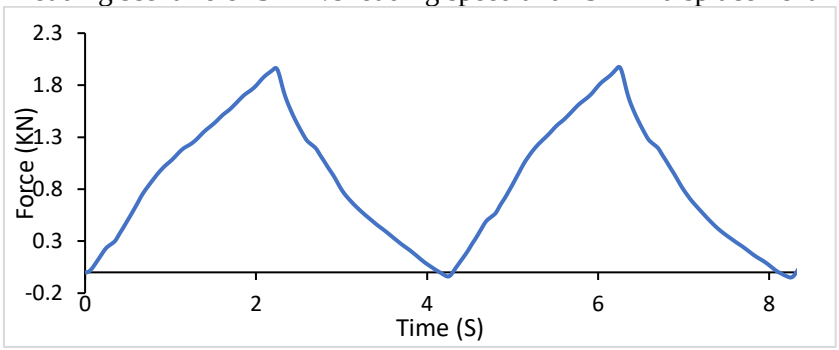

Figure 0.44: Force-time diagram of the harvester under 5 mm/s and Displacement Of 10 mm- 37.88 N/mm spring stiffness

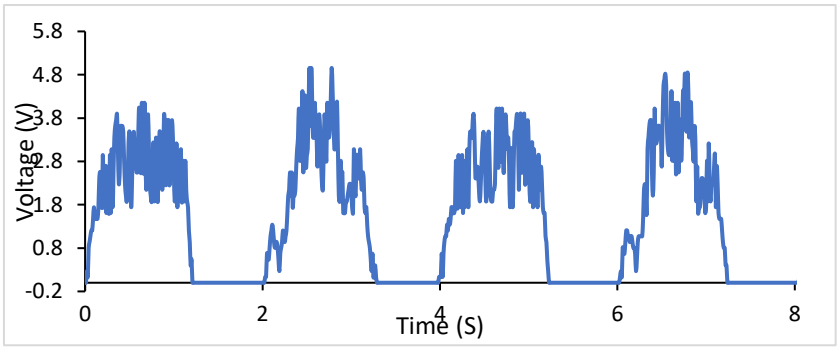

Figure 0.45: Voltage- time of the harvester under loading speed of 5 mm/s and displacement of 10 mm- Spring stiffness 37.88 N/mm

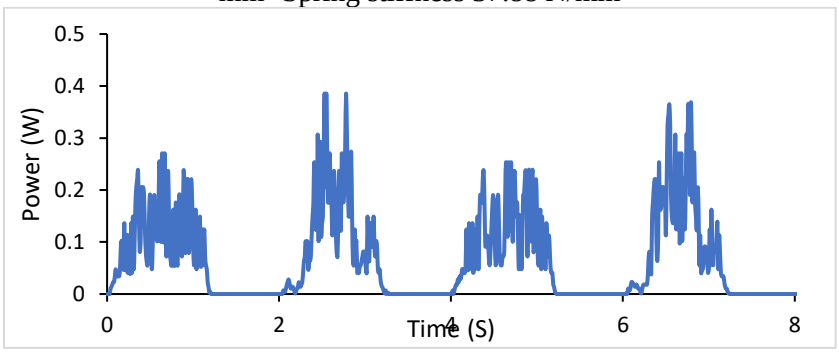

Figure 0.46: Power time diagram of the harvester with the springs' stiffness of 37.88 N/mm, under the loading scenario of 5 mm/s loading speed and 10 mm displacement

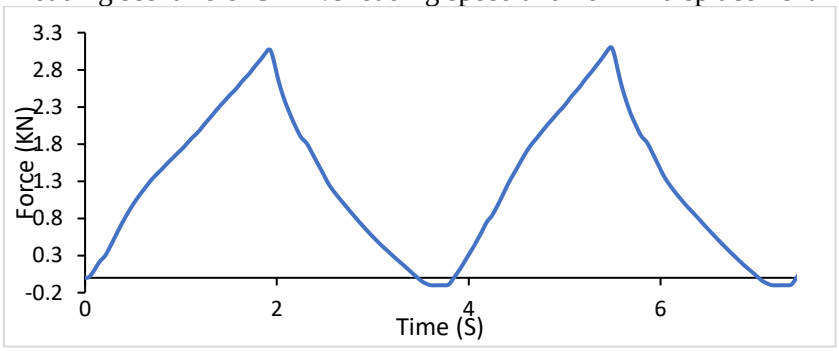

Figure 0.47: Force-time diagram of the harvester under 9 mm/s and Displacement Of 16 mm- 37.88 N/mm spring stiffness

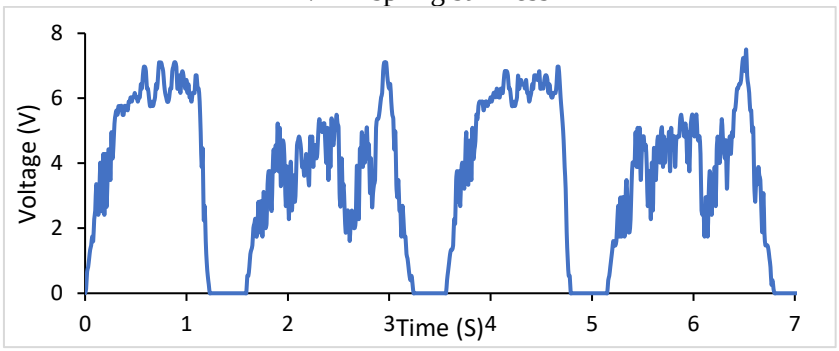

Figure 0.48: Voltage- time of the harvester under loading speed of 9 mm/s and displacement of 16 mm- Spring stiffness 37.88 N/mm

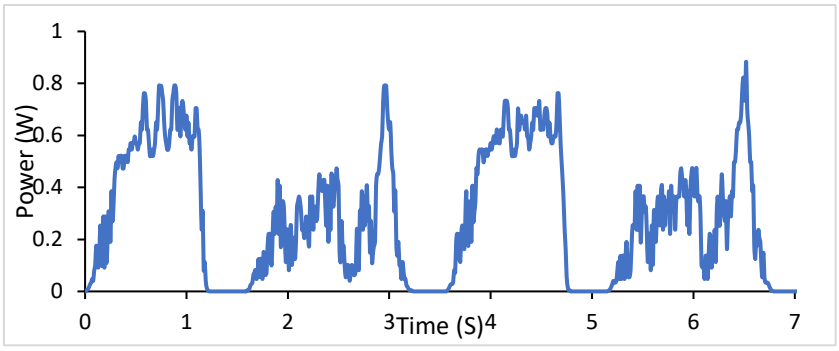

Figure 0.49: Power time diagram of the harvester with the springs' stiffness of 37.88 N/mm, under the loading scenario of 9 mm/s loading speed and 16 mm displacement

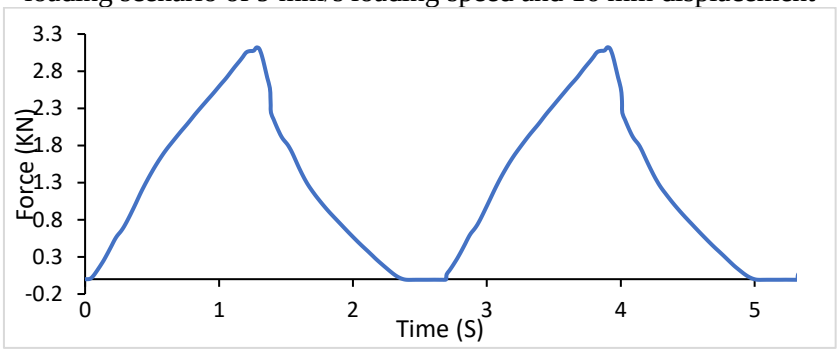

Figure 0.50: Force-time diagram of the harvester under 13 mm/s and Displacement Of 18 mm- 37.88 N/mm spring stiffness

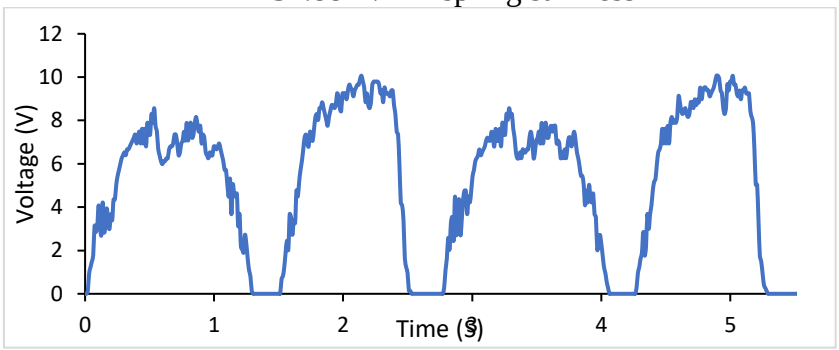

Figure 0.51: Voltage- time of the harvester under loading speed of 13 mm/s and displacement of 18 mm- Spring stiffness 37.88 N/mm

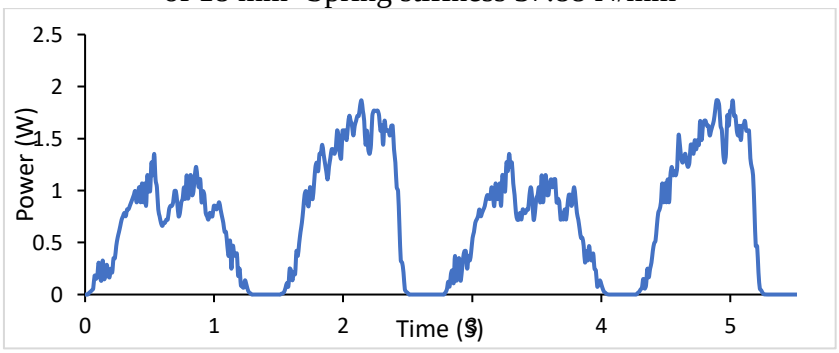

Figure 0.52: Power time diagram of the harvester with the springs' stiffness of 37.88 N/mm, under the loading scenario of 13 mm/s loading speed and 18 mm displacement

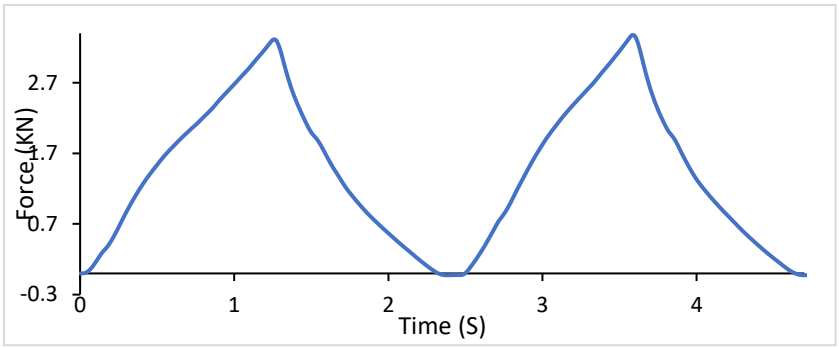

Figure 0.53: Force-time diagram of the harvester under 14.67 mm/s and Displacement Of 18 mm- 37.88 N/mm spring stiffness

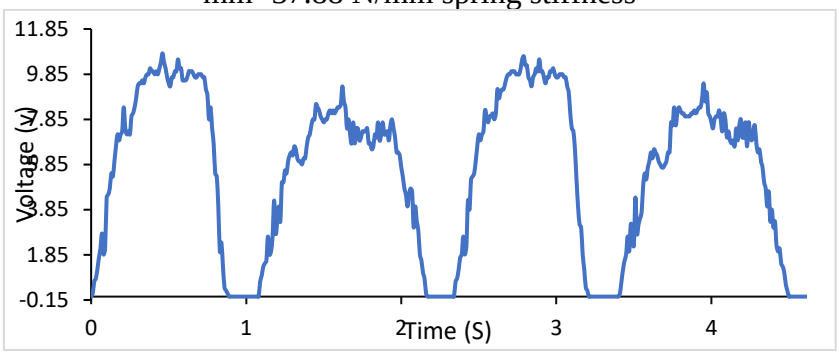

Figure 0.54: Voltage- time of the harvester under loading speed of 14.67 mm/s and displacement of 18 mm- Spring stiffness 37.88 N/mm

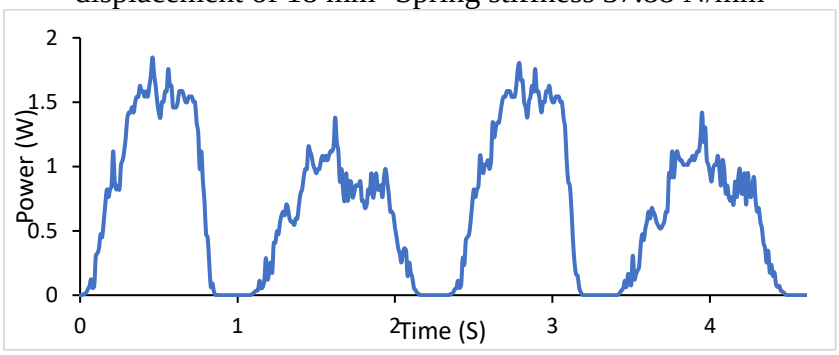

Figure 0.55: Power time diagram of the harvester with the springs' stiffness of 37.88 N/mm, under the loading scenario of 14.67 mm/s loading speed and 18 mm displacement

Spring Set of 43.54 N/mm

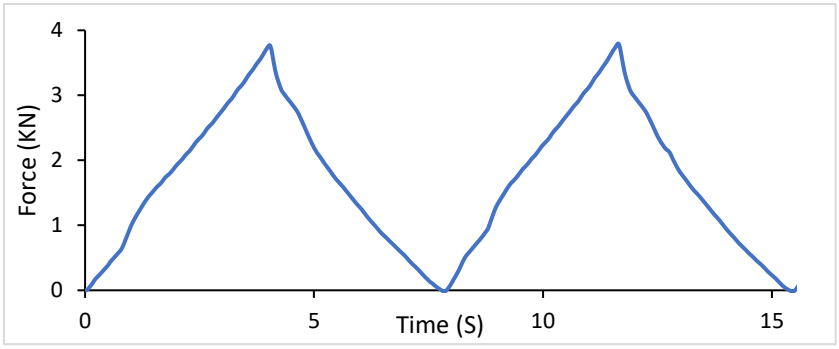

Figure 0.56: Force-time diagram of the harvester under 5 mm/s and Displacement Of 19 mm- 43.54 N/mm spring stiffness

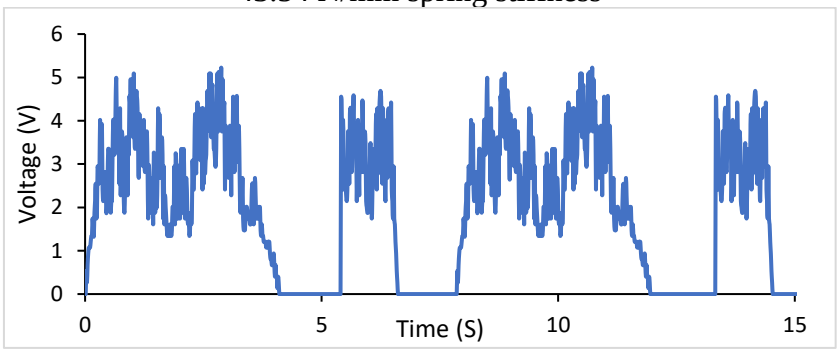

Figure 0.57: Voltage- time of the harvester under loading speed of 5 mm/s and displacement of 19 mm- Spring stiffness 43.54 N/mm

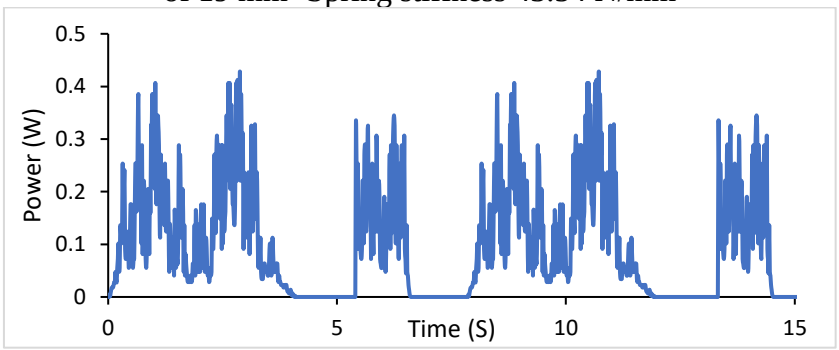

Figure 0.58: Power time diagram of the harvester with the springs' stiffness of 43.54 N/mm, under the loading scenario of 5 mm/s loading speed and 19 mm displacement

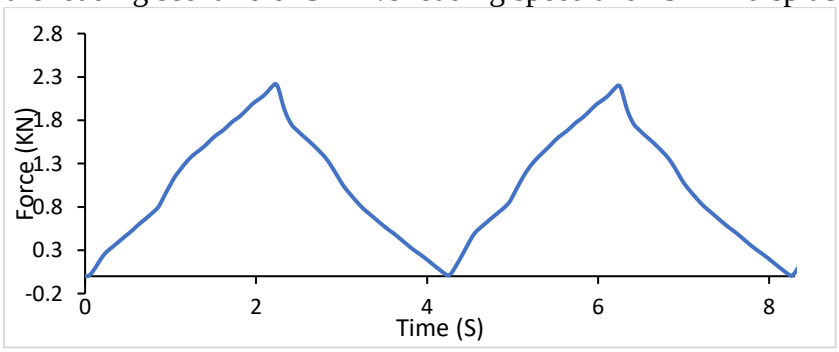

Figure 0.59: Force-time diagram of the harvester under 5 mm/s and Displacement Of 10 mm- 43.54 N/mm spring stiffness

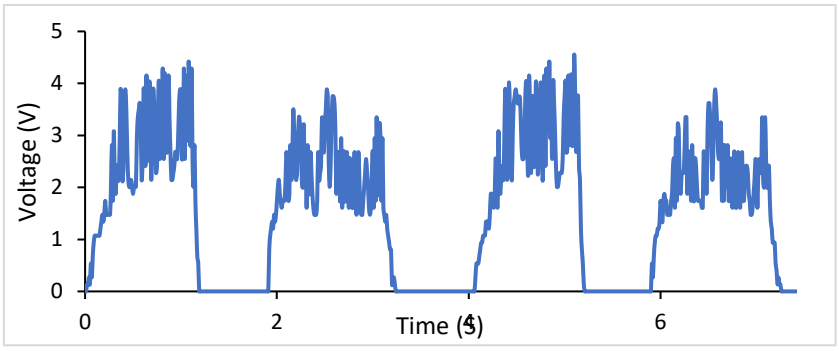

Figure 0.60: Voltage- time of the harvester under loading speed of 5 mm/s and displacement of 10 mm- Spring stiffness 43.54 N/mm

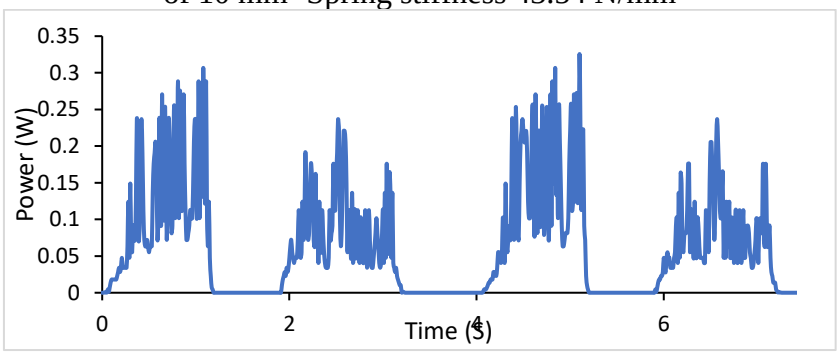

Figure 0.61: Power time diagram of the harvester with the springs' stiffness of 43.54 N/mm, under the loading scenario of 5 mm/s loading speed and 10 mm displacement

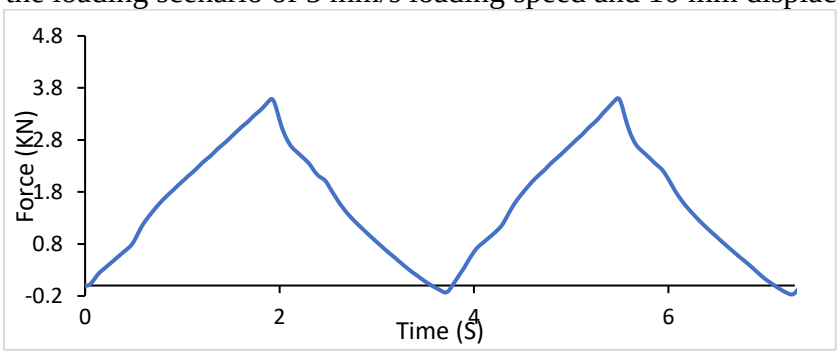

Figure 0.62: Force-time diagram of the harvester under 9 mm/s and Displacement Of 16 mm- 43.54 N/mm spring stiffness

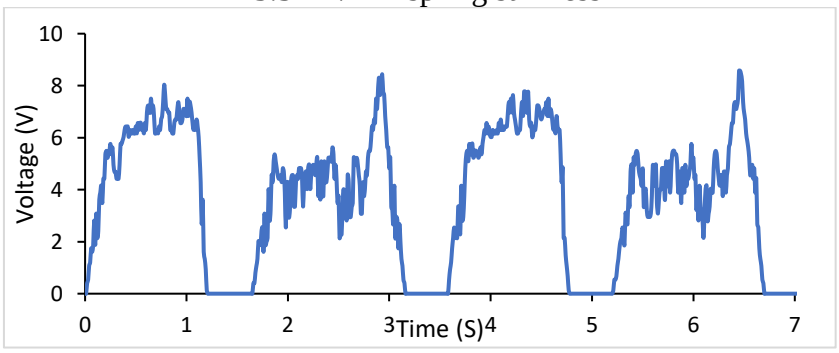

Figure 0.63: Voltage- time of the harvester under loading speed of 9 mm/s and displacement of 16 mm- Spring stiffness 43.54 N/mm

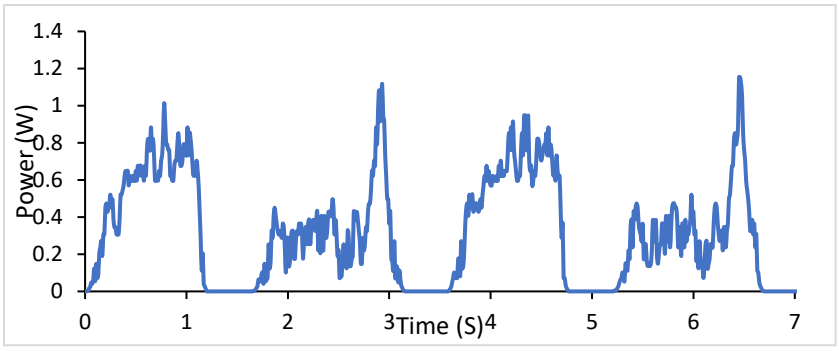

Figure 0.64: Power time diagram of the harvester with the springs' stiffness of 43.54 N/mm, under the loading scenario of 9 mm/s loading speed and 16 mm displacement

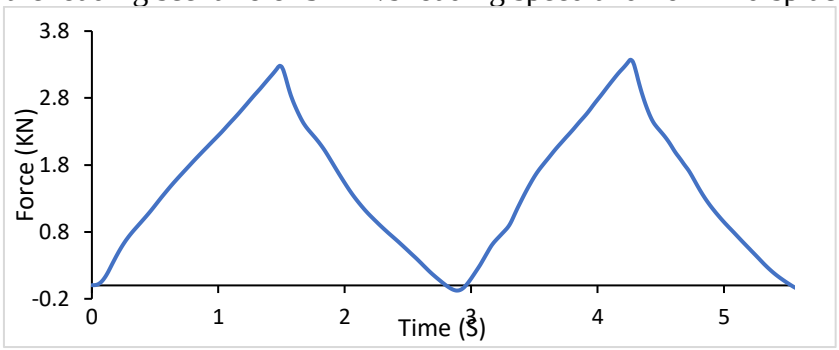

Figure 0.65: Force-time diagram of the harvester under 13 mm/s and Displacement Of 18 mm- 43.54 N/mm spring stiffness

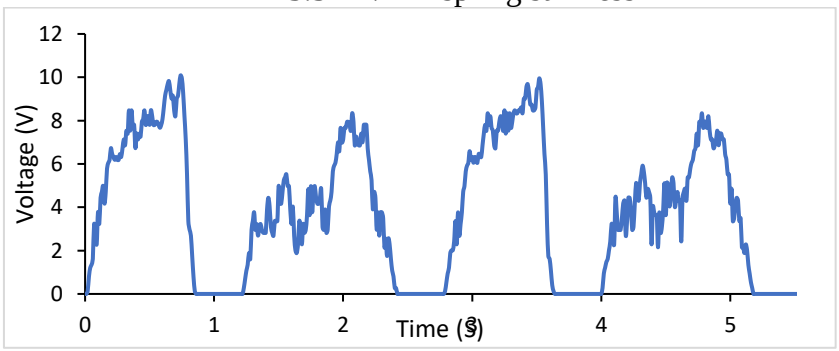

Figure 0.66: Voltage- time of the harvester under loading speed of 13 mm/s and displacement of 18 mm- Spring stiffness 43.54 N/mm

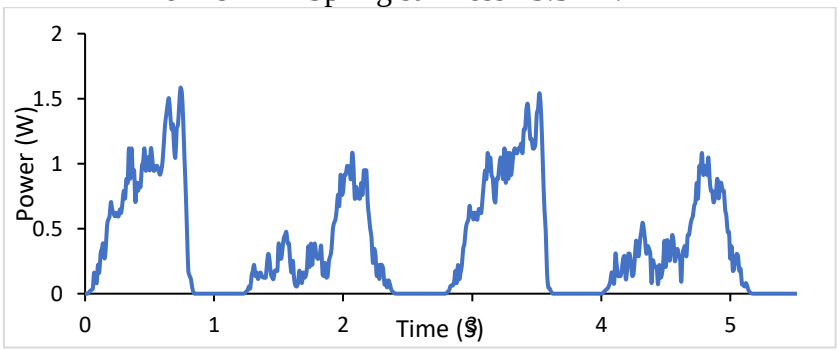

Figure 0.67: Power time diagram of the harvester with the springs' stiffness of 43.54 N/mm, under the loading scenario of 13 mm/s loading speed and 18 mm displacement

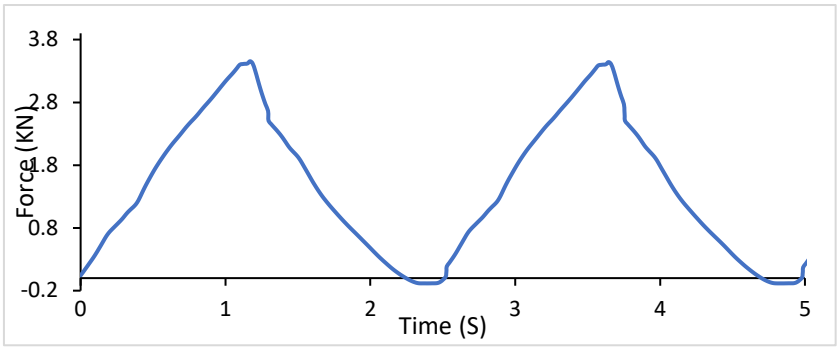

Figure 0.68: Force-time diagram of the harvester under 14.67 mm/s and Displacement Of 18 mm- 43.54 N/mm spring stiffness

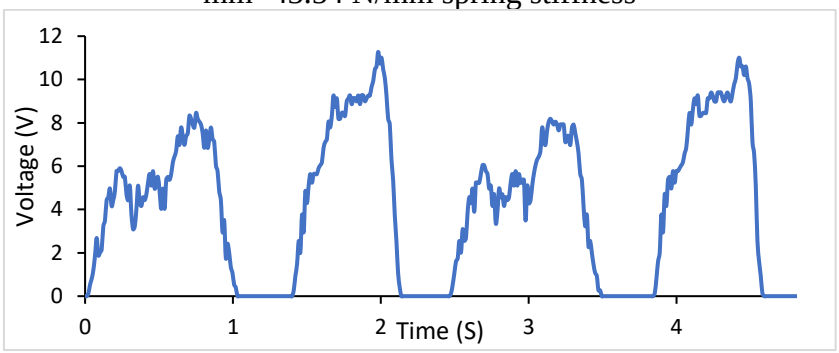

Figure 0.69: Voltage- time of the harvester under loading speed of 14.67 mm/s and displacement of 18 mm- Spring stiffness 43.54 N/mm

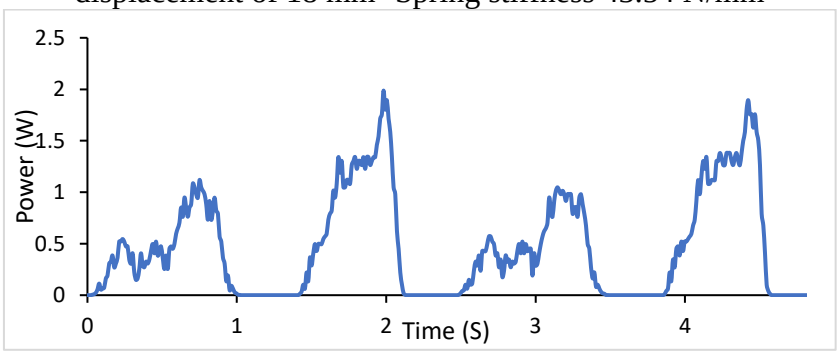

Figure 0.70: Power time diagram of the harvester with the springs' stiffness of 43.54 N/mm, under the loading scenario of 14.67 mm/s loading speed and 18 mm displacement